CORA Cork Open Research Archive
Cartlann Taighde Oscailte Chorcaí

Title	Alternative materials for flexible transparent conductive electrodes
Authors	Lordan, Daniel
Publication date	2017
Original Citation	Lordan, D. 2017. Alternative materials for flexible transparent conductive electrodes. PhD Thesis, University College Cork.
Type of publication	Doctoral thesis
Rights	© 2017, Daniel Lordan. - http://creativecommons.org/licenses/by-nc-nd/3.0/
Download date	2025-07-03 23:07:21
Item downloaded from	https://hdl.handle.net/10468/3891

UCC
University College Cork, Ireland
Coláiste na hOllscoile Corcaigh

Ollscoil na hÉireann

NATIONAL UNIVERSITY OF IRELAND

Alternative materials for flexible transparent conductive electrodes

A thesis Presented to

The National University of Ireland

for the degree of

Doctor of Philosophy

By

Daniel Lordan

Supervised by Dr. Aidan Quinn, Dr. Mícheál Burke & Dr. Mary Manning

Tyndall National Institute

Institiúid Náisiúnta

Tyndall National Institute

University College Cork

April 2017

Table of Contents

Declaration ..... **vii**

Acknowledgements ..... **viii**

Abstract ..... **xi**

Glossary of Acronyms ..... **xiii**

1 Introduction to transparent conductive electrodes

1.1 Introduction 2

1.2 Industry requirements for transparent conductive electrodes 2

1.3 Transparent conductive oxides 6

1.4 Alternative materials to TCO technologies 9

1.5 Figure of merit for transparent conductors 12

1.6 Applications and market 13

1.7 Aim of thesis 14

1.8 Outline of thesis 15

1.9 Bibliography 17

2 Synthesis of graphene for use as a flexible transparent conductive electrode

2.1 Introduction 24

2.2 Crystal and band structure 25

2.3 Electrical properties 28

2.3.1 Graphene field effect device 28

2.4 Optical properties 31

2.4.1 Transmittance 31

2.5 Mechanical properties 33

2.6 Motivation for this work 35

2.7 Graphene fabrication methods 35

2.7.1 Mechanical exfoliation 35

2.7.2 Liquid exfoliation 36

2.7.3 Epitaxial growth of graphene 37

2.7.4 Chemical vapour deposition growth of graphene 38

2.8 Materials and methods 45

2.8.1 Growth of graphene by chemical vapour deposition 45

2.9 Characterisation of graphene, methods and approaches 50

2.9.1 Optical characterisation 50

2.9.2 Visualisation of graphene domains on copper foil 51
2.9.3 Topographical characterisation 56
2.10 Results and Discussion 60
2.10.1 CVD graphene grown on copper foil 60
2.10.2 Optimising graphene growth on Cu foil: Low growth time regime, Cu pre-treatment, substrate geometry and copper foil purity 62
2.10.3 Increasing growth pressure: Effect on domain size 68
2.10.4 Continuous growth of CVD graphene 71
2.11 Conclusions 76
2.12 Bibliography 78

3 Wet chemical transfer of CVD graphene to silicon dioxide and glass substrates

3.1 Introduction and motivation 86
3.2 CVD graphene transfer methods 87
3.2.1 Wet chemical transfer process 87
3.2.2 Dry transfer process 88
3.2.3 Electrochemical delamination 88
3.2.4 Thermal release tape and roll-to-roll transfer process 89
3.3 Materials and methods 90
3.3.1 Tyndall CVD graphene transfer protocol 90
3.3.2 Tyndall transfer protocol with heated acetone 91
3.4 Characterisation 91
3.5 Results and discussion 93
3.5.1 Initial transfer of commercially grown graphene 93
3.5.2 Transfer & characterisation of commercial CVD graphene using transfer protocol and heated acetone 94
3.5.3 Transfer of continuous CVD graphene grown in Tyndall 107
3.5.4 Atomic Force Microscopy of transferred continuous CVD graphene 108
3.5.5 Transparency of continuous CVD graphene 109
3.5.6 Graphene Field Effect Devices (GFEDs) 109
3.6 Conclusion 111
3.7 Bibliography 114

4 Metal meshes on rigid substrates for transparent conductive electrodes

4.1 Introduction and motivation 118
4.2 Thin film deposition methods 123
4.2.1 Atomic Layer Deposition overview 123
4.2.2 ALD film growth by self-limiting half reactions 124

4.2.3 Typical ALD film growth process 126
4.3 Physical vapour deposition techniques 128
4.3.1 Vacuum deposition (evaporation) overview 129
4.3.2 Advantages and disadvantages of PVD, CVD and ALD techniques 129
4.3.3 Zone model diagrams 131
4.3.4 Thin film growth mechanisms 132
4.4 Photolithography, Lift-off and dry etching 134
4.5 Experimental methods 138
4.5.1 Metal thin film growth 138
4.6 Mask Design for lithography 139
4.7 Fabrication of metal mesh structures 142
4.7.1 Preparation of substrates for evaporation, ALD and sputter deposition 142
4.7.2 Platinum mesh structures via evaporation 143
4.7.3 Platinum mesh structures via ALD 143
4.7.4 Platinum mesh structures via sputter deposition 144
4.8 Characterisation 145
4.8.1 Topographical characterisation 145
4.8.2 Optical characterisation 145
4.8.3 Electrical Characterisation 146
4.9 Results and discussion 149
4.9.1 Thin film growth 149
4.9.2 Metal meshes for transparent electrodes 162
4.10 Conclusion 170
4.11 Bibliography 171

5 Metal meshes for use as flexible transparent conductive electrodes

5.1 Introduction 178
5.2 Materials and methods 178
5.2.1 Fabrication of Pt metal meshes on flexible plastic substrates 178
5.3 Characterisation 179
5.3.1 Optical characterisation 179
5.3.2 Electrical characterisation 179
5.4 Results and discussion 179
5.4.1 Transparency and haze of flexible substrates 179
5.4.2 Two terminal resistance, sheet resistance, transparency and haze of transparent metal meshes fabricated on flexible PET 180
5.4.3 Effect of mechanical stability based on fractional resistance change, transparency change and figure of merit 183

5.4.4 SEM comparison of as fabricated and flexed metal meshes on flexible substrates 188
5.5 Conclusion 190
5.6 Bibliography 191

6 Asymmetric pentagonal metal meshes for flexible transparent electrodes and heaters

6.1 Introduction 194
6.2 Materials and methods 195
6.2.1 Fabrication of metal mesh devices on flexible plastic substrates 195
6.3 Characterisation 195
6.3.1 Optical and electrical characterisation 195
6.3.2 Transparent heater characterisation 196
6.4 Results and discussion 196
6.4.1 Transparency and haze of pentagonal metal meshes on flexible PET 196
6.4.2 Two point resistance and sheet resistance of asymmetric pentagonal metal meshes 199
6.4.3 Mechanical stability of pentagonal metal meshes after cyclic bending 201
6.4.4 Platinum pentagonal metal meshes for use as transparent heaters 207
6.4.5 Platinum pentagonal metal mesh and graphene hybrid electrode 214
6.4.6 Platinum pentagonal metal mesh heater as a de-icer 216
6.5 Conclusion 218
6.6 Bibliography 219

7 Conclusion 223

8 Suggestions for future work 227

Appendix A - Degradation of Thermal CVD system in Tyndall 229

Appendix B - Derivations of transmission for mesh geometries 233

Appendix C - Supplementary material for chapter 6 243

Appendix D - Miscellaneous 251

Declaration

This thesis is my own work unless otherwise stated in the relevant sections.

The work presented in this thesis has not been submitted for another degree, either at University College Cork or elsewhere.

The present thesis is submitted for the degree of Doctor of Philosophy at University College Cork.

Daniel Lordan

Signature _____

Date _____

Acknowledgements

Firstly, I would like to thank my three supervisors, Dr. Aidan Quinn, Dr. Mícheál Burke and Dr. Mary Manning for giving me this opportunity to carry out my doctorate thesis. Dr. Aidan Quinn has put up with a lot from me during my postgraduate degree and he was very helpful in regards to preparing reports, presentations, and publications. I felt I was at ease when coming to him with any problems and he is without a doubt the smartest person I have ever met. A very special shout out to Micheal Burke, who wasn't only my supervisor but my friend. I could tell instantly that this guy just oozes science and is very dedicated to his work. I hope he gets to realise his dream of military research. Although Mary was absence for some parts of my degree, she was very insightful and I could come to her with any problems that arose either academic or personal. I would like to acknowledge my thesis committee consisting of a solitary Dr. Simon Elliot for his support, advice and suggestions during my progress review meetings.

I would like to thank all the supervisors, staff members and postdocs in the NTG group. To all past and future students in the group, especially Sean (babez), Amelie, Dan, Keith, Darragh, Colm, Micki, Fabrizio, Carola, Niamh, Caoimhe and Alfonso. We had some great times together and I will always remember it. A big thanks to Roxane Puicervert who was also working on graphene with me (and later became my office buddy). I wish her all the best for the future and I will definitely miss our office chats. I would also like to thank Ethel and Andrea who I lived with for three years when I first started my PhD.

Huge thanks to people outside of the NTG group in Tyndall as well; Dave Pierce was a great friend and we used to have great chats about fantasy football and football in general. Richard Davis and I would chat about video games and always chatted to me when I saw him.

A big thanks to Vince Gallagher from the maintenance team in Tyndall and Sandy Disselduff from Tetreon. These two (especially Vince) were a massive help when setting up the CVD system for graphene growth and if I had problems with recipes. I don't think I could have set up the machine and got any results for my graphene chapter without them. Also I would like to thanks Alan Blake for helping me with the initial use of the ALD reactor. I would also like to thank members of the

Speciality Products and Services group in Tyndall. Mainly Dan O' Connell, Colin Lyons, Joe O' Brien and Alan Hydes for their service. Also Dr. Andreas Amann for helping me with the derivation of the unit cell for the newly discovered pentagon.

I would also like to thank my family. Even though I have six sisters (I'm the youngest), I get on well with all of them. I especially enjoyed coming down home and going for coffee with them. I would especially like to thank my parents who encouraged me to continue my study. Without their support, I don't think this would have been possible. My girlfriend's family, Kaz, Keri (Skinner), Alice and Eva (caaaard boy) were very supportive throughout my Ph.D. I loved coming up to see them in Offaly and Galway.

I would also like to thank a few friends outside of Tyndall. Friends from secondary school who I still keep in contact with such as Finn, Dowd, Conor, Alan and Luke. Also college friends such as Ferdinand (Rio/Les), Diarmuid, Eoin, Niall, QDogg and Keith. I would especially like to thank Sean and Sorcha. Our friendship grew immensely over the course of my postgraduate study and they helped me through the tough times.

But I think the biggest thanks I have to give is to my girlfriend of 11 years Kate Liffey Faherty who I love very much. She has helped me immensely throughout my postgraduate study. Without her, I think I would have given up. But she kept telling me to persist even through the hard times. It was all worth it in the end.

And finally, thank you for reading this thesis.

P.S. A big shout out to Tyrion the hamster. You won't be forgotten.

May you rest in peace.

Abstract

This thesis investigates new alternative materials for flexible transparent electrodes: monolayer graphene and micron-scale metal mesh structures.

Growth of graphene on copper foils by chemical vapour deposition (CVD) was investigated by commissioning and developing a CVD system in Tyndall. Initial growth runs resulted in poor graphene coverage. Several routes for growth improvement were examined: an acid pre-treatment, substrate geometry and growth pressure. Following this improvement, a continuous growth run was carried out displaying high monolayer graphene coverage.

Graphene was transferred to Si/SiO_2 (90 nm thermal oxide) and glass substrates using a wet chemical transfer process. This process involves the use of a polymer which acts as a support mechanism. However, polymer residue can have drastic effects on the electrical performance of CVD graphene films. Therefore an alternative method for polymer removal with the use of heated acetone (~ 60 ^{o}C) was investigated.

Micron-scale platinum mesh structures were fabricated on rigid glass substrates using a range of metal deposition techniques; metal evaporation and lift-off; ALD and dry etching and sputter deposition and dry etching. Square, hexagonal, circular and a new asymmetric pentagonal tiling were utilised as metal meshes. Their performance were investigated along with the metal deposition technique. Evaporation and lift-off provided the most consistent technique in relation to transparency, haze and sheet resistance.

Finally, asymmetric pentagonal platinum meshes were fabricated on flexible transparent substrates using metal evaporation and lift-off. All designs were bent around a radius of curvature (in air) of ~ 3.8 mm up to 1,000 bending cycles for both tension and compression and suggested good performance in comparison to literature. All three designs were used as transparent heaters via Joule heating. All heaters demonstrated good thermal characteristics such as low response times and high thermal resistances. Finally, a pentagonal metal mesh was used to de-ice a glass substrate.

LIST OF ACRONYMS

(In order of appearance in the main text)

OLED	Organic light emitting diode
LCD	Liquid crystal display
TCO	Transparent conductive oxide
TO	Tin oxide
ITO	Tin-doped indium oxide
IO	Indium oxide
RF	Radio Frequency
PET	Polyethylene terephthalate
FTO	Fluorine-doped tin oxide
AZO	Aluminium-doped zinc oxide
CVD	Chemical vapour deposition
PEDOT	Poly(3,4-ethylenedioxythiophene)
PSS	Polystyrensulfonic acid
UV	Ultra-violet
FOM	Figure of merit
PDMS	Polydimethylsiloxane
SDBS	Sodium dodecyl benzonesulfanate
SDS	Sodium dodecyl sulfanate
TFSA	Bis(trifluoromethanesulfonyl)amide
DC	Direct current
EMI	Electromagnetic interference
GFED	Graphene field-effect device
CGS	Centimetre-gram-second

MKS	Metre-kilogram-second
HOPG	Highly ordered pyrolytic graphite
DMF	N,N-dimethylformamide
NMP	N-methylpyrrolidone
LPCVD	Low pressure chemical vapour deposition
IPA	Isopropyl alcohol
APCVD	Atmospheric pressure chemical vapour deposition
PE-CVD	Plasma enhanced chemical vapour deposition
CNW	Carbon nanowall
CLP	Closed loop pressure
SOS	Smart over-temperature system
DI	Deionised
SCCM	Standard cubic centimetres per minute
AFM	Atomic Force Microscopy
AC	Alternating current
SEM	Scanning electron microscope
PMMA	Polymethyl methacrylate
RPM	Revolutions per minute
RIE	Reactive ion etcher
FWHM	Full width at half maximum
ID	Identification
PVD	Physical vapour deposition
ALD	Atomic layer deposition
NIL	Nanoimprint lithography
RML	Rolling mask lithography

EHD	Electrohydrodynamic
ALE	Atomic layer epitaxy
PE-ALD	Plasma-enhanced atomic layer deposition
GPC	Growth per cycle
TMA	Tri-methyl aluminium
RMS	Root mean square
PEN	Polyethylene naphthalate
NA	Not applicable
NW	Nanowire

"*Audere est Facere – To dare is to do*"

Motto of Tottenham Hotspur Football Club

1 Introduction to transparent conductive electrodes

1.1 Introduction

Transparent conductive electrodes are used in a variety of applications such as thin film solar cells, liquid crystal displays, touch panel displays and inorganic/organic light emitting diodes (LEDs) [1-6]. Materials that are highly conductive, such as metals, are opaque and do not allow visible light to transmit through them easily. Conversely, materials that are transparent, such as oxides, are often insulating. The plasma frequency of metals resides in the ultra-violet region and this causes metals to reflect light in the visible range as the frequency is below the plasma frequency [7]. If the frequency of the light is bigger than the plasma frequency, the light is transmitted since the electrons in the metal do not respond quickly enough to screen the light.

The challenge is to decouple the properties of conductors and insulators so that one can achieve a highly transparent material that is also conductive. Past research efforts have involved increasing the conductivity of dielectric materials via doping without altering their intrinsic transparency by much e.g. doping indium oxide with tin [8], doping zinc oxide with aluminium [9] and doping tin oxide with fluorine [10]. There is a high demand in the consumer electronics industry to produce cost efficient, large size and flexible devices. Product markets such as organic light emitting diode (OLED) lighting, wearable electronics and "smart" windows are expected to rise based on consumer demands in the next decade. Based on this market trend, the industry requirements of transparent conductive electrodes is discussed below.

1.2 Industry requirements for transparent conductive electrodes

Industry requirements for transparent conductive electrodes are challenging and include low sheet resistance, high optical transparency, low fractional light scatter (haze), low surface roughness, flexibility, low cost and ease of manufacturing. The intrinsic electrical properties of a material is determined from its conductivity, σ (S/cm) = $n_e e\mu$, where n_e is the free carrier concentration (cm^{-3}), μ ($cm^2V^{-1}S^{-1}$) is the carrier mobility and e (measured in coulombs) is the charge of an electron. The resistivity of a bulk material (Ω-cm), sometimes denoted as the specific/volume resistance is an intrinsic property of a material and is the inverse of conductivity.

Resistivity is defined in terms of resistance (*R*), length (*l*) and cross-sectional area (*A*) of the material as

$$\rho_{Bulk} = \frac{RA}{L} = \frac{R(w.t)}{L} \quad \textbf{(1.1)}$$

Electrical resistivity, which is an intrinsic property of a bulk material should remain constant and should be independent of thickness. However, if the thickness becomes comparable to that of the electron mean free path in the material, the resistivity increases [11, 12]. Other scattering phenomena, such as surface and grain boundary scattering can also increase the resistivity. When the thickness of a thin conductive film is increased, the resistivity decreases to that of bulk. The resistance of a thin conductive film of uniform thickness is described by sheet resistance, *Rs*

$$R_s \equiv \frac{Rw}{L} \quad \textbf{(1.2)}$$

It can be related to its thin film resistivity by multiplying the equation above by the thickness of the film.

$$\rho = R_s.t \quad \textbf{(1.3)}$$

The unit of sheet resistance is Ω. To differentiate it from resistance, sheet resistance is given the units of "ohms per square", Ω/sq. The square unit represents that the value of resistance will remain constant if the measurement is taken over any square area of the film's surface. Sheet resistance can be reduced by increasing the thickness of the conductive layer, but this increase causes losses in the optical transparency of the film. Different transparent conductive electrode applications require differing values of sheet resistance as indicated below in Figure 1.1. The sheet resistance can be measured using a 4 probe method which was first demonstrated by Van der Pauw [13]. This will be discussed in more detail in chapter 4. The Van der Pauw method is usually used for isotropic materials i.e. the sheet resistance is approximately equal in all directions (x and y). However, for some nanomaterials materials such as carbon nanotubes, the sheet resistance in the x and y direction differ greatly due to aggregation [14, 15]. These are called anisotropic materials. Methods such as finite element analysis can be used to calculate the sheet resistance of these anisotropic materials [16].

Application	Required sheet resistance (Ω_{squ})
Antistatic layers	500–2000
Electrodes for touch screens	400–700
Electrodes for light-emitting films (inorganic electroluminescence)	20–120
Electrodes for organic electroluminescence	20
Electrodes for solar cells	8–80
Flexible electrochromics	1–10

Figure 1.1: Typical sheet resistance requirements for differing transparent conductive electrode applications on flexible substrates [17].

Measuring the sheet resistance over large scale i.e. millimetre or centimetre gives a good indication of the suitability of the device at that scale for use as a transparent electrode. However, the sheet resistance is influenced by microscopic features such as defects e.g. cracks, voids, grain boundaries and rough surfaces which can be introduced during film deposition [18]. Thus measuring at large scale suggests that the film is homogenous which may not be the case.

Optical transparency is the ability of light to pass through a material in relation to scattering losses. Devices such as touch screens or LCD displays requires transmittance of $\geq 85\%$. Calculations suggest that thin metal films (< 5 nm) such as platinum can provide a suitable optical transmittance, e.g. > 70% (Figure 1.2) [19]. However evaporated or sputtered Pt films are often discontinuous at these thicknesses, which increases the sheet resistance. Besides high optical transparency, another important optical based parameter for transparent conductive electrodes is optical haze [20, 21]. Haze is defined as percentage of the transmitted light passed through the sample that is diffusively scattered. Low haze is desirable to avoid blurriness [22].

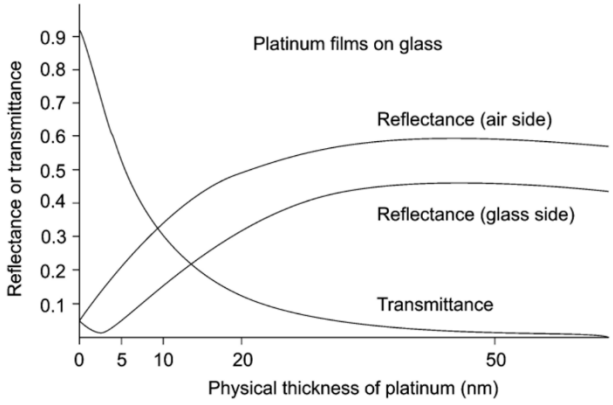

Figure 1.2: Transmittance and reflectance plots for a platinum film on glass (increasing thickness in nm), which were calculated from the optical constants of the bulk metal [19].

Consumer electronic devices usually require a low surface roughness [23]. For example, OLED lighting devices requires roughness values < 10 nm. With the advances of modern mobile phone technology and the dawn of wearable electronics, more and more consumers are searching for mobile phone devices that are durable and thinner. The use of a flexible screen instead of glass is desired to utilise this property. As of April 2016, there are ~ 1.5 million results in relation to broken smart phone screens on Google, which suggest a flexible screen would be in high demand.

Low cost and ease of manufacture are important for transparent conductive electrodes. The cost of materials reflects on the price of said material integrated onto a device. An important selling point for manufacturers is the low cost of their product. Large scale production of transparent conductive electrode based devices is important and factors such as elemental material cost, cost of deposition and the ability for large scale fabrication is of utmost importance. Most flexible electronics will be integrated onto flexible substrates such as plastics and therefore the temperature at which the process is undertaken is important as to not degrade or damage the plastic substrate.

From the criteria mentioned above, many factors have to be taken into consideration when choosing a material for a transparent conductive electrode. Transparent conductive oxides are the most widely used materials for transparent electrode applications, however they have several drawbacks especially in regard to mechanical stability. These issues are discussed below in section 1.3.

1.3 Transparent conductive oxides

Transparent conductive oxides (TCOs) are materials that possess both high optical transparency and high electrical conductivity. The properties of TCOs arise from the use of a highly doped, wide-bandgap semiconductor [24]. High optical transparency is achieved by these materials in the visible region (wavelength, λ in the region of 400 nm to 700 nm) due their wide-bandgap (E_g in the range of 3.2 eV to 4.1 eV) which is larger than photon energies, E_{ph} (in the range of 1.8 eV to 3 eV). The conductive nature of TCOs arises from free charge carriers resulting from deviations in stoichiometry and/or the incorporation of dopants. For example, as deposited indium oxide lacks stoichiometry which gives rise to oxygen vacancies in the crystal lattice. An impurity band is created by these oxygen vacancies which overlaps at the bottom of the conduction band. An oxygen vacancy in indium oxide donates two electrons for conduction [25]. Electrons can also be generated in indium oxide by doping this structure with elements that have a higher valence than indium e.g. tin which donates one electron for conduction [26]. These two processes account for the high conductivity of ITO films. Most commonly utilised TCOs have electrons as free carriers (n-type semiconductors). However, TCOs based on p-type semiconductors have been fabricated, although their properties are much worse than the n-type materials [27]. The electronegativity of oxygen is quite high which results in a strong localisation at the valence band edge in oxygen ions. When p-type carriers i.e. holes are introduced at the valence band edge, they are strongly localised in oxygen ions and a trap is produced. This prevents the holes from migrating within the crystal lattice itself which accounts for the reduced carrier mobilities of p-type TCOs in relation to n-type [27].

The first TCO film was produced in 1907 and consisted of a thin film of cadmium oxide (CdO) which was fabricated by thermal oxidation of a sputter-deposited cadmium film [28]. Currently, the use of this TCO is limited due to toxicity concerns [29]. Oxidation of physical vapour deposited metal films was generally the method used to produce TCO films at this time. Tin oxide (TO) films were first reported before the 1940's, while indium oxide (IO) fabricated by post-oxidiation of indium films was reported in the 1950's. Following the fabrication of CdO by post-oxidation, a pyrolysis method was developed in the 1940's to produce films of TO and

SnO_2. SnO_2 was of interest at the time for anti-static coatings and as use in electroluminescent panels. TO films were used as transparent heaters in aircraft windshields for example [30]. However limited practical applications of TCO films existed at the time. Interest in the transparent conductive electrode industry has increased in the past 50 years, especially in the past 15 years due to them being utilised in consumer devices such as smartphones and tablets.

Currently, the most used commercial transparent conductive oxide in relation to flat panel displays, liquid crystal displays, touch screens and organic solar cells is tin-doped indium oxide (ITO) [31]. ITO consists of a mixture of In_2O_3 (~ 90 % to 95%) and SnO_2 (~ 5 % to 10%). Bandgap ranges of ITO between 3.5 eV and 4.1 eV have been reported in the literature [32, 33]. ITO has high electrical conductivity and high optical transparency, with typical sheet resistance values < 20 Ω/sq and transparencies ~ 85% in the visible region of the spectrum. For example, 700 nm thick ITO films deposited on both rigid and flexible substrates had optical transparency values between 78% and 85% (averaged over the visible electromagnetic spectrum and not including the absorbance of the substrate), with corresponding sheet resistance values between 6 Ω/sq and 9 Ω/sq [8]. These values can be manipulated by changing the thickness of the film or the doping concentration. ITO is highly reflective to thermal infrared radiation due to the existence of the plasma frequency in this frequency range and this attribute has been exploited for its use in reflective coatings for the architectural and automotive industries [34].

ITO can be reproducibly fabricated by many different methods such as electron beam evaporation [35], RF magnetron sputtering [36] and pulsed laser deposition [37] to name a few. Advantages of this material is its high resistance to corrosion, its chemical stability and its proven reliability. However, the scarce nature of indium results in a high material cost [38]. Its supply can also be limited due to political reasons as the most abundant source of indium is located in China. A decrease in electrical conductivity is observed when the material is flexed due to its ceramic nature, a key drawback for flexible electronic applications [39-42]. A plot of resistance versus strain can be seen in Figure 1.3, showing that ITO's resistance can increase dramatically when flexed even at a low (compressive) strain values < 1.7% [40]. It has also been reported that ITO (thickness of ~ 100 nm) coated on PET (thickness of ~ 130 µm) can undergo failure at a strain of ~ 1.2% [43]. Cyclic bending tests have also

been reported to gauge the effect of bending on device performance to mimic repeated consumer device use. ITO also fails in this regard [44]. ITO has been reported to fail after flexing for only ~ 150 cycles around a radius of curvature of 20 mm [45].

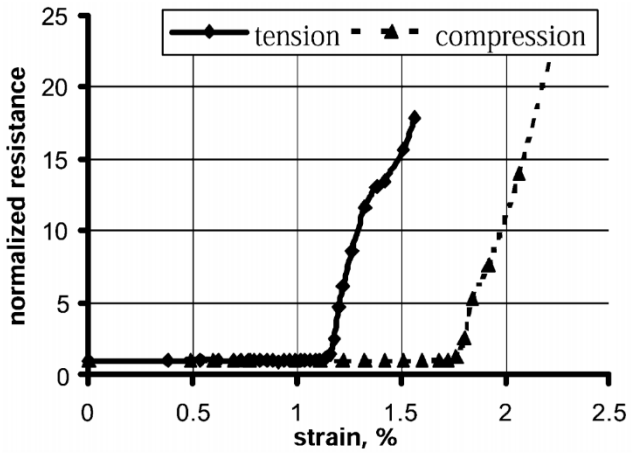

Figure 1.3: Plot of resistance as a function of strain for an ITO film on PET under tension and compression based strain displaying a large resistance change at a relatively low value of strain [40].

The sputter deposition process for ITO is not a straightforward process and a significant amount of indium is wasted. One of the main costs associated with the sputter deposition of ITO is the sputter target. New techniques are being investigated to reduce deposition costs of ITO such as laser sintering [46, 47], sol-gel [48, 49] and tape casting processes [50, 51] Also the high temperature post-deposition annealing process that is needed to lower the sheet resistance is not compatible with flexible plastic substrates [52].

One viable TCO to replace ITO is fluorine doped tin oxide (FTO or $FSnO_2$) [53]. FTO is used in the fabrication of heat-reflecting coatings for architectural glass and as a transparent electrode for solar cells based on thin film amorphous silicon and cadmium telluride. FTO exhibits a similar sheet resistance and transparency to ITO films. However, FTO has the advantage of high thermal stability even above 400 ^{o}C, whereas the properties of ITO degrade [54]. However the larger roughness of FTO films over ITO is problematic for solar cells and touch screen displays [55]. Aluminium doped zinc oxide (AZO) is another possible TCO candidate to replace

ITO. It has the advantage of inexpensive source material cost and low toxicity. It can be used as an antireflective coating for solar cells. However its properties can degrade due to humidity and mechanical flexing [56]. This inability to maintain high electrical conductivity after mechanical flexing is a problem for all TCOs.

Other transparent conductive materials have been sought to replace ITO, especially in regard to integration of these materials on flexible devices. Important factors to consider for future flexible optoelectronic devices include the cost of the fabrication process and the ease of manufacture. The following section briefly discusses various alternative materials to ITO for transparent conductive electrodes.

1.4 Alternative materials to TCO technologies

Graphene is a single-atom thick layer of carbon atoms arranged in a hexagonal lattice structure [57]. It was first isolated in 2004 by the mechanical exfoliation of graphite. Geim and Novoselov were awarded the Nobel Prize in Physics in 2010. However, graphene produced by this method provides micron sized isolated flakes (in addition to thicker flakes). Large scale graphene production was realised in 2009 [58, 59]. This large scale synthesis method on transition metal foils involves the thermal decomposition of methane gas at 1,000 ^{o}C in a chemical vapour deposition (CVD) reactor. This is followed by a transfer process to target substrate. Monolayer graphene has high intrinsic optical transparency of ~ 97.7% (measured transparency values between 97.1% to 97.5% reported) and good mechanical properties (for exfoliated and CVD graphene) [60-66]. However, its sheet resistance of ~ 6 k Ω/sq is too large for use as a transparent electrode. Graphene's sensitivity to ambient adsorbates and polymer residue from large area transfer also present significant challenges [67, 68]. A broad range of sheet resistance values have been reported in literature (R_S ~ 125 Ω/sq to 5590 Ω/sq). Key factors influencing sheet resistance are intentional/unintentional adsorbate doping [69, 70], measurement environment (vaccum vs. ambient conditions) and device size (microns to tens of centimetres) [62-64, 71]. The use of micron scale graphene-based devices is not a true reflection of their electrical properties as chemical residues (etchant and polymer residues) and defects (cracks, wrinkles and domain boundaries) are more prevalent at millimetre scale. The sheet resistance of graphene can be decreased by non-covalent molecular doping [69, 70], but this involves extra processing steps (which may damage the film) and

maintaining the long-term stability of such layers is challenging. Han *et al.* have shown that a transferred stack of four monolayers grown by chemical vapour deposition (CVD) and individually doped before transfer with nitric acid (HNO_3) leads to a total sheet resistance as low as ~ 54 Ω/sq with a transmission of ~ 90% at a wavelength, λ of 550 nm [72]. However, adsorbate-doped devices left in ambient conditions showed increases in sheet resistance of ~ 40% within 3 days [72].

Carbon nanotubes are tubular carbon-based nanomaterials which can be incorporated into conductive polymer support matrices. Carbon nanotube-polymer composite materials possess adequate mechanical flexibility and have the potential for low cost fabrication [73-75]. Sheet resistance values in the range of 50-500 Ω/sq have been reported along with transparency values between 63% and 87% [76-78]. Variation of these parameters arise from the % weight of nanotubes, the thickness of the polymer and whether the composite underwent doping. Carbon nanotube films suffer from high surface roughness which can be reduced by using a polymer but does so at the cost of the transparency [79]. Also, a large junction resistance exists between nanotubes and the films often contain nanotubes of varying lengths, diameters and chiralities [5, 78, 80].

Conductive polymers have also been investigated as alternatives to TCOs. In particular, poly(3,4-ethylenedioxythiophene) commonly referred to as PEDOT is one of the most thoroughly studied polymers and has been used for various transparent conductive electrode applications [81]. It is commonly doped with polystyrensulfonic acid (PSS) which makes the conducting polymer soluble in water. It allows cost-effective fabrication by coating or printing methods [82, 83]. The major challenge in this research area is the improvement of the conductivity and transparency. Transparency values have been reported in the range of 70% to 90% depending on the polymer thickness [84]. For example, a 100 nm thick PEDOT:PSS film has been shown to possess a sheet resistance of 750 Ω/sq and a transparency of 96% (not including the absorbance of the underlying substrate) [85]. The conductive properties of these films can be improved by the addition of high boiling point solvents (R_S ~ 65-176 Ω/sq, T ~ 80-88%) [82] or acids (R_S ~ 39 Ω/sq, T ~ 80%) [86]. Despite the high transparency and mechanical flexibility of PEDOT:PSS [87], its sheet resistance is unstable when exposed to certain stresses such as thermal and/or environmental stresses due to unstable doped states [88].

Metal nanowire networks allow the fabrication of a transparent conductive electrode using solution based processes. Metal nanowire based transparent electrodes have shown to possess good electrical, optical and mechanical properties [89-92]. Sheet resistance values between 6.5 Ω/sq to 38.7 Ω/sq and transparency values between 85% to 91% have been reported for such films [89, 93]. The solution process for nanowire synthesis is also a very cost effective technique and is compatible with roll-to-roll processes [94]. It has been reported that silver nanowires (Ag NWs), with a deposited mass per unit area (M/A) = 47 mg/m^2 and thickness of 107 nm can achieve values of R_s = 13 Ω/sq, T = 85% and are mechanically stable after 1,000 flexing cycles (< 2% change in resistance) [89]. However, metal nanowire networks have a high surface roughness and high haze (when using large nanowire diameters) [21, 90].

One promising candidate that offers solutions for the flexible transparent conductive electrode market is mesh-patterned metal films [95]. Metal meshes fabricated by lithographic methods consist of periodically arranged micron (or sub-micron) scale structures on transparent materials such as rigid glass or flexible plastics. The transparency and sheet resistance can be controlled by varying mesh geometry, linewidth, thickness and resistivity of the metal. The use of metal linewidths ≤ 5 μm are advantageous due to being undetectable by the naked eye [6, 96]. This attribute allows the potential use of metal meshes for applications that require clear visibility such as transparent heaters [97]. Past research efforts on ultra-thin metal meshes have mostly focused on symmetrical geometries such as squares [95, 98] and hexagons [99, 100] along with patterning techniques such as UV lithography [6], nanoimprint lithography [101] and a novel technique of rolling mask lithography [102]. Ghosh et al. reported square Ni (~ 50 nm thick) metal meshes on a 2 nm layer of Ni by UV lithography with values of R_S ~ 28 Ω/sq and T ~ 76.5% using a metal linewidth of 20 μm [95]. Hexagonal Cu (~ 62 nm) metal meshes with metal linewidth of 1 μm by UV lithography have been reported by Kim et al. with values of R_S ~ 6.2 Ω/sq and T ~ 91% when an aluminium doped zinc oxide capping layer was applied (~ 75 nm thick) [99]. Rolith Inc. have fabricated square Al metal meshes (~ 300 nm to 500 nm thick) with sub-micron linewidths (~ 300 nm) by their patented rolling mask lithography with low sheet resistance (~ 3.5 Ω/sq), high transparency (~ 96%) and low haze (4-5%) [103]. A summary table is given below in Table 1.1, showing the parameters achieved by literature and industry in regard to TCOs and new transparent electrode materials.

Table 1.1: Sheet resistance (R_S) and transparency (T) values (not including the underlying substrate) reported in literature for transparent conductive oxides and alternative materials for transparent conductive electrodes along with the associated Figure of Merit (FOM) values. Transparency values denoted by * were averaged over the visible electromagnetic region. Superscripted citations refer to footnotes.

Material Class:	Material:	Substrate:	R_S (Ω/sq):	T (%):	FOM σ_{DC}/σ_{op}:
Transparent conductive oxide	ITO [8]	PET	7	84*	296
	ITO [8]	Glass	9	85*	247
	AZO [9]	Quartz	18.5	93.7	308
	FTO [10]	Glass	19	90*	183
Carbon nanomaterials	Carbon nanotubes [76]	polymer	500	87	5
	Carbon nanotubes [104]	PET	300 [1]	90	12
	Carbon nanotubes [77]	Glass	160 [2]	87	16
	Carbon nanotubes [105]	PET	60 [3]	90.9	73
	Graphene [64]	Glass	1200	97.1	11
	Graphene [71]	PET	5590	97.5*	3
	Graphene [71]	PET	90 [4]	87.9*	31
	Graphene [62]	PET	30 [5]	90	116
Conductive polymer	PEDOT:PSS [85]	PDMS	750	96	12
	PEDOT:PSS [82]	PET	65 [6]	72	16
	PEDOT:PSS [86]	PET	39 [7]	80	41
Transparent metal networks	Ag nanowire network [89]	PET	13	85*	171
	Ag nanowire network [90]	PET	20	80*	80
	Ag nanowire network [106]	PET	35	95.5	231
	Ni mesh [95]	Glass	28 [8]	76.5	22
	Cu mesh [99]	Polyimide	6.2 [9]	91	630
	Al mesh [103]	Glass	3.5	95	2073
	Au mesh [107]	Glass	1	77*	1350

1.5 Figure of merit for transparent conductors

A figure of merit has been proposed to compare different transparent conductive electrode technologies. This figure of merit is the ratio of direct current (DC) conductivity to optical conductivity i.e. it compares the sheet resistance and intrinsic transparency of a transparent conductive electrode. For example, De and Coleman used this figure of merit to compare the sheet resistance and transparency of graphene

[1] 0.1 wt % SWNTs coated with 1 wt % sodium dodecyl benzonesulfanate (SDBS) and 3 % wt Triton X-100. Followed by treatment with fuming sulfuric acid (oleum).
[2] Coated with 1 wt % sodium dodecyl sulfanate (SDS) followed by doping with thionyl chloride ($SOCl_2$).
[3] CNTs dispersed in superacid chlorosulfonic acid.
[4] Transfer of CVD graphene to flexible substrate to create a five layer stack followed by doping with Bis(trifl uoromethanesulfonyl)amide (TFSA).
[5] Transfer of CVD graphene to flexible substrate to create a four layer stack followed by doping with HNO_3.
[6] Exposed to a solvent for 30 minutes, followed by thermal treatment.
[7] Treated with a H_2SO_4.
[8] Includes a ~ 2 nm Ni thin film underneath the metal mesh.
[9] Includes a ~ 75 nm aluminium-doped zinc oxide capping layer.

films to that of ITO and other transparent conductive electrodes [108]. The figure of merit is based on the Lambert-Beer law of a thin metallic film [109]. This figure of merit assumes that there is negligible reflection and that the thickness of the film is much smaller than the wavelength of light used. However it also assumes that there is only one interface present and that the material is homogenous. Although some of the assumptions are not applicable for some transparent conductive electrode technologies e.g. metal meshes, it does provide a method to compare the sheet resistance and transparency to that of ITO or other transparent conductive electrodes. The transparency of a thin conductive film, scales with thickness *t* as [45]

$$T(\lambda) = \left(1 + \frac{Z_0}{2}\,\sigma_{op}(\lambda)t\right)^{-2} \quad \textbf{(1.4)}$$

The sheet resistance and intrinsic transparency of conductive thin films can then be related by

$$T(\lambda) = \left(1 + \frac{Z_0}{2R_s}\frac{\sigma_{op}(\lambda)}{\sigma_{DC}}\right)^{-2} \quad \textbf{(1.5)}$$

where Z_0 = 377 Ω, is the impedance of free space, σ_{op} is the optical conductivity of the sample at λ = 550 nm or averaged over the visible region and σ_{DC} is the DC conductivity of the film [89]. This can be rearranged to give

$$\frac{\sigma_{DC}}{\sigma_{op}} = \frac{188.5}{R_s(T^{-1/2} - 1)} = FOM \quad \textbf{(1.6)}$$

Using this equation, ITO with values of T = 84% and Rs = 7 Ω/sq on PET yields a figure of merit value ~ 296 [8]. See Table 1.1 for Figure of Merit values based on transparent conductive electrodes in literature.

1.6 Applications and market

A constant increase in devices that require a transparent conducting layer have been seen in the past decade. This is due to consumer based devices such as smart phones, E-Readers and tablets gaining momentum in the early 21st century. Therefore this trend is likely to continue for the foreseeable future. Nanomarkets (transparent conductor markets, 2014-2021) expect the use of ITO to grow in the next few years, followed by

steady use and then a decline [110]. The majority of ITOs current and future use is in regard to liquid crystal displays (LCDs) and flat panel displays (FPDs). Following the expected decline, alternative ITO materials are currently in development as previously discussed.

Besides display devices such as flat panel displays, organic light emitting displays and touch screen interfaces, other applications seek the use of a transparent conducting layer. The rapid growth of the electronic device market has increased the amount of electromagnetic interference (EMI) which can cause electronic devices to malfunction and even can be harmful to humans [111]. In many situations, such as an electronic device facility, EMI shielding with a high transparency is required. Anti-static and anti-glare coatings based on transparent conductive electrodes are also being investigated. The electrical conductivity of transparent electrodes are also exploited for use in organic photovoltaics, dye synthesised solar cells and thin-film photovoltaics. Transparent conductive electrodes are also utilised as a window/windscreen de-icing mechanism in automotive and aviation industries [97]. The use of an underlying flexible substrate is becoming more and more predominant for display technologies and solar cells. Thus the use of ITO will dwindle due to its brittle nature. The total transparent conductive electrode market is expected to increase every year as more demand is sought from consumers. The value of the market is expected to increase by $1.5 billion from 2016 to 2021.

1.7 Aim of thesis

The main objective of this thesis was the investigation of alternative materials to ITO for use as transparent conductive electrodes. In regard to graphene, the main aim of the work was to successfully grow graphene by chemical vapour deposition and to increase its growth quality by investigating substrate and pressure effects. Increased growth quality results in larger domains which results in a decrease in electron scattering from domain boundaries or defects, thus reducing sheet resistance. The transfer of graphene from host substrate was also studied in relation to removing residual polymer layers which can have detrimental effects on sheet resistance.

Another objective of this thesis was the investigation of transparent metal mesh structures as another viable alternative to ITO. Three differing metal deposition techniques were investigated to find the most suitable technique. The optical, electrical and surface properties of these films were analysed along with the relative ease of removing excess metal during the fabrication process (lift-off versus dry etching). Following this, the best deposition method was used to apply the transparent metal mesh structures on flexible substrates to test their mechanical stability. The final research chapter discusses the use of these metal meshes on flexible substrates for use as visible transparent.

1.8 Outline of thesis

This thesis is organised into 8 chapters. Chapter 2 involves the growth of CVD graphene. Since this was the first growth of graphene by CVD undertaken at Tyndall, process optimisation was required. Low growth time regimes were used to find the optimum gas pressure and growth time for the system. Substrate (Cu foil) effects such as pre-treatments, geometry and purity were also studied.

CVD graphene grown on micron-scale Cu foil requires a transfer process to target substrates. In chapter 3, a wet chemical transfer process for graphene was undertaken. A polymer layer is used as a mechanical support for the graphene layer during the transfer and is removed by solvent at the end of the process. Graphene's electrical performance is dampened by polymer residue. Therefore, a more extreme solvent clean was used near its boiling point to study the effect of removing residual polymer layers.

Chapter 4 deals with another alternative to ITO technology i.e. micron-scale metal mesh structures. Three methods of metal deposition were applied (atomic layer deposition, electron-beam evaporation and sputter deposition). The growth of ALD Pt layers was investigated as a potential catalyst for graphene and also as a TCO. Subsequently, the electrical and optical properties were measured along with the surface morphology (surface roughness). Once the best deposition method was chosen, the metal mesh structures were applied to flexible plastic substrates to test their mechanical stability (chapter 5). The geometry of the metal mesh itself and its effect on optical and electrical properties were studied. Chapter 6 involves the use of a pentagonal metal mesh as a transparent heater for de-icing purposes. Graphene was

also transferred on top of the mesh and characterised. Chapters 7 and 8 involve the discussion and conclusion of the thesis and suggestions of the future work in regard to metal mesh structures such as failure mode analysis of devices after a number of bending cycles, metal electroplating and investigation of other geometric designs.

1.9 Bibliography

1. Rech, B. and H. Wagner, *Potential of amorphous silicon for solar cells.* Applied Physics A: Materials Science and Processing, 1999, **69**(2), p. 155-167
2. Faÿ, S. and A. Shah, *Zinc Oxide Grown by CVD Process as Transparent Contact for Thin Film Solar Cell Applications*, in *Transparent Conductive Zinc Oxide: Basics and Applications in Thin Film Solar Cells*, K. Ellmer, A. Klein, and B. Rech, Editors. 2008, Springer Berlin Heidelberg. p. 235-302.
3. Madaria, A.R., A. Kumar, and C. Zhou, *Large scale, highly conductive and patterned transparent films of silver nanowires on arbitrary substrates and their application in touch screens.* Nanotechnology, 2011, **22**(24), 245201
4. Ellmer, K., *Past achievements and future challenges in the development of optically transparent electrodes.* Nature Photonics, 2012, **6**(12), p. 809-817
5. Hecht, D.S., L. Hu, and G. Irvin, *Emerging transparent electrodes based on thin films of carbon nanotubes, graphene, and metallic nanostructures.* Advanced Materials, 2011, **23**(13), p. 1482-1513
6. Sam, F.L.M., et al., *Thin film hexagonal gold grids as transparent conducting electrodes in organic light emitting diodes.* Laser and Photonics Reviews, 2014, **8**(1), p. 172-179
7. Dressel, M. and G. Gruener, *Electrodynamics of Solids: Optical Properties of Electrons in Matter - Chapter 5*. 2002: Cambridge University Press.
8. Guillén, C. and J. Herrero, *Comparison study of ITO thin films deposited by sputtering at room temperature onto polymer and glass substrates.* Thin Solid Films, 2005, **480-481**, p. 129-132
9. Yang, W., et al., *Room-temperature deposition of transparent conducting Al-doped ZnO films by RF magnetron sputtering method.* Applied Surface Science, 2009, **255**(11), p. 5669-5673
10. Rakhshani, A.E., Y. Makdisi, and H.A. Ramazaniyan, *Electronic and optical properties of fluorine-doped tin oxide films.* Journal of Applied Physics, 1998, **83**(2), p. 1049-1057
11. Durkan, C. and M.E. Welland, *Size effects in the electrical resistivity of polycrystalline nanowires.* Physical Review B, 2000, **61**(20), p. 14215-14218
12. Fuchs, K., *The conductivity of thin metallic films according to the electron theory of metals.* Mathematical Proceedings of the Cambridge Philosophical Society, 1938, **34**(1), p. 100-108
13. Van der Pauw, L.J., *A method of measuring specific resistivity and Hall effect of discs of arbitrary shape.* Philips Research Reports, 1958, **13**(1), p. 1-9
14. Koh, B. and W. Cheng, *Mechanisms of Carbon Nanotube Aggregation and the Reversion of Carbon Nanotube Aggregates in Aqueous Medium.* Langmuir, 2014, **30**(36), p. 10899-10909
15. Chen, Q., et al., *Aggregation behavior of single-walled carbon nanotubes in dilute aqueous suspension.* Journal of Colloid and Interface Science, 2004, **280**(1), p. 91-97
16. Kang, H., D. Kim, and S. Baik, *Sheet resistance characterization of locally anisotropic transparent conductive films made of aligned metal-enriched single-walled carbon nanotubes.* Physical Chemistry Chemical Physics, 2014, **16**(35), p. 18759-18764

17. Fahland, M., *Reel-to-Reel Processing of Highly Conductive Metal Oxides*, in *Organic Photovoltaics*. 2014, Wiley-VCH Verlag GmbH & Co. KGaA. p. 495-512.
18. Lacy, F., *Developing a theoretical relationship between electrical resistivity, temperature, and film thickness for conductors.* Nanoscale Research Letters, 2011, **6**(1), p. 636-636
19. Macleod, H., A., *Chapter 4 - Antireflection Coatings*, in *Thin-Film Optical Filters, Fourth Edition*. 2010, CRC Press. p. 105-184.
20. Preston, C., et al., *Silver nanowire transparent conducting paper-based electrode with high optical haze.* Journal of Materials Chemistry C, 2014, **2**(7), p. 1248-1254
21. Preston, C., et al., *Optical haze of transparent and conductive silver nanowire films.* Nano Research, 2013, **6**(7), p. 461-468
22. Ye, S., et al., *Metal Nanowire Networks: The Next Generation of Transparent Conductors.* Advanced Materials, 2014, **26**(39), p. 6670-6687
23. Gaynor, W., et al., *Smooth Nanowire/Polymer Composite Transparent Electrodes.* Advanced Materials, 2011, **23**(26), p. 2905-2910
24. Delahoy, A.E. and S. Guo, *Transparent Conducting Oxides for Photovoltaics*, in *Handbook of Photovoltaic Science and Engineering*. 2011, John Wiley & Sons, Ltd. p. 716-796.
25. Luo, S.N., et al., *Effective creation of oxygen vacancies as an electron carrier source in tin-doped indium oxide films by plasma sputtering.* Journal of Applied Physics, 2006, **100**(11), 113701
26. Luo, S., et al., *Effects of hydrogen in working gas on valence states of oxygen in sputter-deposited indium tin oxide thin films.* ACS Applied Materials and Interfaces, 2010, **2**(3), p. 663-668
27. Sheng, S., et al., *p-type transparent conducting oxides.* Physica Status Solidi a-Applications and Materials Science, 2006, **203**(8), p. 1891-1900
28. Bädeker, K., *Über die elektrische Leitfähigkeit und die thermoelektrische Kraft einiger Schwermetallverbindungen.* Ann. Phys., 1907, **22**, p. 749-766
29. Ellmer, K. and A. Klein, *ZnO and Its Applications*, in *Transparent Conductive Zinc Oxide: Basics and Applications in Thin Film Solar Cells*, K. Ellmer, A. Klein, and B. Rech, Editors. 2008, Springer Berlin Heidelberg: Berlin, Heidelberg. p. 1-33.
30. Bright, C., *21 - Transparent conductive thin films*, in *Optical Thin Films and Coatings*. 2013, Woodhead Publishing. p. 741-788.
31. Stadler, A., *Transparent Conducting Oxides—An Up-To-Date Overview*. Materials, 2012, **5**(4), p. 661
32. Fan, J.C.C. and J.B. Goodenough, *X-ray photoemission spectroscopy studies of Sn-doped indium-oxide films.* Journal of Applied Physics, 1977, **48**(8), p. 3524-3531
33. Balasubramanian, N. and A. Subrahmanyam, *Electrical and optical properties of reactively evaporated indium tin oxide (ITO) films-dependence on substrate temperature and tin concentration.* Journal of Physics D: Applied Physics, 1989, **22**(1), p. 206
34. Brewer, S.H. and S. Franzen, *Optical properties of indium tin oxide and fluorine-doped tin oxide surfaces: correlation of reflectivity, skin depth, and plasmon frequency with conductivity.* Journal of Alloys and Compounds, 2002, **338**(1–2), p. 73-79

35. Lien, S.-Y., *Characterization and optimization of ITO thin films for application in heterojunction silicon solar cells.* Thin Solid Films, 2010, **518**(21, Supplement), p. S10-S13
36. Dao, V.A., et al., *rf-Magnetron sputtered ITO thin films for improved heterojunction solar cell applications.* Current Applied Physics, 2010, **10**(3, Supplement), p. S506-S509
37. Petukhov, I.A., et al., *Pulsed laser deposition of conductive indium tin oxide thin films.* Inorganic Materials, 2012, **48**(10), p. 1020-1025
38. O'Connor, B., et al., *Transparent and conductive electrodes based on unpatterned, thin metal films.* Applied Physics Letters, 2008, **93**(22), 223304
39. Wassei, J.K. and R.B. Kaner, *Graphene, a promising transparent conductor.* Materials Today, 2010, **13**(3), p. 52-59
40. Chen, Z., et al., *A mechanical assessment of flexible optoelectronic devices.* Thin Solid Films, 2001, **394**(1-2), p. 202-206
41. Chen, Z., B. Cotterell, and W. Wang, *The fracture of brittle thin films on compliant substrates in flexible displays.* Engineering Fracture Mechanics, 2002, **69**(5), p. 597-603
42. Leterrier, Y., et al., *Mechanical integrity of transparent conductive oxide films for flexible polymer-based displays.* Thin Solid Films, 2004, **460**(1-2), p. 156-166
43. Kang, J., et al., *High-Performance Graphene-Based Transparent Flexible Heaters.* Nano Letters, 2011, **11**(12), p. 5154-5158
44. Cairns, D.R. and G.P. Crawford, *Electromechanical properties of transparent conducting substrates for flexible electronic displays.* Proceedings of the IEEE, 2005, **93**(8), p. 1451-1458
45. De, S., et al., *Transparent, flexible, and highly conductive thin films based on Polymer-nanotube composites.* ACS Nano, 2009, **3**(3), p. 714-720
46. Park, T. and D. Kim, *Excimer laser sintering of indium tin oxide nanoparticles for fabricating thin films of variable thickness on flexible substrates.* Thin Solid Films, 2015, **578**, p. 76-82
47. Watanabe, A. and G. Qin, *Transparent conductive films based on the laser sintering of metal and metal oxide nanoparticles.* Proceedings of SPIE - The International Society for Optical Engineering, 2014, **8968**, 89680q
48. Alam, M.J. and D.C. Cameron, *Optical and electrical properties of transparent conductive ITO thin films deposited by sol-gel process.* Thin Solid Films, 2000, **377-378**, p. 455-459
49. Lee, J.H. and B.O. Park, *Transparent conducting ZnO:Al, In and Sn thin films deposited by the sol-gel method.* Thin Solid Films, 2003, **426**(1-2), p. 94-99
50. Arlindo, E.P.S., et al., *Electrical and optical properties of conductive and transparent Ito@PMMA nanocomposites.* Journal of Physical Chemistry C, 2012, **116**(23), p. 12946-12952
51. Straue, N., et al., *Tape casting of ITO green tapes for flexible electroluminescent lamps.* Journal of the American Ceramic Society, 2012, **95**(2), p. 684-689
52. Masatoshi, H., et al., *Postdeposition Annealing Influence on Sputtered Indium Tin Oxide Film Characteristics.* Japanese Journal of Applied Physics, 1994, **33**(1R), p. 302

53. Kuan, S., X. Yijie, and O. Jianyong, *Next-Generation Transparent Electrode Materials for Organic Solar Cells*, in *Organic Solar Cells*. 2015, CRC Press. p. 43-86.
54. Kerkache, L., et al., *Annealing effect in DC and RF sputtered ITO thin films.* EPJ Applied Physics, 2007, **39**(1), p. 1-5
55. Dahou, F.Z., et al., *Influence of anode roughness and buffer layer nature on organic solar cells performance.* Thin Solid Films, 2010, **518**(21), p. 6117-6122
56. Ando, E. and M. Miyazaki, *Moisture resistance of the low-emissivity coatings with a layer structure of Al-doped ZnO/Ag/Al-doped ZnO.* Thin Solid Films, 2001, **392**(2), p. 289-293
57. Geim, A.K. and K.S. Novoselov, *The rise of graphene.* Nature Materials, 2007, **6**(3), p. 183-191
58. Li, X., et al., *Large-area synthesis of high-quality and uniform graphene films on copper foils.* Science, 2009, **324**(5932), p. 1312-1314
59. Reina, A., et al., *Large area, few-layer graphene films on arbitrary substrates by chemical vapor deposition.* Nano Letters, 2009, **9**(1), p. 30-35
60. Nair, R.R., et al., *Fine Structure Constant Defines Visual Transparency of Graphene.* Science, 2008, **320**(5881), p. 1308-1308
61. Bonaccorso, F., et al., *Graphene photonics and optoelectronics.* Nature Photonics, 2010, **4**(9), p. 611-622
62. Bae, S., et al., *Roll-to-roll production of 30-inch graphene films for transparent electrodes.* Nature Nanotechnology, 2010, **5**(8), p. 574-578
63. Suk, J.W., et al., *Transfer of CVD-Grown Monolayer Graphene onto Arbitrary Substrates.* ACS Nano, 2011, **5**(9), p. 6916-6924
64. Sun, Z., et al., *Growth of graphene from solid carbon sources.* Nature, 2010, **468**(7323), p. 549-552
65. Lee, C., et al., *Measurement of the elastic properties and intrinsic strength of monolayer graphene.* Science, 2008, **321**(5887), p. 385-388
66. Kim, K.S., et al., *Large-scale pattern growth of graphene films for stretchable transparent electrodes.* Nature, 2009, **457**(7230), p. 706-710
67. Novoselov, K.S., et al., *Two-dimensional gas of massless Dirac fermions in graphene.* Nature, 2005, **438**(7065), p. 197-200
68. Chan, J., et al., *Reducing Extrinsic Performance-Limiting Factors in Graphene Grown by Chemical Vapor Deposition.* ACS Nano, 2012, **6**(4), p. 3224-3229
69. Long, B., et al., *Non-covalent functionalization of graphene using self-assembly of alkane-amines.* Advanced Functional Materials, 2012, **22**(4), p. 717-725
70. Zhang, Y., et al., *Non-covalent doping of graphitic carbon nitride polymer with graphene: Controlled electronic structure and enhanced optoelectronic conversion.* Energy and Environmental Science, 2011, **4**(11), p. 4517-4521
71. Kim, D., et al., *Work-Function Engineering of Graphene Anode by Bis(trifluoromethanesulfonyl)amide Doping for Efficient Polymer Light-Emitting Diodes.* Advanced Functional Materials, 2013, **23**(40), p. 5049-5055
72. Han, T.H., et al., *Extremely efficient flexible organic light-emitting diodes with modified graphene anode.* Nature Photonics, 2012, **6**(2), p. 105-110
73. Snow, E.S., et al., *High-mobility carbon-nanotube thin-film transistors on a polymeric substrate.* Applied Physics Letters, 2005, **86**(3), p. 1-3, 033105

74. Cao, Q. and J.A. Rogers, *Ultrathin films of single-walled carbon nanotubes for electronics and sensors: A review of fundamental and applied aspects.* Advanced Materials, 2009, **21**(1), p. 29-53
75. Rouhi, N., D. Jain, and P.J. Burke, *High-performance semiconducting nanotube inks: Progress and prospects.* ACS Nano, 2011, **5**(11), p. 8471-8487
76. Yu, Z., et al., *Intrinsically stretchable polymer light-emitting devices using carbon nanotube-polymer composite electrodes.* Advanced Materials, 2011, **23**(34), p. 3989-3994
77. Zhang, D., et al., *Transparent, conductive, and flexible carbon nanotube films and their application in organic light-emitting diodes.* Nano Letters, 2006, **6**(9), p. 1880-1886
78. Rowell, M.W., et al., *Organic solar cells with carbon nanotube network electrodes.* Applied Physics Letters, 2006, **88**(23), p. 233506
79. Gao, J., et al., *Modification of carbon nanotube transparent conducting films for electrodes in organic light-emitting diodes.* Nanotechnology, 2013, **24**(43), 435201
80. Yao, Z., et al., *Carbon nanotube intramolecular junctions.* Nature, 1999, **402**(6759), p. 273-276
81. Tait, J.G., et al., *Spray coated high-conductivity PEDOT:PSS transparent electrodes for stretchable and mechanically-robust organic solar cells.* Solar Energy Materials and Solar Cells, 2013, **110**, p. 98-106
82. Kim, Y.H., et al., *Highly conductive PEDOT:PSS electrode with optimized solvent and thermal post-treatment for ITO-free organic solar cells.* Advanced Functional Materials, 2011, **21**(6), p. 1076-1081
83. Xiong, Z. and C. Liu, *Optimization of inkjet printed PEDOT:PSS thin films through annealing processes.* Organic Electronics: physics, materials, applications, 2012, **13**(9), p. 1532-1540
84. Wang, P.-C., et al., *Transparent electrodes based on conducting polymers for display applications.* Displays, 2013, **34**(4), p. 301-314
85. Lipomi, D.J., et al., *Stretchable Organic Solar Cells.* Advanced Materials, 2011, **23**(15), p. 1771-1775
86. Xia, Y., K. Sun, and J. Ouyang, *Solution-Processed Metallic Conducting Polymer Films as Transparent Electrode of Optoelectronic Devices.* Advanced Materials, 2012, **24**(18), p. 2436-2440
87. Cho, C.K., et al., *Mechanical flexibility of transparent PEDOT:PSS electrodes prepared by gravure printing for flexible organic solar cells.* Solar Energy Materials and Solar Cells, 2011, **95**(12), p. 3269-3275
88. Vitoratos, E., et al., *Thermal degradation mechanisms of PEDOT:PSS.* Organic Electronics, 2009, **10**(1), p. 61-66
89. De, S., et al., *Silver nanowire networks as flexible, transparent, conducting films: Extremely high DC to optical conductivity ratios.* ACS Nano, 2009, **3**(7), p. 1767-1774
90. Hu, L., et al., *Scalable Coating and Properties of Transparent, Flexible, Silver Nanowire Electrodes.* ACS Nano, 2010, **4**(5), p. 2955-2963
91. Kim, T., et al., *Electrostatic Spray Deposition of Highly Transparent Silver Nanowire Electrode on Flexible Substrate.* ACS Applied Materials & Interfaces, 2013, **5**(3), p. 788-794
92. Lee, J.Y., et al., *Solution-processed metal nanowire mesh transparent electrodes.* Nano Letters, 2008, **8**(2), p. 689-692

93. van de Groep, J., P. Spinelli, and A. Polman, *Transparent Conducting Silver Nanowire Networks.* Nano Letters, 2012, **12**(6), p. 3138-3144
94. Lee, S.J., et al., *A roll-to-roll welding process for planarized silver nanowire electrodes.* Nanoscale, 2014, **6**(20), p. 11828-11834
95. Ghosh, D.S., T.L. Chen, and V. Pruneri, *High figure-of-merit ultrathin metal transparent electrodes incorporating a conductive grid.* Applied Physics Letters, 2010, **96**(4), 041109
96. Philipp, H., *Touch Screen Sensor*. Google Patents: USA.
97. Gupta, R., et al., *Visibly Transparent Heaters.* ACS Applied Materials and Interfaces, 2016, **8**(20), p. 12559-12575
98. Dong, P., et al., *Graphene on Metal Grids as the Transparent Conductive Material for Dye Sensitized Solar Cell.* Journal of Physical Chemistry C, 2014, **118**(45), p. 25863-25868
99. Kim, W.K., et al., *Cu mesh for flexible transparent conductive electrodes.* Scientific Reports, 2015, **5**, 10715
100. Galagan, Y., et al., *ITO-free flexible organic solar cells with printed current collecting grids.* Solar Energy Materials and Solar Cells, 2011, **95**(5), p. 1339-1343
101. Kang, M.G. and L.J. Guo, *Nanoimprinted semitransparent metal electrodes and their application in organic light-emitting diodes.* Advanced Materials, 2007, **19**(10), p. 1391-1396
102. Seitz, O., et al., *Antireflective surface patterned by rolling mask lithography.* Proceedings of SPIE - The International Society for Optical Engineering, 2014, **8974**, 89740v
103. Aryal, M., et al., *Sub-micron transparent metal mesh conductor for touch screen displays.* Digest of Technical Papers - SID International Symposium, 2014, **45**(1), p. 194-196
104. Dan, B., G.C. Irvin, and M. Pasquali, *Continuous and scalable fabrication of transparent conducting carbon nanotube films.* ACS Nano, 2009, **3**(4), p. 835-843
105. Hecht, D.S., et al., *High conductivity transparent carbon nanotube films deposited from superacid.* Nanotechnology, 2011, **22**(7), 075201
106. Jia, Y., et al., *Silver Nanowire Transparent Conductive Films with High Uniformity Fabricated via a Dynamic Heating Method.* ACS Applied Materials & Interfaces, 2016, **8**(15), p. 9865-9871
107. Kiruthika, S., R. Gupta, and G.U. Kulkarni, *Large area defrosting windows based on electrothermal heating of highly conducting and transmitting Ag wire mesh.* RSC Advances, 2014, **4**(91), p. 49745-49751
108. De, S. and J.N. Coleman, *Are there fundamental limitations on the sheet resistance and transmittance of thin graphene films?* ACS Nano, 2010, **4**(5), p. 2713-2720
109. Dressel, M. and G. Gruener, *Electrodynamics of Solids: Optical Properties of Electrons in Matter - Appendix B.* 2002: Cambridge University Press.
110. Media, I. *The End of ITO dominance is in sight*. 2014; Available from: http://www.insightmedia.info/the-end-of-ito-dominance-is-in-sight/.
111. Yang, Y., M.C. Gupta, and K.L. Dudley, *Towards cost-efficient EMI shielding materials using carbon nanostructure-based nanocomposites.* Nanotechnology, 2007, **18**(34), 345701

2 Synthesis of graphene for use as a flexible transparent conductive electrode

2.1 Introduction

Depending on the hybridisation state and atomic arrangement, carbon can form diamond (sp^3-hybridisation) and graphite (sp^2-hybridisation) with the properties of an insulator and zero-gap semiconductor respectively [1]. Diamond and graphite, which are both allotropes of carbon have differing chemical properties. For example, diamond is a very transparent material but a very poor electrical conductor (resistivity, $\rho \sim 10^{16}$ Ω cm) [2]. Graphite is an opaque material but a good electrical conductor ($\rho \sim 4$ to 6×10^{-5} Ω cm) [3].

Monolayer graphene, a one atom thick layer of sp^2-hybridised bonded carbon atoms arranged in a honeycomb lattice structure has received enormous attention since it was first isolated by the mechanical exfoliation of graphite [4]. Graphene was thought to be thermodynamically unstable due to its two-dimensional structure [5]. It was regarded as a structure that could only exist in theory [3, 6] as means to physically make graphene were proving to be futile. Fullerenes (0D) are one example of nano-based carbon materials. A Fullerene consists of both pentagonal and hexagonal lattice structured carbon atoms which can be wrapped up spherically into a "buckyball" for example [7]. Another nano-based carbon material called carbon nanotubes (1D) can be visualised as a graphene layer wrapped up into a cylindrical structure [8] as seen in Figure 2.1.

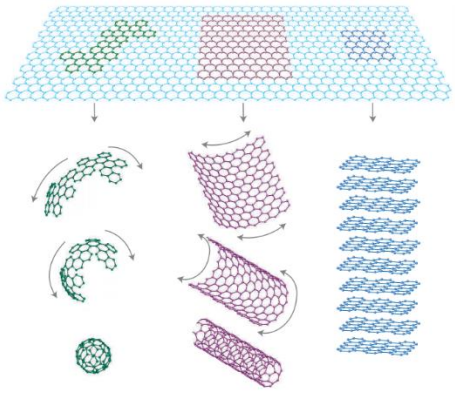

Figure 2.1: Visualisation of 0D fullerenes, 1D nanotubes and 3D stack of graphene layers (graphite) [9].

2.2 Crystal and band structure

Graphite is a 3D material composed of stacked graphene layers in an ABAB format (Figure 2.2 (a)) [10]. This means that for example a carbon atom, denoted by A has neighbours directly above and below it in adjacent planes. Each layer of carbon atoms in graphite is tightly bound within the layer but only weak Van der Waals bonds are present between each layer. This allows each monolayer to move laterally and explains why graphite is used as a lubricant in locks for example. This lateral movement of each monolayer in graphite thus formed the basis of the exfoliation method that produced graphene in the laboratory in 2004 [9].

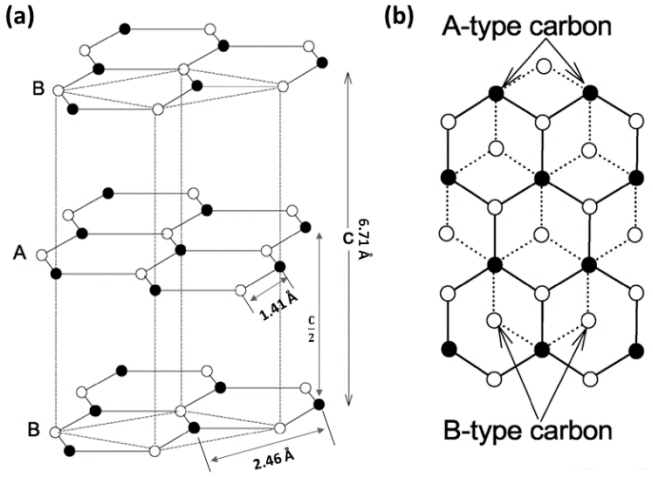

Figure 2.2: (a) The structure of a graphite crystal showing the ABAB format, where A and B denote two separate planes shifted on one another. (b) Top view of the graphite lattice showing the difference in structure of and A and B-type carbon atoms [11].

Graphene has a hexagonal lattice which consists of a basis with two atoms per unit cell, see Figure 2.3. Sp^2-hybridisation is achieved by each carbon atom due to the overlap of an s orbital (*2s*) and two p orbitals ($2p_x$ and $2p_y$). This produces three identical sp^2-hybrid orbitals which are either bonded or anti-bonded depending on the sign of the orbital. All the sp^2 orbitals form strong covalent bonds (σ-bonds) with the sp^2 orbitals of the nearest-neighbour carbon atoms. Sp^2-hybridisation is essential to produce the bond angle of 120^o (hexagonal lattice structure) and produces graphene's mechanical properties. The covalent σ bonds have a bond length of a_0 = 1.42 Å. Each σ-bond has a bonding orbital associated with it and the bonding orbital is occupied by two electrons (spin-up and spin-down). With three of the four valence electrons on

each carbon atom forming the strong covalent σ bonds, the fourth valence electron forms a weak covalent π bond with its three neighbouring carbon atoms. This is due to the $2p_z$ orbital being unaffected by sp^2-hybridisation. The filled π-band is the valence band, while the empty π^*-band is the conduction band. The π and π^*-band contribute to electronic transport in graphene. The lattice vectors for graphene in real space ($\boldsymbol{a}_1$, $\boldsymbol{a}_2$) are given as [12]

$$\boldsymbol{a}_1 = \frac{a}{2}\left(3, \sqrt{3}\right) \ , \ \boldsymbol{a}_2 = \frac{a}{2}\left(3, -\sqrt{3}\right) \tag{2.1}$$

While the lattice vectors in reciprocal space ($\boldsymbol{b}_1$, $\boldsymbol{b}_2$) are given as

$$\boldsymbol{b}_1 = \frac{2\pi}{3a}\left(1, \sqrt{3}\right) \ , \ \boldsymbol{b}_2 = \frac{2\pi}{3a}\left(1, -\sqrt{3}\right) \tag{2.2}$$

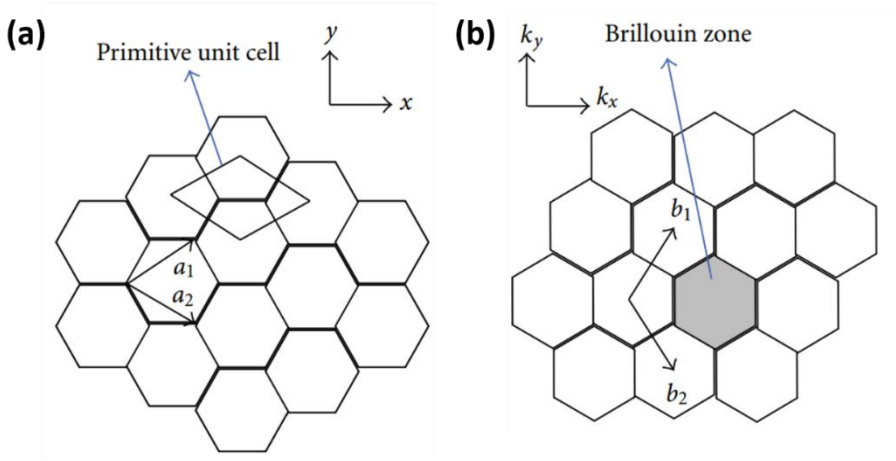

Figure 2.3: (a) Crystal structure of graphene in real space with the hexagonal unit cell and (b) the crystal structure of graphene in reciprocal (momentum) space [13].

Graphene is known as a "semi-metal." Its band structure consists of a zero energy band gap between the valence and conduction bands as seen in Figure 2.4. Electron movement is confined between carbon atoms in the 2D lattice in graphene thus making it a quasi-two-dimensional material. The lack of a third dimension in the graphene produces various novel properties such as large carrier mobilities [14], high Young's modulus [15], high thermal conductivity [16] and high intrinsic optical transmittance [17]. Due to these novel properties graphene has a wide variety of

potential applications such as graphene-based transistors [18, 19], gas sensing [20], biosensing [21], photodetectors [22, 23] and lithium battery [24] research to name a few. Most notably, graphene's property of high intrinsic transmittance (~ 97.7%) makes it an interesting candidate for transparent electrode applications such as touch screens [25-28] and solar cells [29-31]. Usually the standard method to find the electronic band structure of sp^2-hybridised carbon species is by using the tight-binding approximation to study the π-bands [32]. The Brillouin zone consists of two inequivalent points denoted by $\boldsymbol{K}$ and $\boldsymbol{K}'$ as seen in Figure 2.3 (b). Their position in momentum space are given as

$$\boldsymbol{K} = \left(\frac{2\pi}{3a}, \frac{2\pi}{3\sqrt{3}a}\right) \ , \ \boldsymbol{K}' = \left(\frac{2\pi}{3a}, -\frac{2\pi}{3\sqrt{3}a}\right) \tag{2.3}$$

At these two points, the π-band and π^*-bands touch resulting in the Density of States vanishing. Expanding the electronic band structure around the $\boldsymbol{K}$ point and the $\boldsymbol{K}'$ as

$$\boldsymbol{k} = \boldsymbol{K} + \boldsymbol{q} \ , \ \boldsymbol{k}' = \boldsymbol{K}' + \boldsymbol{q}' \tag{2.4}$$

for $|\boldsymbol{q}| \ll |\boldsymbol{K}|$ and $|\boldsymbol{q}'| \ll |\boldsymbol{K}'|$ gives the linear dispersion relation of

$$E_{\pm}(\boldsymbol{q}) \approx \pm \boldsymbol{v_f} |\boldsymbol{q}| \ , \ E_{\pm}(\boldsymbol{q}') \approx \pm \boldsymbol{v_f} |\boldsymbol{q}'| \tag{2.5}$$

where $\boldsymbol{q}$ and $\boldsymbol{q}'$ are the momenta in relation to the $\boldsymbol{K}$ and $\boldsymbol{K}'$ points respectively and v_f is the Fermi velocity (~ 10^6 ms^{-1}) [12]. Electrons that satisfy these conditions are known as Dirac Fermions, meaning that they move like a 2D electron gas and have a net effective rest mass of zero [33]. This property causes non-scattering and non-interactive movement of electrons. The location of the $\boldsymbol{K}$ and $\boldsymbol{K}'$ points are usually denoted as Dirac points and they reside where the valence and conduction bands meet. The Dirac points can also be called charge neutrality points meaning these are the points of maximum resistance. Note that the dispersion relation for graphene near the Dirac points is linear in contrast to the parabolic shape that semiconductor 2D electron gases' possess [34]. Maximum values for electron mobilities > 200,000 $cm^2V^{-1}s^{-1}$ have been measured for suspended graphene at low temperatures (~ 5 K) due to this 2D electron gas behaviour [35].

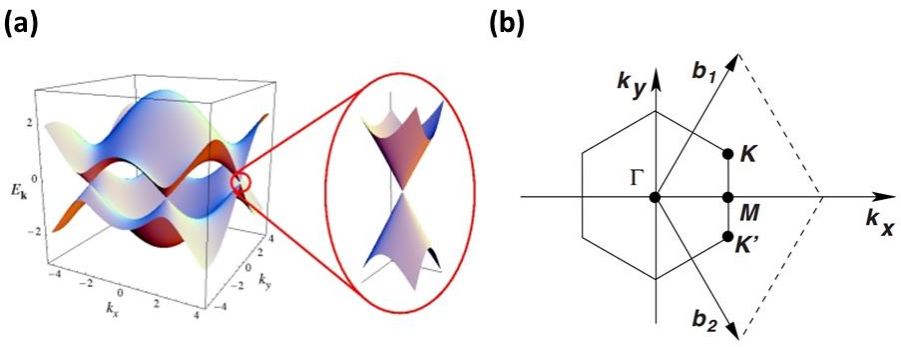

Figure 2.4: (a) Electronic band structure of graphene showing an image of the zero energy band gap between the valence (π) and conduction bands (π^*) at the ***K*** and ***K***' points in momentum space. A magnified region demonstrating the linear dispersion at the ***K*** (***K***') points [12]. (b) The Brillouin zone of graphene showing where the Dirac cones reside (***K*** and ***K***'). The Γ point is the centre of the Brillouin zone, $\boldsymbol{b}_1$ and $\boldsymbol{b}_2$ are the reciprocal lattice vectors and M is a saddle point.

2.3 Electrical properties

2.3.1 Graphene field effect device

To study the electrical properties of graphene, an external electric field is applied to the material. Three terminal graphene field effect devices (GFEDs) can be fabricated to measure carrier mobilities [4]. Back-gated field-effect device measurements can be carried out for graphene transferred onto on dielectric substrates such as (thermally) oxidised silicon (Si/SiO_2). The source and drain contacts on the graphene samples are made by a standard lithography process and lift-off of Au or desired metal and the gate voltage (V_G) is applied to the silicon substrate. To calculate the carrier mobilities of electron and holes, first consider the Drude model for mobility (two-point measurements), ignoring quantum capacitance effects [36]

$$\sigma = \frac{1}{\rho} = ne\mu \qquad \textbf{(2.6)}$$

Where σ is the surface conductivity (the reciprocal of resistivity), n is the density of carriers, e is the charge of the electron and μ is the carrier mobility. When the external gate voltage is applied, a surface charge density is induced and the carrier density can be estimated as

$$n = \frac{\varepsilon V_G}{et_{ox}} = \frac{\varepsilon_0 \varepsilon_r V_G}{et_{ox}} \quad \textbf{(2.7)}$$

Where ε_0 is the electric permittivity of free space, ε_r is the electric permittivity of the insulating material, V_G is the gate voltage, e is the charge of the electron and t_{ox} is the thickness of the dielectric. At the Dirac point, the carrier density is zero. To compensate for doping by ambient adsorbates the gate voltage at the Dirac point (V_D) is subtracted from the gate voltage.

$$n = \frac{\varepsilon_0 \varepsilon_r (V_{G-} V_D)}{et_{ox}} \quad \textbf{(2.8)}$$

$$\sigma = ne\mu = \frac{\varepsilon_0 \varepsilon_r (V_{G-} V_D)\mu}{t_{ox}} \quad \textbf{(2.9)}$$

Solving for the carrier mobility yields

$$\mu = \frac{\sigma t_{ox}}{\varepsilon_0 \varepsilon_r (V_{G-} V_D)} \quad \textbf{(2.10)}$$

To find the carrier mobility in terms of channel length and width of the device, consider the conductance in terms of resistance.

$$G = R^{-1} \quad \textbf{(2.11)}$$

$$R = \frac{1}{G} = \frac{\rho l}{A}, G = \frac{A}{\rho l} = \frac{\sigma A}{l} \quad \textbf{(2.12)}$$

$$\sigma = \frac{Gl}{A} = \frac{Gl}{wt} \quad \textbf{(2.13)}$$

Note that since graphene is a 2D material, it is more correct to utilise the surface conductivity, σ_s, rather than its bulk counterpart

$$\sigma_s = \frac{Gl}{w} \quad \textbf{(2.14)}$$

Substituting this back into equation (2.10), yields a carrier mobility in terms of the channel length (*l*) and channel width (*w*).

$$\mu = \frac{Gl}{w} \frac{t_{ox}}{\varepsilon_0 \varepsilon_r (V_{G-} V_D)} \quad \textbf{(2.15)}$$

The mobility can also be determined by finding the change in the surface conductivity by applying the gate voltage

$$\mu = \frac{d\sigma_s}{dV_G} \frac{1}{C_G} \quad \textbf{(2.16)}$$

Where C_G is the gate capacitance per unit area defined as [35]

$$C_G = \frac{ne}{V_{G-} V_D} \quad \textbf{(2.17)}$$

To find the sheet resistance of the graphene film, the following formula is used

$$R_s = \frac{Rw}{l} \quad \textbf{(2.18)}$$

The maximum value of carrier mobilities of exfoliated graphene at room temperature on SiO_2 was reported to be ~ 40,000 cm^2/Vs [14]. However graphene films grown by CVD have lower reported mobility values of ~ 800 to 16,000 cm^2/Vs due to the presence of domain boundaries and chemical residues from the transfer process [37]. One of the challenges associated with fabrication of field-effect devices is partial delamination of the graphene during CVD transfer and/or subsequent lithographic processing. A general schematic of a graphene field-effect device is shown in Figure 2.5.

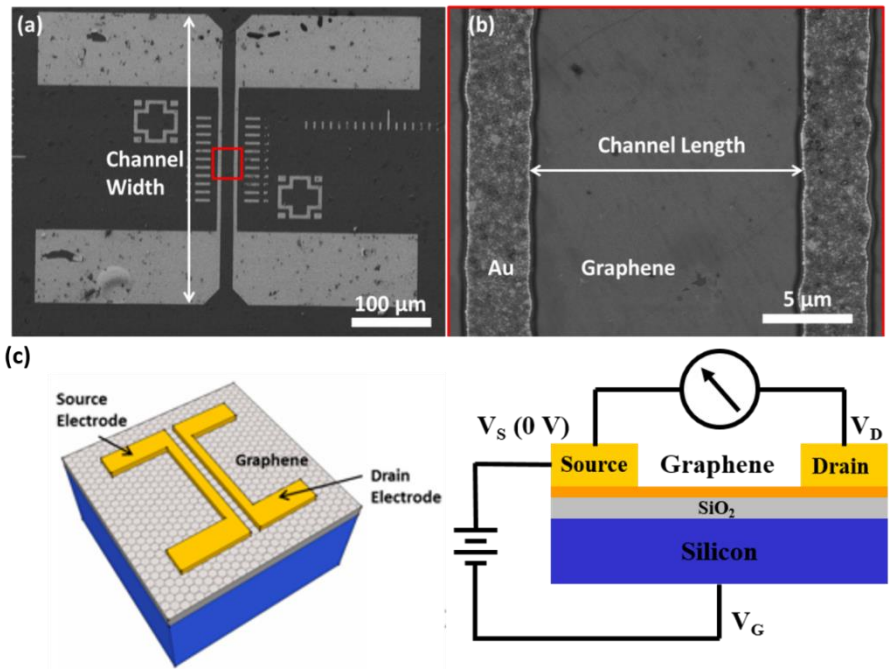

Figure 2.5: (a) SEM image of a GFED fabricated at Tyndall indicating channel width. (b) Magnified SEM image of the centre region indicating channel length. (c) Schematic of GFED operation showing the source and drain electrodes along with the Si back gate.

2.4 Optical properties

2.4.1 Transmittance

The optical conductivity, σ_{op} is commonly used to describe the optical properties of thin films. For graphene's electronic dispersion which is a 2D Dirac spectrum and is conical in nature, the dispersion relation is given as

$$E_{\pm}(\boldsymbol{q}) \approx \boldsymbol{\nu_f}\,|\boldsymbol{q}| = \frac{h}{2\pi}\nu_F \boldsymbol{k} \tag{2.19}$$

where h is Planck's constant, v_F is the fermi velocity ($v_F \sim 10^6$ ms^{-1}) and $\boldsymbol{k}$ is the wave-vector. If the energy of the incoming photon, E, is much larger than both the Fermi energy and thermal energy, the optical conductivity is given as

$$\sigma_{op} = \frac{\pi e^2}{2h} \tag{2.20}$$

The equation above states that the optical conductivity of graphene is defined by universal constants [38, 39] and one can determine the transmittance, adsorption and

reflection from this equation. Most importantly, the transmittance was found by Kuzmenko *et al.* to be

$$T = \left(1 + \frac{2\pi\sigma_{op}}{c}\right)^{-2} = \left(1 + \frac{\pi\alpha}{2}\right)^{-2} \quad \textbf{(2.21)}$$

$$\alpha = \frac{e^2}{\hbar c} \sim \frac{1}{137} \quad \textbf{(2.22)}$$

where c is the speed of light in a vacuum and α is the fine structure constant defined above. In this case the fine structure constant is in centimetre-gram-second (CGS) units instead of the usual SI units of metre kilogram second (MKS). When a variable is small, i.e. $\frac{\pi\alpha}{2} \ll 1$, Newton's Binomial theorem can be applied to approximate the function [40]. This gives an approximate value for graphene's transmittance below.

$$(1+x)^n = \sum_{k=0}^{\infty} \binom{n}{k} x^k = 1 + nx + \frac{n(n-1)}{2!}x^2 + \cdots \quad \textbf{(2.23)}$$

$$T = \left(1 + \frac{\pi\alpha}{2}\right)^{-2} \approx 1 - \pi\alpha \quad \textbf{(2.24)}$$

Therefore the transmittance of a graphene film can be approximated to be $1 - \pi\alpha$ using the first two term of Newton's Binomial expansion. The theoretical opacity of a graphene is inferred as

$$1 - T \approx \pi\alpha \quad \textbf{(2.25)}$$

Nair *et al.*'s study found the value of graphene's intrinsic transparency to be $T = 97.7 \pm 0.1\%$, while the opacity of the graphene was confirmed experimentally as $\kappa = 2.3 \pm 0.1\%$ and is independent of wavelength. The value of graphene's optical conductivity was confirmed as $(1.01 \pm 0.04)\ \sigma_{op}$, which is the behaviour expected for ideal Dirac Fermions [17]. The transmittance of graphene films decreases for increasing number of graphene layers as seen in Figure 2.6 (b). It's also noted that the transmittance of the graphene membrane deviates slightly from the expected theoretical value at wavelengths < 500 nm (Figure 2.6 (b)). Nair *et al.* suggest that this occurs due to

surface contamination of the graphene membranes by hydrocarbons which they confirmed from transmission electron microscopy studies.

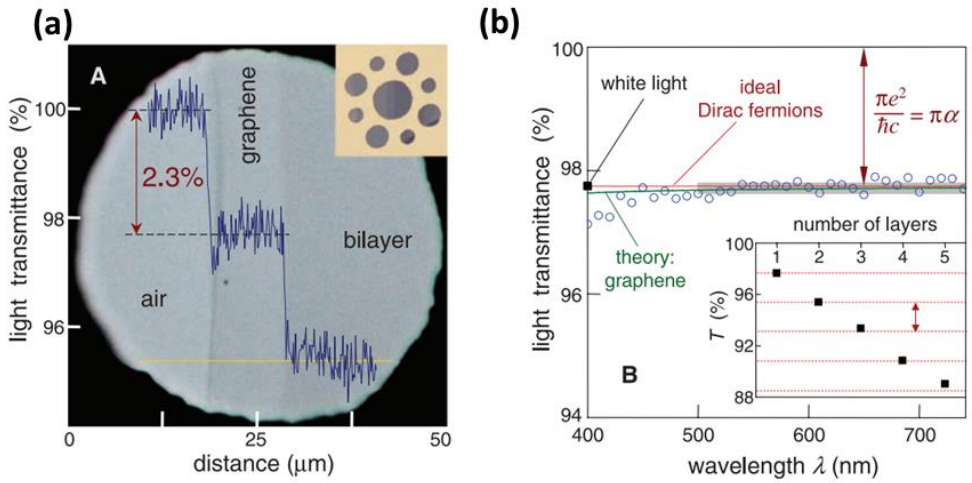

Figure 2.6: (a) A 50 μm aperture partially covered by graphene and a graphene bilayer. The transmittance of the sample was taken along the yellow line showing the opacity of graphene as 2.3% when compared to air. (b) The transmittance spectrum of graphene (open circles) versus wavelength. The behaviour for ideal Dirac Fermions is shown in the red line, while the grey area indicates the standard error for these measurements. Transmittance spectrum as a function of the number of graphene layers is shown with the red dashed line indicating that the transmittance decreases by a factor of $\pi\alpha$ for each layer that is added [17].

2.5 Mechanical properties

The strong covalent σ bonds between carbon atoms in graphene generate its mechanical properties. Lee *et al.* used a form of nanoindentation with atomic force microscopy to measure the mechanical properties of mechanically exfoliated monolayer graphene membranes. The tip with a calibrated spring constant and known radius of curvature was used to apply force on the suspended structure and the deflection was measured. The graphene membranes were suspended over open holes [15]. Measurements have shown that its Young's modulus is ~ 1 TPa and has a 2D tensile strength of 42 Nm^{-1} with a corresponding strain of 25%. The stated values are

for defect-free graphene. These values for graphene were obtained over membrane sizes of 1 µm and 1.5 µm, which are on much smaller scale than the length scale used for commercial materials. For example, stainless steel has a Young's modulus range of ~ 189 GPa to ~ 210 GPa, while borosillicate glass has a Young's modulus range of ~ 61 GPa to ~ 64 GPa [41]. Graphene is a 2D material and therefore its strain energy density is normalised by the area of the graphene sheet rather the volume according to Lee *et al.* [15]. This explains why its 2D tensile strength has units of Nm^{-1} (force/length) instead of Nm^{-2} (force/area). Based on its intrinsic mechanical properties, many publications have transferred CVD graphene to flexible substrates for use as transparent conductive electrodes [25, 30, 42, 43]. Kim *et al.* published work on the first CVD graphene transfer to flexible substrates (PET of thickness 100 µm with a 200 µm layer of PDMS polymer) [43]. The resistance of the graphene film had little variation up to a 2.3 mm bending radius when it was measured perpendicularly to the bending direction y. However the resistance increases to ~ 500 Ω when it is measured parallel to the bending direction. The graphene device can even withstand a bending radius of 0.8 mm, although initially the parallel resistance increases to ~ 4 kΩ before it recovers to a low resistance value showcasing graphene's exceptional mechanical strength.

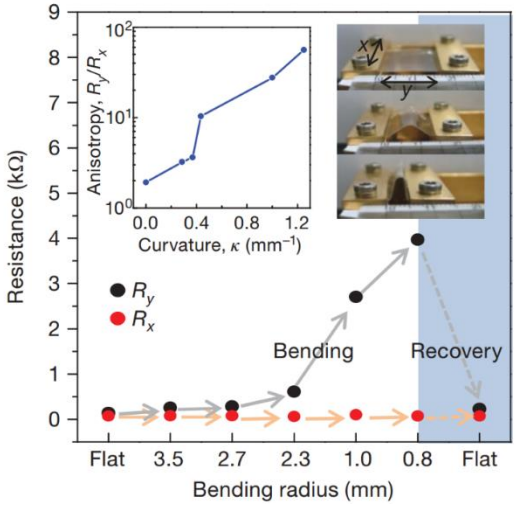

Figure 2.7: Plot of resistance versus bending radius for CVD graphene transferred to a 300 µm thick PDMS/PET substrate. The left inset displays the anisotropy in the four probe resistance measurement (Ry/Rx) when measured parallel (Ry) and perpendicular (Rx) to the bending direction, y. The right inset shows the bending direction (y direction) during the measurements [43].

2.6 Motivation for this work

The focus of this chapter is directed towards understanding the synthesis of graphene by chemical vapour deposition and subsequent characterisation. Initial results displayed non-continuous growth. An important characteristic of large area graphene growth is the graphene domain size and nucleation density. Large graphene domains and a low nucleation density of grains is desired to reduce the amount of charge scattering sites which can cause unwanted increases in the sheet resistance of the film. To improve the growth quality of CVD graphene, growth times of less than 2 minutes were used to visualise the graphene domains before they coalesce. Many factors were studied such as substrate pre-treatment, substrate geometry and purity and the growth pressure to improve the growth quality of CVD graphene. Following the improvement of graphene domain size, a continuous growth run is discussed.

2.7 Graphene fabrication methods

2.7.1 Mechanical exfoliation

The mechanical exfoliation of graphite was the first successful method of fabricating graphene in the laboratory. This was first investigated by Andre Geim and Konstantin Novoselov in the Physics department at the University of Manchester in 2004 [4]. They both received the Nobel Prize for Physics in 2010 regarding this research. The necessary tools for mechanical exfoliation are highly ordered pyrolytic graphite (HOPG) or natural graphite and adhesive tape. The tape is placed down on the graphite and another piece of tape is used to recleave the graphite. A general schematic of this method can be seen in Figure 2.8. The mechanical forces present during the cleaving process are strong enough to break the weak Van der Waals forces between the layers of graphite. However, the method first utilised by Novoselov *et al.* produces graphene of minute size, on the scale of microns. This mechanical cleavage method is unsuitable to scale up for industrial production.

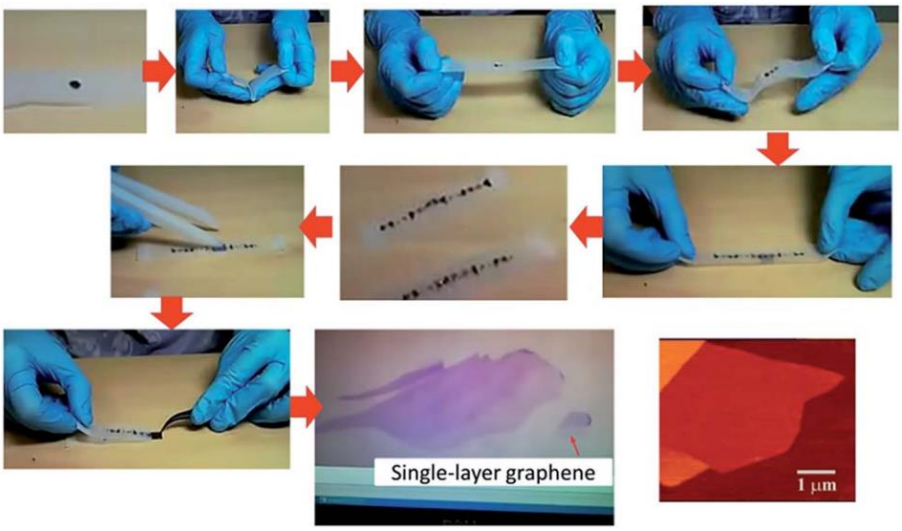

Figure 2.8: Process flow of the scotch tape method, used to mechanically cleave HOPG to produce graphene flakes [44].

2.7.2 Liquid exfoliation

Liquid exfoliation methods have also been demonstrated to produce graphene flakes [45-48]. This method was first demonstrated by Hernandez *et al.* in 2008 [49]. The work consisted of sonication and centrifugation of graphite powder dispersed in organic solvents such as N,N-dimethylformamide (DMF) and N-methylpyrrolidone (NMP). However the graphene produced has a very low concentration (~ 0.01 mg mL^{-1}). Based on this published work, many research groups have increased this concentration by increasing the sonication time, increasing the concentration of initial graphite, solvent exchange methods etc. [46, 50, 51]. One major problem associated with this method is that the graphene that is produced has a high defect density [52], likely due to the sonication method itself which can cause rapid cooling/heating rates and high pressure. However Coleman *et al.* have shown that a suitable solvent with surface energy ~ 68 mJ/m^2 can successfully liquid exfoliate graphene to produce nanosheets with low defect density [53]. However the sheet resistance of these nanosheets varies. For example a graphene nanosheet film had a sheet resistance of ~ 4 kΩ with a corresponding transparency of ~ 76%.

2.7.3 Epitaxial growth of graphene

Another method to produce high quality graphene is that of epitaxial growth via decomposition of SiC. This was first discovered by Claire Berger, Walt de Heer and co-workers [54]. It involves the thermal decomposition of SiC by Si sublimation and the segregation of carbon atoms on graphitic layers. SiC has two polar faces perpendicular to the c-axis. The SiC(0001) (Si-terminated face) has one dangling Si bond/atom, while the C-terminated face, SiC$(000\bar{1})$ has one dangling C atom/bond (Figure 2.9). The carbon segregation can happen on both the Si- terminated face and C-terminated face of the wafer. Epitaxial growth involves low pressures and high temperatures such as 1600 ^{o}C at a pressure of 100 mbar for the Si-face and 1450 ^{o}C and 1 x 10^{-4} mbar for the C-face [55]. Note that both cubic and hexagonal arrangements of SiC exist, but usually graphene is grown on the hexagonal type structure [56]. Two common types of hexagonal structured SiC used are referred to as 6H and 4H. For both the 6H-SiC and 4H-SiC, the unit cell consist of Si–C bilayers. 6H-SiC has a stacking arrangement of ABCACB, while the 4H-SiC has a stacking arrangement of ABCB as seen below in Figure 2.9.

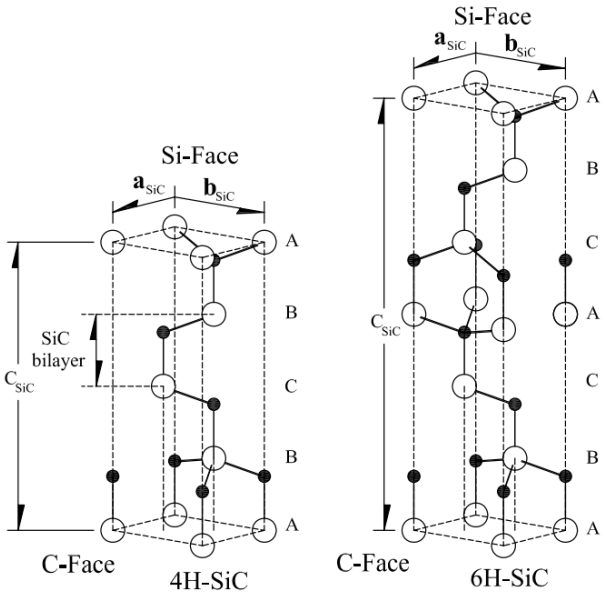

Figure 2.9: The unit cell structure of 4H-SiC and 6H-SiC showing the Si-terminated face and C-terminated face. The dark atoms represent carbon, while the white atoms represent Si. [56].

The formation of few layer graphene is achieved on the Si-face due to this thermal decomposition process, while thicker layer graphene is observed on the C-

face. The epitaxial growth of graphene allows high throughput processing and graphene of high quality. Even multilayer epitaxial graphene films on SiC have shown similar electronic properties compared to an isolated exfoliated sheet, such as a square root dependence on the Landau energy levels when an external magnetic field is applied (i.e. the quantum Hall effect is observable at room temperature) [54, 57, 58]. However, one disadvantage of this technique is the high cost of SiC substrates [59]. Also high temperatures (> 1500 ^{o}C) are required for the decomposition of Si from SiC which requires the use of high cost vacuum systems. It is also difficult to produce continuous high quality graphene during this process due to the cubic structure of SiC on Si which causes large residual stress during graphene formation and leads to film bowing and cracking [60]. The size of the graphene obtained depends on the size of the substrate used. Significant improvements have been shown for the growth of epitaxial graphene on hexagonal SiC. Particularly for the SiC $(000\bar{1})$ face, where the yield of operational switching devices is being characterised per mm^2 rather than µm^2 [56].

2.7.4 Chemical vapour deposition growth of graphene

2.7.4.1 Overview of the growth of graphene by chemical vapour deposition

Since graphene was first fabricated by Geim *et al.*, research has been undertaken to find a method of producing large area graphene while still maintaining its characteristics of high carrier mobilities [14] and transparency [17]. A method of producing graphene films via catalytic chemical vapour deposition (CVD) on transition metal foils was first demonstrated by Rodney S. Ruoff's group in the University of Austin, Texas [61]. It had been known that thin graphitic layers can be grown on transition metal carbide surfaces using CVD of hydrocarbons [62]. Li *et al.* produced a working CVD graphene device transferred to SiO_2 with carrier mobilities of ~ 4050 cm^{2}V^{-1}s^{-1}, with ~ 95% monolayer coverage. CVD has proved to be the best candidate for suitable large scale production of graphene with domain sizes as large as ~ 2 mm along the diagonal reported [63], although grain sizes of ≤ 50 microns are more typical [37, 64-66]. The first demonstration of CVD graphene growth by Li *et al.*, was carried out with a low pressure CVD system (LPCVD) system. Bae *et al.* have

demonstrated the growth and transfer of a 30-inch CVD graphene film onto a transparent substrate (Figure 2.11 (b)).

This synthesis method of graphene involves using a transition metal, usually copper foil as the catalyst material. This foil is heated up in a vacuum system (under hydrogen atmosphere) to temperatures in excess of 1,000 ^{o}C (below the melting point of the copper). The hydrogen helps to reduce contaminants on the foil e.g. oxygen, which can inhibit the growth of high quality CVD graphene [67]. The high temperature is used to increase the grain size of the copper foil. A suitable carbon feedstock such as methane is then introduced into the chamber. At present, the exact mechanisms used in the CVD growth of graphene are still not fully understood. However it is widely believed that graphene growth by CVD is a surface-mediated process [37]. This involves carbon atoms decomposing from the feedstock and nucleating on the surface of the metal catalyst. These nucleated domains then begin to coalesce to form a continuous film of graphene. In the case of growth using methane on Cu foil, decomposition of hydrogen atoms from the CH_4 molecules occur followed by full dehydrogenation. The carbon atoms then begin to migrate on the surface followed by attachment to the surface and finally nucleation and growth of a graphene monolayer (Figure 2.10).

In a crystalline material, a periodic structure is produced when a unit cell containing an array of atoms is repeated. For example, graphene produced by the mechanical exfoliation produces single crystal graphene i.e. the periodic structure remains intact across the material. However, graphene produced by chemical vapour deposition is polycrystalline [68]. Polycrystalline structures consist of smaller single crystal grains with different crystal orientations. When the two domains coalesce, the interface between the two adjacent grains is called a grain or domain boundary. TEM studies have shown that graphene domain boundaries consist of non-hexagonal structures. In fact, graphene domain boundaries consist of alternating pentagonal and heptagonal carbon ring structures and can be thought of as an array of dislocations [69, 70]. One can perceive these domain boundaries as structures that inhibit the propagation of charge carriers i.e. they cause charge carrier scattering which can reduce the electrical performance of graphene films [71, 72]. Weak localisation effects have been observed on isolated graphene domains by magnetotransport measurements when compared to single crystal graphene domains. Therefore domain boundaries

cause strong intervalley scattering of charge carriers. The disordered lattice structure caused by these domain boundaries is consistent with intervalley scattering [73]. Intervalley scattering can be detected by Raman spectroscopy measurements (i.e. the *D* peak), which will be discussed in section 2.9.2.1. Scanning tunnelling spectroscopy measurements have shown that graphene domain boundaries are commonly n-doped [74, 75]. Graphene tends to be p-doped due to contaminants on the surface or due to ambient adsorbates. Thus p-n junctions are formed between a domain and domain boundary. A domain boundary behaves as a potential barrier to charge transport. Scanning tunnelling microscopy analysis has demonstrated that domain boundaries in graphene produce standing wave patterns [75]. Multiple probe scanning tunnelling microscopy measurements have also shown that the resistance of a domain boundary is dependent on the width of the disordered transition region between adjacent domains. For instance, resistivity values in the range of ~ 4,300 μΩcm to ~ 14,300 μΩcm have been measured for CVD graphene domain boundaries [76]. Therefore high quality graphene growth is obtained when the number of nucleation sites is small and the graphene domain size is large (i.e. minimising the amount of domain boundaries).

Copper foils are the primary substrate that is used for CVD growth of graphene. Nickel foils have also been used but the nickel substrate itself is limited by its small grain size, the growth of graphene multilayers at nickel grain boundaries and the high solubility of carbon in the metal [61, 77]. The low solubility of carbon in copper promotes the formation of graphene at the Cu surface [78].

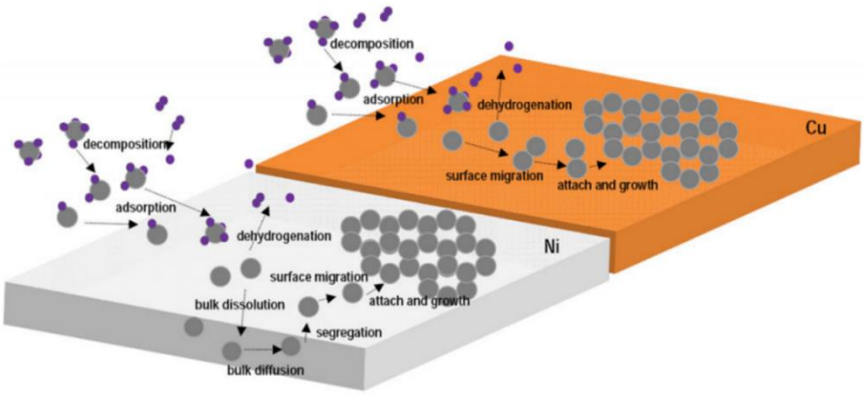

Figure 2.10: Growth kinetics of monolayer graphene by CVD on Ni and Cu foil by a methane precursor, showing dehydrogenation, surface migration and growth for both Ni and Cu substrates [79].

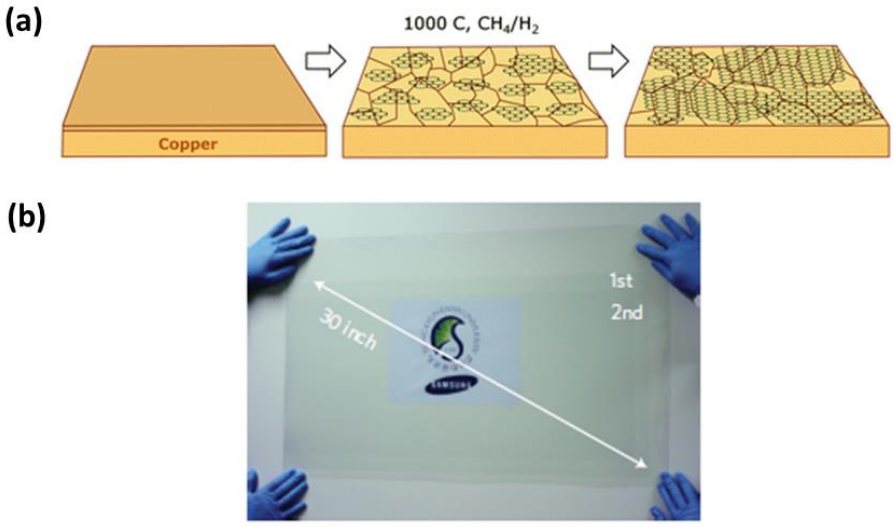

Figure 2.11: (a) CVD growth mechanism for graphene on copper. High temperature annealing in H_2 atmosphere increases the grain size of the copper foil. Carbon species from CH_4 decompose on the copper surface and domain nucleation occurs. These domains coalesce to form a continuous film [80]. (b) 30 inch transfer of graphene to a transparent plastic substrate via thermal release tape [42]**.**

2.7.4.2 Substrate effects

Inherent contaminants present on the copper foil before growth can degrade the quality of graphene grown. To counteract this, pre-treatments have been suggested before loading the growth substrate into the system. For example, an electropolishing technique can be used to reduce the roughness of the copper foil [64] and can also help to remove protective (corrosion-inhibiting) layers if present on the as-purchased foil. Various pre-growth cleaning protocols have been proposed, such as an acetic acid clean [81] and using solvent based cleans such as isopropyl alcohol (IPA) and acetone [82]. Acid pre-treatments have yielded useful results in regard to reducing contamination, while using IPA and acetone produced insufficient cleaning of the copper substrate. Acetone can also induce photo-catalysis of the copper foil when cleaning is not carried out in dark conditions [83].

The geometry and purity of the foil itself can also influence the quality of graphene growth. It was suggested by Chen *et al.* that for LPCVD, copper evaporation plays a major role during the growth process [63]. During LPCVD growth, the copper

film starts to evaporate albeit at a slow rate (Figure 2.12). However, this evaporation increases the roughness of the copper film thus inducing defects and irregularities on the copper substrate which inhibits continuous growth. Purity of the copper foil used in CVD growth of graphene has also been suggested being of critical importance. A higher nucleation density of graphene domains is achieved on low purity foils (99.8%), while higher purity (> 99.8%) foils supress the nucleation density, resulting in larger graphene domains [78].

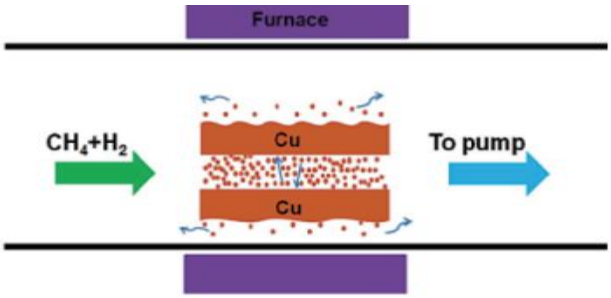

Figure 2.12: Schematic depicting how use of a tube geometry for the copper foil supresses' Cu evaporation during high temperature CVD and leads to a smoother Cu surface [63].

2.7.4.3 Annealing step

Typically the annealing is undertaken under a hydrogen atmosphere. The purpose of the hydrogen gas is to prevent the oxidation of the copper substrate to copper (II) oxide which will damage the graphene grown on the substrate. The use of hydrogen gas in conjunction with the high temperature anneal at 1,000 ^{o}C also increases the grain size of the copper foil and can reduce contaminants. The increased grain size of the copper means that the graphene domain size is less inhibited by the size of copper domains [37]. Although it can be advantageous to anneal for a long time, the integrity of the vacuum seals (i.e. potential for contaminant ingress) and the overall cost of the process have to be taken into account.

2.7.4.4 CVD kinetics

Three main types of CVD systems are low pressure CVD (LPCVD), atmospheric pressure CVD (APCVD) and plasma-enhanced CVD (PECVD). The main advantages

of using LPCVD over APCVD are that the rate of amorphous carbon deposited on metal films is much slower compared to APCVD. This is due to the lower partial pressure of methane in the tube furnace during deposition. Secondly, the use of lower pressure decreases the flammable nature of CH_4 and H_2 if they are mixed together in air. PE-CVD can be used to lower the growth temperature and is discussed at the end of this section, but typically the growth quality is lower than LPCVD and APCVD.

Varying the pressure during the growth step can influence the growth itself. For example, different nucleation shapes can be achieved by having different hydrogen pressures during growth as reported by Vlassiouk *et al.* [78]. A vapour trapping tube was shown to increase the individual graphene domain size inside the tube, while continuous growth is observed for samples placed outside the tube during the same process [84]. Placing the copper foil substrate inside a copper foil enclosure also resulted in a much lower density of domains [85]. The variation of graphene characteristics when placed in an enclosure has been attributed to a much lower methane partial pressure inside the enclosure.

2.7.4.5 Methods to lower the growth temperature

Lowering the process temperature in CVD graphene production is important to reduce costs and failure of the system vacuum seals. For instance Zhang *et al.* first reported graphene growth at temperatures as low as ~ 600 ^{o}C using a liquid-phase precursor, toluene [86]. Though low temperature graphene growth was achieved, the film was not continuous over the whole Cu substrate. Also the Cu foil wass annealed in a hydrogen atmosphere at ~ 980 ^{o}C prior to growth which negates the advantage of using low-temperatures for the growth process. Xue *et al.* demonstrated growing arrays of highly nitrogen doped graphene on a Cu substrate as low as ~ 300 ^{o}C by utilising pyridine molecules on the substrate surface [87]. But these arrays are unsuitable for TCEs, which require a large area continuous layer. At present, low temperature CVD growth of graphene is feasible, but the area coverage and quality of the growth is much worse than the usual high temperature growth process.

Some research groups have utilised plasma-enhanced chemical vapour deposition (PE-CVD) to facilitate low temperature growth of monolayer graphene. Instead of using high temperatures, the system uses a high energy plasma to provide the energy to decompose the precursor molecules. Terasawa *et al.* were able to produce

graphene by PE-CVD at a temperature of ~ 500 ^{o}C [88]. This work was influenced by the fabrication of a carbon nanowall (CNW) by Li *et al.* [89]. The growth of monolayer graphene precedes the formation of a CNW. The Cu foil is annealed at ~ 500 ^{o}C before growth. Even though the low temperature growth is advantageous to reduce strain on the system vacuum seals and power consumption, the high temperature anneal is required to increase the grain size of the metal foil. Terasawa *et al.* reported that grains sizes of 10 nm to 50 nm on Cu were achieved with this PE-CVD method compared to the larger grains sizes between 10 μm to 100 μm when utilising a high temperature anneal (≥ 950 ^{o}C) on the foil before growth. State of the art continuous graphene growth has been observed on Cu foil at a growth temperature of 420 ^{o}C using PE-CVD [90]. However the individual domains (< 200 nm in size) are much smaller than the domain sizes achievable by thermal CVD. One advantage of using low temperature PE-CVD growth of graphene, enables the use of a wider variety of growth substrates (grow directly on target substrate. Due to the use of a high energy plasma, no catalytic substrate is needed for low temperature PE-CVD. For example Chugh *et al.* grew graphene directly on SiO_2 at ~ 650 ^{o}C using a PE-CVD process [91]. However a large defect peak was present on the Raman spectrum even after 10 minutes of growth, indicating poor quality graphene.

Many parameters can influence CVD growth such as; gaseous flow rates, pressure in the system, selection of transition metal substrate, annealing time and temperature, carbon source deposition time and the growth temperature. A two-step CVD process has been reported to provide suitable graphene grain sizes and an overall large continuous film. This high quality film was produced by initially using a low value of pressure and gaseous flow rates to create a low nucleation density and then a continuous film is produced by increasing the flow rates and pressures [37]. However it is suggested that graphene grown via CVD preferentially nucleates from copper grain boundaries or copper surface irregularities, which increase the nucleation density. While there are many advantages to using CVD to grow graphene films, one has to also consider factors such as gas purity, purity of the copper foil and contaminants (from the quartz tube, handling of foil and the cleanliness of the copper foil itself), which all play a major role in the growth of graphene films.

2.8 Materials and methods

2.8.1 Growth of graphene by chemical vapour deposition

2.8.1.1 Operation of CVD system for graphene growth

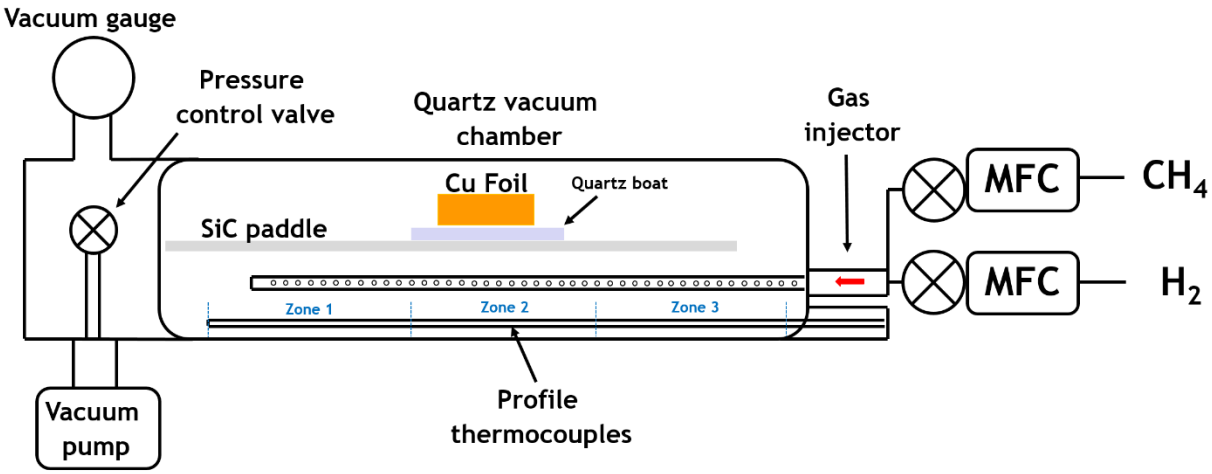

Figure 2.13: General schematic of the CVD furnace system used for graphene growth in Tyndall showing the vacuum gauge, pressure control valve (closed loop pressure valve), vacuum pump, SiC paddle, gas injector, profile thermocouple (three temperature zones) and mass flow controllers (MFCs) for both CH_4 and H_2. The Cu foil is housed on a quartz boat in the centre zone of the quartz tube (thermocouple zone 2).

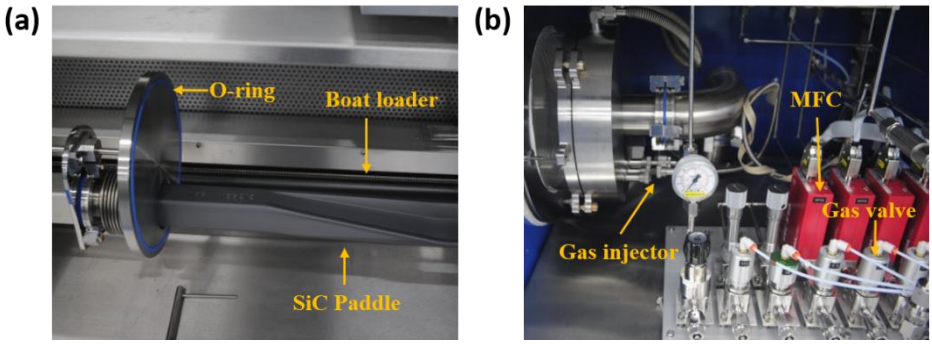

Figure 2.14: (a) Load zone of the CVD furnace showing the front door fluorinated Si O-ring, SiC paddle and boat loader. (b) The source zone which contains all the gas valves, mass flow controllers (MFCs) and the gas injector.

Training for the use of the CVD system was provided by the manufacturer, Tetreon. This CVD system is housed in a clean room fabrication facility which contains the appropriate safety mechanisms. The system was installed with a temperature safety mechanism, whereby the process aborts (all gases are turned off and the system is brought back to room temperature) if the temperature of the system goes above a certain value (~ 1,050 ^{o}C). Also, a leak check was undertaken on the system before each process gases were flown. If the leak rate was high, the process was not undertaken until the origin of the leak was found. Process development was undertaken with help from Vince Gallagher (maintenance team in Tyndall) and Sandy Disselduff (process engineer from Tetreon). This entailed setting up appropriate system checks before a process run, suitable abort processes (e.g. if the system goes over the set temperature in the process recipe), temperature calibration and appropriate temperature and gas ramp up rates. The CVD system in Tyndall is a 3 zone furnace with a 9" diameter quartz tube. Each zone corresponds to a different function of the system. The first zone is the load station. This is where samples are placed on a SiC "paddle" prior to entering the reactor (Figure 2.14 (a)). The paddle is attached to a metallic door. The door seal uses fluorinated silicon O-rings. The second component is the process zone. The process zone is where the growth occurs and consists of a quartz tube (~ 9 inch diameter) to withstand high temperatures. The final zone is the source zone (Figure 2.14 (b)) and this is where all gas valves and mass flow controllers (MFCs) are housed. MFC's allow the operator to decide the amount of flow for a particular gas along with ramp up/down rates. Gases are introduced into the system by the use of a cylindrical quartz rod (gas injector) on the bottom of the quartz tube.

The CVD system is kept under vacuum with a current base pressure of ~ 10 mTorr and is maintained at room temperature between growth runs to prevent damage occurring to the vacuum seals. Prior to processing, the system is vented to atmosphere using nitrogen gas. While this venting process is occurring, pre-treatments can be undertaken to reduce contaminants from the as-received foil. Atmospheric pressure is confirmed by the atmospheric valve (valve 9). The substrate is then placed on a quartz boat the SiC paddle and is loaded into to furnace. A leak check is undertaken to ensure the integrity of the vacuum seals. You want the leak rate to be low (currently ~ 15 mTorr per minute). Residual oxygen can be present due to leaks in the system. Before the temperature is increased, the water cooling mechanism at the front and back of the

system is increased to ~ 6 L/min. The temperature is ramped to 1,000 ^{o}C (or desired temperature) under a hydrogen atmosphere. It is advantageous to place the Cu substrate in the centre of the quartz tube i.e. in thermocouple zone 2 (Figure 2.13) to receive maximum methane flow. An annealing step of the substrate at 1,000 ^{o}C is utilised before growth for a certain time. The methane precursor is then applied for desired time followed by cooling of the system to room temperature (in approximately 6 hours) under a hydrogen atmosphere and removal of the substrate.

Closed loop pressure (CLP) is a method by which a suitable pressure can be achieved in the CVD system during a process. This CLP method was used during CVD processes to achieve a desirable growth pressure. The desirable pressure is achieved by the CLP valve because it regulates the effective pumping speed (referred to as the "angle" in the Operations programme, set to 90^{o} to turn CLP off). Using a higher growth pressure has been shown to increase the graphene domain size. In some cases, it may prove useful to turn the CLP off, i.e. have the pump fully open once the furnace is being cooled to room temperature after growth. This would result in a lower residence time for gas molecules in the system.

2.8.1.2 PC program control for CVD system

The CVD furnace is controlled by using the PC-MUX operation programmes on the computer. The "Process Tube Type" program contains the list of gases available in the system along with their corresponding valves and maximum flow rates. Note that all the valves except valve 9 (atmospheric switch) are normally closed. V9 is closed once atmospheric pressure is achieved in the system. The programme also contains the boat loader position when it is at rest and when in motion and this can also be configured. "Process Workbench" is where CVD recipes can be created. CVD recipes are based on previous conventions and each recipe can contain subrecipes. It is critical to insert suitable shut-down subrecipes that allow the system to abort safely if problems arise. These alarms are called events. Events can arise due to the boat stalling (if the boat is introduced too quickly into the system), gas flow tolerances (if a particular gas is shut off), and temperature tolerances (if one particular zone goes above the set safe temperature) along with many other safety interlocks. A parameter table can also be inserted which is a list of critical parameters. This allows one to change the critical

parameters such as processing temperature, annealing time etc. without having to go through the recipe to change them. The most important program is the "Operations" and this is where the recipe is loaded and contains all parameters in real time such as the temperature of each zone, boat loader position, which gas valves are open, tube pressure and which part of the recipe the programme is on.

In relation to temperature, there are three zones in the process tube with two thermocouples (TCA and TCB). The furnace temperature in each zone is detected by an interface board. Below this is the Smart Over-Temperature System (SOS). This is directly linked to the heating element. Therefore if the temperature goes above the limit set by the SOS, the heating element will trip and no power will be supplied to the furnace. The system uses B-type thermocouples which are accurate at high temperatures but inaccurate at lower temperatures (< 100 ^{o}C). The thermocouple itself is made from platinum and rhodium. In the thermocouple there will be a hot region and a cold region. If the electric field differs between these two regions, then current will flow. The thermocouple outputs a µV value and this is converted to a temperature value which can be read on the PC program. All the data for each run is stored on the "Batch Data Plot" program. This means that information such as gas flow rate, temperature and pressure for a particular run can be exported e.g. to Excel and analysed.

2.8.1.3 Substrate pre-treatment for CVD growth of graphene

Training was provided by clean room fabrication staff for the use of strong acids. A risk assessment (NTG_CRA_58 – Copper foil pre-cleaning for CVD graphene) was undertaken for the dilution of strong acids with deionised water. Acids were applied to deionised water in a fumehood ensuring that the air flow rate was at an acceptable level. The appropriate safety gear (apron, heavy duty gloves and visor) were used during this protocol. Cu foil, 25 µm thick (purity of 99.8%) was purchased from Alfa Aesar (item # 46365). Prior to placing the Cu foil on the SiC paddle before insertion into the CVD furnace, a pre-treatment was carried out to reduce contaminants on the as-received foil. The foil was cut to desired size and placed in a Teflon holder. The Teflon holder was used to hold the copper foil in place during the acid pre-treatment steps (see Figure 2.15). All cutting tools (tweezers, scissors, rulers and scalpels) were

cleaned prior to cutting using IPA wipes. The pre-treatment consisted of first immersing the foil in deionised (DI) water, followed by 5% HCl in DI water, rinsing in DI water, followed by 5% HNO_3 in DI water and a final DI water rinse. This was followed by gently blow drying with a nitrogen gun and cutting the excess foil that was in the Teflon holder. The foil was then placed on the SiC paddle as fast as possible to minimise contamination by ambient particulates and the paddle was inserted into the CVD furnace for growth. As schematic of the acid clean is depicted below in Figure 2.16. This acid clean was developed based on suggestions from Dr. Carl Magnuson from Ruoff's group in Texas.

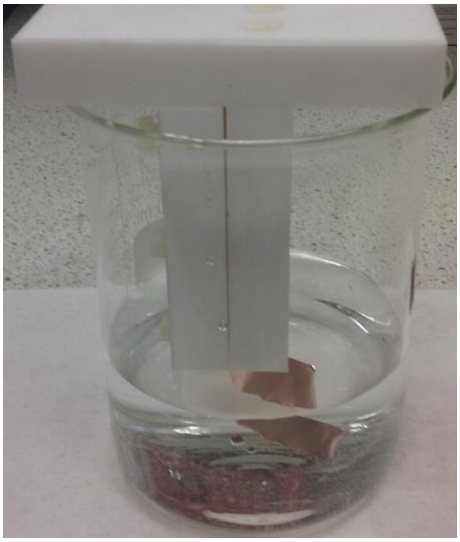

Figure 2.15: Photo of the Teflon holder used to hold the Cu foil in place while carrying out the acid pre-treatment protocol before CVD growth of graphene.

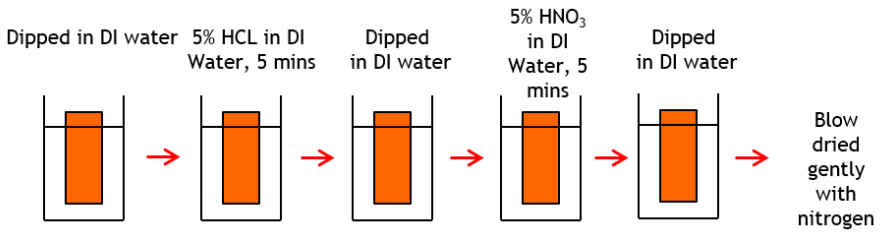

Figure 2.16: Schematic of the acid pre-treatment utilised on the Cu foil before CVD growth of graphene.

2.8.1.4 Substrate geometry and purity for CVD growth of graphene

After the acid pre-treatment step using the Teflon holder, the Cu foil was wrapped around a Teflon rod to produce a Cu foil tube of diameter ~ 10 mm prior to inserting into the CVD system. The foil tube was then placed on the SiC paddle and loaded into the CVD furnace for growth. To study the effect of substrate purity, Cu foil 25 µm thick (purity 99.999%) was purchased from Alfa Aesar (item # 10950).

2.8.1.5 Influence of growth pressure for CVD growth of graphene

To study the effect of growth pressure on the size of graphene domains, three different CVD runs were carried out with different growth pressures on 25 µm thick, high purity copper foils (purity 99.999%). Once pre-treatments were carried out on the as received foil, the samples were inserted into the CVD furnace. The temperature was ramped up to 1035 ^{o}C under 95 SCCM (standard cubic centimetres per minute) of hydrogen, followed by a 15 minute anneal at this temperature. Methane gas was then applied for 25 seconds at this temperature. The pressure was adjusted using the closed loop pressure valve for the following growth pressures: 57 mTorr, 140 mTorr and 450 mTorr.

2.8.1.6 Continuous CVD growth of graphene

For growth runs targeting continuous growth, the temperature was ramped up 1035 ^{o}C under 95 SCCM of hydrogen. 20 SCCM of methane gas at 450 mTorr was utilised for 15 minutes followed by cooling the furnace down to room temperature under 95 SCCM of hydrogen, followed by the removal of the samples.

2.9 Characterisation of graphene, methods and approaches

2.9.1 Optical characterisation

2.9.1.1 Thickness of dielectric layer

High throughput methods of finding graphitic flakes on target substrates was sought when graphene was first isolated in 2004. Blake *et al.* reported the use of specific thicknesses of dielectrics on Si substrates which allows the visualisation of graphene on these substrates [92]. 300 nm of SiO_2 was used initially as it provided good contrast but a slight change in thickness of the dielectric to 315 nm largely reduces the visibility

[9]. Using a Fresnel law based model, the change of contrast by varying the wavelength of light and the dielectric thickness can be calculated. Therefore, the substrate of choice for graphene transfer via CVD or mechanical exfoliation is silicon with a dielectric layer of SiO_2 of 90 nm (thermal oxide), which allows easy visualisation of graphene via optical microscopy using a green light source [92]. Once graphene is transferred successfully to SiO_2, optical characterisation is undertaken with a Zeiss Optical Microscope using a green light filter at various magnifications. Another use of optical microscopy for visualisation of graphene is that it allows one to estimate the number of layers present. The contrast of a graphene film is proportional to layer thickness. Darker graphene films are indicative of bilayer or multilayers. The number of layers can subsequently be confirmed by Atomic Force Microscopy (AFM) and Raman Spectroscopy.

2.9.2 Visualisation of graphene domains on copper foil

A method has been reported that allows fast analysis of initial graphene growth on copper foil via optical microscopy [66]. Jia *et al.* demonstrated that thermal annealing of the Cu foil samples in air after CVD growth of graphene, creates a colour contrast between regions covered by graphene (yellow) and bare copper regions (dark orange). This colour contrast can easily be seen on a standard optical microscope. Bare copper foil samples (#46365 Alfa Aesar) oxidised at temperatures ~ 240 ^{o}C and could be used as references. Initial samples were placed on a hotplate and the temperature was ramped up from ambient temperature to ~ 310 ^{o}C. As soon as the colour of the reference sample started to change, both sample (graphene on copper) and reference (copper only) foils were removed from the hotplate. This method is depicted in Figure 2.17 below.

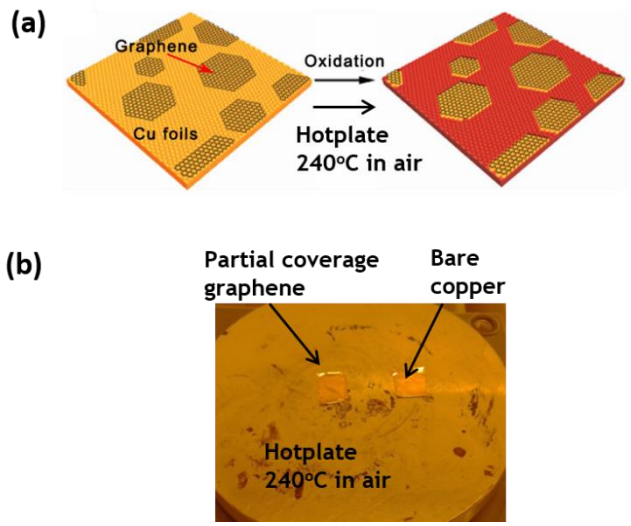

Figure 2.17: (a) Schematic showing the method of annealing the copper foil with graphene coverage which allows rapid optical analysis of graphene on copper foil [66]. (b) Photo depicting this method where the copper foil oxidises at ~ 240 ^{o}C. The bare piece of copper foil was used as a reference. As soon as the bare piece of foil oxidised, the copper foil with partial coverage of graphene was removed from the hotplate.

2.9.2.1 Raman Spectroscopy

Non-destructive methods for material characterisation are desirable in both industry and academic research. One type of non-destructive spectroscopic characterisation technique is Raman spectroscopy which involves the inelastic scattering of photons. Most of the photons undergo elastic scattering (Rayleigh scattering). However, a tiny fraction (10^{-7}) of these photons undergo inelastic scattering and this is referred to as the Raman effect [93]. The scattering occurs because the incident electromagnetic radiation induces a dipole moment, in the molecule it interacts with

$$\boldsymbol{P} = \alpha \boldsymbol{E} \qquad \textbf{(2.26)}$$

where α is the atomic polarizability and $\boldsymbol{E}$ is the electric field strength of the incident wave. To observe the Raman effect, there must be a change in the polarizability of a molecule as it vibrates. This can thought of as the selection rule for Raman. The inelastic scattering of a photon can be divided into two categories denoted as Stokes or Anti Stokes-Raman scattering as can be seen in Figure 2.18. In the Stokes case, the incident radiation, $E = h\nu_0$, excites the molecule to a virtual energy state and after a finite time this energy is released in the form of a photon and the atom goes into a

vibrationally excited state. Thus a net loss of energy occurs, $\Delta E = h\nu_0 - h\nu_m$, which is lost to the outgoing photon which has a lower frequency than the incident photon. For the Anti-Stokes case, the incident radiation excites an atom which is already in an excited state. Since the ground state is preferred by electrons at room temperature, Stokes-Raman scattering is usually observed unless the sample is in a higher state due to thermal excitations or otherwise. Experimentally, this Raman shift is observed by impinging electromagnetic radiation of a suitable frequency to excite the material and measuring the back scatter with a spectrometer.

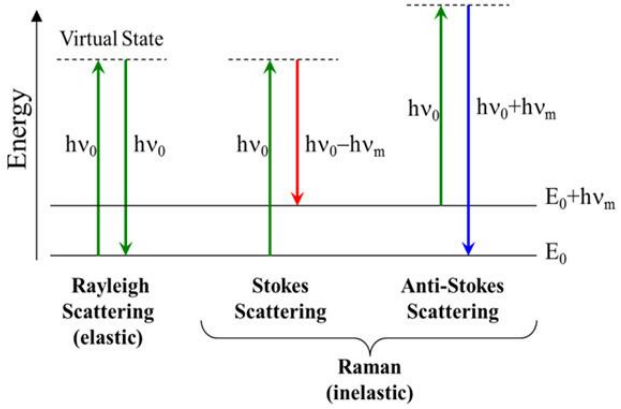

Figure 2.18: Energy transitions for Rayleigh scattering (elastic) and Raman scattering (inelastic) where ν_o denotes the frequency of the impinging electromagnetic radiation and ν_m denotes the frequency of a given vibrational or rotational mode [94].

Thus, Raman spectroscopy is a vibrational spectroscopic technique and can be used to find a unique chemical signature of materials by quantifying low energy excitations such as phonons. The data collected by a Raman spectrometer is usually in units of Intensity Counts versus Raman shift (in units of cm^{-1}, i.e wavenumbers).

Raman Spectroscopy of graphene

Raman spectroscopy of bulk graphite was first undertaken by Tuinstra and Koenig in 1970 [95] showing Raman active peaks at wavenumbers of ~ 1575 cm^{-1} and ~ 1355 cm^{-1}. Raman spectroscopy of graphene was first investigated in 2006 by Ferrari *et al.* Fortunately, monolayer graphene has a characteristic Raman spectrum consisting of three main peaks, these are conventionally called the *D* (peak position ~ 1350 cm^{-1}), *G* (peak position ~ 1580 cm^{-1}) and *2D* (peak position ~ 2700 cm^{-1}) (sometimes denoted as *G'*) peaks [96, 97]. This allows accurate distinction between monolayer, bilayer and

multilayer graphene (graphite). An understanding of the phonon dispersion of sp^2 bonded carbon species is key to interpreting the Raman spectrum [98]. In graphene there are two atoms per unit cell and there are six phonon dispersions. For the six phonon dispersion modes, three consist of optical (*O*) phonons, while the other three consist of acoustic (*A*) phonons. For all three acoustic and all three optical phonon modes, one is an out-of plane phonon mode (*oT*), while the other two are in-plane modes, one parallel (longitudinal L) and one perpendicular (transverse T). Thus starting from the *Γ* point (highest energy) in the Brillouin zone, the phonon modes are denoted as *LO*, *iTO*, *oTO*, *LA*, *iTA* and *oTA* as shown in Figure 2.19.

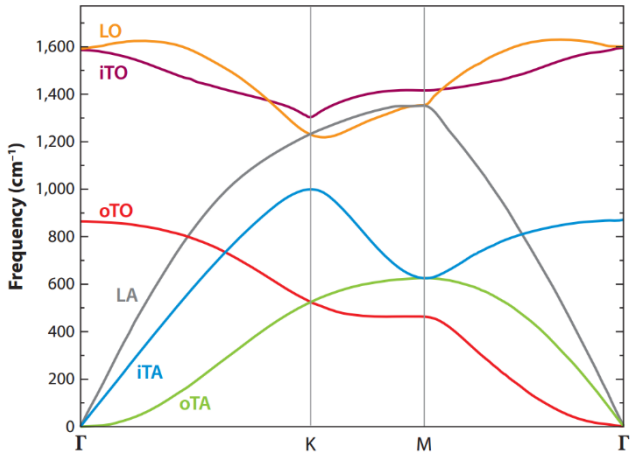

Figure 2.19: Phonon dispersion relation of graphene showing the *LO*, *iTO*, *oTO*, *LA*, *iTA*, and *oTA* phonon modes at the *Γ*, ***K***(***K*** ') and *M* saddle points [98].

The optical phonons present in the zone-center (*Γ*) and zone edge (***K*** and ***K'***) region are Raman active. The *D* peak results from defects in the graphene film and are regarded as entities that break the translational symmetry of graphene's hexagonal lattice structure. Therefore graphene's Raman defects are mainly caused by the edge effects of graphene and crystalline defects such as vacancies. For example, graphene grown by CVD can have defects associated with transfer residue and domain boundaries. Also the change of graphene's hybridisation state from sp^2 to sp^3-hybridisation is considered a defect as this breaks the translational symmetry of the graphene lattice. The *G* peak results from the radial breathing mode of carbon atoms when excitation occurs. The *2D* peak results from a two phonon excitation [99]. The *D* and *2D* peaks are the result of a double resonance process. This begins with an electron of wave-vector ***k*** around momentum space, ***K***, absorbing a photon of energy

E_0. The electron is inelastically scattered by a defect or phonon comprising of a wave-vector $\boldsymbol{q}$ and energy E_{phonon} to a $\boldsymbol{K}'$ point with a wave-vector $\boldsymbol{k} + \boldsymbol{q}$. The electron is then scattered back to a *k* state and emits a photon due to electron-hole recombination at a *k* state. This can also be denoted as intervalley scattering i.e. scattering from the $\boldsymbol{K}$ point to the $\boldsymbol{K'}$ point. In the *D* band case, one scattering process consists of one elastic scattering event by the defects in the crystal, while the other consists of inelastic scattering by emitting or absorbing a phonon. In the case of the *2D* peak, both the scattering events are inelastic and two phonons are involved in this process as seen in Figure 2.20.

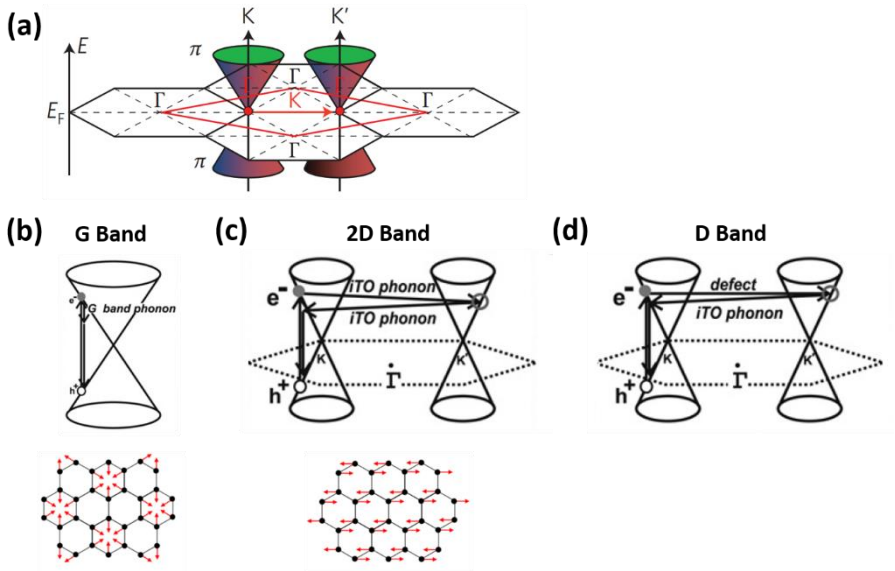

Figure 2.20: (a) Electronic Brillouin zones of graphene (shown as black hexagons), the first-phonon Brillouin zone (shown as a red rhombus) and schematic of Dirac cones (electronic dispersion) [99]. (b) First order *G* band process [97]. (c) Two-phonon second-order resonance Raman spectrum processes for the double resonance *2D* band. (d) One-phonon second-order double resonance process for the *D* band.

The previously quoted values for the *D*, *G* and *2D* peaks for graphene are observed when using a 514 nm wavelength laser (green laser) [96]. The wavelength of the incoming electromagnetic radiation influences the position of the three characteristic Raman peaks of graphene i.e. the *D*, *G* and *2D* peaks. For sp^2 carbon ring structures e.g. graphene, the dispersion of the G peak saturates at ~ 1,600 cm^{-1} [100]. However, the *D* peak is always dispersive regardless of the laser wavelength

that is used. This is because it originates from a double resonant Raman process [101, 102]. This is also true for the *2D* peak because it's the first overtone of the *D* peak. Hence, if the wavelength of the laser light is changed, the Raman peak positions for the *D* and *2D* peaks will shift. For example, the *2D* peak blue shifts by ~ 70 cm^{-1} when using a laser wavelength of 457 nm in comparison to a laser wavelength of 633 nm [103]. Using a specific laser wavelength, allows one to compare peak positions of the *G* peak and more specifically the *D* and *2D* peaks to those obtained in the literature. A laser wavelength of 514 nm is used extensively in the literature [96, 103, 104] and is used throughout this thesis.

Note that in this chapter, Raman spectra were taken on hotplate annealed (ambient annealed) Cu foil which results in a large background and typically only the *2D* graphene peak is seen. Raman spectra of graphene on annealed Cu foil in this work were taken with a Renishaw Raman Spectroscopy system which has a laser power of 11 mW at a wavelength of 514 nm. A large laser power was needed due to the large background present on the Raman spectra due to the copper foil. All spectra were taken at an exposure time of 10 s and an objective lens of 50x magnification.

2.9.3 Topographical characterisation

2.9.3.1 Atomic force microscopy

Atomic Force Microscopy (AFM) is an important characterisation technique used to study the surface topography of a certain material. The technique was first reported in 1986 and is based on the Scanning Tunneling Microscopy technique. Atomic resolution is possible with the AFM, however the resolution is limited by the radius of curvature of the tip. The basic operation of an Atomic Force Microscope operating in alternating current (AC) mode is as follows.

- A laser shines onto a cantilever beam with a pyramidal tip at one end. Typically the cantilever is made of silicon or silicon nitride and the radius of curvature of the pyramidal tip is of the order of nanometres. The laser spot is aligned on to the back side of the probe cantilever. The laser spot is then reflected onto a photodiode.

- This cantilever is made to oscillate near its resonant frequency, lightly contacting the surface at the bottom of its swing.
- While the tip is scanning across the sample (x,y), the interaction between the tip and sample is kept constant during the scan by a feedback mechanism.
- The feedback mechanism adjusts the distance between the tip and sample surface (z piezo displacement) to maintain a constant oscillation amplitude.
- An accurate topographical image is achieved if the tip-sample interaction is homogenous across the sample.

Topographical information of graphene samples measured using AFM, included height values and roughness analysis. AFM scans were taken with a Veeco D3100 AFM. The scan rate for was usually set at 0.7 Hz or below depending on the amount of contaminants on the sample. Roughness analysis can be indicative of contaminants on the graphene film or can show the effect of solvent cleaning or annealing in a rapid thermal annealer (RTA) for example. AFM analysis is a slow throughput process and therefore was carried out once a graphene monolayer had been confirmed via optical microscopy and Raman spectroscopy.

2.9.3.2 Scanning electron microscopy

A scanning electron microscope (SEM) uses secondary electrons (or backscattered electrons) to resolve an image. These electrons are generated when a primary beam is focused on the sample. A cold-cathode field-emission SEM uses a very high electric field to emit electrons rather than thermionic emission from a heated filament [105, 106]. The electrons are accelerated to the anode by the use of a strong electric field. Electromagnetic lenses are used to direct the beam of electrons to the surface of the sample under study. The image is resolved on a monitor by a detector which detects the electrons that are deflected or emitted from the sample. A high vacuum ($\sim 10^{-10}$ Torr) in the electron gun chamber is required for the SEM to provide a controlled electron beam. The specimen chamber pressure is $\sim 10^{-6}$ Torr.

Inspection of the surface is possible using two different types of electrons, secondary and backscattered electrons. Backscattered electrons are a result of an elastic collision between incident electrons and specimen electrons. Conversely, secondary electrons are the result of inelastic collisions between the specimen and incident electrons. Backscattered electrons provide elemental contrast. In a beam-

specimen interaction, the number of backscattered electrons which are produced is proportional to the atomic number of the specimen atoms. Therefore a brighter image will be produced for elements with a high atomic number when compared to elements with a lower atomic number [105]. Secondary electrons provide topographical detail due to a small escape depth when compared to backscattered electrons which have a larger escape depth. Secondary electrons provide higher resolution in SEM images (~ 10 nm).

The accelerating voltage is another important parameter for the SEM [105]. When using a high accelerating voltage, the electron beam penetration is greater which results in a higher number of backscattered electrons. However, this reduces the spatial resolution of the image. Using lower acclerating voltages can give more secondary electrons in comparison to using high accelerating voltages. To obtain an image with good contrast, a suitable ratio of backscattered to secondary electrons is important. Throughout this thesis, a low accelerating voltage of ~3 kV was used to achieve suitable topographical information.

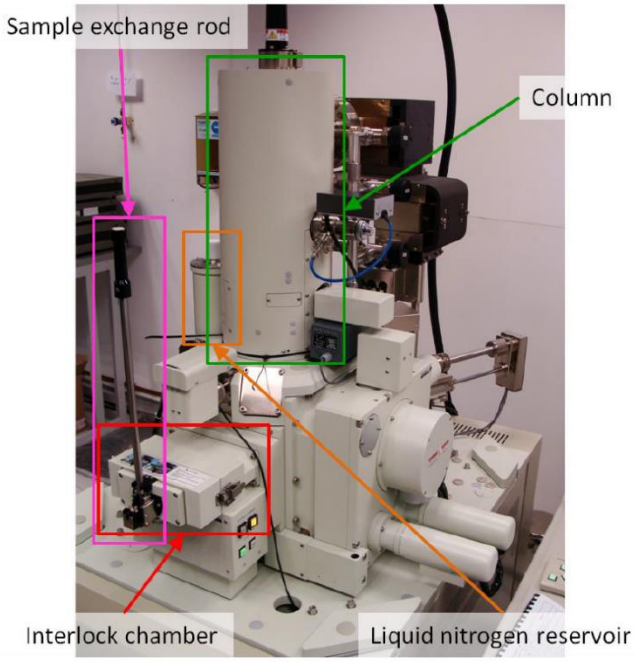

Figure 2.21: A photo of a JEOL JSM-7500F field emission scanning electron microscope showing the interlock chamber which is used to input samples into the chamber by using the sample exchange rod. The column holds all the optics in the instrument.

SEM images were taken using a JEOL JSM-7500F field-emission SEM. The 25 µm thick Cu foil was placed on a SiO_2 chip (corners of the foil wrapped around the chip) prior to loading. The screw clamps on the brass specimen holder would cause the foil to wrinkle, hence the use of a SiO_2 sample as a base. The sample was loaded into the specimen chamber and it was evacuated to a pressure of ~ 9.6 x 10^{-6} Torr. Images were taken at an acceleration voltage of 3 kV and an emission current between 5 µA and 10 µA.

2.10 Results and Discussion

2.10.1 CVD graphene grown on copper foil

Initial CVD runs were based on the parameters used by Bae *et al.* [42] using the operation of the CVD system as described in section 2.8.1.1. The CVD process run (run 2) involved a temperature ramp up to 1,000 ^{o}C under 25 SCCM of H_2 (pressure of ~ 25 mTorr), followed by a 15 minute anneal at 1,000 ^{o}C under 25 SCCM of H_2 (pressure ~ 24 mTorr), followed by 30 minutes of CH_4 deposition (50 SCCM) at the same temperature with a pressure of ~ 350 mTorr using the CLP valve. The system was allowed to cool to room temperature to unload the samples. As mentioned in Section 2.8.1.1, the cool down time from growth temperature to room temperature was ~ 6 hours for all runs. If the system is cooled down to room temperature too quickly, wrinkles start to form on the graphene film. These wrinkles are caused by compressive stress during the cooling process due to the different thermal expansion coefficients of graphene and copper [107]. It is important to have an adequate cool down time to minimise the presence of wrinkles on the graphene film. The wrinkles can act as charge carrier scattering sites which can increase the sheet resistance. However it has been reported that domain boundaries affect the resistivity of the graphene film more so than wrinkles [108]. Wrinkles can also originate from the fact the growth substrate is not entirely flat due to the existence of grain boundaries [109] and step edges [110].

The hydrogen gas was present in all stages of the process run (temperature ramp up, anneal, growth and cool down). The Cu substrates were mounted vertically in the wafer slots on the quartz boat. However due to the fragile nature of the copper foil, wrinkling occurred. Wrinkling of the substrate can inhibit continuous growth from occurring as depicted in Figure 2.22, where graphene growth (darker contrast) is not continuous. The presence of graphene was confirmed by Raman spectroscopy, which will be discussed in the next section. Studying initial runs via the SEM also confirmed the large presence of contaminants on the foil. Subsequent runs were carried out by changing parameters such as the pressure during annealing/growth using the closed loop pressure (CLP) valve. However changing the pressure while keeping the other parameters constant did not reduce the amount of contamination on the samples after growth. To avoid wrinkling, the foil was placed flat on the quartz boat but poor quality graphene growth was also observed. To improve the growth quality of graphene by CVD, parameters such as Cu foil pre-treatments, geometry of the foil, the

purity of the foil and the growth pressure were investigated and are discussed in subsequent sections.

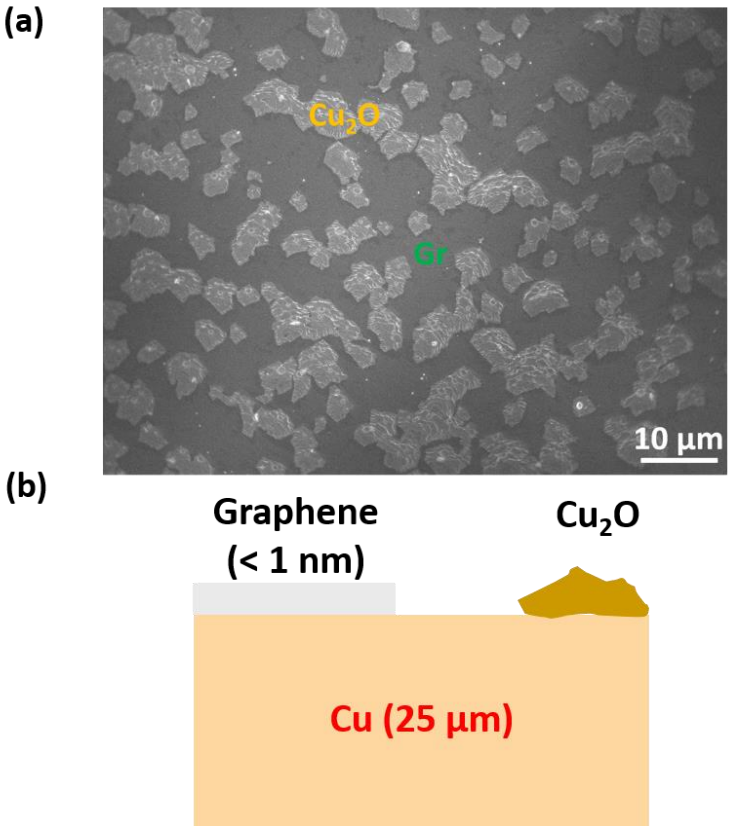

Figure 2.22: (a) SEM image of a representative initial graphene CVD process run (run 2) after ambient annealing on a hotplate. The CVD process consisted of a 15 minute anneal in H_2 at 1,000 ^oC followed by 50 SCCM of CH_4 for 40 minutes at a pressure of ~ 350 mTorr. The hydrogen gas was present in all stages of the process run (temperature ramp up, anneal, growth and cool down). Graphene is denoted as "Gr" and copper oxide is denoted by "Cu_2O". The growth is not continuous as evident from the SEM image & (b) schematic of the SEM image in part (a). The numbers in brackets represent the thickness of the Cu foil and the thickness of graphene.

2.10.2 Optimising graphene growth on Cu foil: Low growth time regime, Cu pre-treatment, substrate geometry and copper foil purity

Graphene preferentially nucleates at copper grain boundaries before coalescing into a complete film. For high quality graphene growth via CVD, it is critical for the domain size to be as large as possible. To study the nucleation density and domain size, graphene was grown by CVD on copper foil with minimal carbon deposition times (i.e. growth times < 2 minutes). This presents an efficient way of analysing the growth by changing any of the critical parameters; temperature, annealing time, gas flow rates and pressures before the nucleation points coalesce. Samples were analysed via SEM and optical microscopy. Graphene domains were visualised on optical microscopy images using a hotplate annealing step as described earlier in section 2.9.2. The colour contrast between graphene and the oxidised copper can easily be seen on a standard microscope as seen in Figure 2.23 (a). The Raman spectrum of graphene on oxidised copper displays a large background due to the copper foil but the *G* peak and *2D* peak can still be seen on the spectrum (Figure 2.23 (b)) with values of ~ 1594 cm^{-1} and ~ 2687 cm^{-1} respectively. Raman peaks present from < 1,300 cm^{-1} are from the oxidised Cu foil itself. These peak positions are ~ 149 cm^{-1}, ~ 214 cm^{-1}, ~ 534 cm^{-1} and ~ 643 cm^{-1} which correspond to the Raman peaks of Cu_2O [111, 112].

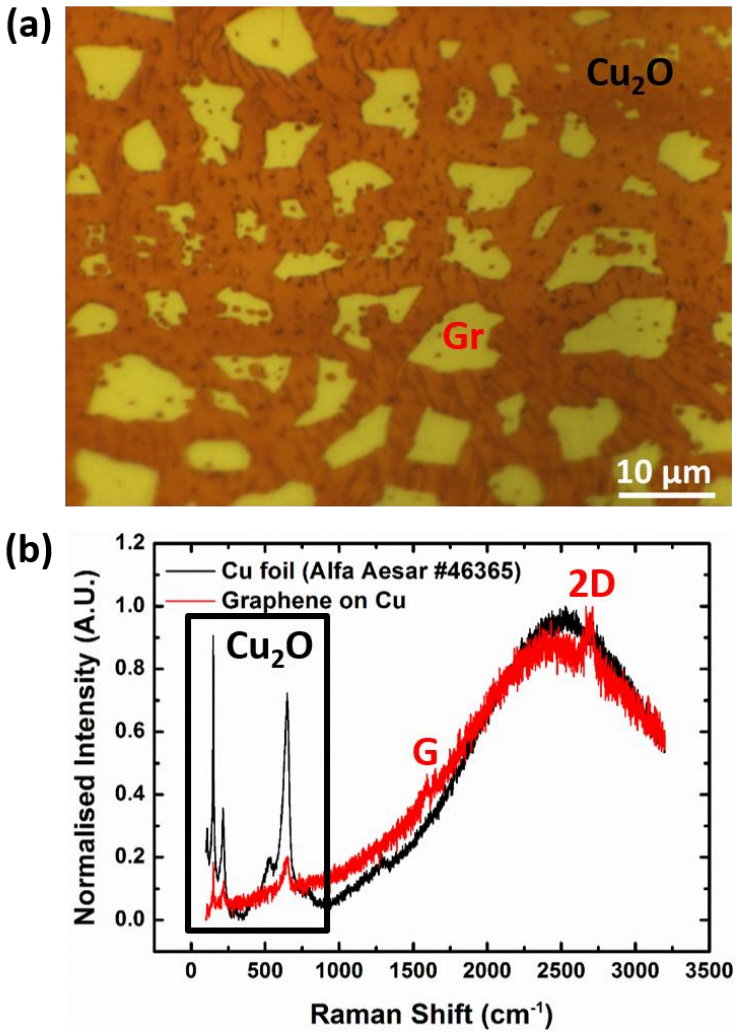

Figure 2.23: (a) 100 x magnification optical microscopy image of CVD Run 45 after with a growth time of 1 minute at ~ 1,035 ^{o}C (450 mTorr CLP) after using the hotplate annealing method (ambient annealing) [66]. Graphene are the yellow shapes denoted by "Gr". The oxidised copper confirmed by Raman as Cu_2O is denoted by "Cu_2O". (b) Raman spectrum of graphene (yellow shapes) on ambient annealed Cu foil showing the *G* and *2D* peaks. Note that the large background exists due to the copper foil and the Raman spectrum of the foil itself is included. The Raman peaks < 1,300 cm^{-1} are the Raman peaks of Cu_2O, i.e. ~ 149 cm^{-1}, ~ 214 cm^{-1}, ~ 534 cm^{-1} and ~ 643 cm^{-1} [111, 112].

.

The first initial growth run was carried out with a methane deposition time of 1 minute at 1,000 ^{o}C with a 15 minute H_2 anneal at the same temperature. The copper was placed flat on the quartz boat with no pre-treatment before CVD growth. The CLP

was set at 450 mTorr during the growth process (turned off after growth). A copper enclosure was suggested to provide better growth. Therefore a copper box was made from the #46365 foil from Alfa Aesar. The copper foil sample was placed inside the box before inserting into the CVD chamber, however there was no discernible difference using this method and the contamination on the copper foil post-growth was quite large. Chen *et al.* discussed the effect of a rough Cu surface on graphene growth [63]. The authors hypothesised that when the copper evaporates in the inner surface of the copper tube due to the high temperatures of the CVD process, it redeposits on the inner surface of the tube, so that only a minute amount of copper is lost through evaporation (e.g. the outer ends of the tube). This reduces the roughness of the copper surface which helps to supress the nucleation density i.e. large graphene domains are grown. When a graphene domain is grown on the foil, it inhibits the evaporation of the copper below it. Therefore the copper foil was rolled up into a form of tubes (diameter ~ 10 mm) to supress the evaporation of copper at high temperatures. This was placed on the quartz boat parallel to flow. The foil was also aligned perpendicular to the gas flow in a subsequent run but displayed insufficient growth of graphene. The geometry of tube is suggested to suppress the evaporation of copper during LPCVD and inhibits the roughness increasing on the copper substrate.

Alfa Aesar were adamant that the copper foil came in pristine condition and did not need any further cleaning. However, many groups in literature utilise some form of pre-treatment before growth as the quality of the Cu foil differs from batch to batch. The copper foil was pre-treated with an acid clean suggested through correspondence with Dr. Carl Magnuson from the Ruoff group in Texas as described in section 2.8.1.3. The copper foil was held in place using a Teflon holder when undertaking the acid clean. The first step suggested was placing the copper foil in acetone however copper foil photo-catalyses when placed in acetone when it's not carried out in dark conditions [83]. Therefore this step was abandoned. The acid clean was successful in removing a large amount of the contaminants on the copper foil (Figure 2.24 (a) and (b) with corresponding schematics in Figure 2.24 (c) and (d)) which are suspected to be CuO nanodots in the literature [113]. They are referred to herein as contaminant nanodots. However it is clear that the density of nucleation sites has slightly increased (Figure 2.24 (b)). Although this is undesirable, it is much more important to remove contaminants which have a negative effect on the electrical

characteristics of continuous graphene films e.g. more domains are produced which increases the likelihood of electrons scattering. Kim *et al.* demonstrated this by comparing the sheet resistance of graphene films grown on as received foil and those of foil with an acid pre-treatment (5% (w/w) HNO_3 for 30 seconds) [81]. A larger sheet resistance variation was observed for graphene grown on un-treated foil samples. Sheet resistance, $R_{S,}$ values were in the range of ~ 241 Ω/sq to ~ 295 Ω/sq (treated foil) versus R_S in the range of ~ 368 Ω/sq to ~ 650 Ω/sq (un-treated foil).

Following this, a comparison was made between sheet and tube Cu foil geometry (acid pre-treatment utilised). Using the sheet geometry and an acid pre-treatment resulted in mean area and perimeter values of ~ 6.4 ± 4.6 μm^2 and ~ 11.2 ± 4.9 µm (averaged across four SEM images). Utilising a tube geometry resulted in larger graphene domains (averaged across four SEM images). An area value of ~ 34.8 ± 28.2 μm^2 and a perimeter value of ~ 27.9 ± 12.9 µm were measured for a tube geometry with an acid pre-treatment. The large standard deviation of the area value for tube geometry suggests that although the graphene domain size is increasing across the sample, small domains are still present. The domain sizes compare favourably with literature i.e. domain sizes of ~ 20 µm achieved using a two-step CVD process [37] and other reported domain sizes on the order of tens of micrometres [71, 114]. Representative SEM images of graphene domains of sheet and tube geometry are shown below (Figure 2.25 (a) and (b) with corresponding schematics in Figure 2.25 (c) and (d)). This novel method was utilised in literature to achieve graphene domain sizes of ~ 2 mm along the diagonal. However, this was achieved for a low methane partial pressure (~ 9 mTorr) which is comparable to the current base pressure of the CVD system in Tyndall (~ 10 mTorr). Also the growth occured at 1,035 ^oC for 6 hours [63] and full surface coverage was not achieved. The growth time of 6 hours utilised in the publication was not used herein. It is not a realistic growth time for that temperature due to the integrity of the vacuum seals on the CVD system and the overall cost of the process.

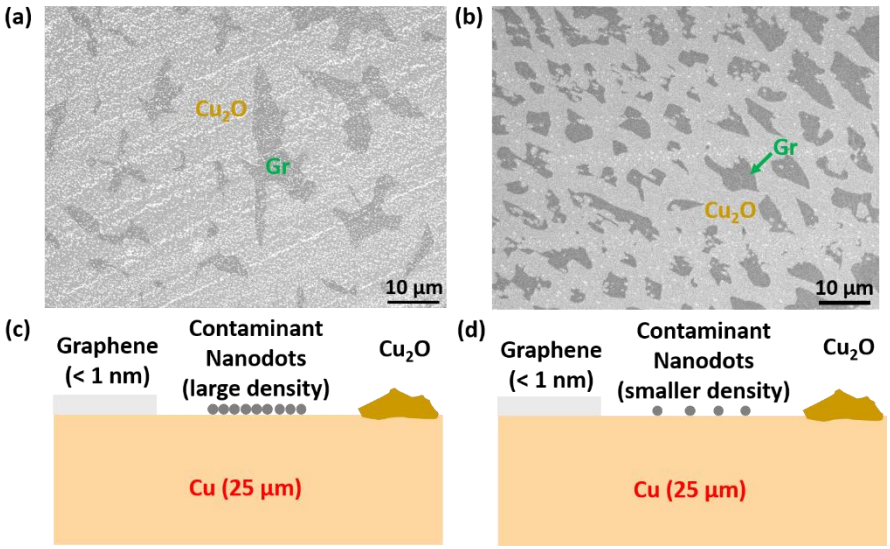

Figure 2.24: (a) Representative SEM image of graphene grown on copper after ambient annealing on a hotplate. The growth was carried out using a CH_4 deposition time of 1 minute at 1,035 ^{o}C using a pressure of 450 mTorr via the CLP valve with no acid pre-treatment. (b) Representative SEM image of graphene grown on copper after ambient annealing on a hotplate. The same growth parameters were used as in the first SEM image but an acid pre-treatment was also utlised. A drastic decrease in the number of contaminants is evident, however the nucleation density is larger. (c) Schematic of the SEM image in part (a) & (d) schematic of the SEM image in part (b) depicting the lower density of contaminant nanodots after the acid pre-treatment of the foil before growth. The numbers in brackets represent the thickness of the Cu foil and the thickness of graphene.

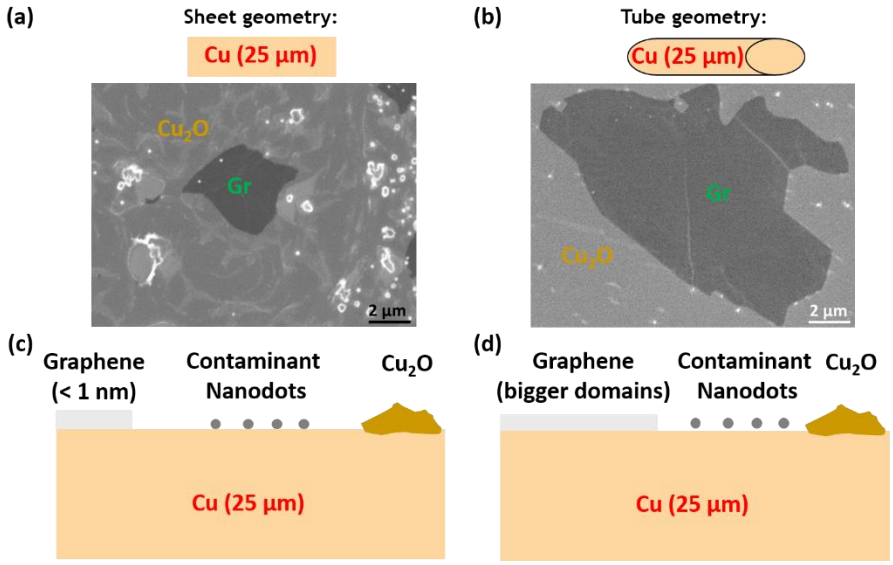

Figure 2.25: (a) Representative SEM image of graphene grown on a copper sheet after ambient annealing on a hotplate. The growth was carried out using a CH_4 deposition time of 1 minute at 1,035 ^{o}C at a pressure of 450 mTorr via the CLP valve. (b) Representative SEM image of graphene grown on copper after ambient annealing on a hotplate. The growth parameters were the same as in the first SEM image except the copper is in the form of tube geometry (~ 10 mm diameter), showing an increase in domain size when coppered to sheet geometry. (c) Schematic of the SEM image in part (a) & (d) schematic of the SEM image in part (b) showing the increased domain size when using a copper tube geometry in relation to sheet geometry. The numbers in brackets represent the thickness of the Cu foil and the thickness of graphene.

Following the minute growth regime on low purity foil (99.8%), high purity foil (99.999%) was utilised for a comparison. From the subsequent SEM and optical images, it appeared that the growth time of 1 minute (for high purity foils) was too long to achieve single nucleation points (it appeared that nucleation points had already coalesced). However the SEM images (Figure 2.26) suggest that graphene growth occurs at a much rapid rate than when utilising higher purity foils and with larger domains. The use of an acid pre-treatment on higher purity foils allows a more rapid and continuous growth of CVD graphene when compared to un-treated high purity foils (more graphene coverage when utilising acid pre-treatment). Huang *et al.* demonstrated that the use of higher purity foils (99.999%) instead of lower purity foils

(99.8%) resulted in larger graphene domains (470 ± 36 nm versus 250 ± 11 nm) and higher carrier mobilities (7,300 ± 1100 $cm^2 V^{-1} s^{-1}$ versus 1,000 ± 750 $cm^2 V^{-1} s^{-1}$) [69].

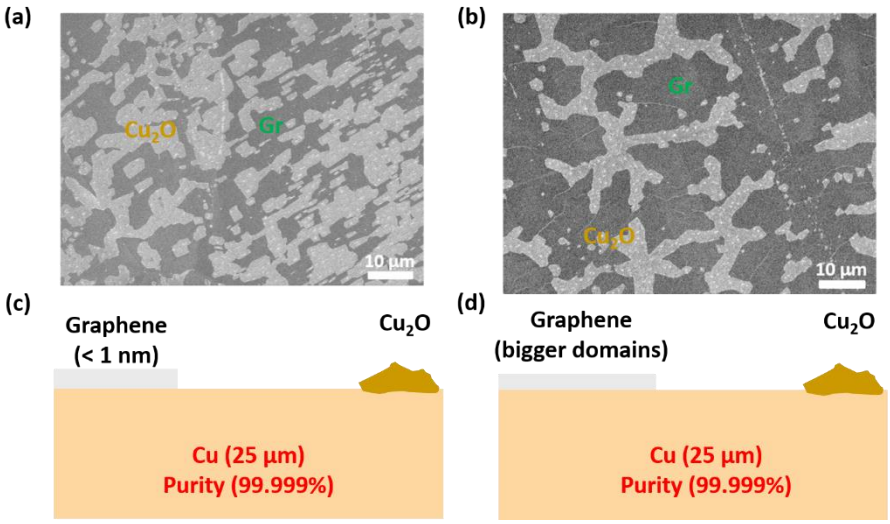

Figure 2.26: (a) Representative SEM image of graphene grown on un-treated high purity copper foil (99.999%) after ambient annealing on a hotplate. The growth was carried out using a CH_4 deposition time of 1 minute at 1,035 ^oC using a pressure of 450 mTorr. (b) Representative SEM image of graphene grown on copper after ambient annealing on a hotplate. The same growth parameters were used as in the first SEM image (using high purity foil), but an acid pre-treatment was also utlised. Across all the SEM and optical images, graphene growth utilising high purity foil occurred at a faster rate than when using lower purity foil (99.8%). (c) schematic of the SEM image in part (a) & (d) schematic of the SEM image in part (b) showing the increased domain size when utilising an acid pre-treatment when compared to untreated foil. The numbers in brackets represent the thickness of the Cu foil and the thickness of graphene.

2.10.3 Increasing growth pressure: Effect on domain size

To improve the initial growth and to study the effect of the pressure on the domain size, the pressure was raised from 57 mTorr to 140 mTorr and subsequently to 450 mTorr, keeping the growth time of 25 seconds and the temperature of 1035 ^oC constant. The size of graphene domains was measured on four 100x optical images for each data set using ImageJ. The free hand tool in ImageJ was used to measure the domains. For this analysis the domain area range was set between 10 μm^2 to 150 μm^2.

The distribution of domain area and perimeter values becomes larger as the pressure is increased from 57 mTorr (domain area ~ 17 ± 5 μm^2, domain perimeter ~ 19 ± 5 µm) to 140 mTorr (domain area ~ 32 ± 19 μm^2, domain perimeter ~ 27 ± 11 µm) and subsequently to 450 mTorr (domain area ~ 69 ± 40 μm^2, domain perimeter ~ 40 ± 15 µm), see Figure 2.28. However, larger domains are present after increasing the growth pressure. For example, maximum domain areas of ~ 30 μm^2, ~ 100 μm^2 and ~ 150 μm^2 were measured when increasing the growth pressure from 57 mTorr to 140 mTorr and subsequently to 450 mTorr. This is also evident for the domain perimeter (~ 30 µm, ~65 µm and ~ 80 µm). This suggests that although the average domain size is increasing, small domains are still present. Note that this pressure study was undertaken on high purity foils and explains why the domain area is much larger when compared to the value achieved in the previous section when utilising an acid pre-treatment with tube geometry. The mean nucleation density per optical image slightly decreased from ~ 22 to ~ 17 domains when increasing the pressure from 140 mTorr to 450 mTorr. The increase in domain size and decrease in nucleation density shows in particular how important the pressure setpoint is in regards to graphene growth by CVD. Since the CLP valve is used to regulate the pressure, a high residence time for particles exists for higher pressures (the pump is not fully open). Vlassiouk *et al.* noted that APCVD is preferred over LPCVD as it negates the effect of copper evaporation during the CVD process. However the highest pressure chosen herein of ~ 450 mTorr was chosen because the system has a high pressure setpoint of ~ 0.5 Torr and going above this pressure causes the CVD process to abort.

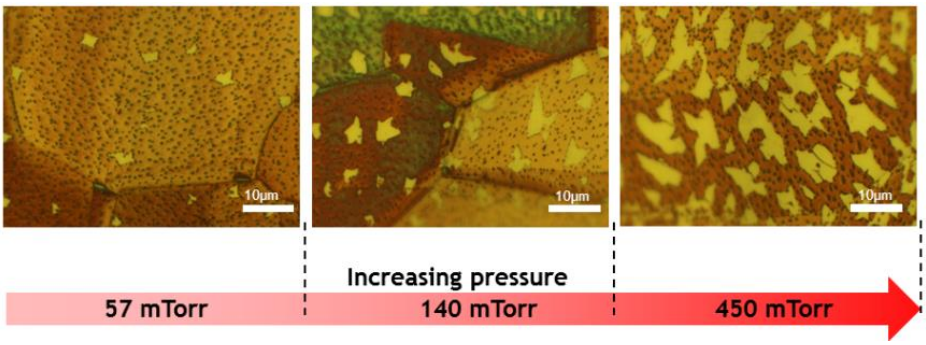

Figure 2.27: Optical images of CVD graphene growth on copper after ambient annealing on a hotplate, showing the effect of increasing the chamber pressure on the size of domains. The three pressures (57 mTorr, 140mTorr and 450 mTorr) represent three different CVD runs. In all three cases, the H_2 annealing time (15 minutes) and temperature (~ 1,035 ^oC), the growth time (~ 25 seconds) and growth temperature (~ 1,035 ^oC) were constant.

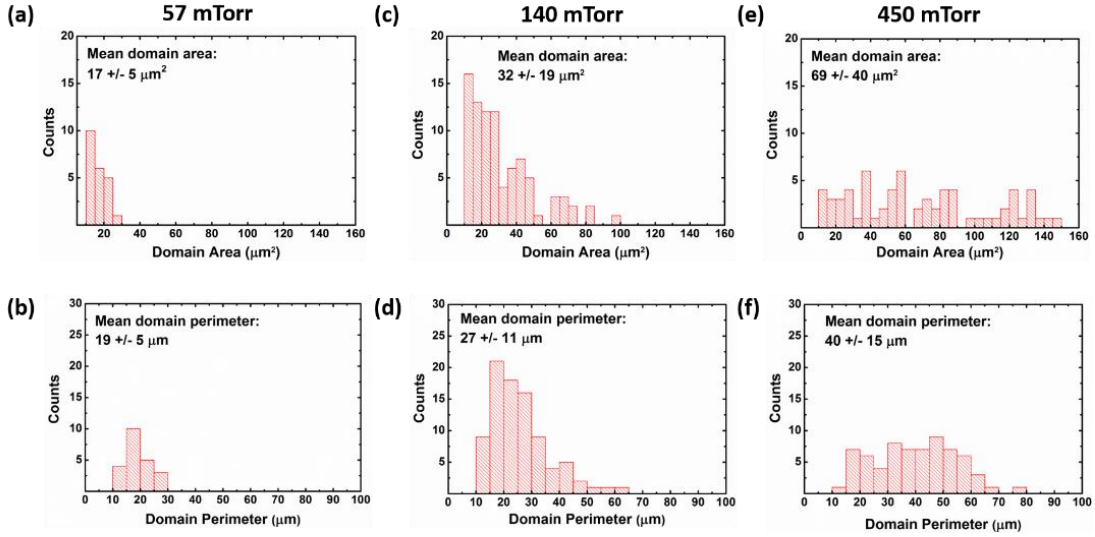

Figure 2.28: Histogram data showing the distribution of domain areas and domain perimeters respectively for pressures of (a) & (b) 57 mTorr, (c) & (d) 140 mTorr, (e) & (f) 450 mTorr. The distribution of the area and perimeter of domains becomes larger as the pressure increases. This analysis was carried out on four 100 x optical images for each run using ImageJ.

2.10.4 Continuous growth of CVD graphene

Using the information from the low growth regime along with investigating the geometry of the copper, the effect of an acid pre-treatment and the use of higher purity foil, a continuous growth run (run 48) was carried out using the method in section 2.8.1.6. The growth time for the continuous run was set at 15 minutes. Stage 1 is the temperature ramp up to 1,035 ^{o}C under 95 SCCM of H_2, stage 2 is the annealing at 1,035 ^{o}C for 15 minutes, stage 3 is the methane deposition (20 SCCM) for 15 mins at 450 mTorr and stage 4 is the cool down in hydrogen to room temperature. Analysing the SEM and annealed optical images (Figure 2.29) show that the film is mostly continuous. Raman spectroscopy was used to confirm that graphene was present on different points across the sample as well as regions of minute Cu_2O. A representative Raman spectrum taken from one region from Figure 2.29 (a) is shown in Figure 2.30 displaying the *2D* peak (~ 2712 cm^{-1}). A copper grain boundary is present in Figure 2.29 (a) and suggests that the graphene growth is not inhibited by copper grain boundaries. Impurities (grey coloured) can be seen in both SEM images (Figure 2.29 (c) and (d)). A summary of the chronological timeline of the CVD system in Tyndall is given in Table 2.1.

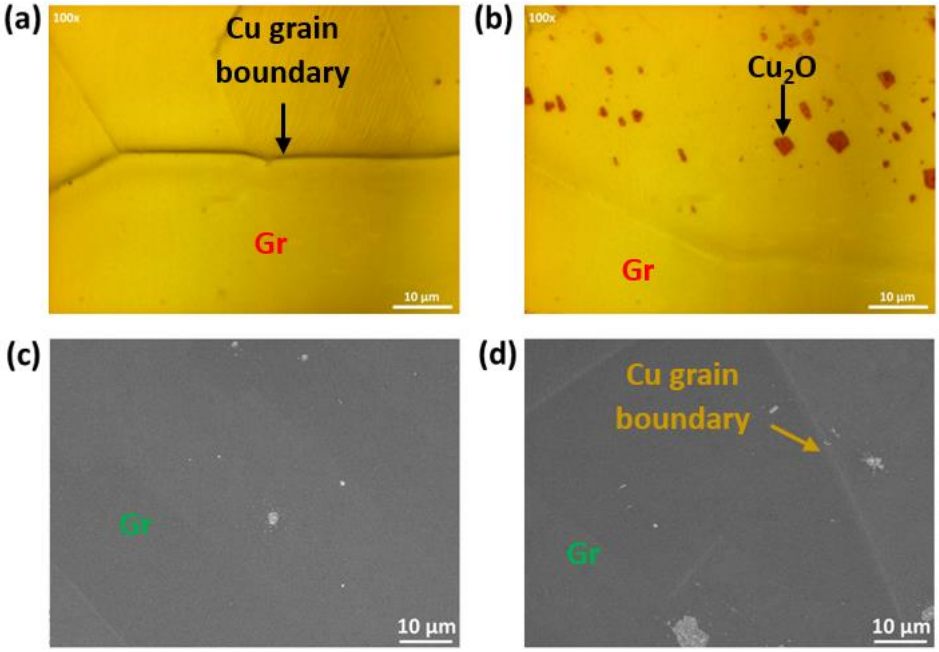

Figure 2.29: (a) 100x optical image (after ambient annealing) of a continuous graphene CVD run on copper (15 minutes CH_4 deposition at 1,035 ^oC with 450 mTorr CLP) confirmed by Raman spectroscopy showing the presence of a large area graphene coverage and copper grain boundaries. (b) 100x optical image of a continuous graphene CVD run (after ambient annealing) showing the presence of minute copper oxide confirmed by Raman spectroscopy. (c) & (d) Representative SEM image showing the minute presence of copper and a copper grain boundary, along with large area graphene coverage. Scale bars are 10 µm.

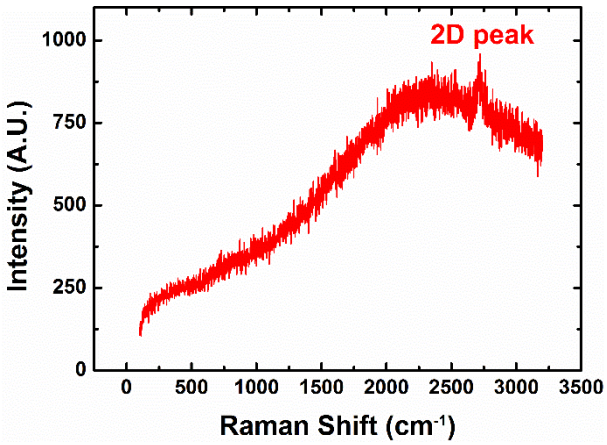

Figure 2.30: Representative Raman spectrum of graphene (yellow coloured regions from Figure 2.29 (a) and (b)) showing the presence of the *2D* peak at ~ 2712 cm^{-1}.

Following the first continuous CVD run, many runs were undertaken using the same growth parameters (15 minutes CH_4 deposition at 1,035 ^oC with a pressure of ~ 450 mTorr via CLP). Three CVD runs in total displayed similar growth as run 48 above (Figure A.1 in Appendix A) which correspond to CVD runs 49, 50 and 51. High growth coverage was observed by using optical microscopy and SEM. The subsequent five continuous methane growth runs which correspond to CVD runs 63, 64, 65, 69 and 72 using the same parameters displayed a lower coverage of graphene on surface via optical microscopy and SEM analysis (Figure A.2 in Appendix A). One of the goals of the research project was the realisation of the growth of CVD graphene at low growth temperatures using a toluene precursor. Note that CVD graphene growth results using toluene are not included in this thesis, as no observable growth occurred below 1,000 ^oC (over 16 growth runs). The toluene precursor was used for three runs corresponding to runs 59, 60 and 62 in between the next set of continuous methane growth runs mentioned previously (CVD runs 63, 64, 65, 69 and 72). The toluene precursor was flown in the same tube that was used for methane growth. This may be one reason why growth quality with the methane precursor degraded due to contamination.

The next method to improve growth quality was to use an acid pre-treatment on the foil, followed by annealing for 15 minutes at 1,035 ^oC in the CVD system, removing the foil, applying an acid pre-treatment again and placing the foil in the CVD system for the growth of CVD graphene (15 minutes CH_4 deposition at 1,035 ^oC with a pressure of 450 mTorr via CLP). This method was suggested by Dr. Carl Magnuson from the Ruoff group and corresponds to run 76. Low graphene coverage was still present after growth (Figure A.3 in Appendix A). Another method to improve the reliability of CVD graphene growth was to increase the annealing and growth time from 15 minutes each, to 30 minutes each (Figure 2.31 (a)) and subsequently 45 minutes each. However, O-ring failure (Figure 2.31 (b)) on the front and back door of the CVD system was noted after four runs (runs 78, 81, 83, and 86) and the annealing and growth time were reduced back to 15 minutes. Following inadequate coverage, the copper foil was placed in the CVD system between two quartz wafers, which was first suggested by Chen *et al.* to improve CVD graphene growth [63]. However, no graphene growth was observed for these two runs (corresponding to runs 99 and 100)

using quartz wafer enclosures. Also these runs displayed a large density of contaminant nanodots.

The next step was to replace the quartz tube, the quartz gas injector and the quartz sheath for the thermocouples. Copper residue was present on the front and back ends of the quartz tube. This is due to Cu evaporation during process runs over an extended period of time. Images of the growth runs (runs 108 and 109) after the quartz tube was replaced are giving in the Figure A.4, Appendix A. The use of a vapour trapping tube was suggested to increase the domains size of CVD graphene [84]. Images of these growth runs are given in the Figure A.5, Appendix A. One run consisted of vapour trapping tube with a 2" diameter (run 112), while the other tube had a diameter of 1" (run 113). In both cases, low graphene coverage was still observed after growth. The last step which was suggested by Dr. Carl Magnuson was the use of a gas purifier for the methane line. This gas purifier was placed in the gas line just before the methane gas enters the CVD system. The growth quality of the two subsequent CVD runs (runs 124 and 125) did improve in relation to previous runs but was still not as continuous as the first four continuous growth runs (see Figure A.6, Appendix A). A summary of the chronological timeline of the CVD system in Tyndall is given in Table 2.1.

This author proposes the use of a smaller CVD system for graphene growth along with a methane purifier. Therefore, one can ensure that the quartz tube can be cleaned regularly. The outer diameter of the quartz tube in the CVD system in Tyndall is ~ 9 inches. This makes it difficult to remove it from the system as it can easily be damaged. The large size also makes it difficult and costly to replace and clean. Quartz tube diameters for graphene growth in many literature publications are ≤ 6 inches [37, 64, 84, 115]. Improved growth quality was observed after a methane gas purifier was installed in the gas line. The author also proposes the use of a designated quartz tube if utilising more than one carbon precursor as to avoid contamination. Due to the need for regular cleaning of the large diameter quartz tube along with the cost associated with cleaning and replacing the large diameter quartz tube and due to the unreliable nature of the CVD system in Tyndall, CVD graphene growth was not pursued any further in this thesis.

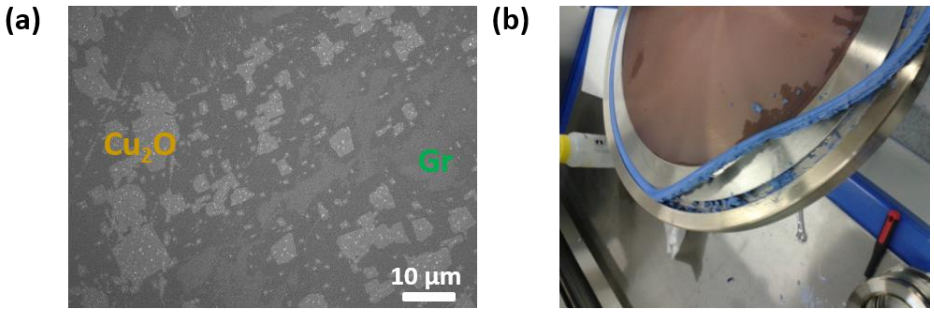

Figure 2.31: (a) Representative SEM image of poor graphene growth (30 minutes CH_4 deposition at 1,035 ^oC with 450 mTorr CLP) after ambient annealing showing a significant presence of Cu_2O (confirmed by Raman). (b) O-ring vacuum seal failure due to repeated use of a longer growth i.e. 45 minutes at 1,035 ^oC.

Table 2.1: Summary showing the chronological timeline of the CVD system in Tyndall.

Date:	Run numbers:	Comment:
Jan – July 2013		CVD system training and process development.
Aug 2013		CVD system fully commissioned by Tetreon.
Aug – Sept 2013	2 to 20	Initial CVD growth runs.
Oct 2013 – Feb 2014	20 to 47	Low growth time regime CVD runs. Study of acid pre-treatments, differing tube geometries, higher purity foils and growth pressures.
Mar 2014	48 to 51	Successful continuous CVD graphene growth runs.
April 2014	59, 60 and 62	First use of the toluene precursor for CVD growth of graphene.
April – May 2014	63, 64, 65, 69 and 72	Poor graphene coverage using same continuous growth run parameters as runs 48 to 51.
May 2014	76	Method suggested by Dr. Carl Magnuson.
May – June 2014	78, 81, 83 and 86	Increased the annealing and growth time to 30 minutes (runs 78 & 81) and 45 minutes (runs 83 & 86).
July 2014	99 and 100	Placed the copper foil between two quartz wafers in both CVD runs.
Aug 2014	108 and 109	Quartz tube was removed and replaced. Two growth runs were carried out using the same parameters as first four successful CVD runs (runs 48 to 51).
Aug 2014	112 and 113	Use of 2” and 1” quartz vapour trapping tubes for CVD growth of graphene.
Mar 2015	124 and 125	A gas purifier was installed in the methane gas line. Two growth runs were carried out using the same parameters as first four successful CVD runs (runs 48 to 51).

2.11 Conclusions

The first CVD runs were based on the procedure by Bae *et al.* and resulted in poor quality graphene as evident from the initial SEM images. The contaminants present on the samples after CVD growth have detrimental effects on the quality and performance of these graphene films and have suggested to result in poorer graphene growth quality. These contaminants can arise due to gas purity, insufficient copper pre-treatment and due to the fact that the system is not entirely leak tight.

Initial growth runs were undertaken and involved using a low methane deposition time (< 2 minutes) on copper foil (purity 99.8%). This method allows one to study the initial growth of graphene films on copper foil which allows optimisation of the growth parameters such as growth temperature and the pressure in the system during growth. The critical factors during initial growth runs are the graphene domain sizes and the nucleation density. It is most desirable to have large graphene domain sizes along with a low nucleation density as these lead to higher quality graphene growth at longer growth times. A lower nucleation density results in a lower density of charge scattering sites.

Throughout this chapter, a method suggested by Jia *et al.* which allows fast analysis of initial growth via optical microscopy was used [66]. This method involves oxidising the copper foil after growth which causes a colour contrast between the copper substrate and the graphene. To counteract the presence of contaminants on the copper foil and to improve growth quality (i.e. larger graphene domains), an acid clean was used on the copper foil (purity 99.8%) before inserting into the CVD system. Using this acid clean along with a sheet geometry resulted in mean domain area and perimeter values of ~ 6.4 μm^2 and ~ 11.2 µm.

It was found that copper evaporation plays a major role during growth and leads to a rougher copper surface [63]. Thus the copper foil was rolled up into the form of a tube and resulted in better graphene growth. The average area and perimeter domain sizes after utilising an acid pre-treatment with tube geometry were ~ 34.8 μm^2 and ~ 27.9 µm respectively. The pressure utilised during the growth step was also analysed using three different growth pressures of 57 mTorr, 140 mTorr and 450 mTorr on higher purity copper foils (99.999%). The highest growth pressure of ~ 450 mTorr using the CLP valve resulted in larger graphene domains in comparison to the

lower growth pressures. The mean domain area increased from ~ 17 μm^2 to ~ 69 μm^2 when the pressure was increased from 57 mTorr to 450 mTorr. The nucleation density decreased from ~ 22 to ~ 17 when increasing the growth pressure from 140 mTorr to 450 mTorr. This was most likely due to a higher residence time of methane in the process tube and the fact that a growth pressure as close as possible to the pressure utilised during APCVD, which is preferred.

Following from the improvement of growth quality by using an acid pre-treatment, tube geometry, higher purity copper foil and higher growth pressure, a continuous CVD run was undertaken with a methane deposition times of 15 minutes at 1,035 ^oC. SEM and optical analysis after growth suggested large area continuous growth of graphene on copper foil and a minute presence of copper. A further three continuous growth runs were obtained using the same parameters. However, problems with the reliability of the CVD system began to appear in subsequent runs.

Although the results in this chapter are not an advance over the start of the art in the literature, a few important issues were raised. In the literature, the discussion of the reliability of graphene growth via CVD is overlooked. It's often suggested that CVD graphene growth is a trivial process. From this chapter, it is clear that this is not the case. Regular system maintenance is required to maintain the growth quality of graphene obtained by a CVD system. The author proposes the use of small diameter quartz vacuum tube which would allow regular cleaning (to avoid contamination in the system) of the tube with ease along with the installation of a gas purifier for the methane gas line.

In conclusion, large area CVD graphene was successfully grown on copper foil. Growth quality was improved by investigating the effect of substrate pre-treatments, substrate geometry, substrate purity and growth pressure. However, graphene grown on copper foil limits its analysis and subsequent use as a transparent electrode. Commonly, a transfer process is used to transfer the film to target substrates followed by further analysis. In the next chapter, the transfer process of graphene from host substrate to target substrate is discussed and analysed.

2.12 Bibliography

1. Hirsch, A., *The era of carbon allotropes.* Nature Materials, 2010, **9**(11), p. 868-871
2. May, P.W., *CVD diamond: a new technology for the future?* Endeavour, 1995, **19**(3), p. 101-106
3. Wallace, P.R., *The Band Theory of Graphite.* Physical Review, 1947, **71**(9), p. 622-634
4. Novoselov, K.S., et al., *Electric field effect in atomically thin carbon films.* Science, 2004, **306**(5696), p. 666-669
5. Starke, U. and C. Riedl, *Epitaxial graphene on SiC(0001) and : From surface reconstructions to carbon electronics.* Journal of Physics Condensed Matter, 2009, **21**(13), 134016
6. Slonczewski, J.C. and P.R. Weiss, *Band Structure of Graphite.* Physical Review, 1958, **109**(2), p. 272-279
7. Chuvilin, A., et al., *Direct transformation of graphene to fullerene.* Nature Chemistry, 2010, **2**(6), p. 450-453
8. Falcao, E.H.L. and F. Wudl, *Carbon allotropes: beyond graphite and diamond.* Journal of Chemical Technology & Biotechnology, 2007, **82**(6), p. 524-531
9. Geim, A.K. and K.S. Novoselov, *The rise of graphene.* Nature Materials, 2007, **6**(3), p. 183-191
10. McClure, J.W., *Band Structure of Graphite and de Haas-van Alphen Effect.* Physical Review, 1957, **108**(3), p. 612-618
11. Milev, A.S., et al., *Unoccupied electronic structure of ball-milled graphite.* Physical Chemistry Chemical Physics, 2010, **12**(25), p. 6685-6691
12. Castro Neto, A.H., et al., *The electronic properties of graphene.* Reviews of Modern Physics, 2009, **81**(1), p. 109-162
13. Fathi, D., *A review of electronic band structure of graphene and carbon nanotubes using tight binding.* Journal of Nanotechnology, 2011, 471241
14. Chen, J.H., et al., *Intrinsic and extrinsic performance limits of graphene devices on SiO 2.* Nature Nanotechnology, 2008, **3**(4), p. 206-209
15. Lee, C., et al., *Measurement of the elastic properties and intrinsic strength of monolayer graphene.* Science, 2008, **321**(5887), p. 385-388
16. Balandin, A.A., et al., *Superior thermal conductivity of single-layer graphene.* Nano Letters, 2008, **8**(3), p. 902-907
17. Nair, R.R., et al., *Fine structure constant defines visual transparency of graphene.* Science, 2008, **320**(5881), p. 1308-1308
18. Liao, L., et al., *High-speed graphene transistors with a self-aligned nanowire gate.* Nature, 2010, **467**(7313), p. 305-308
19. Schwierz, F., *Graphene transistors.* Nature Nanotechnology, 2010, **5**(7), p. 487-496
20. Schedin, F., et al., *Detection of individual gas molecules adsorbed on graphene.* Nature Materials, 2007, **6**(9), p. 652-655
21. Shao, Y., et al., *Graphene based electrochemical sensors and biosensors: A review.* Electroanalysis, 2010, **22**(10), p. 1027-1036
22. Mueller, T., F. Xia, and P. Avouris, *Graphene photodetectors for high-speed optical communications.* Nature Photonics, 2010, **4**(5), p. 297-301
23. Xia, F., et al., *Ultrafast graphene photodetector.* Nature Nanotechnology, 2009, **4**(12), p. 839-843

24. Reddy, A.L.M., et al., *Synthesis of nitrogen-doped graphene films for lithium battery application.* ACS Nano, 2010, **4**(11), p. 6337-6342
25. Wassei, J.K. and R.B. Kaner, *Graphene, a promising transparent conductor.* Materials Today, 2010, **13**(3), p. 52-59
26. Hecht, D.S., L. Hu, and G. Irvin, *Emerging transparent electrodes based on thin films of carbon nanotubes, graphene, and metallic nanostructures.* Advanced Materials, 2011, **23**(13), p. 1482-1513
27. Li, X., et al., *Transfer of Large-Area Graphene Films for High-Performance Transparent Conductive Electrodes.* Nano Letters, 2009, **9**(12), p. 4359-4363
28. Cai, W., et al., *Large area few-layer graphene/graphite films as transparent thin conducting electrodes.* Applied Physics Letters, 2009, **95**(12), 123115
29. Wang, X., L. Zhi, and K. Müllen, *Transparent, conductive graphene electrodes for dye-sensitized solar cells.* Nano Letters, 2008, **8**(1), p. 323-327
30. Gomez De Arco, L., et al., *Continuous, highly flexible, and transparent graphene films by chemical vapor deposition for organic photovoltaics.* ACS Nano, 2010, **4**(5), p. 2865-2873
31. Miao, X., et al., *High Efficiency Graphene Solar Cells by Chemical Doping.* Nano Letters, 2012, **12**(6), p. 2745-2750
32. Reich, S., et al., *Tight-binding description of graphene.* Physical Review B - Condensed Matter and Materials Physics, 2002, **66**(3), p. 354121-354125
33. Novoselov, K.S., et al., *Two-dimensional gas of massless Dirac fermions in graphene.* Nature, 2005, **438**(7065), p. 197-200
34. Santander-Syro, A.F., et al., *Two-dimensional electron gas with universal subbands at the surface of SrTiO3.* Nature, 2011, **469**(7329), p. 189-193
35. Bolotin, K.I., et al., *Ultrahigh electron mobility in suspended graphene.* Solid State Communications, 2008, **146**(9–10), p. 351-355
36. Long, B., et al., *Non-covalent functionalization of graphene using self-assembly of alkane-amines.* Advanced Functional Materials, 2012, **22**(4), p. 717-725
37. Li, X.S., et al., *Graphene Films with Large Domain Size by a Two-Step Chemical Vapor Deposition Process.* Nano Letters, 2010, **10**(11), p. 4328-4334
38. Kuzmenko, A.B., et al., *Universal Optical Conductance of Graphite.* Physical Review Letters, 2008, **100**(11), p. 117401
39. Gusynin, V.P., S.G. Sharapov, and J.P. Carbotte, *Unusual Microwave Response of Dirac Quasiparticles in Graphene.* Physical Review Letters, 2006, **96**(25), 256802
40. Morales, J. and A. Flores-Riveros, *The generalization of the binomial theorem.* Journal of Mathematical Physics, 1989, **30**(2), p. 393-397
41. *Cambridge University Engineering Department - Materials Data Book*
42. Bae, S., et al., *Roll-to-roll production of 30-inch graphene films for transparent electrodes.* Nature Nanotechnology, 2010, **5**(8), p. 574-578
43. Kim, K.S., et al., *Large-scale pattern growth of graphene films for stretchable transparent electrodes.* Nature, 2009, **457**(7230), p. 706-710
44. Yi, M. and Z. Shen, *A review on mechanical exfoliation for the scalable production of graphene.* Journal of Materials Chemistry A, 2015, **3**(22), p. 11700-11715
45. Bourlinos, A.B., et al., *Liquid-Phase Exfoliation of Graphite Towards Solubilized Graphenes.* Small, 2009, **5**(16), p. 1841-1845

46. Lotya, M., et al., *Liquid phase production of graphene by exfoliation of graphite in surfactant/water solutions.* Journal of the American Chemical Society, 2009, **131**(10), p. 3611-3620
47. Paton, K.R., et al., *Scalable production of large quantities of defect-free few-layer graphene by shear exfoliation in liquids.* Nature Materials, 2014, **13**(6), p. 624-630
48. Ciesielski, A. and P. Samorì, *Graphene via sonication assisted liquid-phase exfoliation.* Chemical Society Reviews, 2014, **43**(1), p. 381-398
49. Hernandez, Y., et al., *High-yield production of graphene by liquid-phase exfoliation of graphite.* Nature Nanotechnology, 2008, **3**(9), p. 563-568
50. Nuvoli, D., et al., *High concentration few-layer graphene sheets obtained by liquid phase exfoliation of graphite in ionic liquid.* Journal of Materials Chemistry, 2011, **21**(10), p. 3428-3431
51. Zhou, X., et al., *Dispersion of graphene sheets in ionic liquid [bmim][PF6] stabilized by an ionic liquid polymer.* Chemical Communications, 2010, **46**(3), p. 386-388
52. Bracamonte, M.V., et al., *On the nature of defects in liquid-phase exfoliated graphene.* Journal of Physical Chemistry C, 2014, **118**(28), p. 15455-15459
53. Coleman, J.N., *Liquid exfoliation of defect-free graphene.* Accounts of Chemical Research, 2013, **46**(1), p. 14-22
54. Berger, C., et al., *Electronic confinement and coherence in patterned epitaxial graphene.* Science, 2006, **312**(5777), p. 1191-1196
55. Robinson, J.A., et al., *Correlating Raman Spectral Signatures with Carrier Mobility in Epitaxial Graphene: A Guide to Achieving High Mobility on the Wafer Scale.* Nano Letters, 2009, **9**(8), p. 2873-2876
56. Hass, J., W.A. De Heer, and E.H. Conrad, *The growth and morphology of epitaxial multilayer graphene.* Journal of Physics Condensed Matter, 2008, **20**(32), 323202
57. Sadowski, M.L., et al., *Magnetospectroscopy of epitaxial few-layer graphene.* Solid State Communications, 2007, **143**(1–2), p. 123-125
58. Walt, A.d.H., et al., *Epitaxial graphene electronic structure and transport.* Journal of Physics D: Applied Physics, 2010, **43**(37), 374007
59. Suemitsu, M. and H. Fukidome, *Epitaxial graphene on silicon substrates.* Journal of Physics D: Applied Physics, 2010, **43**(37), 374012
60. Bonaccorso, F., et al., *Production and processing of graphene and 2d crystals.* Materials Today, 2012, **15**(12), p. 564-589
61. Li, X.S., et al., *Large-Area Synthesis of High-Quality and Uniform Graphene Films on Copper Foils.* Science, 2009, **324**(5932), p. 1312-1314
62. Obraztsov, A.N., et al., *Chemical vapor deposition of thin graphite films of nanometer thickness.* Carbon, 2007, **45**(10), p. 2017-2021
63. Chen, S., et al., *Millimeter-Size Single-Crystal Graphene by Suppressing Evaporative Loss of Cu During Low Pressure Chemical Vapor Deposition.* Advanced Materials, 2013, **25**(14), p. 2062-2065
64. Vlassiouk, I., et al., *Large scale atmospheric pressure chemical vapor deposition of graphene.* Carbon, 2013, **54**, p. 58-67
65. Ryu, J., et al., *Fast Synthesis of High-Performance Graphene Films by Hydrogen-Free Rapid Thermal Chemical Vapor Deposition.* ACS Nano, 2014, **8**(1), p. 950-956
66. Jia, C., et al., *Direct Optical Characterization of Graphene Growth and Domains on Growth Substrates.* Scientific Reports, 2012, **2**, 707

67. Wei, W., et al., *Control of thickness uniformity and grain size in graphene films for transparent conductive electrodes.* Nanotechnology, 2012, **23**(3), 035603
68. Wood, J.D., et al., *Effects of Polycrystalline Cu Substrate on Graphene Growth by Chemical Vapor Deposition.* Nano Letters, 2011, **11**(11), p. 4547-4554
69. Huang, P.Y., et al., *Grains and grain boundaries in single-layer graphene atomic patchwork quilts.* Nature, 2011, **469**(7330), p. 389-392
70. Kim, K., et al., *Grain Boundary Mapping in Polycrystalline Graphene.* ACS Nano, 2011, **5**(3), p. 2142-2146
71. Yu, Q., et al., *Control and characterization of individual grains and grain boundaries in graphene grown by chemical vapour deposition.* Nat Mater, 2011, **10**(6), p. 443-449
72. Jauregui, L.A., et al., *Electronic properties of grains and grain boundaries in graphene grown by chemical vapor deposition.* Solid State Communications, 2011, **151**(16), p. 1100-1104
73. Yazyev, O.V. and Y.P. Chen, *Polycrystalline graphene and other two-dimensional materials.* Nat Nano, 2014, **9**(10), p. 755-767
74. Tapasztó, L., et al., *Mapping the electronic properties of individual graphene grain boundaries.* Applied Physics Letters, 2012, **100**(5), 053114
75. Koepke, J.C., et al., *Atomic-scale evidence for potential barriers and strong carrier scattering at graphene grain boundaries: A scanning tunneling microscopy study.* ACS Nano, 2013, **7**(1), p. 75-86
76. Clark, K.W., et al., *Spatially Resolved Mapping of Electrical Conductivity across Individual Domain (Grain) Boundaries in Graphene.* ACS Nano, 2013, **7**(9), p. 7956-7966
77. Reina, A., et al., *Large area, few-layer graphene films on arbitrary substrates by chemical vapor deposition.* Nano Letters, 2009, **9**(1), p. 30-35
78. Vlassiouk, I., et al., *Role of Hydrogen in Chemical Vapor Deposition Growth of Large Single-Crystal Graphene.* Acs Nano, 2011, **5**(7), p. 6069-6076
79. Muñoz, R. and C. Gómez-Aleixandre, *Review of CVD synthesis of graphene.* Chemical Vapor Deposition, 2013, **19**(10-12), p. 297-322
80. Mattevi, C., H. Kim, and M. Chhowalla, *A review of chemical vapour deposition of graphene on copper.* Journal of Materials Chemistry, 2011, **21**(10), p. 3324-3334
81. Kim, S.M., et al., *The effect of copper pre-cleaning on graphene synthesis.* Nanotechnology, 2013, **24**(36), 365602
82. Vlassiouk, I., et al., *Graphene Nucleation Density on Copper: Fundamental Role of Background Pressure.* Journal of Physical Chemistry C, 2013, **117**(37), p. 18919-18926
83. Kagwade, S.V., et al., *Photochemical breakdown of acetone on copper.* Electrochimica Acta, 2001, **46**(15), p. 2337-2342
84. Zhang, Y., et al., *Vapor trapping growth of single-crystalline graphene flowers: Synthesis, morphology, and electronic properties.* Nano Letters, 2012, **12**(6), p. 2810-2816
85. Li, X., et al., *Large-area graphene single crystals grown by low-pressure chemical vapor deposition of methane on copper.* Journal of the American Chemical Society, 2011, **133**(9), p. 2816-2819
86. Zhang, B., et al., *Low-Temperature Chemical Vapor Deposition Growth of Graphene from Toluene on Electropolished Copper Foils.* Acs Nano, 2012, **6**(3), p. 2471-2476

87. Xue, Y., et al., *Low temperature growth of highly nitrogen-doped single crystal graphene arrays by chemical vapor deposition.* Journal of the American Chemical Society, 2012, **134**(27), p. 11060-11063
88. Terasawa, T.O. and K. Saiki, *Growth of graphene on Cu by plasma enhanced chemical vapor deposition.* Carbon, 2012, **50**(3), p. 869-874
89. Li, J., et al., *Carbon nanowalls grown by microwave plasma enhanced chemical vapor deposition during the carbonization of polyacrylonitrile fibers.* Journal of Applied Physics, 2013, **113**(2), 024313
90. Boyd, D.A., et al., *Single-step deposition of high-mobility graphene at reduced temperatures.* Nature Communications, 2015, **6**, 6620
91. Chugh, S., et al., *Comparison of graphene growth on arbitrary non-catalytic substrates using low-temperature PECVD.* Carbon, 2015, **93**, p. 393-399
92. Blake, P., et al., *Making graphene visible.* Applied Physics Letters, 2007, **91**(6), 063124
93. Hildebrandt, F.S.a.P., *Vibrational Spectroscopy in Life Science.* 2008
94. *Theory of Raman scattering*. Available from: http://bwtek.com/raman-theory-of-raman-scattering/.
95. Tuinstra, F. and J.L. Koenig, *RAMAN SPECTRUM OF GRAPHITE.* Journal of Chemical Physics, 1970, **53**(3), p. 1126-1130
96. Ferrari, A.C., et al., *Raman spectrum of graphene and graphene layers.* Physical Review Letters, 2006, **97**(18), 187401
97. Malard, L.M., et al., *Raman spectroscopy in graphene.* Physics Reports, 2009, **473**(5-6), p. 51-87
98. Dresselhaus, M.S., A. Jorio, and R. Saito, *Characterizing graphene, graphite, and carbon nanotubes by Raman spectroscopy.* Annual Review of Condensed Matter Physics, 2010, **1**, p. 89-108
99. Ferrari, A.C. and D.M. Basko, *Raman spectroscopy as a versatile tool for studying the properties of graphene.* Nat Nano, 2013, **8**(4), p. 235-246
100. Cançado, L.G., et al., *Quantifying Defects in Graphene via Raman Spectroscopy at Different Excitation Energies.* Nano Letters, 2011, **11**(8), p. 3190-3196
101. Ferrari, A.C. and J. Robertson, *Resonant Raman spectroscopy of disordered, amorphous, and diamondlike carbon.* Physical Review B, 2001, **64**(7), 075414
102. Ferrari, A.C. and J. Robertson, *Interpretation of Raman spectra of disordered and amorphous carbon.* Physical Review B, 2000, **61**(20), p. 14095-14107
103. Klar, P., et al., *Raman scattering efficiency of graphene.* Physical Review B - Condensed Matter and Materials Physics, 2013, **87**(20), 205435
104. Dresselhaus, M.S., et al., *Defect characterization in graphene and carbon nanotubes using Raman spectroscopy.* Philosophical Transactions of the Royal Society A: Mathematical, Physical and Engineering Sciences, 2010, **368**(1932), p. 5355-5377
105. Postek, M.T., *Scanning Electron Microscopy: A Student's Handbook*. 1980: Ladd Research Industries, Incorporated.
106. Reimer, L., *Introduction, in Scanning Electron Microscopy: Physics of Image Formation and Microanalysis*. 1998: Springer Berlin Heidelberg: Berlin, Heidelberg.
107. Meng, L., et al., *Hierarchy of graphene wrinkles induced by thermal strain engineering.* Applied Physics Letters, 2013, **103**(25), 251610

108. Ahmad, M., et al., *Nanoscale investigation of charge transport at the grain boundaries and wrinkles in graphene film.* Nanotechnology, 2012, **23**(28), 285705
109. Chae, S.J., et al., *Synthesis of large-area graphene layers on poly-nickel substrate by chemical vapor deposition: Wrinkle formation.* Advanced Materials, 2009, **21**(22), p. 2328-2333
110. Rasool, H.I., et al., *Continuity of graphene on polycrystalline copper.* Nano Letters, 2011, **11**(1), p. 251-256
111. Yin, X., et al., *Evolution of the Raman spectrum of graphene grown on copper upon oxidation of the substrate.* Nano Research, 2014, **7**(11), p. 1613-1622
112. Tognana, S., W. Salgueiro, and M.B. Valcarce, *A micro-Raman study of Cu-particulate-filled epoxy matrix composites.* Express Polymer Letters, 2014, **8**(5), p. 312-321
113. Liu, J., et al., *Large-area synthesis of high-quality and uniform monolayer graphene without unexpected bilayer regions.* Journal of Alloys and Compounds, 2014, **615**, p. 415-418
114. Li, X., et al., *Evolution of graphene growth on Ni and Cu by carbon isotope labeling.* Nano Letters, 2009, **9**(12), p. 4268-4272
115. Banszerus, L., et al., *Ultrahigh-mobility graphene devices from chemical vapor deposition on reusable copper.* Science Advances, 2015, **1**(6)

3 Wet chemical transfer of CVD graphene to silicon dioxide and glass substrates

3.1 Introduction and motivation

Graphene grown on copper foil limits the analysis and the use of the graphene films. A transfer process is required to transfer the graphene film to target substrates. The main transfer process reported in literature is that of a wet chemical transfer and is utilised herein. However this wet transfer process introduces chemical residues and contaminants which can alter graphene's properties. A non-optimised transfer process can make the growth improvement redundant. A polymer e.g. polymethyl methacrylate (PMMA) support layer is critical for this transfer process. PMMA forms a strong Van der Waals interaction with graphene [1], which makes it difficult to remove all of the polymer and results in the presence of residual layers. These residual polymer layers can have detrimental effects on the sheet resistance as it may increase the density of carrier scattering sites [2]. In literature, various reports have been published in relation to removal of residual polymer. Annealing at elevated temperatures has been suggested to remove residual layers [3]. However annealing does not totally remove the polymer and high annealing can also perturb the sp^2 hybridisation of carbon atoms in graphene [4]. Therefore an alternative method of residual polymer layer removal is reported in this work. Non-destructive techniques have also been studied in the literature in relation to CVD graphene transfer. These include electrochemical delamination and dry transfer processes. A brief synopsis of these techniques is included.

3.2 CVD graphene transfer methods

3.2.1 Wet chemical transfer process

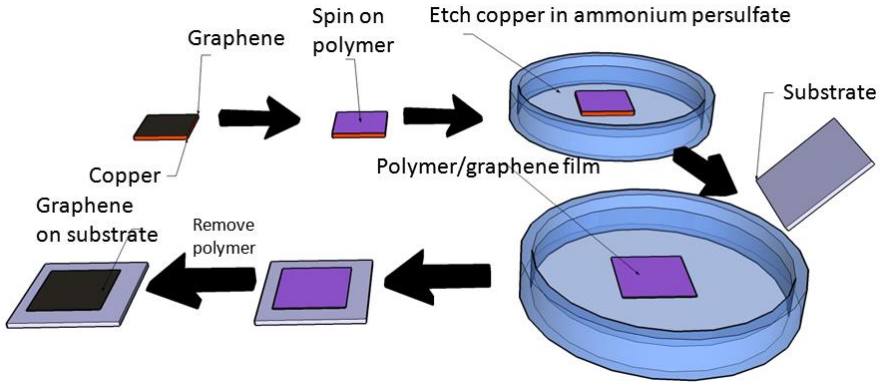

Figure 3.1: Basic principle behind the wet chemical transfer of CVD grown graphene to arbitrary substrates.

The most commonly utilised transfer of graphene to arbitrary substrates in literature publications involves wet chemical processes [5-9]. A basic schematic of this process is depicted in Figure 3.1. A polymer-based material, usually polymethyl methacrylate (PMMA) is used as a mechanical support for the graphene film during the transfer. Once graphene is grown by CVD on copper foil, PMMA is drop-cast onto the foil, spun at a certain RPM (revolutions per minute) and baked. Groups have mainly used either chlorobenzene [5] or anisole [1] as the PMMA solvent for graphene transfer. Anisole is less toxic than chlorobenzene, however it has a lower viscosity with regard to drop-casting and spinning.

Graphene grows on each side of the copper foil during CVD growth. Thus it is essential to remove the back-side graphene before chemical etching of copper takes place. If the back-side graphene is left on the copper foil, it can damage the PMMA layer after chemically etching the copper foil. An oxygen plasma can be used to etch the back-side graphene as the bombardment of the substrate with ions is sufficient in removing the atom thick layer [1]. Removal of the back-side graphene layer can be confirmed via Raman spectroscopy. Chemical processes have also been reported as methods to remove the backside graphene, particularly a nitric acid etch [10].

The copper itself is then chemically etched in an ammonium persulfate or iron nitrate solution [9] diluted in deionised water and the graphene/PMMA film is

transferred to a substrate of choice. The PMMA layer is subsequently removed by placing the sample in acetone. Since graphene is one atom thick it is susceptible to surface contamination. This wet chemical transfer process therefore, can increase the sheet resistance of graphene films due to polymer and chemical residues as mentioned previously [11]. Methods to counteract chemical residues include annealing in different gaseous environments (e.g. H_2 [12] and Ar/H_2 [4]) to remove some residual polymer layers. Li *et al.* produced one of the first working CVD graphene device transferred to SiO_2 with carrier mobilities of ~ 4050 $cm^2V^{-1}s^{-1}$ and with 95% monolayer coverage [6].

3.2.2 Dry transfer process

Dry transfer techniques have been reported which allow the transfer of graphene to target substrates without the use of chemical based processes. Graphene was transferred to a polystyrene substrate that was treated with an azide-based molecule to promote adhesion [13]. The two films were bought together using a nano imprinter and then separated which resulted in graphene transfer to the polystyrene substrate. Mobility values of ~ 1140 cm^2/Vs were achieved by this method. The dry transfer method has also been demonstrated by placing graphene-Cu foil onto a polymer using a hot press machine followed by subsequent peeling of the copper foil from the polymer-graphene stack [14].

3.2.3 Electrochemical delamination

The wet chemical etching of the copper foil usually requires immersion overnight and results in copper and etchant residues. A method to delaminate the PMMA-graphene stack from the copper foil has been reported [15]. This delamination involves using a PMMA-graphene-Cu cathode and a glassy carbon anode. A direct current voltage is applied while the electrodes are immersed in a 0.05 M solution of $K_2S_2O_8$ in water. Delamination occurs due to the presence of hydrogen bubbles which emerge at the graphene-Cu interface due to the electrolysis of water. This delamination technique also potentially allows re-use of the copper foil catalyst material for growth which reduce costs.

However it has been suggested that the previous electrochemical delamination procedure introduces cracks on the graphene film due to the hydrogen bubbles [16]. The strong interaction between the graphene and copper foil can be minimised by

introducing a thin layer of copper oxide at the interface of the graphene and Cu foil [17]. The thin oxide layer is created by the permeation of air at the graphene domain boundaries. The oxide layer can be created at room temperature with moderate humidity (~ 50%). Statistical analysis has shown the "bubble-free" method of delamination results in lower sheet resistance values, lower defect density and lower exposed substrate area [16]. The "bubble-free" method produced a sheet resistance value of ~ 773 ± 241 Ω/sq while the bubble delamination produced higher values of ~ 2607 ± 1652 Ω/sq.

A newer method of using deionised water for delamination has also been reported and can reduce chemical contamination of the graphene film [18]. DI water has the ability to penetrate the interface between the graphene and copper and allows the separation of the two layers. This separation is achieved by immersing the PMMA-graphene-Cu foil stack in deionised water at 90 ^{o}C for 2 hours.

3.2.4 Thermal release tape and roll-to-roll transfer process

Another method that allows the realisation of large scale graphene transfer is by using a thermal release tape in conjunction with a roll-to-roll process. Bae *et al.*, first demonstrated the use of a roll-to-roll process for the transfer of CVD graphene. Firstly, graphene was grown on Cu foil via chemical vapour depositon. The thermal release tape was then applied to the Cu-graphene stack by two rollers. The Cu foil was then etched by 0.1 M ammonium persulfate. The graphene was then transferred to a (~ 188 μm thick) polyethylene terephthalate (PET) substrate through the use of the two rollers. The thermal release tape was then removed via heating (~ 90 ^{o}C to 120 ^{o}C). Graphene films on PET of size 400 mm x 300 mm with sheet resistance values of ~ 249 ± 17 Ω/sq (without intentional doping) have also been transferred using this roll-to-roll process with a thermal release tape [19]. However, mechanical defects can arise when removing the thermal release tape itself. The roll-to-roll process can also induce mechanical defects when using rigid substrates. Kang *et al.* utilised a "hot pressing" method to transfer CVD graphene on Si/SiO_2 which formed less defects in comparison to using the standard roll-to-roll transfer process to rigid substrates [20].

3.3 Materials and methods

3.3.1 Tyndall CVD graphene transfer protocol

All graphene transfer steps pertaining to wet chemical usage were carried out in a fumehood in a laboratory with the appropriate safety mechanisms. Training was completed on all equipment used in this chapter. The risks associated with the transfer of graphene to rigid substrates were assessed and documented as NTG_CRA_35 – graphene transfer protocol. A 4" graphene on copper foil (thickness of 18 μm) sample was purchased from Graphenea Inc. Prior to processing, the foil was cut with a scissors to sample sizes of 16 mm x 16 mm. The sample was placed on a spin coater and PMMA 950K, 7% PMMA in anisole (MicroChem) was applied at 4,000 RPM for 50 s. The samples were then placed in an oven at 180 ^{o}C for 5 minutes. To remove the back-side graphene, the samples were placed PMMA side down in an Oxford Reactive Ion Etcher (RIE) system. Glass slides with paraffin oil were placed near the edges of the sample, to prevent them falling into the chamber during processing (Figure 3.2). The samples were transferred to the chamber and it was evacuated to ~ 10^{-6} Torr. An oxygen plasma for 90 s at 100 W with an O_2 flow of 50 standard cubic centimeters per minute (SCCM) was used to remove the atom thick layer. The samples were then cut to desired size of 8 mm x 8 mm and were left overnight (PMMA side facing upwards) in a 0.1 M solution of ammonium persulfate in DI water to wet etch the copper. The PMMA-graphene films were transferred to DI water for 3 hours. These films were then transferred to Si/SiO_2 (90 nm thermal oxide) or glass substrates and left to dry overnight in a vacuum desiccator. Prior to PMMA removal, the samples were placed on a hotplate at 180 ^{o}C for 5 minutes to promote adhesion between the graphene and substrate. PMMA was removed by immersing the samples in acetone at room temperature for an hour followed by an IPA and DI water rinse. The samples were then left in a vacuum desiccator overnight to dry. Subsequent optical, AFM and Raman analysis was undertaken. Optical microscopy images were taken at north, south, east, west and center regions of the samples.The use of the RIE along with the hard baking in a convection oven proved essential to improve the transfer process.

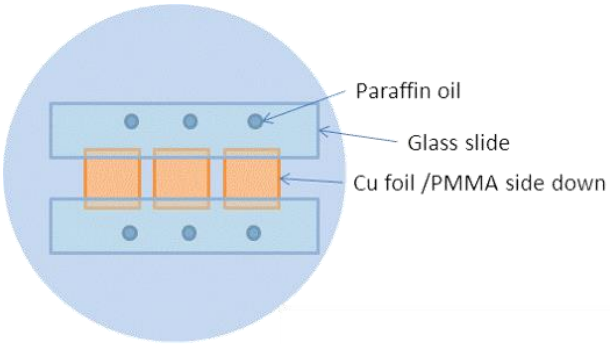

Figure 3.2: Schematic of procedure used in the reactive ion etcher (RIE) system to remove the back-side graphene. Paraffin oil is used to hold the glass slides in place (i.e. hold the Cu samples in place) during processing.

3.3.2 Tyndall transfer protocol with heated acetone

The effect of heating the acetone on the removal of residual PMMA layers on eight samples was studied. These samples were placed individually in acetone at 60 ^{o}C for ten minutes followed by subsequent analysis (optical, Raman and AFM). Due to the low throughput of the atomic force microscopy (AFM), only four samples out of the set were analysed. This heated acetone protocol method was repeated once more along with the analysis. Since there's a different contrast between graphene and SiO_2 substrate, ImageJ was used to map the area covered by graphene. This analysis was undertaken on 10x magnification optical images for all three data sets (post-transfer, post-first acetone clean and post-second acetone clean). ImageJ was also used to study particulates seen on the AFM images post-transfer and after the two cleans.

3.4 Characterisation

Optical. Optical microscopy images were taken using a Zeiss optical microscope in reflection mode. The transparency values of the graphene film on glass were found by using a Perkin Elmer 950 Spectrophotometer. A blank measurement was taken before starting the measurement set. The graphene film on glass substrate was referenced against air and the glass substrate itself. The transparency values were taken at a wavelength of 550 nm.

Raman spectroscopy was undertaken with a laser power of 1.1 mW and an exposure time of 10 s. The characteristic wavenumber values of the peaks for pristine graphene are *D* (~ 1350 cm^{-1}), *G* (~ 1580 cm^{-1}) and *2D* (~ 2700 cm^{-1}). Monolayer

graphene is confirmed by these peaks. A sharp *2D* peak with a FWHM < 30 cm^{-1} along with a ratio of I_{2D}/I_G > 1 is indicative of a graphene monolayer [21]. It is also an advantage of producing graphene with a minute I_D/I_G ratio (i.e. small *D* peak intensity). Note that the Raman spectrum of bilayer or multilayer graphene differs slightly from that of a monolayer as seen in Figure 3.3. For monolayer graphene, the *2D* peak can be fitted with one Lorentzian [22], while for bilayer graphene four Lorentzians are needed to fit the peak [23]. The *D* peak at ~ 1350 cm^{-1} is the main peak for characterizing graphene's defects but other defect peaks also occur at are usually denoted by *D'*(~ 1630 cm^{-1}), *D* + *D''* (~ 2450 cm^{-1}), *D* + *D'* (~ 2940 cm^{-1}) and *2D'* (~ 3260 cm^{-1}) as seen in Figure 3.4.

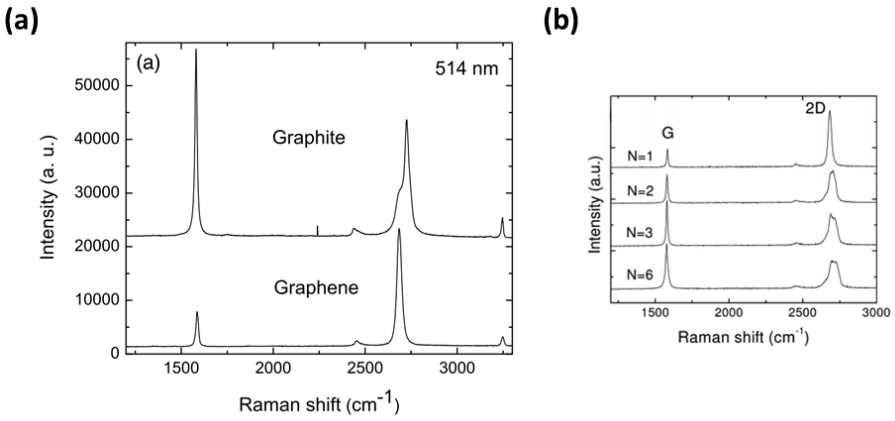

Figure 3.3: (a) Raman spectrum of monolayer graphene and bulk graphite using a 514 nm wavelength laser [21] & (b) Raman spectra of varying layer thicknesses of graphene denoted by N: N =1 (monolayer), N = 2 (bilayer) etc. [24].

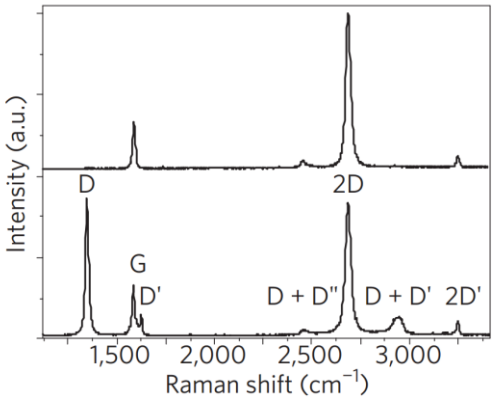

Figure 3.4: (a) Raman spectrum of pristine graphene compared to a Raman spectrum of defected graphene showing the *D*, *D'*, *D* + *D''*, *D* + *D'* and the *2D'* peaks [22].

AFM. Atomic force microscopy (AFM) was utilised to study the surface topography of monolayer graphene films transferred to arbitrary substrates as described in section 2.9.3.1.

Field-effect devices. In order to assess the carrier mobilities of graphene, back-gated, field effect devices were fabricated on Si/SiO_2 (90 nm thermal oxide) using optical lithography, metal evaporation (Ti 5-10 nm adhesion layer, Au 100-200 nm) and lift-off. This process was undertaken by my colleague Roxane Puicervert.

3.5 Results and discussion

3.5.1 Initial transfer of commercially grown graphene

Process optimisation was undertaken to improve the area of graphene transferred (Figure 3.5). Significant changes included increasing the spin speed to 4,000 RPM to reduce the PMMA thickness, increasing the PMMA bake temperature to 180 ^{o}C to ensure proper adhesion to the Cu-graphene stack, the removal of the backside graphene by using an O_2 plasma in a reactive ion etcher (100 W, 90 s) [25, 26], the use of a vacuum desiccator to dry the film overnight [9] and the baking of the PMMA-graphene stack on Si/SiO_2 (90 nm thermal oxide) at 180 ^{o}C for 5 minutes before PMMA removal. This allows the reflow of PMMA and helps to flatten the stack (PMMA-graphene) to ensure less cracks and defects are prevalent after PMMA removal [9]. A schematic of the improved transfer protocol (compared to original protocol) is shown below in Figure 3.6.

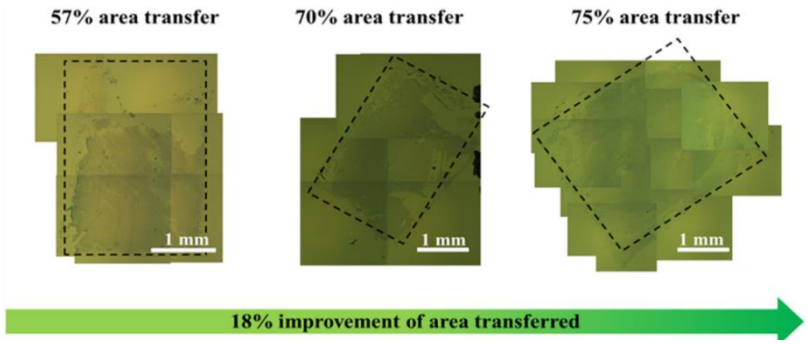

Figure 3.5: Optical images of transferred graphene progress in area transfer using initial transfer protocol, followed by the changes indicated above in the text.

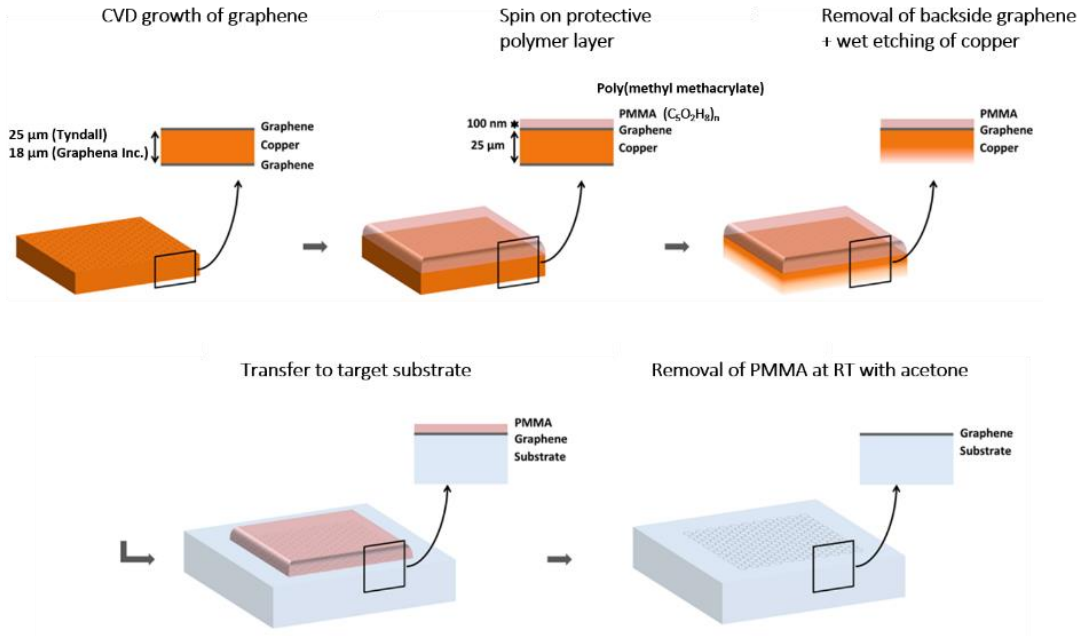

Figure 3.6: Schematic showing the procedure for an improved graphene transfer protocol (compared to initial protocol) to arbitrary substrates.

3.5.2 Transfer & characterisation of commercial CVD graphene using transfer protocol and heated acetone

Sixteen CVD graphene films were transferred to Si/SiO_2 (90 nm thermal oxide) using the transfer protocol in section 3.3.1. After the transfer process, optical inspection was undertaken. Only half of the devices displayed adequate graphene coverage for further analysis. A heated acetone clean protocol described in section 3.3.2 was used to study the removal of residual PMMA layers on these eight devices. Few literature reports exist for PMMA removal with heated acetone [27-29]. However, the PMMA removal

step with heated acetone was only used to remove the initial PMMA layer and not PMMA residue in the aforementioned publications. To this author's knowledge, no such reports exist for the removal of residual PMMA with heated acetone and the effect it has on graphene coverage, roughness and Raman data.

Optical images of the first method set (post-transfer) suggest areas of continuous graphene growth. However areas with low graphene coverage were present on some devices which may be due to the growth process applied by the manufacturer. From the subsequent first heated acetone clean, all devices have a decrease in graphene area (Figure 3.7(a)). In some cases, it appears that the graphene area is slightly increasing but this is probably due to the difficulty of finding the exact same area on the optical microscope without the use of metal alignment marks. The second heated acetone clean results in further reduction of graphene area (the exception is sample A3). A histogram of the mean ratio of the two areas was created using ImageJ (Figure 3.7 (a)). It has been documented that acetone is insufficient in completely removing residual PMMA residues due to their strong Van der Waals interaction with graphene [1, 30, 31]. However, the Van der Waals interaction between the transferred graphene and substrate is weak. Also cracks and chemical residue from the transfer process reduce the adhesion of the graphene to the substrate even more [32]. Due to this weak adhesion, water molecules can easily permeate into this interface [2, 33]. Therefore, the heated acetone may have to ability to permeate into the interface between the graphene and Si/SiO_2 substrate and may be causing the partial removal of graphene. Also the clean is more aggressive than room temperature PMMA removal as the temperature of the acetone (~ 60 ^{o}C) is above the boiling point stated by the manufacturer of ~ 56 ^{o}C [34]. A summary of the data in Figure 3.7 is given below in Table 3.1. See Figure 3.7 (b), (c) and (d) for a visual example of the decrease in graphene coverage for device A16 after each clean.

Table 3.1: The effect of using two subsequent heated acetone cleans to remove residual PMMA in relation to graphene coverage for each device on Si/SiO_2 (90 nm thermal oxide). All devices were fabricated using the same preparation protocol i.e. section 3.3.1 and section 3.3.2.

Device ID:	Mean ratio of graphene coverage to total area Post-transfer:	Mean ratio of graphene coverage to total area 1st heated acetone clean:	Mean ratio of graphene coverage to total area 2nd heated acetone clean:
A3	0.82 ± 0.15	0.84 ± 0.14	0.83 ± 0.06
A6	0.75 ± 0.19	0.77 ± 0.09	0.71 ± 0.07
A8	0.85 ± 0.11	0.77 ± 0.11	0.70 ± 0.13
A10	0.92 ± 0.06	0.93 ± 0.04	0.71 ± 0.28
A12	0.90 ± 0.04	0.69 ± 0.11	0.63 ± 0.12
A13	0.75 ± 0.04	0.53 ± 0.05	0.45 ± 0.05
A14	0.96 ± 0.01	0.87 ± 0.08	0.81 ± 0.06
A16	0.93 ± 0.10	0.81 ± 0.10	0.74 ± 0.14

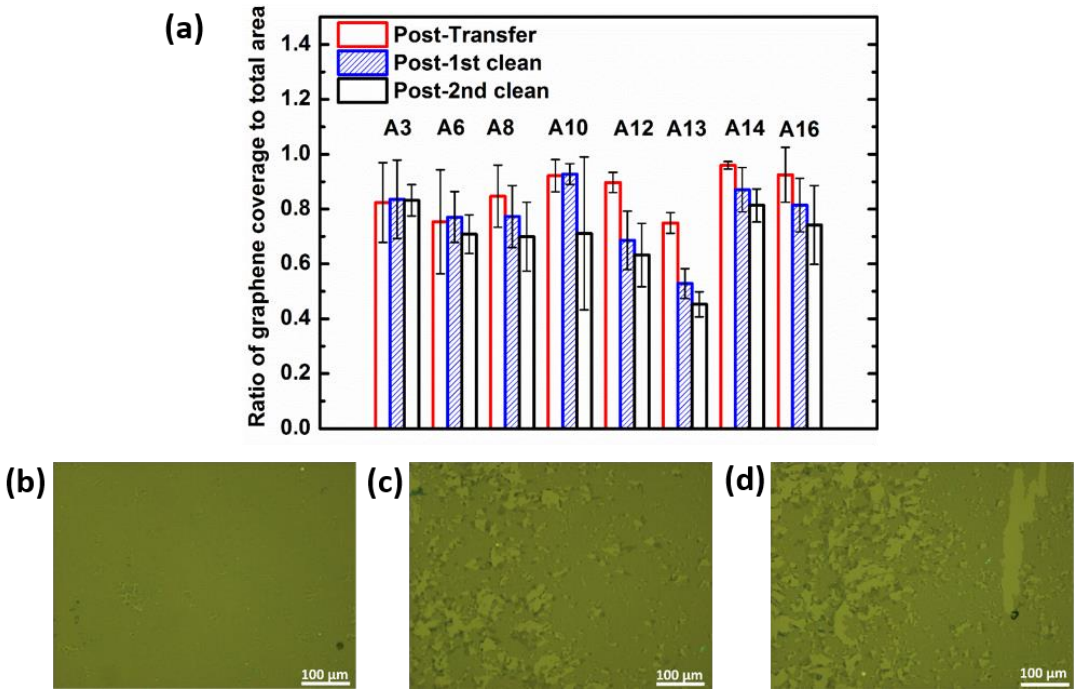

Figure 3.7: (a) Histogram of the mean ratio of graphene coverage to total area based on 10x magnification optical images over 8 samples found using ImageJ analysis software. 10x magnification optical image of the west region on sample A16 (b) post-transfer, (c) first post-heated acetone clean and (d) second post-heated acetone clean showing the reduction in graphene area (more tears present). Scale bars are 100 µm.

The effect of each clean was also investigated at the sub-micron scale. AFM analysis was undertaken on four devices; A3, A6, A14 and A16. A scan size of 5 µm x 5 µm was used and roughness measurements were taken using a 1 µm x 1 µm box size making a conscious effort to not include wrinkles or other defects that may have skewed the data. The Si/SiO_2 (90 nm thermal oxide) substrates did not have metal alignment marks, which made it difficult to find the exact same position each time on a particular device. But four regions (north, south, east and west) with multiple scans were analysed for each device to remove this uncertainty. The root mean square roughness (R_q) averaged of all devices was found to be ~ 1.3 ± 0.3 nm, which agrees favourably with values of ~ 0.9 nm [8] and ~ 1.24 nm [26] reported in the literature over the same sized area (1 µm x 1 µm). For example, the roughness of an exfoliated graphene flake of R_q ~ 0.54 nm (over a 1 µm x 1 µm area) [12] is much less than that of the post-transfer CVD graphene devices herein (R_q ~ 1.3 ± 0.3 nm). Although exfoliated samples suffer from tape residue, PMMA residue from CVD transfer is more undesirable as tape residue can easily be removed by thermal annealing [35]. The average roughness (R_a) based on all devices herein was found to be ~ 0.8 ± 0.2 nm. Following the first heated acetone clean, the R_q and R_a values (averaged over all devices) reduced to ~ 0.5 ± 0.2 nm and ~ 0.3 ± 0.1 nm respectively. The R_q and R_a values (averaged over all devices) after the second heated acetone clean were unchanged from the previous clean at ~ 0.5 ± 0.2 nm and ~ 0.3 ± 0.1 nm respectively. An example of three AFM scans of device A16 west region after each method can be seen in (Figure 3.8).

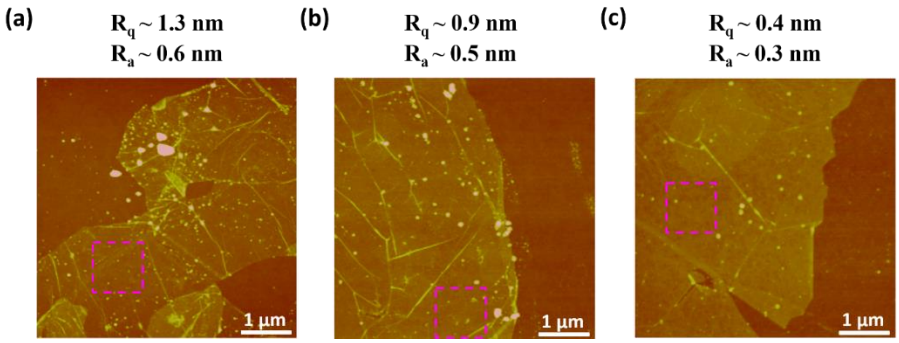

Figure 3.8: 5 µm x 5 µm AFM scan of sample A16 west region for (a) post-transfer, (b) first heated acetone clean and (c) second heated acetone clean. In each case various 1 µm x 1 µm roughness measurements were taken on each image (pink outlined square). For all devices, north,

From this data, an overlapping histogram was created to see the difference in roughness values between the three sample states (post-transfer, first heated acetone clean and second heated acetone clean) for all four devices (Figure 3.9). Though the mean values for both R_q and R_a remained unchanged from the first to second clean, the number of measurements with lower roughness values was larger after the second clean. A wider distribution of R_q values were present for post-transfer devices, i.e. R_q values in the range of ~ 0.6 nm to ~ 2.2 nm were observed (Figure 3.9 (a)). After the first heated acetone clean, the R_q distribution becomes narrower with values between ~ 0.2 nm to ~ 1.1 nm. After the second clean, the distribution is slightly narrower (R_q in the range of ~ 0.2 nm to ~ 0.9 nm) but a distinct shoulder is still present. Similar behaviour is observed for R_a (mean roughness) values (Figure 3.9 (b)). Initially a wider distribution of values is observed (R_a in the range of ~ 0.4 nm to ~ 1.4 nm) and the distribution becomes narrower after the first clean (R_a in the range of ~ 0.2 nm to ~ 0.6 nm) and subsequent second clean (R_a in the range of ~ 0.2 nm to ~ 0.5 nm). The R_q value (averaged over all devices) of ~ 0.5 ± 0.2 nm compares favourably with the R_q value of ~ 0.3 nm achieved by annealing CVD graphene on Si/SiO_2 (300 nm thermal oxide) for 90 minutes at 500 ^oC in an H_2/Ar atmosphere [36]. However, their graphene coverage is still intact after annealing compared to this heated acetone clean. The reduction in roughness suggests that the heated acetone is aiding to reduce the amount of residual PMMA but this clean is causing the graphene coverage to decrease on large scale, as evident from prior optical analysis. One method to counteract this

effect would be vacuum annealing to degas water vapour from the graphene substrate interface to create better adhesion. However over time under ambient conditions, water vapour is expected to permeate this surface leading to a decrease in adhesion [37].

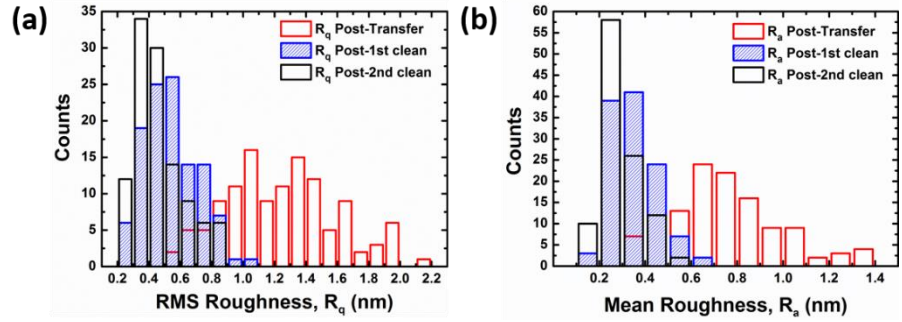

Figure 3.9: Overlapping histograms of (a) root mean square roughness, R_q values over the three sample states (post-transfer, first heated acetone and second heated acetone clean) and (b) Mean roughness, R_a values of the three sample sets. In both cases, the R_q and R_a values are decreasing after every clean and the distribution becomes narrower.

Nanoscale islands (referred to herein as "particles") present on the AFM images were also analysed using ImageJ software. A zoomed in region of 2.5 µm x 2.5 µm was used and the pixel count of each image was identical at 372 x 372 pixels. A binary image was created and to ensure wrinkles on the images were not being counted, a circularity value of 0.5 to 1 was chosen, where the value of 1 is a perfect circle (bottom images of Figure 3.10). A reduction in mean particle counts per AFM scan (two scans per region, four regions in total i.e. north, south, east and west) was measured from the post-transfer samples to those with the second heated acetone clean. In particular a drastic reduction can be seen after the first heated acetone clean in the histogram (Figure 3.11). This also correlates with the roughness data, which changes drastically from the after the first clean but not much change is seen from the second. A summary of the mean number of particles per AFM scan (two scans per region, four regions in total i.e. north, south, east and west) for post-transfer devices and post-heated acetone cleans is given in Table 3.2. Although there are less particles present on the AFM scans after the two heated acetone cleans, it was evident in some cases that the maximum particle size was increasing. The maximum particle area was found by using ImageJ. For instance, the maximum particle area increased from 0.013

μm^2 to 0.022 μm^2 for device A3 after two heated acetone cleans (see Table 3.3). The increase in maximum particle area is possibly due to surface diffusion and aggregation of PMMA in addition to desorption.

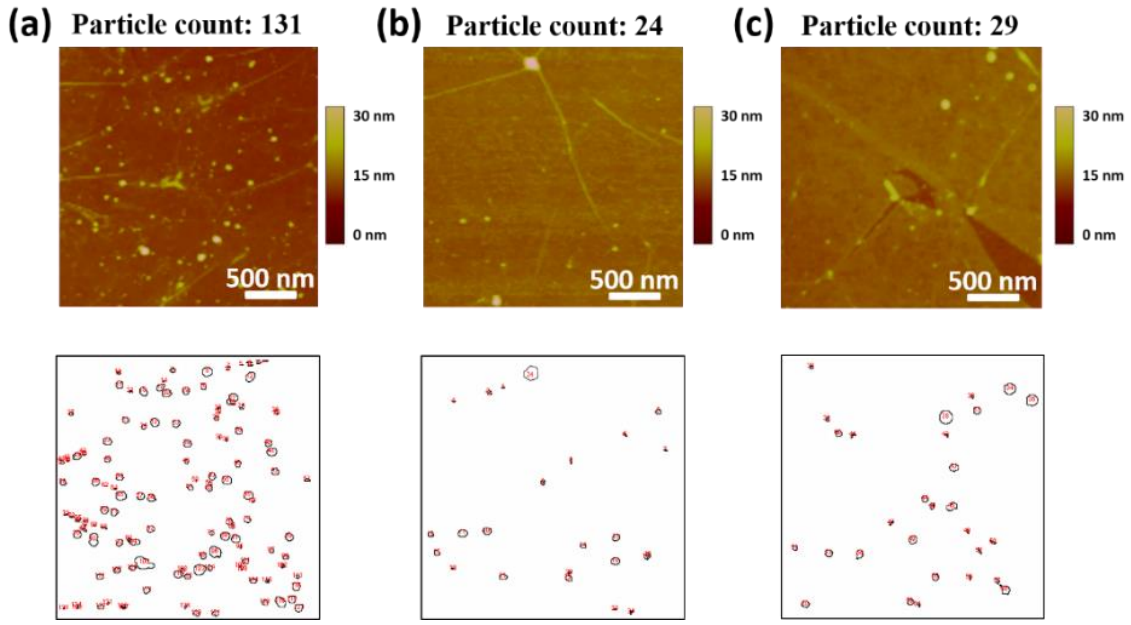

Figure 3.10: 2.5 µm x 2.5 µm AFM scans of A16 taken at one west region of (a) post-transfer, (b) first heated acetone clean and (c) second heated acetone clean. The corresponding ImageJ binary images are below each AFM scan image. To ensure wrinkles and tears were not counted, a value of 0.5 to 1 was used for the circularity.

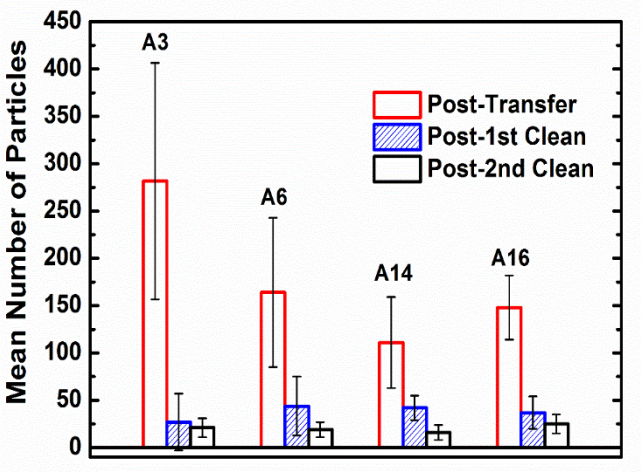

Figure 3.11: Histogram showing the mean number of particulates per AFM scan (two scans per region, four regions in total i.e. north, south, east and west) for four devices A3, A6, A14 and A16 in relation to the three sample sets (post-transfer, first heated acetone clean and second heated acetone clean). A reduction in the mean particle count per region is seen from the post-transfer samples to the second heated acetone clean. However, the largest reduction is seen after the first clean and suggests it would be beneficial to only do one heated acetone clean (this correlates with optical microscopy and roughness data).

Table 3.2: The effect of using two subsequent heated acetone cleans to remove residual PMMA in relation to mean particle counts per AFM scan (two scans per region, four regions in total i.e. north, south, east and west) on CVD graphene devices on Si/SiO_2 (90 nm thermal oxide).

Device ID:	Mean particle count (Post-transfer):	Mean particle count (1^{st} heated acetone clean):	Mean particle count (2^{nd} heated acetone clean):
A3	282	27	21
A6	164	44	19
A14	111	42	16
A16	148	37	25

Table 3.3: The maximum particle area (μm^2) per device measured using ImageJ data from AFM images of CVD graphene devices on Si/SiO_2 (90 nm thermal oxide).

Device ID:	Maximum particle area (μm^2) Post-transfer:	Maximum particle area (μm^2) 1st heated acetone clean:	Maximum particle area (μm^2) 2nd heated acetone clean:
A3	0.013	0.015	0.022
A6	0.024	0.034	0.018
A14	0.012	0.022	0.039
A16	0.020	0.014	0.025

From the optical microscopy analysis and AFM analysis (roughness and mean particle count), it appears that it would be beneficial to stop the cleaning after one heated acetone clean. A large reduction in graphene coverage is evident for some devices after the second heated acetone clean (see Figure 3.7 and Table 3.1), which may be detrimental for the sheet resistance of these devices. A large reduction in R_q and R_a values are seen after the first heated acetone clean (Figure 3.9), with a minute reduction after the subsequent second clean. This is also evident for mean particle count (see Figure 3.11 and Table 3.2).

Raman analysis was undertaken on all eight devices. Twenty spectra were taken for each sample for each data set. Five regions were analysed (north, south, east, west and center) with four spectra per region (160 spectra in total for each data set). An example of Raman spectra for device A16 after each clean is depicted in Figure 3.12. *G* peak positions of ~ 1590 cm^{-1} (post-transfer), ~ 1586 cm^{-1} (post-first clean) and ~ 1591 cm^{-1} (post-second clean) were measured along with *2D* peak positions of ~ 2689 cm^{-1} (post-transfer), 2692 cm^{-1} (post-first clean) and 2691 cm^{-1} (post-second clean). Two defect peaks were present in the three spectra. *D* peak positions of ~ 1347 cm^{-1} (post-transfer), 1351 cm^{-1} (post-first clean) and ~ 1348 cm^{-1} (post-second clean) were noted along with *D + D''* peak positions of ~ 2460 cm^{-1} (post-transfer), ~ 2461 cm^{-1} (post-first clean) and ~ 2461 cm^{-1} (post-second clean) were achieved. Another

important factor for Raman analysis of graphene is the ratio of I_{2D}/I_G. A ratio value > 1 indicates monolayer graphene. I_{2D}/I_G ratios were > 1.4 for all three spectra. The I_D/I_G value which is the ratio of the intensity of the *D* peak to the intensity of the *G* peak were all < 0.12 which suggests low defect graphene.

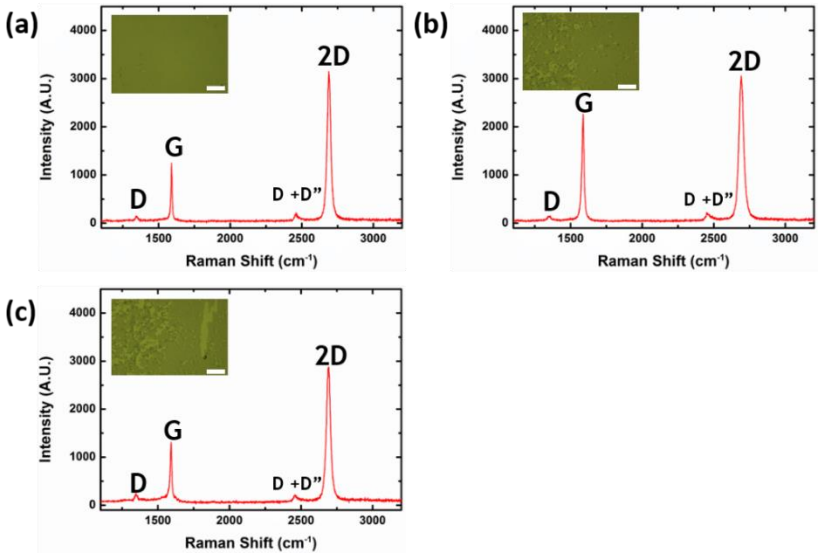

Figure 3.12: Raman spectra of device A16 (west region) (a) post-transfer, (b) post-first heated acetone clean and (c) post-second heated acetone clean. The *D*, *G*, *D + D"* and *2D* peaks are all labelled. Inset images are representative 10x optical microscopy images (scale bars are 100 µm).

Figure 3.13 shows histograms collated of *G* peak position, full width at half maximum (FWHM) of the *G* peak, *2D* peak position and FWHM-*2D*. The average values of the *G* peak position on post-transfer devices (~ 1589 ± 3 cm^{-1}), post-first clean (~ 1589 ± 2 cm^{-1}) and post-second clean (~ 1589 ± 2 cm^{-1}) are in agreement with PMMA assisted graphene transfer values (e.g. ~ 1560 cm^{-1} to 1620 cm^{-1}) [6]. From Figure 3.13 (a), the distribution of the *G* peak position becomes narrower after each successive clean, which suggests a more homogenous surface. This is also evident for the distribution of the *2D* peak positions (Figure 3.13 (c)). Mean values of ~ 2691 ± 3 cm^{-1} (post-transfer), ~ 2690 ± 3 cm^{-1} (post-first clean) and ~ 2690 ± 2 cm^{-1} (post-second clean) were measured for the *2D* peak which are in agreement with literature values (e.g. ~ 2660 cm^{-1} to 2700 cm^{-1}) [6]. All *2D* peaks were fitted with a single Lorentzian confirming monolayer graphene [21].

Residual PMMA on the graphene surface has the ability to cause p-doping [2, 38]. A slight decrease in the standard deviation of the *G* peak position is observed after the two acetone cleans which may suggest a reduction in p-doping i.e. a reduction of residual PMMA. However the standard deviation is small for the *G* peak. A small change in the standard deviation is also seen for the *2D* peak positions. For example Pirkle *et al.* found that Raman shifts after annealing (to remove residual PMMA) indicated increased p-doping (blue shift of mean *G* peak position by ~ 5.8 cm^{-1} and blue shift of *2D* peak position by ~ 2.8 cm^{-1}), while electrical measurements suggested a decrease in p-doping [2]. The difference was attributed to Raman measurements undertaken in air which can cause unwanted adsorbate doping, while electrical measurements were undertaken in vacuum. The full width at half maximum (FWHM) of the *2D* peaks herein were measured as: ~ 32 ± 3 cm^{-1} (post-transfer), ~ 32 ± 3 cm^{-1} (post-first clean) and ~ 34 ± 3 cm^{-1} (post-second clean) which resulted in sharp *2D* peaks and is in agreement with the FWHM-*2D* value of ~ 30 cm^{-1} for monolayer graphene [21]. The FWHM of the *G* peak positions were measured as: ~ 13 ± 2 cm^{-1} (post-transfer), ~ 14 ± 2 cm^{-1} (post-first clean) and ~ 14 ± 2 cm^{-1} (post-second clean). The *D*-peak, which is the main Raman peak associated with defects and disorder is present on many of the spectra (present in > 85% of spectra) and mean values of ~ 1350 ± 3 cm^{-1} (post-transfer), ~ 1349 ± 4 cm^{-1} (post-first clean) and ~ 1349 ± 4 cm^{-1} (post-second clean) are in agreement with literature values (e.g. ~ 1300 cm^{-1} to 1400 cm^{-1}) for CVD graphene [6]. The *D + D''* defect peak is present in > 90% of spectra with mean values of ~ 2459 ± 2 cm^{-1} (post-transfer), ~ 2458 ± 2 cm^{-1} (post-first clean) and ~ 2458 ± 2 cm^{-1} (post-second clean). These are in good agreement with the expected value of ~ 2450 cm^{-1} [39].

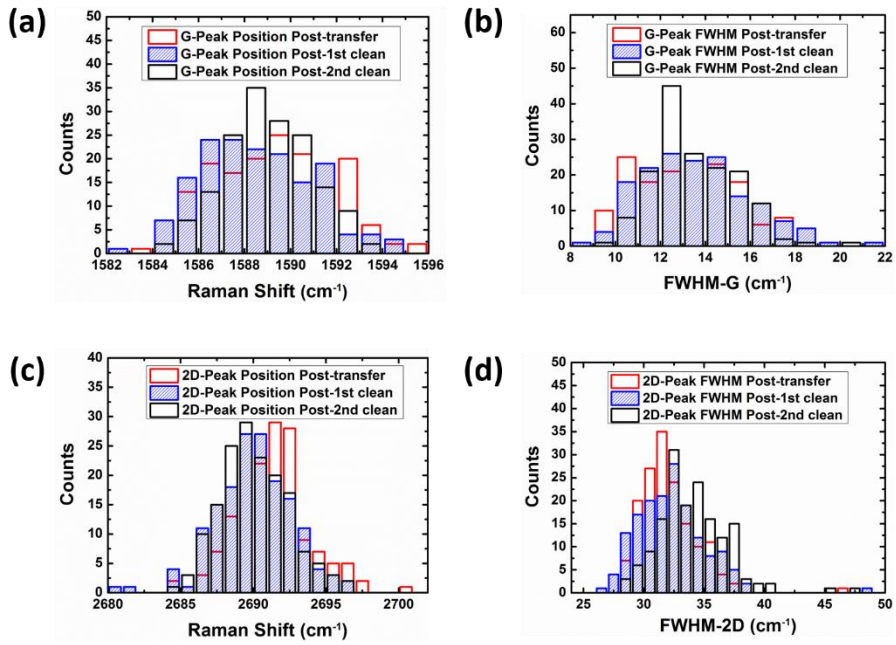

Figure 3.13: Histogram showing the number of counts in relation to (a) *G* peak position, (b) FWHM-*G*, (c) *2D* peak position and (d) FWHM-2*D*. In all cases the distribution is narrowing after successive cleans, suggesting a more homogenous surface.

A histogram of the ratio of I_{2D}/I_G values were also created (Figure 3.14 (a)). Ratio values of ~ 2.7 ± 0.5 (post-transfer), ~ 2.5 ± 0.6 (post-first clean) and ~ 2.4 ± 0.5 (post-second clean) were achieved. It is suggested that an increase in I_{2D}/I_G results in a decrease in doping and a reduction of contaminants [40]. However, the value of I_{2D}/I_G decreases slightly after the first and second cleans when compared to the post-transfer value but is possible due to minute adsorbate doping from undertaking Raman measurements in air. Another important ratio is the intensity of the *D* peak to that of the *G* peak i.e. I_D/I_G. Most Raman spectra had values of $I_D/I_G < 0.2$ (Figure 3.14 (b)) which suggests a low density of graphene defects.

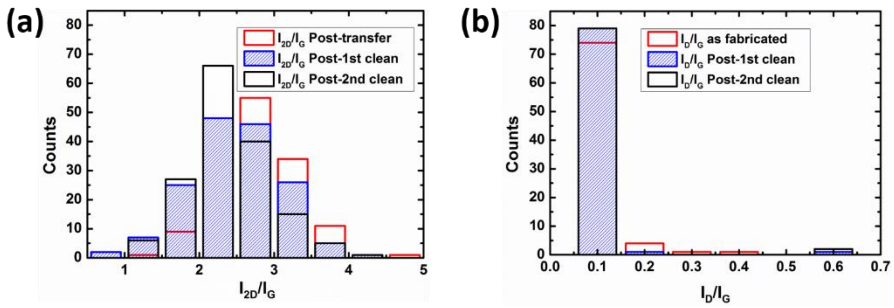

Figure 3.14: Histogram showing the number of counts in relation to (a) I_{2D}/I_G and (b) I_D/I_G. The mean value of I_{2D}/I_G (~ 2.4 ± 0.5) and the values of I_D/I_G < 0.2 after the second heated acetone clean suggests high quality low defect monolayer graphene.

Raman scatter plots were created of the FWHM-*G* as a function of *G* peak position, FHWM-*2D* as a function of *2D* peak position, *2D* peak position as a function of *G* peak position and I_{2D}/I_G as a function of *G* peak position were created (Figure 3.15). The outliers of each plot have decreased after two successive heated acetone cleans, which suggests that surface is more homogenous.

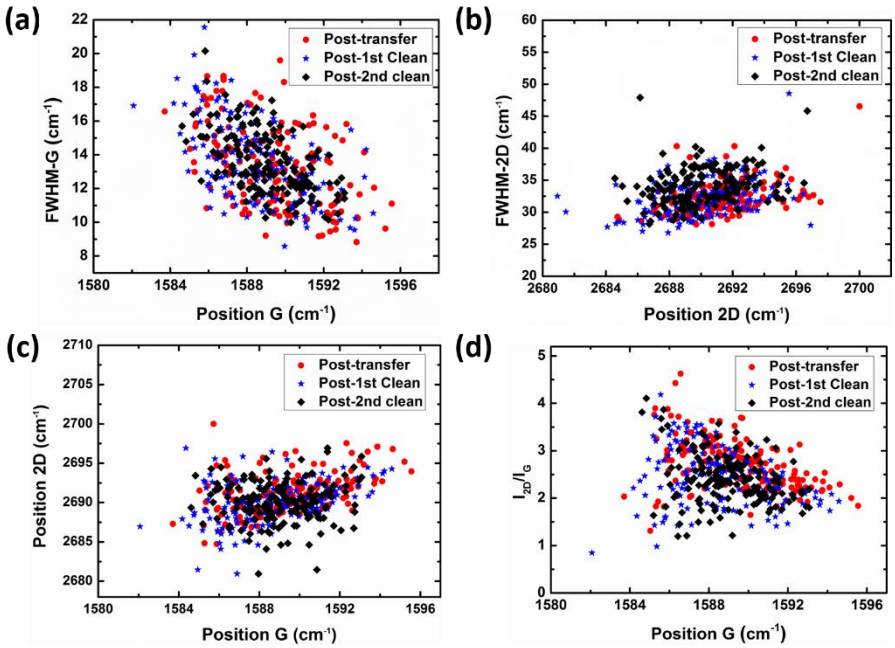

Figure 3.15: Raman scatter plots of the whole sample set of (a) FWHM-*G* as a function of *G* peak position, (b) FHWM-*2D* as a function of *2D* peak position, (c) *2D* peak position as a function of *G* peak position and (d) I_{2D}/I_G as a function of *G* peak position.

3.5.3 Transfer of continuous CVD graphene grown in Tyndall[a]

This section discusses the transfer and subsequent characterisation of as grown CVD graphene on copper foil in Tyndall from the previous chapter to Si/SiO_2 (90 thermal oxide) and glass substrates. After SEM analysis on copper foil post-CVD growth in the previous chapter, suitable growth runs were used for transfer to silicon substrate with a dielectric layer, SiO_2 of 90 nm thermal oxide. The continuous CVD graphene growth run from the previous chapter was used. The growth process involved a methane deposition time of 15 minutes methane at 1,035 ^oC using a pressure of 450 mTorr via the closed loop pressure valve. A large area of 15 x 15 mm was transferred to glass using the previously stated transfer process (Figure 3.16 (a)). The subsequent Raman spectrum was taken (Figure 3.16 (b)). The *G* peak value was measured as ~ 1586 cm^{-1} with a FWHM of ~ 18 cm^{-1}. The *2D* peak (~ 2692 cm^{-1}) was fitted with a single Lorentzian and has a FWHM of ~ 34 cm^{-1}, which confirms monolayer graphene [21]. The *D* peak (~ 1350 cm^{-1}) and *D + D''* (~ 2461 cm^{-1}) defect peak are also present. The ratio of I_{2D}/I_G ~ 3.5 and the ratio of I_D/I_G ~ 0.14 suggests high quality graphene.

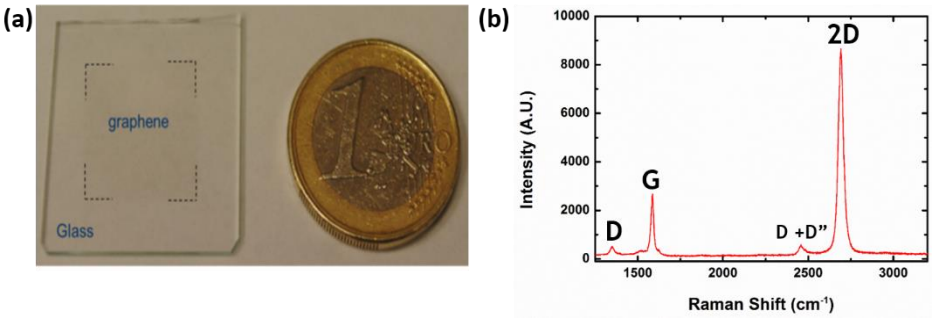

Figure 3.16: (a) Photograph of large area (15 mm x 15 mm) of continuous Tyndall CVD graphene transferred to a glass substrate & (b) representative Raman spectra of transferred graphene showing the *G* (~ 1586 cm^{-1}) and *2D* (~ 2692 cm^{-1}) peaks along with the *D* (~ 1350cm^{-1}) and *D + D''* (~ 2461 cm^{-1}) defect peaks.

[a] CVD graphene transfer to glass and SiO_2 was undertaken by Ms. Roxane Puicervert in Tyndall (Nanotechnology group).

3.5.4 Atomic Force Microscopy of transferred continuous CVD graphene[b]

Atomic for microscopy was undertaken on transferred graphene samples to investigate the quality of the transferred film. Roughness measurements (1 μm x 1 μm) were undertaken over a 2 μm x 2 μm scan as seen in Figure 3.17. Wrinkles, cracks as well as nanoscale and larger islands (possibly due to process residue) are observed on the transferred samples. The root mean square roughness (R_q) of the transferred graphene on Si/SiO_2 ranged from ~ 0.6 nm to over 1.4 nm depending on where the roughness was taken (it is essential to take the roughness on areas were no particle contaminants are present). To decrease the roughness of the graphene film, the sample was annealed in an argon environment at 500 ^oC for 10 minutes to remove any surface contamination or impurities on the surface. From the resulting AFM in the same region, there is a drastic decreased in the roughness to an R_q value of ~ 0.2 nm, which agrees with literature reports. As in the previous study, it appears that although the roughness decreased after annealing, cluster type structures are present (see Figure 3.17 (b)). What is also evident is that annealing was unsuccessful in totally removing residual PMMA, a problem noted in the literature [2, 31].

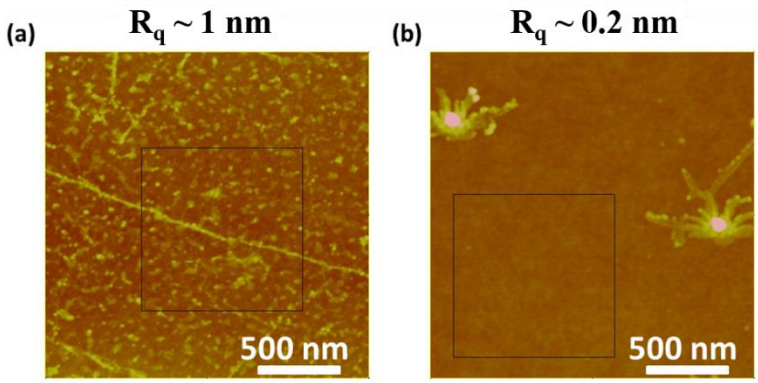

Figure 3.17: (a) Tapping-mode AFM image and R_q roughness data for a CVD graphene sample following transfer onto a Si/SiO_2 (90 nm thermal oxide) substrate. (b) Tapping-mode AFM image and R_q data for CVD graphene sample following transfer and annealing in argon at 500 ^oC for 10 minutes showing the drastic reduction in contaminants and the decrease in the roughness. However cluster type structures are present after the annealing process.

[b] AFM characterisation was undertaken by Ms. Roxane Puicervert in Tyndall (Nanotechnology group).

3.5.5 Transparency of continuous CVD graphene[c]

For transparency measurements, a graphene film grown on copper in the CVD system was transferred to a glass substrate using the transfer process as mentioned previously. Transparency measurements were taken by colleague Roxane Puicervert. The sample was mounted in the Perkin Elmer Spectrophotometer and it was referenced against air and a blank glass reference substrate. The resulting transmission spectra show a high transparency of ~ 97 % at a wavelength of 550 nm versus the blank glass substrate, which agrees favourably with the intrinsic transparency of monolayer graphene (~ 97.7%) [41] and other values reported by literature (~ 97% to ~ 97.5%) [9, 42, 43].

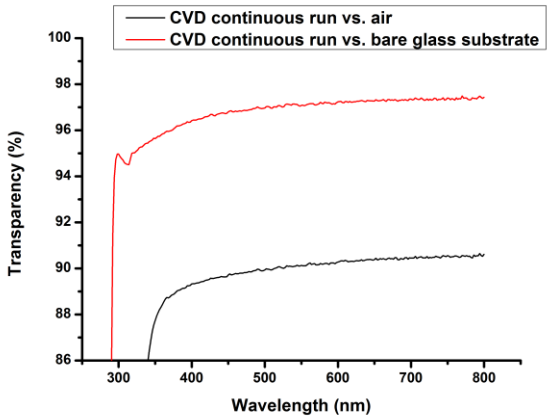

Figure 3.18: Optical transmission data for a CVD graphene film transferred onto glass measured versus a blank glass slide (red curve) and measured versus air (black curve).

3.5.6 Graphene Field Effect Devices (GFEDs)[d]

To measure the carrier mobilities and sheet resistance of CVD grown graphene, a GFED (micron scale device) was fabricated using the procedure from section 3.4. One challenge with the fabrications of GFEDs is the partial delamination of graphene after the lithography process as seen in Figure 3.19 (c). The partial delamination of graphene may have an influence on the sheet resistance i.e. it may increase it. This is a common obstacle that if often overlooked in the literature [44, 45]. The device itself shows a sheet resistance of ~ 2.4 kΩ/sq with low hysteresis (micron scale device). As

[c] Optical analysis was undertaken by Ms. Roxane Puicervert in Tyndall (Nanotechnology group).
[d] Graphene field effect devices were fabricated and analysed by Ms. Roxane Puicervert in Tyndall (Nanotechnology group).

fabricated field effect devices generally showed maximum two probe resistance at a positive gate voltage which is indicative of net p-doping. To reduce contaminants and the influence of adsorbate dopants on the GFED, the sample was annealed in an argon atmosphere at 500 ^{o}C for 10 minutes. Graphene is very sensitive to ambient adsorbates [46]. These adsorbates can have detrimental effects on the electrical characteristics and stability of graphene-based devices [46-48]. These measurements were undertaken in vacuum to remove the influence of ambient adsorbate doping on the sheet resistance of graphene films. Since graphene is one atom thick, it is susceptible to anything that lands on the surface e.g. moisture in the air. Taking sheet resistance measurements of graphene under vacuum is a common practice in literature [2, 49, 50] and thus the sheet resistance values herein represent a lower bound. Non-covalent molecular functionalisation with bis(trifluoromethanesulfonyl)amide (TFSA) which is a p-dopant was used to lower the sheet resistance of the graphene film. Non-covalent functionalisation is desired as to not perturb the sp^2-hybridisation of graphene [51]. This aspect is critical in relation to graphene based electronic devices. Even a low density of sp^3-hybridisation strongly affects the delocalisation of electrons within a graphene layer [52]. Following the functionalisation, the device showed a dramatic reductions in measured sheet resistance (2.4 kΩ/sq to 404 Ω/sq after functionalisation) with no appreciable maxima in the measured resistance versus gate voltage (i.e. Dirac Point > 30-40 V, implying a strong net p-doping regime) as seen in Figure 3.19. The channel width was estimated based on the area with the shortest continuous graphene coverage as current follows the past of least resistance. For example, Kim *et al.* reported pristine monolayer graphene with a sheet resistance of ~ 5590 Ω/sq and the sheet resistance decreased to ~ 2340 Ω/sq after doping with TFSA [53]. It has been demonstrated that visible light is not absorbed by TFSA [54] and the transparency of the doped graphene sample herein was similar to that of un-doped graphene (~ 97%).

(a)

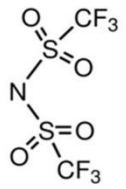

(b)

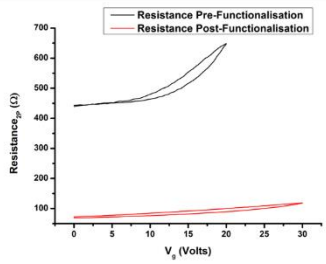

(c)

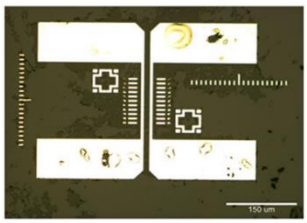

(d)

	Pre-functionalisation	Post-functionalisation
Channel length (gap)	13 µm	13 µm
Width (estimated)	72 µm	72 µm
Resistance at 0 V	435 Ω	73 Ω
Sheet resistance at 0 V	2.4 kΩ/sq	0.4 kΩ/sq
Dirac Point	> 20 V	> 30 V

Figure 3.19: (a) Structure of the TFSA molecule. (b) Graph of Resistance versus Gate Voltage GFED on the same sample pre and post-functionalisation showing a decrease in the sheet resistance. (c) Optical microscopy image of the GFED (scale bar is 150 µm). (d) Table of extracted electrical results. A sheet resistance of 404 Ω/sq for the graphene film was achieved after functionalisation. The estimated channel width was the width measured based on the area with the shortest continuous graphene coverage.

The previous measurements were taken on a micron scale device. The sheet resistance was also measured on a millimetre scale device using a digital multimeter and conductive silver paint. Sheet resistance values in the order of ~ 1 kΩ/sq were measured. The larger sheet resistance of the as fabricated micron scale device (~ 2.4 kΩ/sq) could be due to lithographic residue when fabricating the metal contacts. Sheet resistance differences could also occur due to contact resistance and film cracks. The millimetre scale device was measured under ambient conditions and therefore ambient adsorbate doping of this device could have reduced the sheet resistance.

3.6 Conclusion

Following on from the previous chapter, which discussed growth of graphene by CVD, a transfer process is required to remove the graphene from the host substrate and transfer it to glass or SiO_2 (90 nm thermal oxide) for further analysis. The most common transfer process is that of a wet chemical process. This involves using a polymer i.e. PMMA as a mechanical support for the graphene during the transfer process. The backside graphene is then removed by an oxygen plasma. The copper foil is then etched and the PMMA-graphene film is transferred to substrate of choice.

The PMMA is subsequently removed by immersing the sample in acetone. However, many research publications have noted the existence of residual polymer layers which can increase the sheet resistance of the film.

A few literature publications report on the use of heated acetone on the removal of the initial PMMA layer. However, to this author's knowledge, no reports exist for the investigation of the removal of residual PMMA layers with heated acetone. The use of statistics represents a novel approach in gauging the effect of using acetone at elevated temperatures (to remove residual PMMA) on graphene coverage, roughness, particle count and Raman. 16 devices in total were used for this study. However only 8 samples were suitable for further statistical analysis.

From the optical analysis, it was clear that the heated acetone clean resulted in partial removal of graphene coverage. This may be due to poor adhesion between the graphene and substrate, which may allowed the heated acetone to penetrate this interface layer. The heated acetone clean is more aggressive than the room temperature equivalent as it is above its boiling point. To gauge the effect of the clean on the removal of residual PMMA, AFM roughness measurements were undertaken. It was clear that the first heated acetone clean had a large influence on the roughness of the film with a large decrease for both root mean square roughness (~ 1.3 ± 0.3 nm to ~ 0.5 ± 0.2 nm) and mean roughness (~ 0.8 ± 0.2 nm to ~ 0.3 ± 0.1 nm). In all cases, the histogram distribution narrowed after successive cleans. The roughness of the sample set was similar after the second clean. Particulate counting on AFM images decreased after each subsequent clean. For example, device A3 initially had a particle count of ~ 282 post-transfer but after the second heated acetone clean, this reduced to ~ 21 particles. This suggests that the increased (maximum) particle size observed after subsequent cleans may result from PMMA migration and redeposition into large islands as the maximum particle area increases after subsequent cleans. The mean *G* and *2D* peak positions were stable after each data set. Each *2D* peak was fitted with a single Lorentzian which confirms monolayer graphene. The large number of spectra with $I_D/I_G \leq 0.2$ suggests low defected graphene films after the two heated acetone cleans. Statistical analysis suggests it would be beneficial to carry out only one heated acetone clean.

In the previous chapter, a continuous growth run was undertaken following the efforts to increase the graphene domain size. This continuous growth run was then transferred to SiO_2 and glass substrates for further analysis. The transparency of the graphene film was measured as ~ 97% at a wavelength of 550 nm. The surface roughness of the film decreased by ~ 0.8 nm to ~ 0.2 nm after annealing in Ar for 10 minutes at 500 ^oC but larger spherical particles are present. The sheet resistance of the graphene film transferred to Si/SiO_2 (90 nm thermal oxide) was measured as ~ 2.4 kΩ/sq. The graphene film was then functionalised with a p-dopant (TFSA) and produced a sheet resistance of ~ 404 Ω/sq (micron scale). Following this, resistance values in the order of kΩ was measured for large area graphene (mm scale) using a multimeter.

The high intrinsic transparency of monolayer graphene (~ 97.7%) is very advantageous for use in the transparent conductive electrode industry. However, the sheet resistance of graphene films is very large, which has limited it use for these applications. Since the reliability of the CVD system herein started to decrease after the first few successful continuous growth runs and the undesirable large sheet resistance value for CVD graphene after functionalisation, another type of alternative material (discussed in chapter 1) for use as a transparent conductive electrode was sought. The alternative martial chosen in this case was transparent metal meshes which will be discussed in subsequent chapters.

3.7 Bibliography

1. Liang, X., et al., *Toward Clean and Crackless Transfer of Graphene.* Acs Nano, 2011, **5**(11), p. 9144-9153
2. Pirkle, A., et al., *The effect of chemical residues on the physical and electrical properties of chemical vapor deposited graphene transferred to SiO2.* Applied Physics Letters, 2011, **99**(12), 122108
3. Kumar, K., Y.-S. Kim, and E.-H. Yang, *The influence of thermal annealing to remove polymeric residue on the electronic doping and morphological characteristics of graphene.* Carbon, 2013, **65**, p. 35-45
4. Lin, Y.-C., et al., *Graphene Annealing: How Clean Can It Be?* Nano Letters, 2012, **12**(1), p. 414-419
5. Li, X., et al., *Transfer of Large-Area Graphene Films for High-Performance Transparent Conductive Electrodes.* Nano Letters, 2009, **9**(12), p. 4359-4363
6. Li, X.S., et al., *Large-Area Synthesis of High-Quality and Uniform Graphene Films on Copper Foils.* Science, 2009, **324**(5932), p. 1312-1314
7. Kim, B.J., et al., *High-performance flexible graphene field effect transistors with ion gel gate dielectrics.* Nano Letters, 2010, **10**(9), p. 3464-3466
8. Gomez De Arco, L., et al., *Continuous, highly flexible, and transparent graphene films by chemical vapor deposition for organic photovoltaics.* ACS Nano, 2010, **4**(5), p. 2865-2873
9. Suk, J.W., et al., *Transfer of CVD-Grown Monolayer Graphene onto Arbitrary Substrates.* ACS Nano, 2011, **5**(9), p. 6916-6924
10. Ren, Y., et al., *An improved method for transferring graphene grown by chemical vapor deposition.* Nano, 2012, **7**(1), 1150001
11. Chan, J., et al., *Reducing extrinsic performance-limiting factors in graphene grown by chemical vapor deposition.* ACS Nano, 2012, **6**(4), p. 3224-3229
12. Chan Wook, J., et al., *Rapid-thermal-annealing surface treatment for restoring the intrinsic properties of graphene field-effect transistors.* Nanotechnology, 2013, **24**(40), 405301
13. Fechine, G.J.M., et al., *Direct dry transfer of chemical vapor deposition graphene to polymeric substrates.* Carbon, 2015, **83**, p. 224-231
14. Lock, E.H., et al., *High-Quality Uniform Dry Transfer of Graphene to Polymers.* Nano Letters, 2012, **12**(1), p. 102-107
15. Wang, Y., et al., *Electrochemical Delamination of CVD-Grown Graphene Film: Toward the Recyclable Use of Copper Catalyst.* Acs Nano, 2011, **5**(12), p. 9927-9933
16. Cherian, C.T., et al., *'Bubble-Free' Electrochemical Delamination of CVD Graphene Films.* Small, 2015, **11**(2), p. 189-194
17. Lu, A.-Y., et al., *Decoupling of CVD graphene by controlled oxidation of recrystallized Cu.* RSC Advances, 2012, **2**(7), p. 3008-3013
18. Gupta, P., et al., *A facile process for soak-and-peel delamination of CVD graphene from substrates using water.* Scientific Reports, 2014, **4**, 3882
19. Ryu, J., et al., *Fast Synthesis of High-Performance Graphene Films by Hydrogen-Free Rapid Thermal Chemical Vapor Deposition.* ACS Nano, 2014, **8**(1), p. 950-956
20. Kang, J., et al., *Efficient Transfer of Large-Area Graphene Films onto Rigid Substrates by Hot Pressing.* ACS Nano, 2012, **6**(6), p. 5360-5365
21. Ferrari, A.C., et al., *Raman spectrum of graphene and graphene layers.* Physical Review Letters, 2006, **97**(18), 187401

22. Ferrari, A.C. and D.M. Basko, *Raman spectroscopy as a versatile tool for studying the properties of graphene.* Nat Nano, 2013, **8**(4), p. 235-246
23. Frank, O., et al., *Phonon and structural changes in deformed bernal stacked bilayer graphene.* Nano Letters, 2012, **12**(2), p. 687-693
24. Casiraghi, C., et al., *Rayleigh Imaging of Graphene and Graphene Layers.* Nano Letters, 2007, **7**(9), p. 2711-2717
25. Banerjee, S., et al., *Electrochemistry at the Edge of a Single Graphene Layer in a Nanopore.* ACS Nano, 2013, **7**(1), p. 834-843
26. Joshua, D.W., et al., *Annealing free, clean graphene transfer using alternative polymer scaffolds.* Nanotechnology, 2015, **26**(5), 055302
27. Gao, G., et al., *Heat-Initiated Chemical Functionalization of Graphene.* Scientific Reports, 2016, **6**, 20034
28. Guermoune, A., et al., *Chemical vapor deposition synthesis of graphene on copper with methanol, ethanol, and propanol precursors.* Carbon, 2011, **49**(13), p. 4204-4210
29. Campos-Delgado, J., et al., *CVD synthesis of mono- and few-layer graphene using alcohols at low hydrogen concentration and atmospheric pressure.* Chemical Physics Letters, 2013, **584**, p. 142-146
30. Mun, J.H. and B.J. Cho, *Synthesis of Monolayer Graphene Having a Negligible Amount of Wrinkles by Stress Relaxation.* Nano Letters, 2013, **13**(6), p. 2496-2499
31. Cheng, Z., et al., *Toward Intrinsic Graphene Surfaces: A Systematic Study on Thermal Annealing and Wet-Chemical Treatment of SiO2-Supported Graphene Devices.* Nano Letters, 2011, **11**(2), p. 767-771
32. Jung, W., et al., *Prevention of Water Permeation by Strong Adhesion Between Graphene and SiO2 Substrate.* Small, 2014, **10**(9), p. 1704-1711
33. Tan, L., et al., *Direct growth of ultrafast transparent single-layer graphene defoggers.* Small, 2015, **11**(15), p. 1840-1846
34. Aldrich, S. *Acetone Data Sheet*. 03/07/2015]; Available from: http://www.sigmaaldrich.com/MSDS/MSDS/DisplayMSDSPage.do?country=IE&language=en&productNumber=32201&brand=RIEDEL&PageToGoToURL=http%3A%2F%2Fwww.sigmaaldrich.com%2Fcatalog%2Fproduct%2Friedel%2F32201%3Flang%3Den.
35. Huang, Y., et al., *Reliable Exfoliation of Large-Area High-Quality Flakes of Graphene and Other Two-Dimensional Materials.* ACS Nano, 2015, **9**(11), p. 10612-10620
36. Ki Kang, K., et al., *Enhancing the conductivity of transparent graphene films via doping.* Nanotechnology, 2010, **21**(28), 285205
37. Tien, D.H., et al., *Characterization of Graphene-based FET Fabricated using a Shadow Mask.* Scientific Reports, 2016, **6**, 25050
38. Deng, C., et al., *Reversible Charge-Transfer Doping in Graphene due to Reaction with Polymer Residues.* The Journal of Physical Chemistry C, 2014, **118**(25), p. 13890-13897
39. Nemanich, R.J. and S.A. Solin, *First- and second-order Raman scattering from finite-size crystals of graphite.* Physical Review B, 1979, **20**(2), p. 392-401
40. Casiraghi, C., et al., *Raman fingerprint of charged impurities in graphene.* Applied Physics Letters, 2007, **91**(23), 233108
41. Nair, R.R., et al., *Fine structure constant defines visual transparency of graphene.* Science, 2008, **320**(5881), p. 1308-1308

42. Bae, S., et al., *Roll-to-roll production of 30-inch graphene films for transparent electrodes.* Nature Nanotechnology, 2010, **5**(8), p. 574-578
43. Bonaccorso, F., et al., *Graphene photonics and optoelectronics.* Nature Photonics, 2010, **4**(9), p. 611-622
44. Kumar, S., et al., *Reliable processing of graphene using metal etchmasks.* Nanoscale Research Letters, 2011, **6**(1), 390
45. Lee, Y., et al., *Wafer-Scale Synthesis and Transfer of Graphene Films.* Nano Letters, 2010, **10**(2), p. 490-493
46. Levesque, P.L., et al., *Probing Charge Transfer at Surfaces Using Graphene Transistors.* Nano Letters, 2011, **11**(1), p. 132-137
47. Lohmann, T., K. von Klitzing, and J.H. Smet, *Four-Terminal Magneto-Transport in Graphene p-n Junctions Created by Spatially Selective Doping.* Nano Letters, 2009, **9**(5), p. 1973-1979
48. Blake, P., et al., *Influence of metal contacts and charge inhomogeneity on transport properties of graphene near the neutrality point.* Solid State Communications, 2009, **149**(27–28), p. 1068-1071
49. Joshi, P., et al., *Intrinsic doping and gate hysteresis in graphene field effect devices fabricated on SiO2 substrates.* Journal of Physics: Condensed Matter, 2010, **22**(33), 334214
50. Kumar, S., et al., *Graphene field emission devices.* Applied Physics Letters, 2014, **105**(10), 103107
51. Georgakilas, V., et al., *Functionalization of Graphene: Covalent and Non-Covalent Approaches, Derivatives and Applications.* Chemical Reviews, 2012, **112**(11), p. 6156-6214
52. Xiao-Yan, F., et al., *Effects of electron-transfer chemical modification on the electrical characteristics of graphene.* Nanotechnology, 2010, **21**(47), 475208
53. Kim, D., et al., *Work-Function Engineering of Graphene Anode by Bis(trifluoromethanesulfonyl)amide Doping for Efficient Polymer Light-Emitting Diodes.* Advanced Functional Materials, 2013, **23**(40), p. 5049-5055
54. Kim, S.M., et al., *Transparent Organic P-Dopant in Carbon Nanotubes: Bis(trifluoromethanesulfonyl)imide.* ACS Nano, 2010, **4**(11), p. 6998-7004

4 Metal meshes on rigid substrates for transparent conductive electrodes

4.1 Introduction and motivation

Until recent times, minimal research has been undertaken to use highly conductive materials (such as metals) as transparent electrodes, due to their poor transparency. Metal deposition can occur from various methods such as physical vapour deposition (PVD) e.g. evaporation and sputter deposition, and atomic layer deposition (ALD). One current research field in the transparent conductive electrode industry is that of fabricating transparent metal mesh structures, which involve the use of a repeatable or a randomised structural metal mesh on transparent substrates such as glass or flexible plastics [1-6]. The thickness of the metal, the linewidth and open area of the mesh can be manipulated to produce a transparent conductive electrode with a low sheet resistance, high transparency and low haze. Many methods of fabricating metal mesh structures on glass or flexible substrates have been reported in literature and include ultra-violet (UV) lithography [1, 7-9], nano-imprint lithography (NIL) [10-12], grain boundary lithography [13], solution-based metal nanowire networks [4, 14, 15] and various printing methods [16-18]. All of these methods have their own advantages and disadvantages in relation to cost, reproducibility and the ability to resolve certain feature sizes. A brief overview is provided below. The various methods are compared in Table 4.1 and the state of the art is presented in Table 4.2.

UV lithography is a common method used to apply certain features to target substrate by the use of photoresist and a chrome mask (which includes the desired features) [19]. One advantage of using this technique is that it is reproducible as it has been used extensively in the semiconductor industry. However, it is challenging to achieve linewidths < 5 μm by UV lithography which are undetectable by the naked eye.

Nano-imprint lithography (NIL) involves creating an imprint followed by pattern transfer [30]. A PDMS mould is created from a master wafer (usually SiO_2), which contains the desired features (sub-micron critical dimensions). This mould is placed in contact with a target substrate covered by resist, followed by curing, removing the mould from the substrate and removing residual resist. The resolution of NIL is dependent on the mould and resist. The desired features on the SiO_2 master

wafer are initially created by electron-beam lithography (e-beam lithography), which is an expensive and timely process.

Rolith Inc. have developed a transparent conductive electrode called "Nanoweb", which is a sub-micron transparent metal mesh network. The nanoweb is created by rolling mask lithography (RML®) [20, 21], which is implemented using a cylindrical lithography mask. The UV-light source is embedded in the cylindrical mask itself and is transmitted through the mask as it rolls across the substrate. Sub-micron metal linewidths such as those used by Rolith Inc. are preferred for metal mesh technologies. They limit the effect of parasitic interference patterns i.e. Moiré fringes which can induce blurriness when the transparent electrode is applied over display architecture [20].

Metal mesh structures can also be fabricated by using a bilayer lift-off metallisation process (grain boundary lithography) reported by Guo *et al.* [13]. A gap is created in the material between neighbouring grains and metal is evaporated into the gaps between neighbouring grains in a polycrystalline film to produce a nanomesh network. One advantage of this technique is that the width between neighbouring grains can be controlled depending on the acid etching time. In comparison with standard UV lithography, grain boundary lithography offers accurate sub-micron resolution and undercut control. However, this novel approach of fabricating metal mesh networks has only been reported by one research group and thus the feasibility in regards to costing and reproducibility is unknown.

Mesh networks based on arrays of nanowires have been fabricated by various groups. This method provides transparent metal meshes with good flexibility [4]. However the surface of these materials are rough in nature [22]. The fabrication of metal nanostructures can involve complicated synthesis methods which prove difficult to produce them in large quantities [23]. The use of solution based nanowires also increases the likelihood of contamination from the wet chemical process.

Screen printing such as inkjet printing with nanoparticle inks, is a maskless, non-contact printing technology. It offers the advantages of high volume production, efficient material utilisation compared to conventional vacuum deposition processes and low fabrication costs [24, 25]. It has been demonstrated on glass, metal foil and plastic. However, this fabrication technique is still in its infancy. Using the smallest

commercial inkjet nozzle (~ 1 pico litre), the resolution is limited to between 20 µm and 30 µm which is undesired as it is still detectable by the naked eye [26]. Some research groups have suggested the use of electrohydrodynamic (EHD) screen printing to replace the standard form [18, 27-29]. Elongation of the ink on the tip of the nozzle is achieved by applying an electric field. This elongation allows the ink to disperse into droplets with sizes smaller than that of the nozzle tip. This EHD method allows higher resolution linewidths < 10 µm [18].

Table 4.1: Advantages and disadvantages of fabrication techniques to produce metal mesh structures.

Fabrication method:	Advantages:	Disadvantages:
UV lithography	-Reproducible process -Ability to use lift-off or dry etching methods -Wafer scale patterning	-Challenging (expensive) to achieve sub-micron resolution -Time consuming
NIL	-Sub-micron resolution (lower haze) -High throughput process	-Costly to produce master wafer
Grain boundary lithography	-Sub-micron resolution -Accurate undercut control	-Still in its infancy, only demonstrated by one research group
Solution based nanowires	-Sub-micron resolution -Low resistance change when flexed	-Large surface roughness -Contamination from wet chemical process -Large haze
Screen printing	-Low cost -High volume production -Efficient material utilisation	-Limited to 20 µm to 30 µm resolution if not using EHD printing -Unable to achieve sub-micron resolution
Rolling mask lithography	-Sub-micron resolution	-High initial cost -Only demonstrated by one industrial company

From literature publications, the realisation of metal mesh structures as alternatives to ITO technologies is usually based on pattern fabrication techniques i.e UV lithography, nanoimprint lithography etc. along with the use of symmetrical geometries such as squares and hexagons. One of the goals of this research work was to assess the effect of geometry (symmetric and asymmetric), metal linewidth and mesh open area on the electrical and optical properties of transparent metal mesh structures. While extensive work on symmetrical patterns for metal meshes have been reported i.e. squares [1, 8, 18] and hexagons [7, 30], there have been very few reports on asymmetric metal meshes, such as grain boundary lithography. To our knowledge, there have been no reports on uniform asymmetric designs. It's thought that the use of asymmetric metal meshes may have the potential for good mechanical stability due to force distribution when under strain. A new asymmetric pentagonal design discovered in 2015 [31] was included in this study along with a symmetric hexagon, square and circle design. UV-lithography was utilised to apply geometric features on target substrates due to the methods reproducibility and ease of use. Metal was deposited using methods such as physical vapour deposition e.g. electron-beam evaporation and sputter deposition [32, 33] along with atomic layer deposition [34]. These three methods were used to assess the effect of the deposition method on structural, electrical and optical performance of transparent metal mesh films. These were chosen over other solution based metal synthesis methods such as nanowires or inkjet printing due to availability and known use. Table 4.2 below shows literature values for transparent metal meshes based on differing fabrication techniques. The RML® method by Rolith appears to be the best alternative to ITO technology [20].

Table 4.2: Literature table of transparent metal meshes by different fabrication techniques. Superscripted citations refer to footnotes.

Fabrication method:	Metal:	Geometry:	R_S (Ω/sq):	T_{mesh} (%)[a]:	T_{total} (%)[b]:	Haze (%):	Figure of merit[d]:
UV lithography	Cu [1],[1]	Square	6.5	81	75	-[c]	261
	Ni [1],[1]	Square	28	82	76.5	-	65
	Au [7]	Hexagon	15	63	59	-	48
	Pt [8],[2]	Square	3	80	74		532
NIL	Al [11]	Square	13	81	75	-	131
	Cu [10]	Square	22	84	78	-	94
	Au [12]	Square	12	74		-	97
Grain boundary lithography	Au [13]	Random	21	83	77	3	92
Nanowire network in solution	Ag [35]	Random	45	77	72	12	30
	Ag [36]	Random	13	85	79	-	171
	Ag [14]	Random	10	90	84	-	348
Printing (ink)	Ag [18]	Square	5	90	82	-	697
	Ag [28]	Square	7	84	78	-	296
	Ag [29]		1.5	78	73	-	950
Rolling mask lithography (Rolith)	Ag [20]	Square	5	96	89	5	1828
	Al [20]	Square	3.5	96	89	5	2612

[a]Transparency does not include the effect of the underlying substrate. [b]Transparency includes the effect of the underlying substrate. If not stated in the literature report, a transparency value of ~ 93% was used for the underlying substrate to calculate the total transparency i.e. $T_{total} = T_{substrate}$ x T_{mesh}. [c]Dash (-) indicates lack of reported data. [d]Figure of merit as defined in equation 1.6 on page 13 in chapter 1.

[1] Utilised a 2 nm thick Ni film underneath the mesh.
[2] Utilised a graphene layer with the metal grid.

4.2 Thin film deposition methods

4.2.1 Atomic Layer Deposition overview

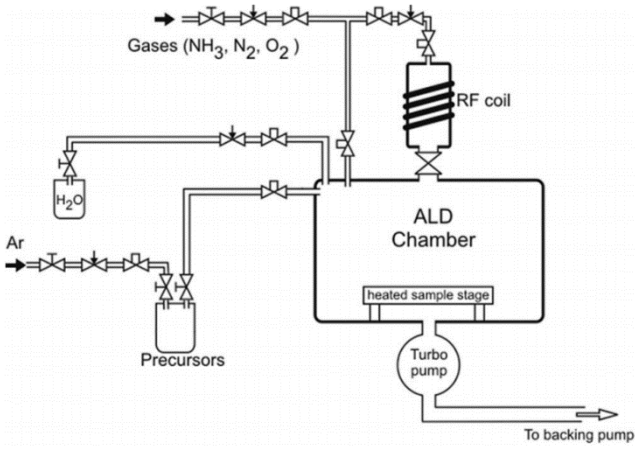

Figure 4.1: Schematic of a typical ALD reactor with an RF coil for PE-ALD [37].

Atomic layer deposition (ALD) is a vapour-phase process which allows atomic level thickness control. Ultra-thin films are synthesised sub-monolayer by sub-monolayer by utilising two self-limiting gas-surface reaction cycles. The technique was first developed in the 1960s in the Soviet Union by Aleskovskii and further work was done by Suntola in Finland in the 1970s [38, 39]. At the time it was commonly referred to as Atomic Layer Epitaxy (ALE) and was utilised to create large flat panel displays based on thin film electroluminescence [40-42]. ALD can produce conformal thin films in the nanometre range due to successive, surface-controlled reactions. ALD growth is based on chemical mechanisms and is a sub-set of chemical vapour deposition (CVD). In contrast to CVD processes, ALD involves alternating pulses of precursors which react to create the desired film often at much lower temperatures than CVD [43]. Initially, interest in the ALD technique was scarce due to its low deposition rate. However, interest in this topic started to peak in the 1990s originating from silicon based microelectronics for ultra-thin gate dielectrics [44-46].

Currently, many different types of ALD growth techniques are available. The most common ALD process is thermal ALD. Thermal ALD relies on elevated temperatures in the reactor chamber to aid the surface reactions. A plasma can also be

used in the reactor during ALD growth and is commonly referred to as plasma-enhanced atomic layer deposition (PE-ALD).

4.2.2 ALD film growth by self-limiting half reactions

ALD is a surface-controlled growth process. The growth of films by ALD is based on two self-terminating gas-surface reactions. Gas-surface reactions occur when a molecule is in close proximity to a substrate surface. The molecule is attracted to the surface by Van der Waals or dipole forces. A colliding particle onto the substrate surface can be physisorbed (weakly bound) if it is not deflected back into the path of the originating gas. Weakly bound molecules on the surface can be desorbed by thermal energy for example. For optimum ALD growth to occur, the molecule has to chemisorb (chemically bound) onto the surface of the substrate. The three main chemisorption mechanisms are ligand exchange, dissociation and association [38], see Figure 4.2. Effects such as surface roughness, crystal orientation, surface energy effects and the possible formation of interfacial layers at the surface of the substrate can affect growth by ALD. These effects are usually referred to as substrate effects.

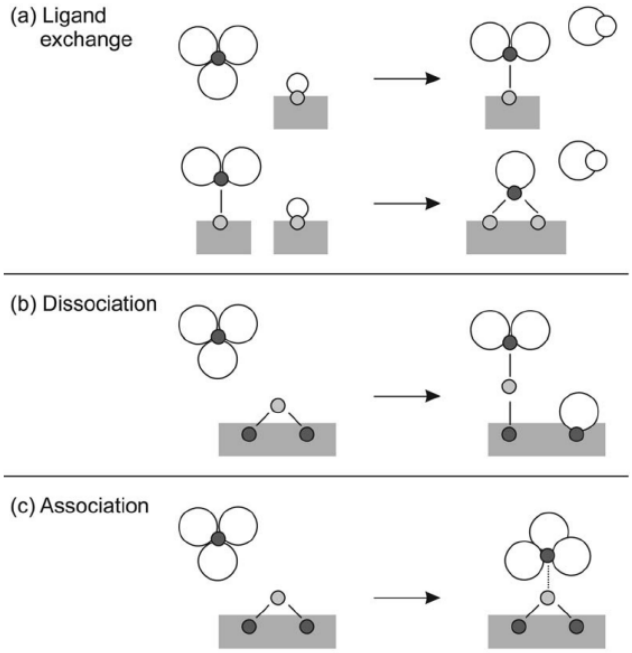

Figure 4.2: Schematic showing three different mechanisms for chemisorption: (a) Ligand exchange, (b) Dissociation & (c) Association. Note that the molecule has three ligands in this example [38].

The three main parameters that determine deposition features of ALD films are the reactor temperature, the substrate on which growth will occur and the gases utilised (precursor and reactant gases) [47]. As previously discussed, ALD growth is based on self-limiting reactions and relies on chemisorption mechanisms rather than physisorption. In regard to temperature, every ALD process is tailored to have a suitable temperature so that the physisorbtion of ligands is minimised [48]. Decomposition of an ALD precursor or reactive gas is undesired as the process will then proceed in a CVD type manner. Therefore a suitable temperature is utilised to prevent the thermal decomposition of the gases. Every ALD process has its own specific "ALD temperature window" (Figure 4.3). This window represents the ideal temperature range for an ALD growth process [49]. A temperature below and above this window alters the growth per cycle (GPC). When the temperature is below this "ALD Window", the GPC can increase due to the presence of condensation on the reactor walls or on the substrates themselves. The GPC can decrease due to a lack of thermal energy, which is used to complete the chemical reaction during a thermal ALD process. To benefit from the advantages of ALD growth, it is of utmost importance to discover and operate within the designated ALD window for a particular process.

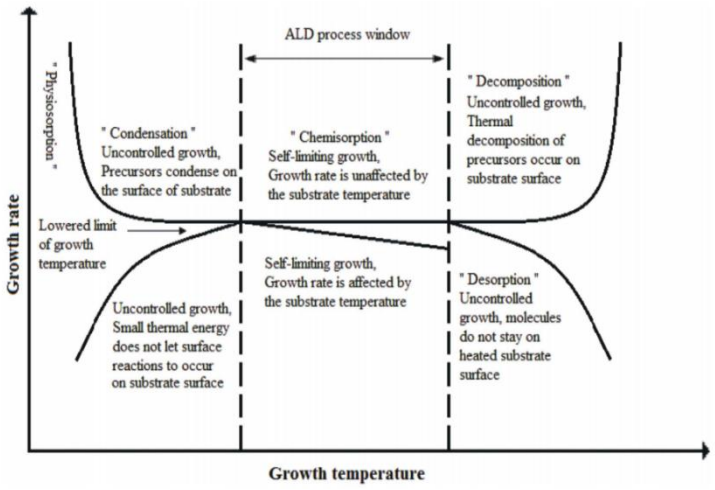

Figure 4.3: How the ALD growth process changes with temperature [50].

A second critical parameter of ALD growth is the substrate on which the growth will occur. Before ALD growth begins, the substrate must initially be

functionalised with reactive sites [51]. During the first half reaction cycle, sub-monolayer growth is achieved due to the interaction between the precursor and the reactive sites on the substrate. Once the reactive sites on the substrate are exhausted, i.e. when a sub-monolayer of material is grown from the interaction between reactive sites and the precursor, the reaction terminates. This is referred to as a self-limiting or self-terminating process. This new sub-monolayer of material provides suitable reaction sites for the reactive gas. Before and after the reactive gas is pulsed, a purge gas is used to remove excess precursor/reactive gas and unwanted by-products. The second half reaction also creates a sub-monolayer of material which is functionalised with reactive sites suitable for the precursor used initially. This is also a self-limiting process. These two half reactions produce the target thin film and are repeated for desired film thickness.

The third important parameter for ALD growth is the precursor and reactive gases used. The precursor is typically a volatile compound and both the precursor and reactive gases must saturate all available adsorption sites on the substrate to achieve a continuous sub-monolayer. This continuous sub-monolayer growth is achieved by their concentrations in the gas phase which must exceed a certain threshold value [52]. This threshold value is determined from experimental analysis of the desired film properties and the deposition rates of the film. The purging step undertaken after each half reaction cycle is critical to ensure unwanted by products and excess precursor or reactive gas molecules reach a trace level concentration. Without this reactor purging step, it is difficult to control the growth per cycle for a particular ALD process. Since ALD involves self-limiting half reactions, excess precursor/reactive gases does not react with themselves. Therefore ALD is not affected by differences in the precursor and reactant flux on the substrate in the reactor during growth. This in contrast to both chemical vapour deposition and physical vapour deposition techniques.

4.2.3 Typical ALD film growth process

A typical ALD process is based on two self-limiting half reaction cycles which are repeated n times. Each ALD cycle generally contains four steps (Figure 4.4). Precursors can be in liquid phase or solid phase and are changed to a vapour before

use by heating the precursor jackets that surround the precursor bottle. The four steps in a typical ALD cycle are;

1. Exposing the substrate to a precursor vapour

2. Purging the ALD reactor

3. Exposing the substrate to a reactive gas

4. Purging the ALD reactor

In step one; the substrate surface is exposed to a particular precursor gas. The precursor is typically a volatile compound, which consist of a metal atom with ligands attached to it. These ligands generally consist of halide (Cl or F) or organic groups (methyl or dimethylamido) [53]. The precursor of choice bounds to the surface via chemisorption. This occurs in a self-limiting manner. No further reactions are observed once the surface is covered with a sub-monolayer of precursor material. The next step involves a purge step. The reactor is purged with an inert gas. This purge step removes excess precursor and unwanted by-products. The third step involves using a reactant. This reactant vapour reacts in a self-limiting manner with the ligands of the chemisorbed precursor from step one. ALD growth relies on factors such as the precursor, the substrate and the final desired film. For example, ALD growth of Al_2O_3 occurs provided that the substrate surface is covered by hydroxyl groups (OH^-) before the Al precursor, TMA (Tri Methyl Aluminium) is pulsed for the first time. Typically ALD growth rates are quite stable which increases its reproducibility. The final step is to purge the reactor with inert gas. This removes the excess reactant gas from the previous step that did not react with the surface. Once these four steps are over, this procedure is repeated for the desired number of cycles.

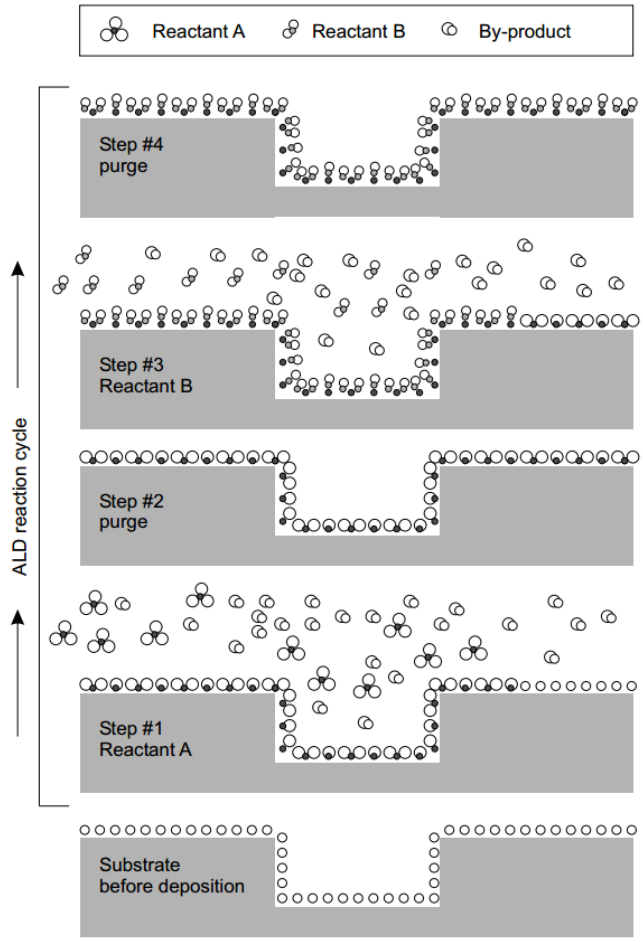

Figure 4.4: Schematic representation of one ALD cycle [38].

4.3 Physical vapour deposition techniques

Physical vapour deposition (PVD) is an atomistic growth technique whereby material is vapourised and transported through a vacuum or low pressure gaseous environment where it finally condenses on a target substrate. PVD techniques have the ability to deposit films in nanometre or micrometre range with typical deposition rates of 1 nm/s to 10 nm/s [54]. The substrates can vary in size depending on the reactor. Besides deposition of elemental materials, PVD can also deposit alloys as well as compounds using a reactive deposition process. In this process, the reaction of the depositing material with the ambient gas environment forms a compound on the target substrate. Quasi-reactive deposition is the formation of a compound material by using a partial pressure of reactive gas in the deposition chamber. For example, ITO is formed from an ITO sputtering target combined with utilising a partial pressure of an oxygen plasma in the chamber [55].

For PVD techniques, noble metals such as Au, Ag and Pt are used as materials for electrical contacts due to their low resistivity and resistance to corrosion. However the adhesion of such noble metals with regards to oxide or oxidised layers on the target substrate are poor. Before deposition of the desired metal, a thin metal layer (~ 5 to 20 nm, depending on the application) such as Ti and Cr is applied which acts as an adhesive layer [56]. The techniques of PVD described herein are vacuum deposition (evaporation) and sputter deposition. Growth models of thin films have been used to describe the mechanisms by which nucleation and crystallisation occur for thin film growth and is described in section 4.3.4.

4.3.1 Vacuum deposition (evaporation) overview

Vacuum evaporation is a commonly used deposition technique in materials science. The source material to be deposited begins as a solid and turns into a vapour. The material finally recondenses to a solid on the target substrate to be coated. The transition of the material from solid to vapour phase can be achieved by three methods: sublimation, melting and vaporisation [57]. Two common types of vacuum deposition methods are thermal evaporation and electron-beam (e-beam) evaporation. Thermal evaporation uses resistive heating to heat the deposit material, while e-beam evaporation uses a high energy electron-beam. E-beam evaporation is preferred in this work as thermal evaporation is more suitable for low melting point materials. Also during thermal evaporation, the material and the crucible (where the material is placed before evaporation) are both heated and thus impurities located in the crucible diffuse into the chamber. For vacuum deposition methods a chamber pressure of $<< 10^{-4}$ Torr is required for particles to have a long mean free path. Bombarding a target surface with high energy ions (usually inert gas ions

#for metals) can also be utilised to remove atoms through “sputtering” and deposit them onto a substrate [58].

4.3.2 Advantages and disadvantages of PVD, CVD and ALD techniques

The advantages and disadvantages of PVD techniques (thermal evaporation, e-beam evaporation and sputter deposition are included below in Table 4.3. For CVD, the low pressure CVD (LPCVD) regime is listed as this was the type of CVD system used to grow graphene in a previous chapter.

Table 4.3: Advantages and disadvantages of PVD techniques (thermal evaporation, e-beam evaporation and sputter deposition), CVD and ALD.

Deposition method:	Advantages:	Disadvantages:
ALD	-Atomic level thickness control -Conformal coatings for high aspect ratio structures -Lower temperature than CVD -Ability to coat heat sensitive materials such as polymers and bio-materials	-Slow deposition rate -Requires dry etching process rather than lift-off in most cases -Unrealistic in producing films > 50 nm due to its low deposition rate -Precursors are expensive and wasted due to non-optimisation of usage
LPCVD	-Excellent thickness uniformity and purity -Reliable/Reproducible -Homogenous layers	-Slow deposition rate -High temperatures required (~ 600 ^{o}C to 1,000 ^{o}C) -Substrate compatibility with high temperatures
Thermal evaporation	-Suitable for low melting point materials -High purity films -Less surface damage when compared to sputtering	-Use of an adhesion layer when depositing noble metals -Unable to deposit alloys effectively -Contamination from the crucible -Poor film thickness uniformity -Unable to use high melting point materials (i.e. Pt)
Electron-beam evaporation	-Able to use high melting point materials in comparison to thermal evaporation -Minimal contamination from crucible	-Use of an adhesion layer when depositing noble metals -Poor thickness uniformity (due to the electron beam being a point source)
Sputter deposition	-High thickness uniformity -Ability to deposit alloys and compounds	-Use of an adhesion layer when depositing noble metals -More surface damage when compared to evaporation

4.3.3 Zone model diagrams

To correlate the microstructure of thin films based on growth parameters, many zone structure diagrams have been proposed [59, 60]. These zone diagrams were based on studies of thin film growth with optical and scanning electron microscopy. Differing zone models were developed based on the ratio of $\frac{T}{T_m}$ in relation to the atomic level growth process and subsequent microstructures, where T is the temperature of the substrate and T_m is the melting point of the deposit. In general, coating growth occurs in three steps (Figure 4.5) [60]. The first step involves the transportation of coating species to the substrate. The second step involves the adsorption, surface diffusion and incorporation of the species into the coating or their release from the deposit material by sputtering or thermal desorption. The final step involves bulk diffusion into the substrate. The Thornton zone model (Figure 4.6), is a growth model used to describe sputter deposition in relation to the inert gas pressure, substrate temperature and melting point temperature of the deposit used during the process [61].

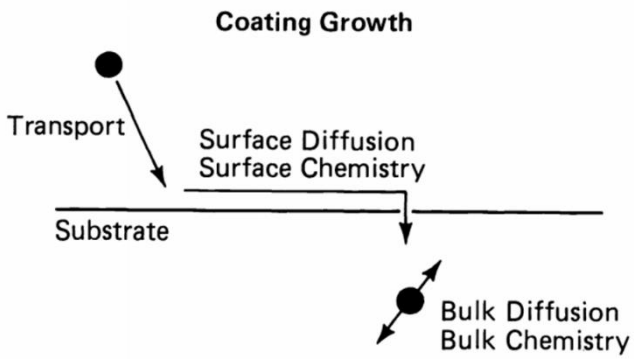

Figure 4.5: Schematic showing the three fundamental steps of deposit vapour transport, surface diffusion and bulk diffusion with regard to the condensation of a vapour during film growth [61].

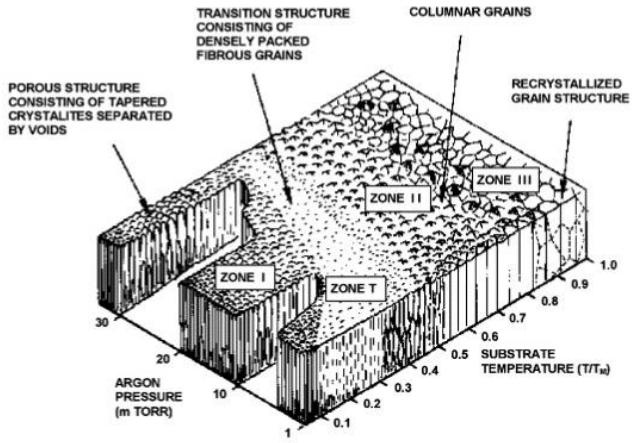

Figure 4.6: Schematic of the four zone Thornton growth model for sputter deposition which relates the inert gas pressure, substrate temperature and melting point temperature of the deposit. Each zone corresponds to a different growth mode [61].

4.3.4 Thin film growth mechanisms

Previously, the influence of growth parameters on the structure and microstructure of thin films was discussed. However, the physical mechanisms by which nucleation and crystallisation of thin films occur on target substrates is of great importance. Through studies of thin film growth by utilizing X-ray diffraction, optical diffraction and electron diffraction established that there are three main mechanisms through which nucleation and crystallisation occur [62, 63]. This three mechanisms are based on the Frank-Van der Merwe model, the Volmer-Weber model and the Stranski-Krastanov model (Figure 4.7) [64]. All three models depend on the thermodynamic parameters of the depositing material (Gibbs free energy) and the interfacial energy between adatoms (atoms that reside on a crystal surface) and the surface of the substrate itself.

For the Frank-Van der Merwe model, monolayer islands of the depositing material nucleate, resulting in a complete continuous monolayer of the deposit [62]. This process repeats so that the depositing material grows in a layer-by-layer manner. In the Volmer-Weber model, the binding energy between adatoms is greater than the interfacial energy between an adatom and the substrate. This results in the growth of discrete nuclei on the substrate surface (island like growth). A continuous layer is formed once the discrete nuclei grow in size and intersperse with each other. The last model, Stranski-Krastanov, is a mixture of the two previous models. Initial layer-by-

layer growth is observed followed by discrete island formation. Three-dimensional growth follows the layer-by-layer growth due to the lattice mismatch becoming more prominent between the substrate and depositing material as the thickness of the layer increases.

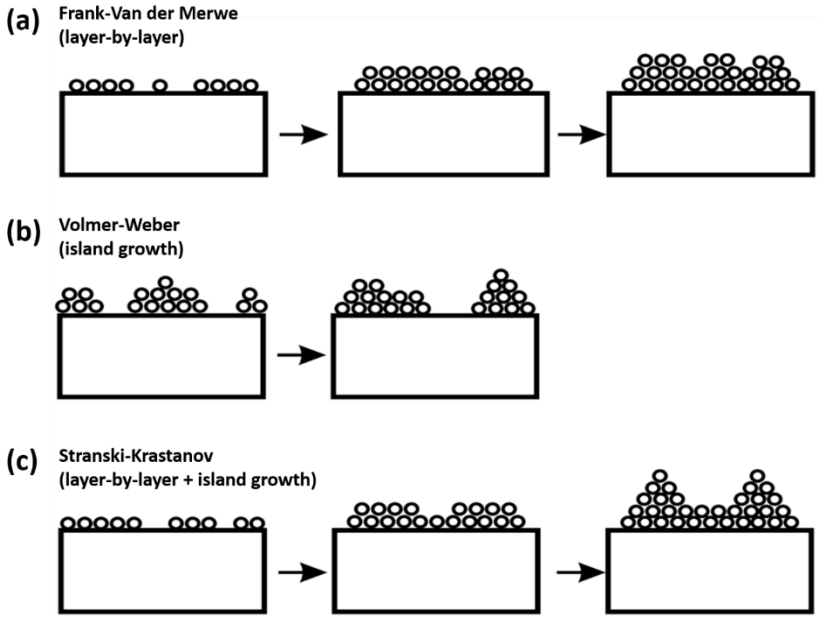

Figure 4.7: The three mechanisms of thin film growth which are (a) Frank-Van der Merwe which involves layer-by-layer growth, (b) Volmer-Weber which results in island like growth and (c) Stranski-Krastanov which is a mixture of the two previous growth mechanisms [63].

Earlier work by Young and Dupré on the relationship between adhesion and contact angles allowed Bauer to show that surface energies affect which growth mechanism occurs [62, 65]. The Young-Dupré equation can be stated as

$$\gamma_{sv} = \gamma_i + \gamma_n \cos\beta \qquad \textbf{(4.1)}$$

Where γ_{sv} is the surface energy of the substrate plane, γ_i is the interfacial energy at the planar solid-solid boundary under the island, γ_n is the surface energy of the island facet plane and β is the contact angle. A schematic of surface energies for island type growth can be seen in Figure 4.8.

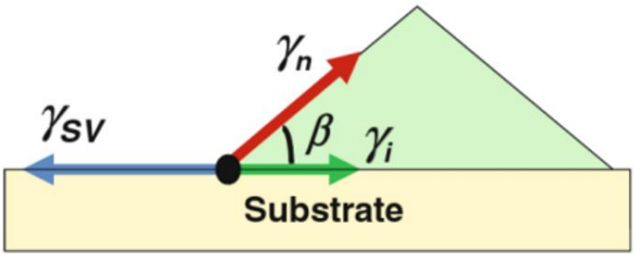

Figure 4.8: Surface energies for a Volmer-Weber growth mechanism [65].

For layer-by-layer growth (Frank-Van der Merwe model), the contact angle, $\beta = 0$ or is undefined, therefore the Young- Dupré equation becomes

$$\gamma_{sv} \geq \gamma_i + \gamma_n \tag{4.2}$$

For layer-by-layer growth, there is no way to define the contact angle, hence $\text{Cos}\theta \geq 1$. For the Volmer-Weber mechanism which results in island type growth, $0 < \text{Cos}\theta < 1$, therefore

$$\gamma_{sv} < \gamma_i + \gamma_n \tag{4.3}$$

However the intermediate case of Stranski-Krastanov growth cannot be describe easily by the Young-Dupré equation. Surface energy consideration is not sufficient to describe the growth modes stated if the deposition does not occur at thermodynamic equilibrium which is often the case. One must consider kinetic factors if this is true.

4.4 Photolithography, Lift-off and dry etching

A common technique of applying geometric patterns on substrates is by the use of photolithography [19]. The basic components of photolithography are a chrome mask which contain the patterns to be applied, photoresists (positive and negative), a mask aligner and a UV light source. Masks can be divided into two categories; a clear-field or dark-field mask which can be seen in Figure 4.9. A mask is said to be clear-field (positive) if the patterns to be developed are opaque and dark-field (negative) if the patterns to be developed are clear.

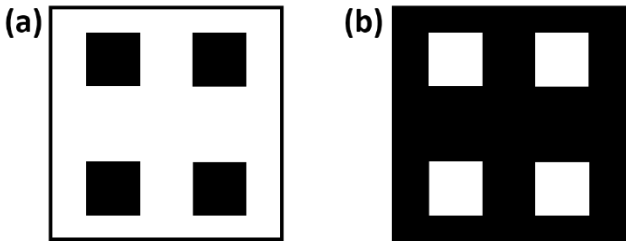

Figure 4.9: Schematics of (a) clear-field mask and (b) dark-field mask.

Four subsets of the photolithography technique in regard to optical exposure are contact, proximity, projection and immersion photolithography. Contact lithography consists of the mask being in direct contact with the resist and substrate. This technique is inexpensive compared to the other photolithography techniques, e.g. projection However, the mask can degrade due to being in direct contact with the resist and substrate. Also any particle defects on the mask are transferred to the substrate. Non-uniform resolution of applied features can also occur due to wafer bowing which causes variations of the gap size between the mask and substrate. Proximity lithography is a technique, where a small gap exists between the mask and resist (between 25 µm and 50 µm). This prevents mask degradation. Both contact and proximity lithography are limited by Fresnel diffraction [66]. Contact lithography can achieve resolutions of ~ 1 µm, while proximity limits the resolution to 5 µm. Projection lithography whereby an image of the mask is projected away from the mask and is de-magnified to a smaller image allows resolutions < 1 µm. No degradation of the mask is observed due to it being a non-contact method and particle defects from the mask are de-magnified. However, this equipment is very expensive and involves a complicated optics system. The resolution of projection lithography is given by $0.5 \times \frac{\lambda}{NA}$, where λ is the wavelength of UV light (~ 400 nm) and *NA* is the numerical aperture of the optics. Finally, immersion lithography is technique used in the manufacture of integrated circuits [67]. This technique involves the use of a liquid below the last lens with a refractive index > 1 i.e. greater than the index of air.

The two categories of photoresist are positive resist and negative resist. After UV light exposure, a latent image of the mask patterns are created where no light exposure is present for positive resists. The exposed area is soluble to resist developer. While conversely, negative photoresist leave a latent image of the mask patterns where light exposure is present. The exposed area is insoluble to resist developer. The choice

of photoresist is critical for photolithography. It has to be compatible with all materials being used on the substrate. Thickness of the photoresist is also important for generating an under-cut during lift-off or for controlling the etch rate when using dry-etching.

Oxide substrate surfaces such as SiO_2 are hydrophilic in nature due to a layer of physisorbed water on the surface from ambient humidity. This water layer causes poor resist adhesion and will allow the resist developer or etch chemicals to penetrate the resist-substrate interface and can cause unwanted undercutting or delamination of the resist [19]. Prior to applying the resist, a dehydration bake step is undertaken. However the surface is still covered by hydroxyl groups, hence the surface is still hydrophilic. A common resist adhesion promotor i.e. Hexamethyldisilazane (HMDS), consists of siloxane linkages (Si-O-Si).

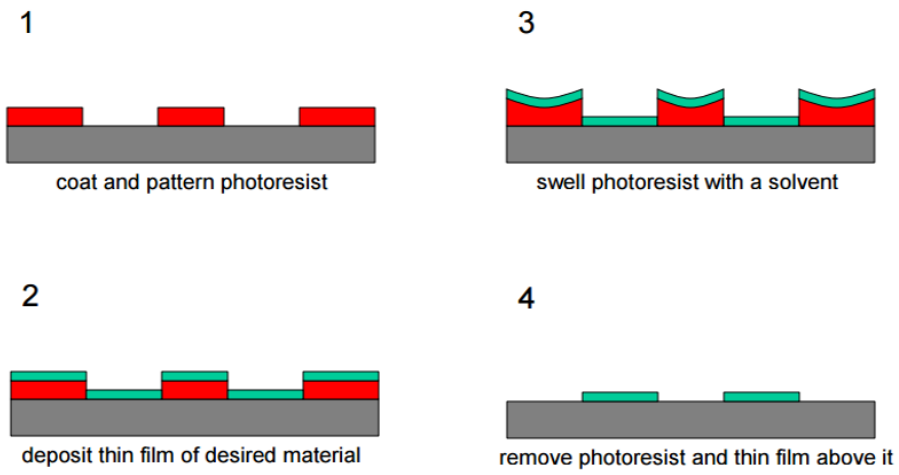

Figure 4.10: Process flow for a metal lift-off lithography process.

In a lift-off process, the photoresist forms a mould, into which the desired material is deposited (Figure 4.10). A lift-off resist such as LOR3A is applied to the substrate by spin-coating. The substrate is then placed in a Mask Aligner, which is used to align the geometric patterns on the mask followed by making contact with the substrate. The patterns are then applied by UV light exposure and resist development. The resist developer is used to create an undercut and removes resist from unwanted areas. The metal is then deposited onto the substrate via physical vapour deposition

techniques. The unwanted metal material is “lifted off” using a resist-remover such as R1165.

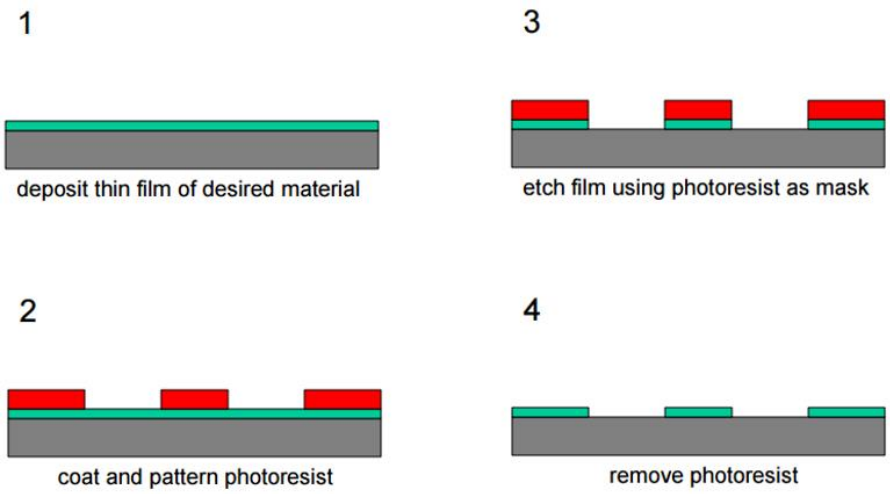

Figure 4.11: Process flow for a dry etching process.

In an etching process (wet or dry etching), the desired material is already deposited on the substrate e.g. ALD platinum. The mask forms a protective layer to the etchant. To remove the excess material, an etching method is undertaken (Figure 4.11). Wet etching involves using liquid chemicals to remove the excess metal, while dry etching involves the use of gases (usually a plasma of reactive gases such as BCl_3 mixed with an inert gas such as Ar). Etch selectivity depends on the etch rates between different materials. A wet etch of Pt can be achieved by using a chemical mixture of HCl, HNO_3 and DI water known as Aqua Regia [68]. Pt can also be dry etched by using a mixture of BCl_3 in Ar. One advantage of dry etching over wet etching is that a dry etching process typically etches anisotropically (orientation dependent) [69, 70]. This allows the patterning of very narrow lines or high aspect ratio structures. Wet etching is generally isotropic, meaning the wet etchant chemicals have a uniform etch rate in all directions. Etching rates depend on temperature, etchant concentration/gas mixture and crystallographic orientation.

4.5 Experimental methods

4.5.1 Metal thin film growth

4.5.1.1 ALD Al_2O_3 and ALD Pt thickness in relation to cycle number

To find the thickness of ALD Al_2O_3 in relation to cycle number, Al_2O_3 was grown on bare Si substrate at 90 cycles using an ALD reactor (Cambridge Nanotech Fiji system). A tri-methyl aluminium (TMA) precursor and water vapour as the reactant. The temperature of the reactor was kept constant during the process (250 ^oC). The TMA precursor pulse time was set at 0.06 s and the water vapour reaction gas pulse time was set 0.06 s. The thickness of the Al_2O_3 layer on Si was found by using an ellipsometer. To find the thickness of ALD Pt in relation to cycle number, 350 cycles of Pt was grown on an oxide layer of Al_2O_3. Firstly, an Al_2O_3 layer was grown on Si AMAT trench structures via ALD for 90 cycles using the parameters that were given at the start of this section. Once the oxide growth was completed (90 cycles in total), ALD platinum was grown using $MeCpPtMe_3$ and O_2 as the precursor and reactant gas respectively at a reactor temperature of 250 ^oC. The Pt precursor ($MeCpPtMe_3$) pulse time was set at 1 s and the oxygen reactant gas pulse time was set 60 s. To find the thickness of the ALD Al_2O_3 and ALD Pt film on the Si AMAT trench structures, cross-sectional SEM (X-SEM) was undertaken.

4.5.1.2 Growth of metal ALD thin films

To study the effect of metal thickness in relation to transmission and sheet resistance, thin metal films were fabricated using an ALD reactor (Cambridge Nanotech Fiji system). The starting substrates were 100 mm diameter, 500 µm thick borofloat-33 glass wafers which were purchased from University wafer Inc. (item #517) and four 2 cm x 2 cm Si samples from the internal fabrication facility. The substrates were loaded into the ALD chamber and the chamber was evacuated to ~ 190 mTorr. Before Pt deposition in the ALD reactor, a thin layer (~ 10 nm) of Al_2O_3 was deposited prior to the metal. This was achieved by using a tri-methyl aluminium (TMA) precursor and water vapour as the reactant. The TMA precursor pulse time was set at 0.06 s and the water vapour reaction gas pulse time was set 0.06 s. This was repeated for 90 cycles. ALD Pt growth was achieved by using $MeCpPtMe_3$ and O_2 as the precursor and reactant gas respectively at a reactor temperature of 250 ^oC. The Pt precursor pulse

time was set at 1 s and the oxygen reactant gas pulse time was set 60 s. Ar was used as the carrier gas at a flow rate of 40 standard cubic centimetres per minute (SCCM) in both ALD Al_2O_3 and ALD Pt growth. Nitrogen was used as the purge gas between precursor and reactant pulses in both cases. ALD Pt films were grown on borofloat-Al_2O_3 and Si-Al_2O_3 based on cycle number for the following thicknesses; 1 nm, 3nm, 5 nm, 8 nm, 10 nm, 15 nm, 20 nm, 30 nm and 50 nm

4.5.1.3 Growth of E-beam evaporated metal thin films

Pt thin films were grown on bare Si with a 10 nm layer of Al_2O_3 via ALD. The samples were placed in a Temescal FC2000 electron-beam evaporator chamber. Prior to metal evaporation, the chamber pressure was evacuated down to < 5 x 10^{-7} Torr. A 10 nm Ti (adhesion layer) was then evaporated at ~ 0.3 nm/s. Pt was evaporated at a rate of ~ 0.1 nm/s. The following Pt thicknesses on Si-Al_2O_3 (10 nm)-Ti (10 nm) were evaporated; 3nm, 5 nm, 8 nm, 10 nm, 15 nm, 20 nm and 50 nm.

4.6 Mask Design for lithography

Before the lithography mask with the mesh designs was created, the transparency of a mesh structure was approximated. The transparency of a metal mesh structure, T_{mesh} can be approximated as (assuming 100% opacity for the metal)

$$T_{mesh} = 1 - \frac{A_{metal}}{A_{total}} \tag{4.4}$$

where A_{metal} is the area within the unit cell covered by metal and A_{total} is the total unit cell area. For example, Ghosh *et al.* found the optimum grid spacing in relation to linewidth for a square mesh using Haacke's figure of merit [71] Φ_{TE}, followed by substituting in the formulas for the sheet resistance and transparency of a metal mesh as defined by Ghosh *et al.* [1]. Haacke's figure of merit is defined as

$$\Phi_{TE} = \frac{T^{10}}{R_s} \tag{4.5}$$

where T is the transparency of the metal grid and Rs is the sheet resistance of the grid. Assuming that the "Fill factor" (F_f) which is defined as the ratio of linewidth to pitch (grid spacing + linewidth) [1] is << 1, Newton's Binomial theorem can be applied to the function [72]. The derivative of this function was set to zero and thus the highest figure of merit (Haacke) is obtained when the grid spacing is equal to 39 times the linewidth. Taking this into consideration various square metal meshes were designed to achieve a lower transmission threshold of the mesh itself of ~ 80%. Values of $\frac{1}{F_f}$ = 10, 20, 30, 40 and 50 were used with linewidths of 1 µm, 2 µm, 3 µm, 4 µm and 5 µm (except for values of $\frac{1}{F_f}$ = 50 for 1 µm, 2 µm and 3 µm where other geometries were placed on the mask). Twenty one square designs were present on the mask in total with the smaller linewidths (1 µm, 2 µm and 3 µm) placed in the centre area of the mask to allow these smaller linewidths to be resolved more easily.

Four hexagonal designs were placed on the mask to target a lower transmission threshold of the mesh itself of ~ 75%. Three of which had a linewidth of 5 µm and an increasing hexagon height (including the hexagon base linewidth) of 50 µm, 100 µm and 150 µm. These roughly fit into the same area of corresponding square designs of linewidth 5 µm with values of $\frac{1}{F_f}$ = 10, 20 and 30. Hexagonal designs have previously been published in literature [7, 30, 73]. One of the hexagonal designs on the mask was based off a design published by Kim *et al.* with a linewidth of 1 µm and a hexagon height (excluding linewidth) of 30 µm. This design was shown to have the best figure of merit value. To this author's knowledge, no publications exist with regular circular mesh designs, therefore two designs were added with a linewidth of 5 µm and an outer diameter of 27.5 µm and 52.5 µm respectively with a lower transmission threshold target of ~ 50%.

For the last geometric design, a pentagon was chosen. However, normal pentagons (equal side lengths and equal angles between each side) cannot tile a plane. A new pentagonal design was found in 2015 by Mann *et al.* [31]. This was the first pentagon discovered in 30 years [74] and the 15th non-regular pentagon that can be repeatedly tiled so that no gaps or overlaps exist. For example, all triangles and all four sided shapes can be repeatedly tiled. However, pentagons remain an active research area in mathematics as they are the only part of the "gon" family that is not

yet fully understood. It was found in 1963 that there exists three different types of convex hexagons that can tile a plane [75]. Above that where the number of sides, n ≥ 7 (heptagon, octagon etc.), no other shapes tile a plane without leaving voids or overlaps [76]. An artist rendering of this pentagon tile can be seen Figure 4.12. Three pentagon designs were utilised on the mask, with each three having a linewidth of 5 µm and a length of side d as 25 µm, 50 µm and 75 µm. A lower transmission threshold of ~ 70% was targeted with these devices. It's thought that the use of an asymmetric metal mesh design may have the potential ability for force distribution when under strain. This becomes more apparent in the subsequent two chapters.

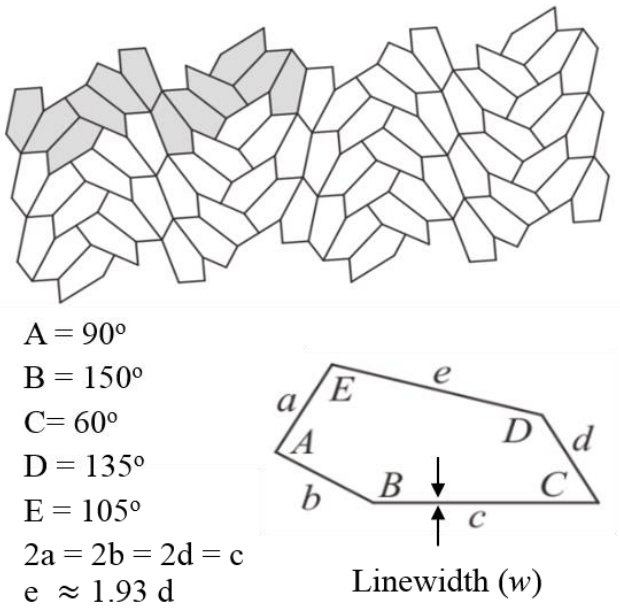

Figure 4.12: The 15th type of pentagon tiling discovered in 2015 [77].

Based on the designs proposed, each die on the mask of total size 12 mm x 15 mm, contains the mesh designs repeated to cover an area of 7 mm x 11 mm with two solid contacts either side of size 7 mm x 2 mm. To ensure the accuracy of the Van der Pauw method, which suggests having the points of probe contact as close to the edge of the sample as possible, each mesh design was repeated four times with size of 2 mm x 2 mm with contacts of size 200 µm x 200 µm at each corner. An identifier was placed on the top left corner of the die to make identification easier. A schematic of the final die design can be seen below in Figure 4.13. Derivations for the transparency of a metal mesh based on the unit cell of each geometry is given in Appendix B.

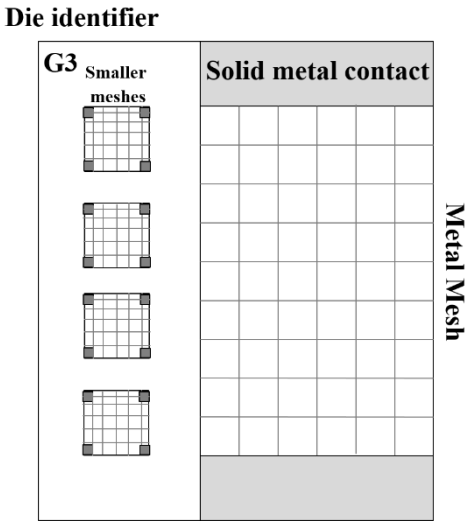

Figure 4.13: The final mesh die design for the photolithography masks which contain the die identifier, two solid metal contacts on either side of the mesh along with four smaller mesh designs (same linewidth and geometry as the larger mesh) with four small contact pads at each corner for 4 terminal (sheet resistance) measurements.

4.7 Fabrication of metal mesh structures

4.7.1 Preparation of substrates for evaporation, ALD and sputter deposition

100 mm diameter, 500 µm thick borofloat-glass 33 wafers were purchased from University wafer Inc. (item #517). To ensure lit-off resist adhesion (for e-beam evaporated meshes) to the borosilicate wafer, a thin dielectric layer was deposited prior to metal evaporation. The substrate was loaded into the ALD chamber and evacuated to ~ 190 mTorr. A ~ 10 nm layer of Al_2O_3 was applied on the borofloat glass wafer by an ALD reactor (Cambridge Nanotech Fiji system) using a tri-methyl aluminium (TMA) precursor at a constant pressure (~ 420 mTorr) and water vapour as the reactant gas at a constant temperature (250 ^oC). Ar was used as the carrier gas at a flow rate of 40 standard cubic centimetres per minute (SCCM). The TMA precursor pulse time was set at 0.06 s followed by a 10 s nitrogen purge to remove excess precursor. The water vapour reaction gas pulse time was set at 0.06 s followed by another 10 s N_2 purge. This reaction was repeated for 90 cycles until the desired thickness of Al_2O_3

was achieved (~ 10 nm). The same layer was also applied before depositing desired ALD metal for ALD based metal meshes.

4.7.2 Platinum mesh structures via evaporation[a]

The metal mesh structures were applied on the borofloat-Al_2O_3 (10 nm) wafer by UV lithography, metal evaporation and lift-off. Hexamethyldisilazane (HMDS) was spun on the wafer using a Laurell WS400 spinner at 3,000 RPM for 50 s to promote resist adhesion. LOR3A was spun on the wafer at 3,000 RPM for 50 s to produce a nominal thickness of ~ 300 nm followed by baking on a hotplate at 150 ^oC for 3 minutes. Again HMDS was applied at 3,000 RPM for 50 s followed by S1805 at 3,000 RPM for 50 s to produce desired thickness of ~ 450 nm. This was then baked at 115 ^oC for 2 minutes on a hotplate. The wafer was then placed in a Karl Suss MA1006 mask aligner for 3.5 s (exposure dose ~ 35 mJ/cm^2) using a dark-field Chrome mask (Compugraphics) containing the mesh designs. The patterns were developed using MF319 Developer for 45 s and immediately placed in DI water to stop the reaction. The wafer was then placed in a Temescal FC2000 electron-beam evaporator system. Prior to evaporation, the chamber pressure was evacuated down to < 5 x 10^{-7} Torr. Ti (adhesion layer) was then evaporated at ~ 0.3 nm/s until nominal thickness of ~ 10 nm was achieved. Pt was evaporated at a rate of ~ 0.1 nm/s until nominal thickness of ~ 50 nm. Lift-off of the metal was achieved by placing the wafer in R1165 Resist Remover at 90 ^oC followed by a DI water rinse.

4.7.3 Platinum mesh structures via ALD[b]

Appropriate training for the use of the ALD reactor was provided by Mr. Alan Blake. All Tyndall safety procedures were adhered to when operating the reactor. The surface preparation prior to metal deposition is the same as seen in section 4.7.1. After the thin Al_2O_3 layer is applied, Pt is grown by using $MeCpPtMe_3$ and O_2 as the precursor and reactant gas respectively at a temperature of 250 ^oC. Ar was used as the carrier gas at a flow rate of 40 standard cubic centimetres per minute (SCCM). The Pt precursor pulse time was set at 1 s and the oxygen reactant gas pulse time was set 60 s. A nitrogen

[a] UV lithography, metal evaporation and lift-off was carried out by Mr. Dan O' Connell and Mr. Colin Lyons in Tyndall (Speciality Product and Services group).
[b] Lithography was carried out by Mr. Dan O' Connell in Tyndall (Speciality Product and Services group). Dry etching was carried out by Mr. Alan Hydes in Tyndall (Speciality Product and Services group).

purge gas was used between precursor and reactant pulses. This reaction was repeated for 1458 cycles until the desired thickness of ~ 50 nm was achieved. The metal mesh structures were applied on the Al_2O_3 (10 nm) – Pt (50 nm) films using photolithography and dry etching. HMDS was spun on at 4,000 RPM for 50 s using a Laurell WS400 spinner. S1813 was then deposited using the same parameters. The substrate was placed on a hot plate for 2 minutes at 115 ^oC. The wafer was then placed in a Karl Suss MA1006 mask aligner for 6 s (exposure dose ~ 70 mJ/cm2) using a clear-field Chrome mask containing the mesh designs. The patterns were developed using MF319 Developer for 40 s and immediately placed in DI water to stop the reaction Dry etching was carried out using a STS Multiplex ICP etcher. The wafer was cleaved into four quarter pieces by using a diamond scribe and thin sheet of aluminium. The quarter wafer piece was placed on a ceramic carrier, held in place by the use of fomblin oil. The carrier was loaded into the instrument and the chamber was evacuated to ~ 3 x 10^{-6} Torr. Dry etching was achieved by flowing a mixture of Ar:BCl_3 (20 SCCM:10 SCCM) at a pressure of 2.5 mTorr, with a 750 W RF coil power. A camera system is in place so that the etch can be watched in real time. The etch time was between 4 and 8 minutes depending on the laser end point data and the visualisation of the etching in real time.

4.7.4 Platinum mesh structures via sputter deposition[c]

The metal structures were applied on borofloat-Al_2O_3 wafers by DC magnetron sputtering of Ti and Pt along with photolithography and dry etching (described in the previous section 4.7.3). The wafer was loaded into a Nordiko Advanced Energy NDX 2500-W Magnetron Drive RF Generator Hybrid System. The RF generator was used to complete an RF roughening step (to improve adhesion) prior to the metal sputtering process on the substrate at 1 kW for 25 minutes. Prior to metal deposition, the pressure in the chamber was ~ 4.1 x 10^{-7} Torr. Titanium was deposited at a rate of 40 Å/min until desired thickness (~ 10 nm), followed by platinum deposition at a rate of 44 Å/min until desired thickness (~ 50 nm). Dry etching was carried out by using the procedure in the previous section.

[c] Sputter deposition was carried out by Mrs. Margaret Hegarty in Tyndall (Speciality Product and Services group).

4.8 Characterisation

4.8.1 Topographical characterisation

Topographical information was found using a Veeco D3100 atomic force microscope (AFM). Measurements were taken in tapping mode with a scan speed between 0.5 Hz and 1 Hz at a resolution of 256 samples/line. Roughness measurements were taken over the same sized area. Height measurements were also taken using a Tencor P-10 Surface Profiler. A JOEL JSM-7500 F scanning electron microscope (SEM) was used to study the surface of the mesh samples. Images were taken at an accelerated voltage of 1 kV and an emission current between 5 μA and 10 μA. The screw tips on the brass sample holder were placed on the electrode pads of the mesh samples to minimize the charging effects of the underlying substrate.

4.8.2 Optical characterisation

Optical microscopy images were taken using a Leica DMRB microscope in transmission mode at 5x, 10x and 50x magnifications. Transmission measurements were taken using a Perkin Elmer Lambda 950 spectrophotometer at a wavelength, λ, range between 250 nm and 800 nm. In line with common practice, transparency values of metal mesh samples are reported at 550 nm (the midpoint of the visible electromagnetic spectrum) [1, 2, 30]. Samples were placed in a custom Teflon holder fabricated to ensure the same area of the mesh was evaluated each time. The samples were held in place with double sided tape which touched the backside of the sample (support ends). A blank measurement was always taken before starting the measurement set. Sample measurements were first taken versus blank substrate (air). To find the transparency of the mesh itself (without substrate absorbance), the sample was measured against a reference sample i.e. a Borofloat (University Wafer Inc., item # 517) glass-Al_2O_3-Pt mesh sample was measured against a borofloat-Al_2O_3 sample. Optical haze values were found by taking the transmission spectrum of each sample against air in the standard setup and by taking the same measurements using an integrating sphere. An integrating sphere allows the instrument to spatially integrate radiant flux (electromagnetic radiation transmitted or reflected from the sample). Therefore an integrating sphere setup gives transmission values which contain both

transmitted and scattered light. A typical setup is shown below (Figure 4.14). The optical haze is found by using equation (4.6) below, where T_{int} and T are the transparency values at λ = 550 nm for an integrating sphere and standard setup.

$$Haze = \frac{T_{int} - T}{T_{int}} \quad \textbf{(4.6)}$$

$$Haze = \frac{(Transmitted\ light + Scattered\ light) - Transmitted\ light}{Transmitted\ light + scattered\ light} \quad \textbf{(4.7)}$$

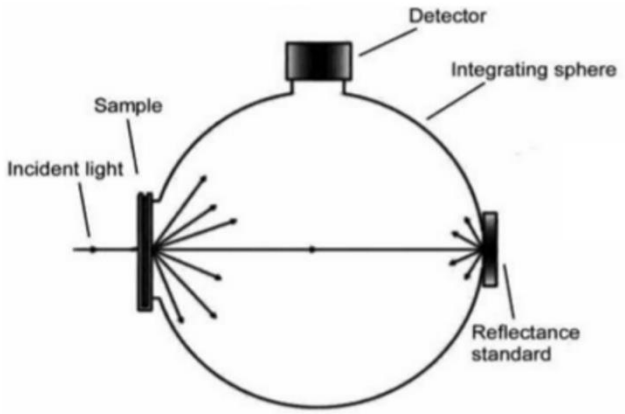

Figure 4.14: Schematic of a standard integrating sphere setup showing the sample, white reflectance standard and a photosensitive detector [78]. The transmittance of the device i.e. specular transmittance is measured directly opposite the sample. The total transmittance (transmitted and scattered light) is measured using the detector at the top of the schematic. The haze value is the ratio of the difference between total and specular transmittance to total transmittance.

4.8.3 Electrical Characterisation

The electrical surface properties of a film is measured in sheet resistance denoted by R_s, and has the units of Ω/sq. The resistivity of a film is given by

$$\rho = R_s . t \quad \textbf{(4.8)}$$

where ρ is the resistivity and t is its thickness. By definition, intrinsic properties of materials such as resistivity and conductivity should be constant and independent of size for bulk materials. However, this is not the case for thin films. The electrical conductivity of a metal thin film is affected as soon as its thickness becomes comparable to that of the electronic mean free path [79]. An electron mean free path of 23 nm for platinum has been measured at room temperature [80]. The resistivity of thin metal films is larger than that of bulk values. As the thickness of the metal increases, the resistivity decreases to that of bulk.

Electrical characterisation was carried out by using both 2-terminal and 4-terminal probe methods. An automated 4-probe system was used for ALD thin films and a manual prober was used for metal mesh structures. For both automated and manual 4 terminal probe measurements, the Van der Pauw method of finding the sheet resistance of an arbitrary shape was used [81]. An in-line 4 terminal probe system is depicted in Figure 4.15.

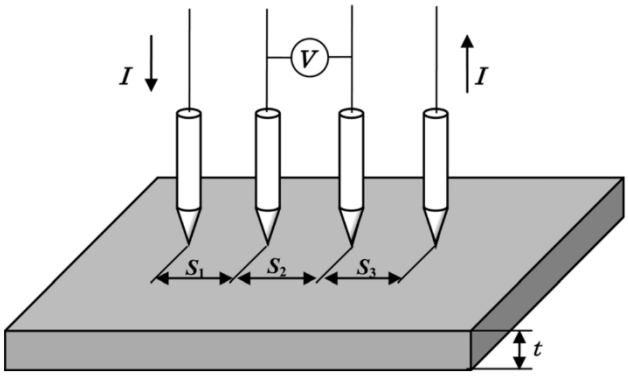

Figure 4.15: A schematic of an automated 4 terminal probe system on a material of thickness, *t*, showing the equidistant nature of the probes [82].

Note that the there is an equidistant separation between each probe. The method depicted in Figure 4.15 was not used to measure the sheet resistance in this thesis as it only measures the sheet resistance in the direction of the four probes. While the average sheet resistance is measured over all directions for the standard Van der Pauw method. To ensure the accuracy of the Van der Pauw method for the manual system,

it is essential to have the metal contacts as close to the corners of the sample as possible as discussed previously. There are 8 configurations in total containing vertical and horizontal resistance measurements along with reverse polarity. For example $R_{12,43}$ means applying a current in the direction of terminal 1 to 2 and measuring the corresponding voltage change on the other two terminals as shown in Figure 4.16.

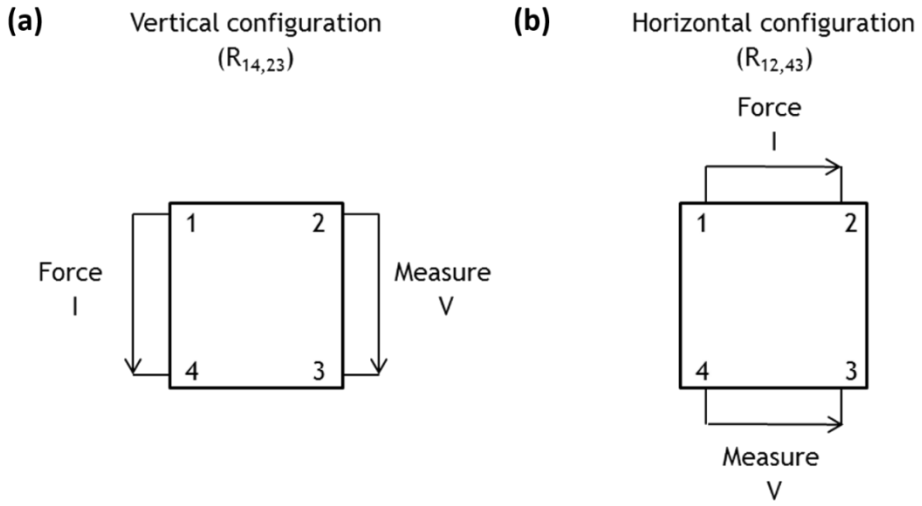

Figure 4.16: Example schematics of the Van der Pauw method for (a) 4 terminal vertical resistance measurements & (b) 4 terminal horizontal resistance measurements where the notation is given as $R_{I,V}$.

The values of horizontal and vertical resistances, are related to *Rs* by the Van der Pauw formula

$$e^{-\left(\frac{\pi R_{vertical}}{R_s}\right)} + e^{-\left(\frac{\pi R_{horizontal}}{R_s}\right)} = 1 \qquad \textbf{(4.9)}$$

where $R_{vertical}$ and $R_{horizontal}$ are the averaged vertical and horizontal resistance values. To find the value of R_s, the sheet resistance of metal film is given as

$$R_s = \frac{R_{average}\,\pi}{ln2} f \qquad \textbf{(4.10)}$$

where

$$R_{average} = \frac{R_{horizontal} + R_{vertical}}{2} \qquad \textbf{(4.11)}$$

and *f* is the Van der Pauw correction factor which is the ratio of the horizontal to vertical 4 terminal resistance. If this ratio was bigger than one, the corresponding value of *f* was found from literature [83].

Automated electrical measurements were taken using a TENCOR Prometrix Omnimap RS35e in air with a probe separation of ~ 1.016 mm. The wafer flat was placed away from the machine in all cases. 48 measurements were taken around the center of the wafer. Manual 2-terminal and 4-terminal electrical measurements were performed at room temperature under ambient conditions using an Agilent E5270B parameter analyser interfaced to a LakeShore Desert TTPX probe station (10 mV – 200 mV bias voltage range). Resistance values for individual configurations were extracted from linear regression of measured current voltage data, which also provided a calculated fractional error (LINEST function in Excel). The total fractional error in each 4-probe resistance measurement, $\frac{\Delta R_T}{R_T}$, was found summing the fractional errors for each of the 8 measurement configurations.

4.9 Results and discussion

4.9.1 Thin film growth

Prior to development of the patterned meshes, a growth study for atomic layer deposition of Pt was undertaken to assess its suitability as a catalyst for graphene and as a transparent conductive electrode.

4.9.1.1 Estimation of ALD Al_2O_3 and ALD Pt thickness

To find the thickness of Al_2O_3 in relation to cycle number, 90 cycles of Al_2O_3 was grown on Si using an ALD reactor as described in section 4.5.1.1. The thickness of Al_2O_3 was calculated to be ~ 10 nm using ellipsometry measurements. Unfortunately, the ellipsometer did not have an accurate model for ALD Pt deposited on Si. Following 90 cycles of Al_2O_3 growth, ALD Pt (350 cycles) was grown on a trench structure (provided by James Connolly, Applied Materials – AMAT). Cross-sectional SEM (X-SEM) measurements on a mechanically cleaved sample out yielded a net thickness ~ 12 nm of Pt (Figure 4.17) (using previous knowledge of 90 cycles of Al_2O_3 ~ 10 nm). This corresponds to an average growth per cycle (GPC) ~ 0.3 Å/cycle (including

incubation cycles for nucleation). GPC values in the range ~ 0.45-0.8 Å/cycle have been reported in literature for ALD Pt films deposited at 250 °C [84-86].

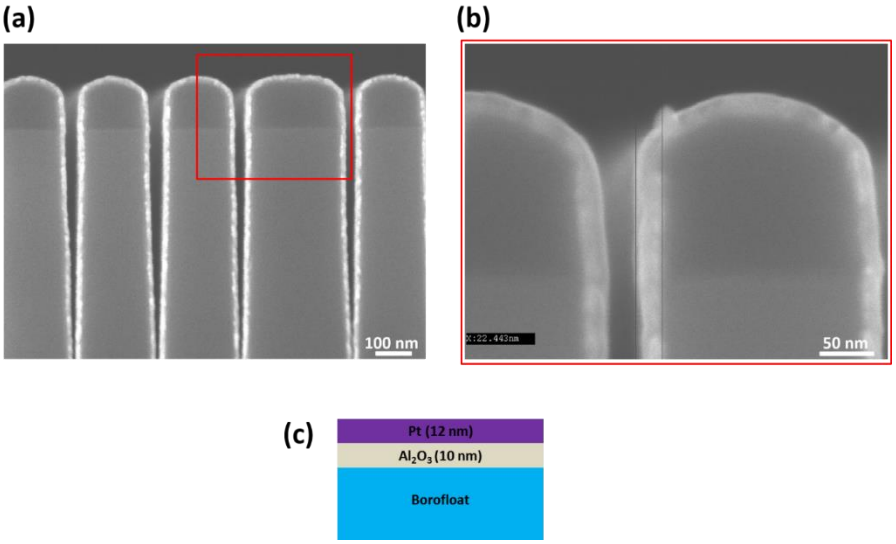

Figure 4.17: (a) SEM image of AMAT trench sample coated with 90 cycles of Al_2O_3 and 350 cycles of Pt, (b) zoomed SEM region showing the combined thickness of Al_2O_3-Pt as ~ 22 nm and (c) layer stack of the sample depicting the thickness of Al_2O_3 and Pt on borofloat.

4.9.1.2 Growth of metal ALD films

ALD Pt films with nominal thicknesses of 1 nm, 3 nm, 5 nm, 8 nm, 10 nm, 15 nm, 20 nm, 30 nm, 40 nm and 50 nm were grown on borofloat glass coated with 10 nm ALD Al_2O_3 for optical transparency and AFM measurements. Films were also grown on Si (native oxide) coated with 10 nm ALD Al_2O_3 for SEM inspection and manual 4 probe measurements. For two (nominal) thicknesses (5 nm and 20 nm), control samples were also prepared on bare substrates, i.e. without the 10 nm ALD Al_2O_3. After each growth run, the sheet resistance (R_s) value of the film was measured in air (on borofloat) using a 4-terminal automated prober in the Block A cleanroom. Measurements were taken at multiple locations around the centre of the wafer. Films with nominal thickness < 8 nm did not yield measurable sheet resistances, suggesting discontinuous films (see Table 4.4). The difference in opacity of the increasing thickness of Pt can be seen in Figure 4.18 below.

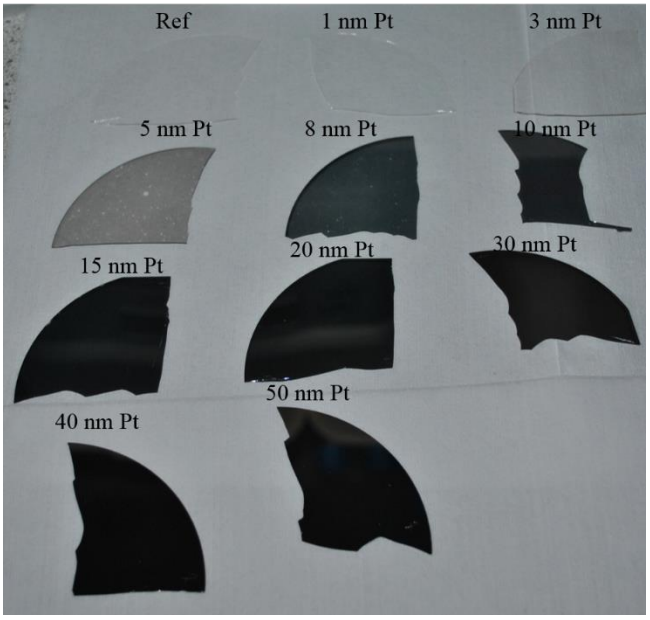

Figure 4.18: Photo of borofloat-Al_2O_3 (10 nm) reference sample and varying thickness of ALD Pt grown on borofloat-Al_2O_3 showing the increase in opacity as the Pt thickness is increased.

Transmission spectra were measured for each sample versus air and also versus a reference sample (borofloat glass with 10 nm Al_2O_3 or borofloat glass for the control samples) (Figure 4.19). The data for the 1 nm nominal thickness and the 5 nm control sample (no Al_2O_3 underlayer, see also photo in Figure 4.20) are close to the measurement limit of the instrument suggesting little or no growth. The transmittance spectrum for the 3 nm (nominal) film shows a measurable response at lower wavelengths, suggesting growth of isolated islands.

The transmission spectra of the 5 nm and 20 nm films with and without Al_2O_3 underlayers show substantially different behaviours and indicate challenges nucleating Pt films on bare glass. Using the wavelength value of 550 nm, the transmission values of the 5 nm Pt film with and without the Al_2O_3 layer are ~ 74% and ~ 99.6% respectively. The transmission values of the 20 nm Pt film with and without the Al_2O_3 layer are ~ 5% and ~ 14% respectively. The transmission differences for these films can also be clearly seen by eye (photos in Figure 4.20).

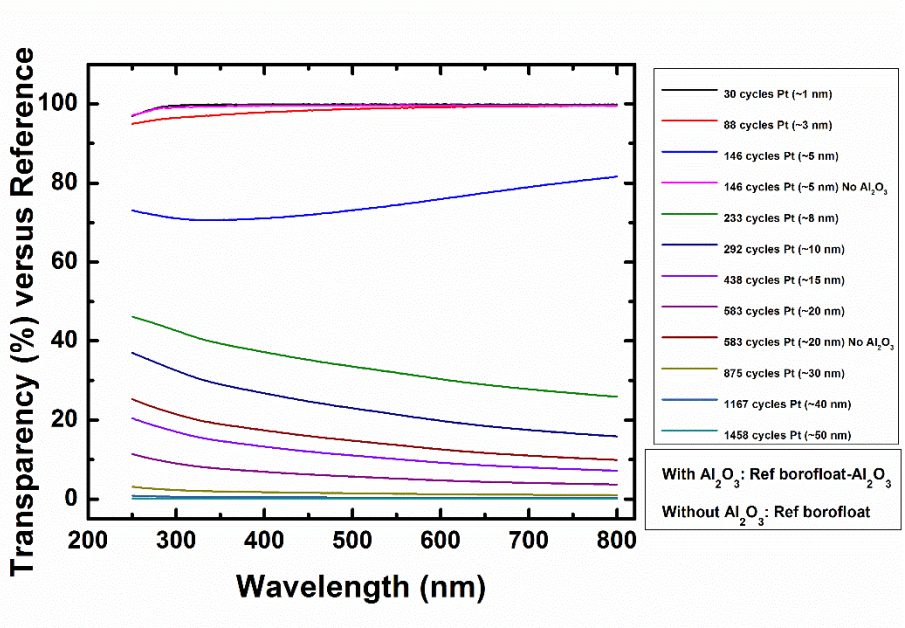

Figure 4.19: Transparency versus reference sample for varying ALD Pt thickness on borofloat-Al_2O_3 (reference sample of borofloat-Al_2O_3) and borofloat (reference sample of borofloat).

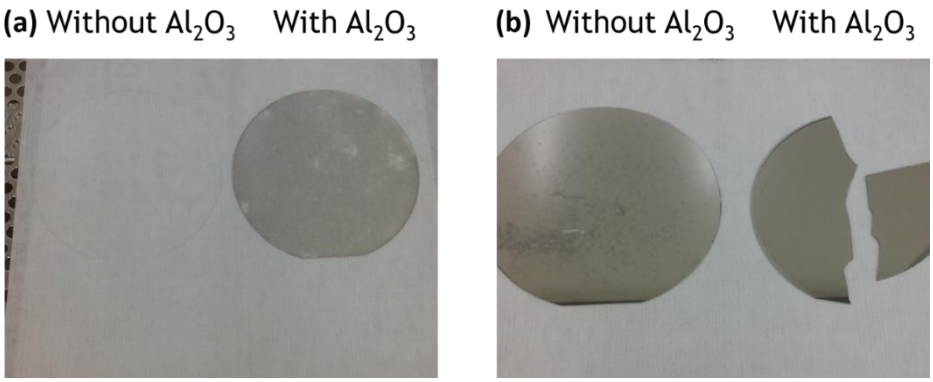

Figure 4.20: Photos showing the difference in (a) 5 nm Pt film with and without an Al_2O_3 layer and (b) 20 nm Pt film with and without an Al_2O_3 layer clearly showing the larger opaque nature of films with the thin dielectric layer.

The sheet resistance values of the films (on Si with native oxide) were also measured with a parameter analyser interfaced to a vacuum probe station to compare to the figures achieved using the 4 terminal probe in the Si fab (on borofloat). These measurements were performed using the Van der Pauw method. One of the main criteria of this technique is that the probes are placed as close to each corner of the sample (~ 1.5 cm x 1.5 cm) as possible [129]. There was no discernible difference in

sheet resistance values when measurements were taken under vacuum and in air. Good agreement was found between the two sets of sheet resistance measurements (Figure 4.21) for film thicknesses above 8 nm. The 1 nm, 3 nm and 5 nm samples yielded noise-level currents (< 1 pA) for bias voltages up to 10 V. The resistivity of the ALD platinum thin films can be estimated by using equation (4.8). The estimated resistivity values for ALD Pt thin films for both automated and manual measurements are given in Table 4.4.

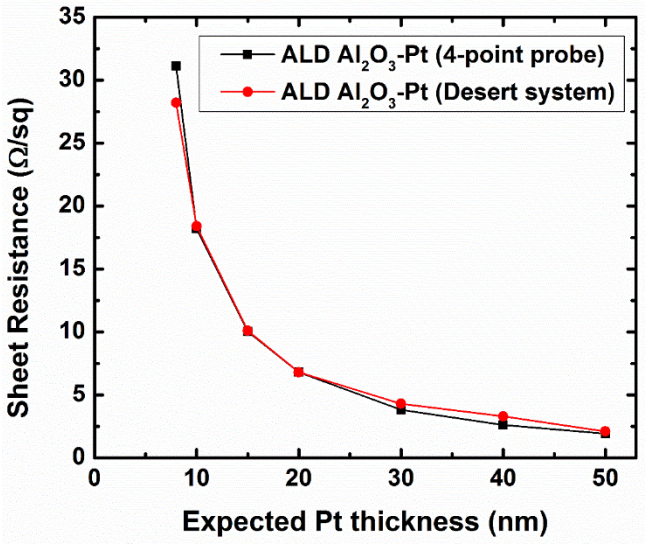

Figure 4.21: Plot of sheet resistance versus expected Pt thickness comparing values measured using the automated 4 terminal prober in the Si fab (growth on borofloat) and the Desert system (growth on Si with native oxide).

Table 4.4: Sheet resistance (automated and manual), estimated resistivity values (equation (4.8)) and % transparency (at a wavelength of 550 nm versus air and versus reference sample) of differing ALD Pt thicknesses (ALD cycle number). The dash (-) indicates unmeasurable data.

Al_2O_3 Thickness (nm):	No of ALD cycles:	Expected Pt thickness (nm):	R_s (automated) (Ω/sq):	R_s (Manual) (Ω/sq):	Estimated ρ (automated) (μΩcm):	Estimated ρ (Manual) (μΩcm):	T_{film} (%)[a]:	T_{total} (%)[b]:
10	30	1	-	-	-	-	99.9	92.7
10	88	3	-	-	-	-	98.9	91.9
10	146	5	-	-	-	-	74.4	69.1
0	146	5	-	-	-	-	99.6	92.9
10	233	8	31.1	29.6	25	24	32	29.7
10	292	10	18.2	18.9	18	19	21.4	19.9
10	438	15	10	10.3	15	15	10.1	9.4
10	583	20	6.8	6.8	14	14	5.2	4.8
0	583	20	13.2	13.1	26	26	13.7	12.7
10	875	30	3.8	4.3	11	13	1.4	1.3
10	1167	40	2.6	3.3	10	13	0.4	0.3
10	1458	50	1.9	2.1	10	11	0.1	0.1

[a]Transparency of the Pt thin film itself (without substrate absorbance) at a wavelength, λ, of 550 nm. [b]Transparency of the Pt thin film including the effect of the substrate at λ = 550 nm.

SEM data were acquired for the 5 nm (nominal) Pt thickness films grown on Si-SiO_2 (native)-Al_2O_3 and also Si-SiO_2 (native); see Figure 4.22. While both samples show evidence of island-like growth, the sample with the Al_2O_3 underlayer shows larger islands and a greater degree of coalescence, in agreement with the optical transmittance measurements from samples deposited on glass/Al_2O_3 and glass (control).

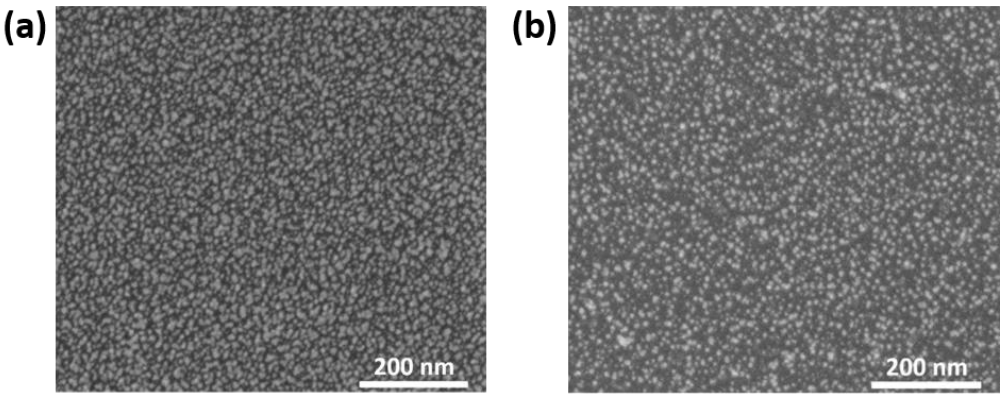

Figure 4.22: (a) SEM image of 5 nm ALD Pt on Si (native oxide) - Al_2O_3 (10 nm) (b) SEM image of 5 nm ALD Pt on Si (native oxide).

AFM and SEM data acquired for the 20 nm nominal Pt thickness show similar behaviour (see Figure 4.23 and Figure 4.24). The AFM data for the film with the Al_2O_3 underlayer (1 µm x 1 µm scan, Figure 4.23 (a)) show a smooth coalesced film with RMS roughness (averaged over six scans) of 1.0 ± 0.8 nm. By contrast, the film without the Al_2O_3 underlayer (Figure 4.23b) shows more evidence of island-like growth with island heights ranging from 5 nm to 17 nm (Figure 4.24) and RMS roughness of 2.6 ± 1.8 nm.

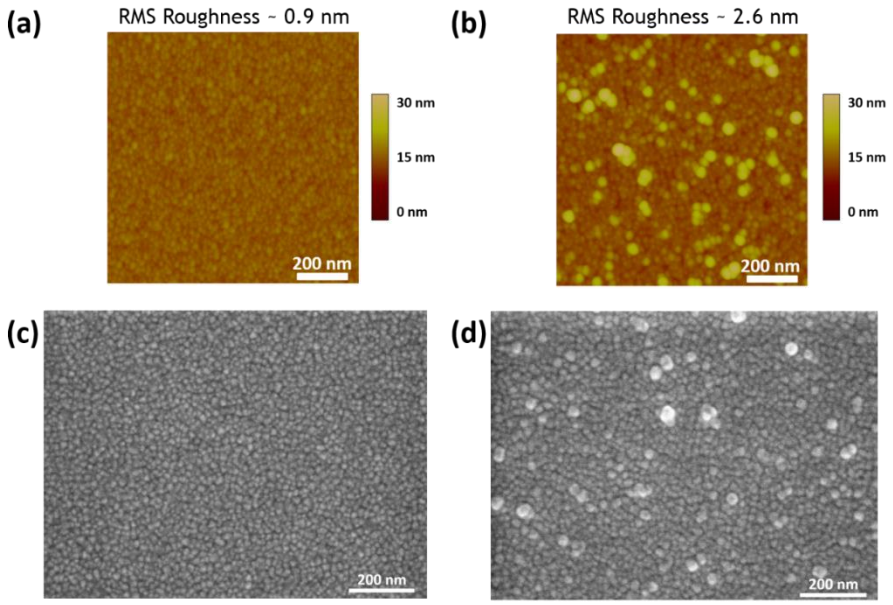

Figure 4.23: (a) 1 µm x 1 µm scan of 20 nm ALD Pt on borofloat-Al_2O_3 (10 nm), (b) 1 µm x 1 µm scan of 20 nm ALD Pt on borofloat. (c) SEM image of 20 nm ALD Pt on Si (native oxide) - Al_2O_3 (10 nm), (d) SEM image of 20 nm ALD Pt on Si (native oxide).

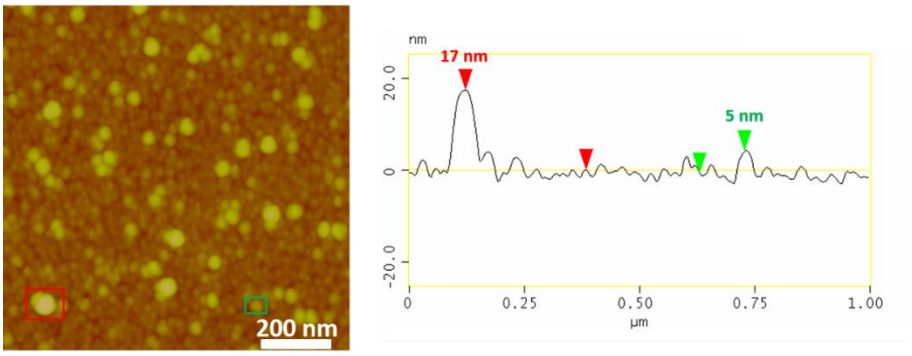

Figure 4.24: (a) 1 µm x 1 µm scan of 20 nm ALD Pt on borofloat showing the presence of particles with heights of 5 nm and 17 nm.

SEM images were acquired for ALD Pt on Si(native oxide)-Al_2O_3 with nominal thicknesses of 3 nm (Figure 4.25 (a)), 5 nm (Figure 4.25 (b)), 8 nm (Figure 4.26 (a)), 10 nm (Figure 4.26 (b)),, 15 nm (Figure 4.27 (a)), 20 nm (Figure 4.27 (b)) and 50 nm (Figure 4.28). The data set highlight the various stages of film growth: island nucleation, growth and coalescence. For example, the mean island diameter (3 images, 10 measurements each) for the 3 nm nominal Pt thickness sample (Figure 4.25 (a)) was 12 ± 2 nm. For the 5 nm Pt film (Figure 4.25 (b)), the mean diameter was measured as 19 ± 4 nm.

Taken together, the data indicate high-quality Pt films can be grown by ALD with continuous films formed for nominal thicknesses of 8 nm or more (estimated based on the measured thickness of a 12 nm Pt film). Multiplying the measured sheet resistance values with the nominal thickness yields resistivity estimates. The resistivity changes with thickness (equation (4.8)). For example, films < 8 nm are discontinuous and lead to a higher resistivity value compared to bulk films. When the thickness increases above 8 nm, the film becomes more continuous i.e. grain coalescence occurs and leads to a reduction of the resistivity. For film thickness > 8 nm, the resistivity might vary with thickness due to the presence of cracks on the film surface which act as carrier scattering sites. Estimated resistivity values range from ~ 25 µΩcm for the 8 nm film to ~ 14 µΩcm for the 20 nm film and to ~ 11 µΩcm for the 30 nm film (i.e. approaching resistivity of bulk Pt e.g. ~ 11 µΩcm), see Table 4.4. Resistivity estimates for ALD Pt films were similar for both 4 terminal automated (measured in air, probe separation ~ 1.016 mm) and 4 terminal manual (measured in air, probe separation ~ 15 mm) measurements. These results compare very favourably

with previously reported resistivity values for electrodeposited polycrystalline Pt nanowires ~ 70 nm diameter (~ 33 μΩcm) and nanowires formed by decomposition of a Pt precursor using a focused ion beam (~ 2200 μΩcm) [87].

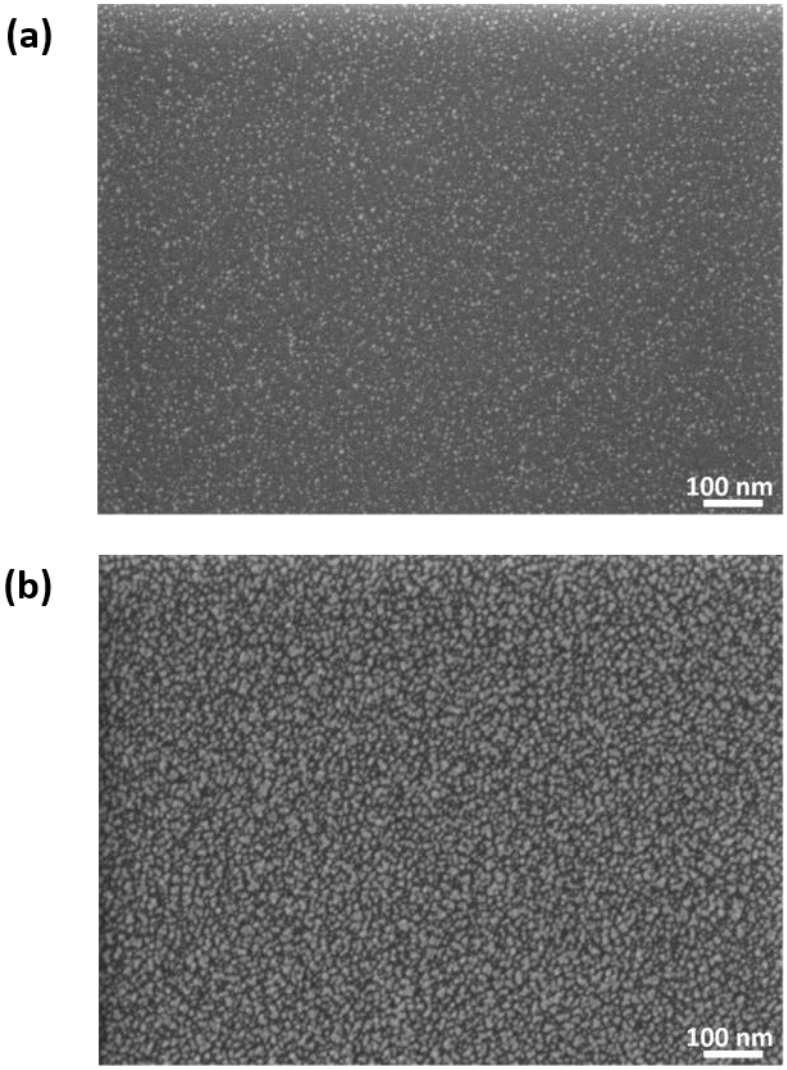

Figure 4.25: SEM images of borofloat-Al_2O_3 with Pt thicknesses of (a) 3 nm and (b) 5 nm.

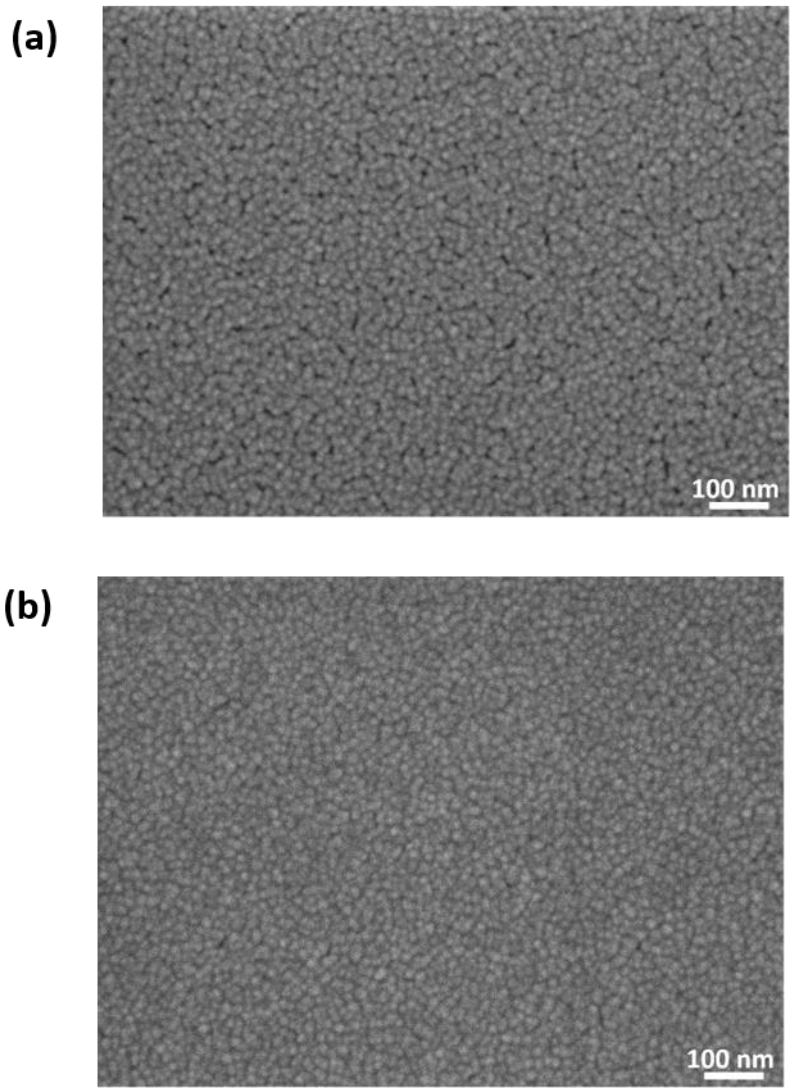

Figure 4.26: SEM images of borofloat-Al_2O_3 with Pt thicknesses of (a) 8 nm and (b) 10 nm.

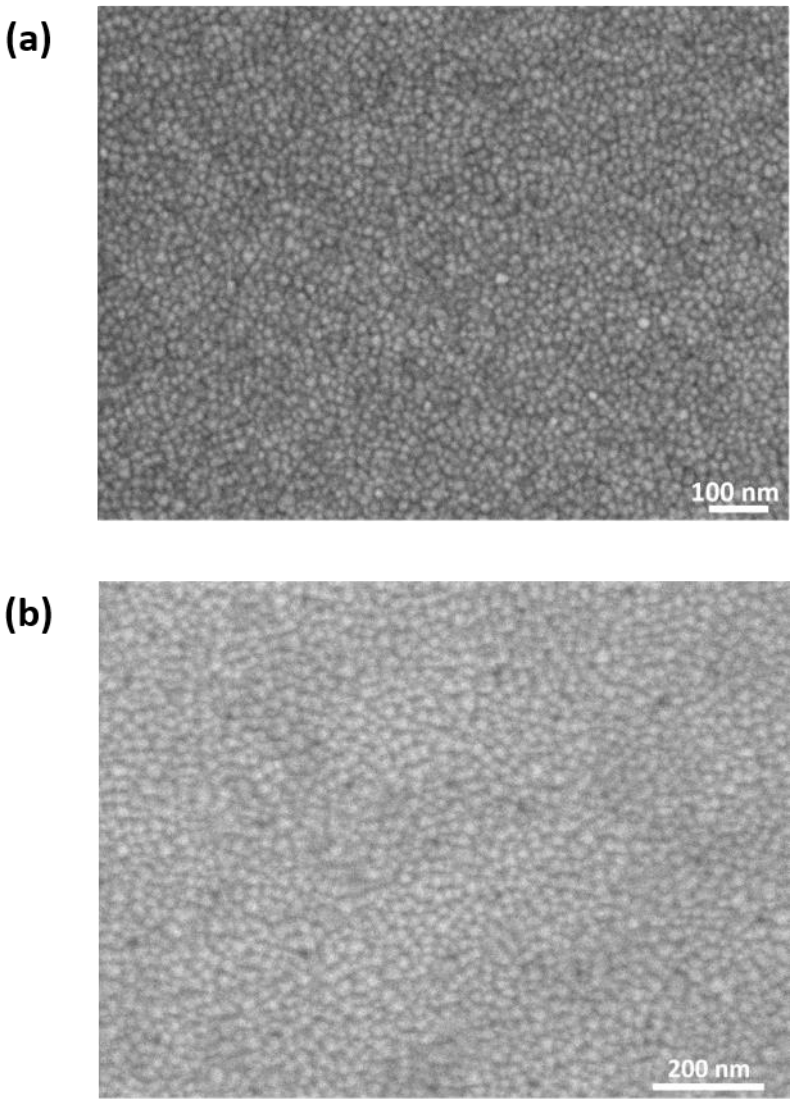

Figure 4.27: SEM images of borofloat-Al_2O_3 with Pt thicknesses of (a) 15 nm and (b) 20 nm.

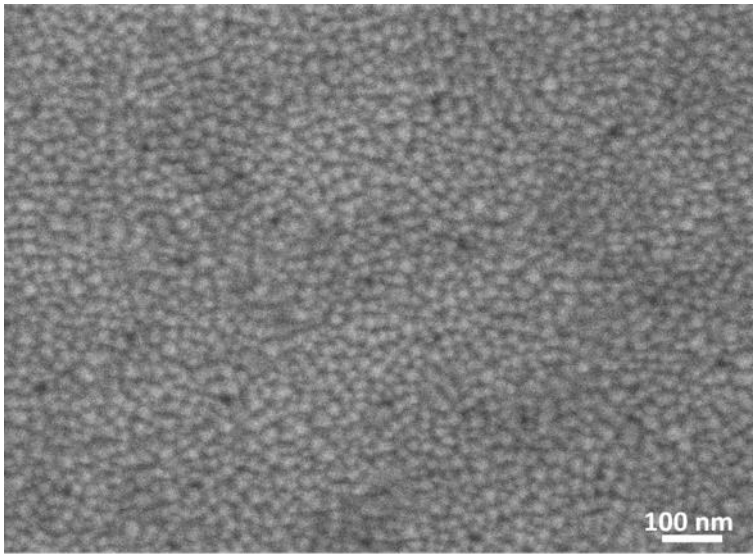

Figure 4.28: SEM image of borofloat-Al_2O_3 with a Pt thicknesses of 50 nm.

4.9.1.3 Growth of E-beam evaporated Pt thin films

Pt thin films with a 10 nm Ti adhesion layer were grown on Si-Al_2O_3 (10 nm) as described in section 4.5.1.3. SEM image of a 50 nm Pt film on Si-Al_2O_3 (10 nm)-Ti (10 nm) is shown in Figure 4.29. Note that lower Pt thicknesses ($\leq$ 20 nm) are not shown. The use of a conducting Ti layer underneath the Pt made it very difficult to create a contrast on the SEM to observe the Pt grains correctly. The sheet resistance of the films were found by using the same method for manual measurements as in section 4.9.1.2.

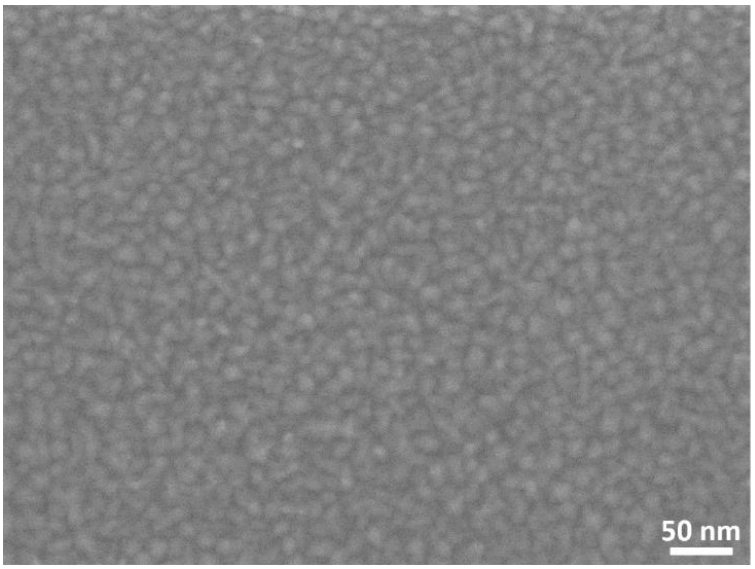

Figure 4.29: SEM image of a Ti (10 nm)/Pt (50 nm) film on Si-Al_2O_3 (10 nm).

The sheet resistance of the Pt film itself was estimated by assuming that the Ti and Pt layers behave as resistors in parallel. Using equation (4.12) below, approximate values for the sheet resistance of the Pt films were found. A ~ 10 nm Ti layer was evaporated onto Si-Al_2O_3 (10 nm) to find the film's sheet resistance value (measured as ~ 117.3 Ω/sq). All values for sheet resistance are given below in Table 4.5.

$$\frac{1}{R_{s,Total}} \approx \frac{1}{R_{s,Ti}} + \frac{1}{R_{s,Pt}} \qquad \textbf{(4.12)}$$

Table 4.5: Total sheet resistance values of evaporated Ti:Pt films, sheet resistance values of the evaporated Pt films (equation **(**4.12)) when removing the influence of the 10 nm Ti layer on the sheet resistance and the resulting resistivity values (equation (4.8)).

Ti Thickness (nm):	Expected Pt thickness (nm):	Total R_s of Ti:Pt (Ω/sq):	R_s of Pt (Ω/sq):	Expected ρ of Pt (μΩcm):
10	3	69.8	172.6	52
10	5	43.9	70	35
10	8	24	30.2	24
10	10	18.5	22	22
10	15	11.5	12.7	19
10	20	8.1	8.8	18
10	50	3	3	15
10	-[a]	117.3	-	-

[a]Dash (-) indicates the absence of Pt evaporation.

As for the ALD Pt films, the resistivity can also be estimated using equation (4.8) for evaporated Pt. The resistivity values range from ~ 24 μΩcm for the 8 nm evaporated Pt film to ~ 18 μΩcm for the 20 nm film and to ~ 15 μΩcm for the 50 nm film, i.e. decreasing to bulk Pt resistivity (see Table 4.5) Thus, the resistivity values for the evaporated Pt films compare favourably with the ALD Pt films. The sheet resistance of the 10 nm Ti adhesion layer is ~ 117 Ω/sq which corresponds to ~ 117

μΩcm. This value represent an upper bound as a TiO_2 layer readily forms when Ti is exposed to air.

4.9.2 Metal meshes for transparent electrodes

Titanium (adhesion layer, nominal thickness of 10 nm):Platinum (nominal thickness of 50 nm) meshes were fabricated on 0.5 mm thick borofloat glass substrates either by evaporation and lift-off (section 4.7.2), ALD and dry etching (section 4.7.3) or sputter deposition and dry etching (section 4.7.4). In all cases a 10 nm Al_2O_3 layer was deposited on the borofloat glass wafers before metal deposition (section 4.7.1). In the case of evaporated and sputtered meshes, a 10 nm Ti adhesion layer was applied before the Pt layer. Transmission optical images (10x magnification) of Pt meshes by lithography, evaporation and lift-off with metal linewidths of 5 μm are shown below in Figure 4.30 for square (19% metal area coverage), hexagonal (22% metal area coverage), circular (47% metal area coverage) and pentagonal meshes (27% metal area coverage).

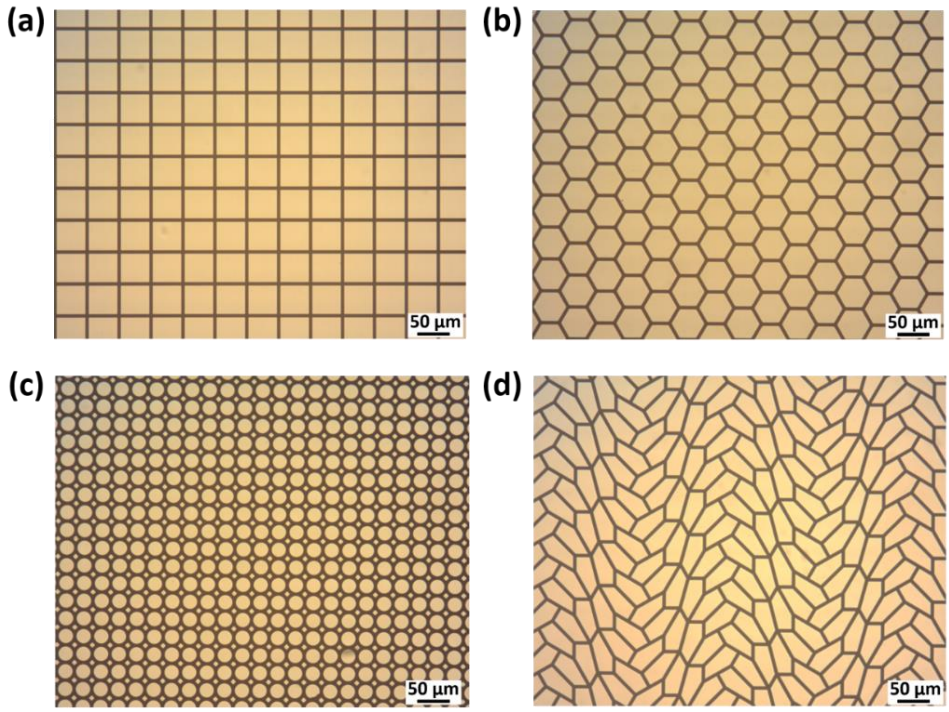

Figure 4.30: Transmission mode optical images (10x magnification) with metal linewidths of 5 μm of (a) square mesh (19% metal area coverage), (b) hexagonal mesh (22% metal area coverage), (c) circular mesh (47% metal area coverage) and (d) pentagonal mesh (27% metal area coverage) by electron beam evaporation of Ti (adhesion layer, nominal thickness of 10 nm) and Pt (nominal thickness of 50 nm).

4.9.2.1 Transmission spectra and haze of rigid reference substrates

Transmission spectra were taken of the reference samples before each corresponding measurement set (Figure 4.31). The 0.5 mm thick borofloat substrate yielded a transparency value of ~ 92.3% at a wavelength of 550 nm. The inclusion of a 10 nm film of Al_2O_3 on the borofloat resulted in a minimal loss of transparency of < 1% (T ~ 92%). The optical haze value of the borofloat substrate was quite low < 1% and stayed below 1% even with the inclusion of the 10 nm Al_2O_3 film.

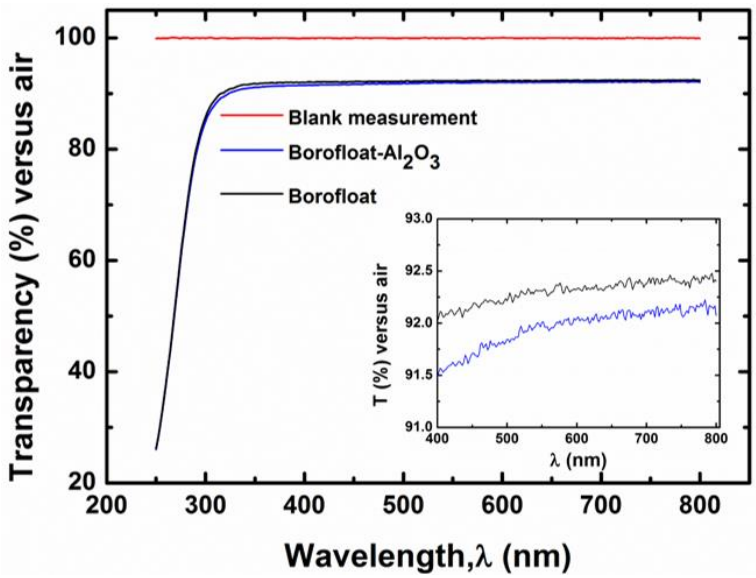

Figure 4.31: (a) Transparency versus wavelength of rigid substrates i.e. a blank measurement (air), borofloat and borofloat-Al_2O_3. (Inset) Zoomed in transmission plot of borofloat and borofloat Al_2O_3.

4.9.2.2 Measured transparency values versus expected values

To ensure the accuracy of the derivations of the unit cell for each shape, the measured transparency values (T_{mesh}, measured against reference substrate) were compared to the derived values (T_{ideal}) for devices fabricated by lithography, metal evaporation and liftoff. Measured transparency values of the square meshes (linewidths ranging from 1 µm to 5 µm) were always slightly below the ideal values, T_{ideal} - $T_{mesh} \leq 4\%$. This discrepancy could arise from patterning effects (e.g., rounded corners in square meshes (see Figure 4.32 (a)), as well as processing residue on the substrates. For example, AFM data (Figure 4.32 (a)) show particulates on the substrate, likely due to

liftoff residue. The measured transparency values of the other geometric designs (circles, hexagons and pentagons) showed similar behavior (T_{ideal} - $T_{mesh} \leq 4\%$).

4.9.2.3 Surface comparison of evaporated, ALD and sputtered Pt meshes and its effect on sheet resistance, transparency and haze

To make a comparison between the three types of deposition/patterning methods, AFM and SEM analysis were undertaken on a square mesh (2 µm linewidth, 5% metal area coverage) for each deposition method. AFM images were taken at a scan size of 5 µm x 5 µm and 10 µm x 10 µm at a scan speed of 0.5 Hz for measurements on the mesh and substrate respectively. Roughness measurements on the regions of glass/Al_2O_3 substrate for each sample type were calculated using a box size of 2.5 µm x 2.5 µm. The evaporated mesh sample (Figure 4.32 (a)) yielded the smoothest surfaces of the three deposition methods for both the metal lines and the substrate, although some nanoscale particulates can be observed in the AFM image. The substrate RMS roughness value was 1.7 ± 0.2 nm.

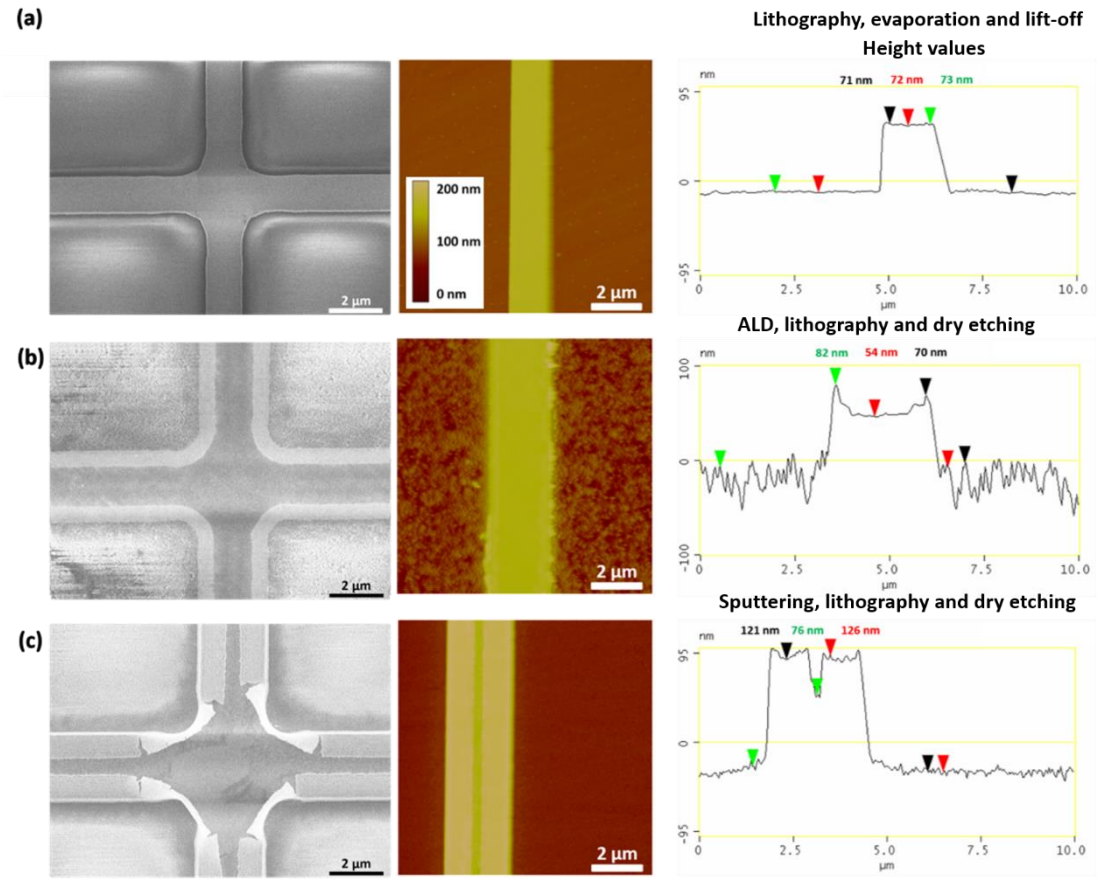

Figure 4.32: (a) SEM image (left), AFM image (middle) and AFM line profile (right) for part of a square mesh (2 µm linewidth) prepared by lithography (positive resist), metal evaporation (Ti 10 nm, Pt 50 nm) and lift-off on borofloat/Al_2O_3(10 nm). (b) Corresponding data for same mesh design fabricated using ALD Pt (nominally 50 nm), lithography (negative resist) and dry etching (c) Data for mesh fabricated using sputtering (Ti 10 nm, Pt 50 nm), lithography and dry etching.

The ALD mesh substrate (Figure 4.32 (b), ALD deposition, lithography and dry etching) showed increased substrate RMS roughness (14 ± 1 nm) as well as broadened (~ 4 µm wide) non-uniform mesh features. At the edges of the mesh structures, bands of excess material are present. These appear as light-grey bands in the SEM image and as "rabbit ears" in the AFM line profile. These edge bands are ~ 30 nm higher than the metal features, suggesting re-deposition of the ALD Pt and/or photoresist residue during the sidewall dry etching. The topography of the sputtered mesh (Figure 4.32 (c)) sample is not as regular as the evaporated mesh sample but smoother than the ALD sample, with a substrate RMS roughness of ~ 4 ± 1 nm. The

mesh structures show broadened features (~ 3 μm wide) and unusual topography, with edge features (~ 50 nm high) that appear to have folded back onto the metal surface. One possible explanation could be an undercut of the Ti layer during sidewall etching, leaving ~ 50 nm high Pt "wings" which folded back onto the mesh. Although the same dry etching recipe was used for both the sputtered Pt and the ALD Pt, the difference in the substrate roughness suggests that additional process development may be required for the ALD Pt etch. The process uses a reflectance end-point detection method and this can be challenging for ultra-thin layers.

For evaporated and sputtered metal meshes, the nominal thickness of Ti (adhesion layer) was 10 nm and Pt was 50 nm. While for ALD metal meshes, the nominal thickness of Pt was 50 nm. However, AFM and Tencor Profilometer (60 measurements) data confirmed that the thickness of Ti and Pt for evaporated meshes were comparable at ~ 72 ± 2 nm (AFM) and ~ 75 ± 4 nm (profilometer). With this increased height (expected total device thickness of 60 nm), it's expected that the sheet resistance will be reduced. For instance, the sheet resistance, transparency (measured against air) and haze were measured as ~ 190 Ω/sq, 86% and 3% respectively. An average step height of ~ 78 ± 24 nm (AFM) and ~ 88 ± 4 nm (profilometer) were measured for the ALD mesh. The sputtered mesh revealed average step heights of ~ 108 ± 2 nm (AFM) and ~ 133 ± 7 nm (profilometer). The increased metal thickness for ALD and sputtered meshes, is due to the insufficient dry etching as mentioned previously. In the case of the ALD sample, the dry etching was unable to completely remove the metal in areas which should have been transparent at the end of the process. This relates to the higher substrate roughness (~ 14 ± 1 nm), lower sheet resistance (~ 75 Ω/sq), lower transparency (~ 76%) and higher haze (~ 11%) when compared to the evaporated mesh. An increased surface roughness results in a higher probability of light scatter. The dry etching process for the sputtered sample was more successful than the ALD sample for removing metal from areas which should have been transparent at the end of the process. But edge features appear to have folded back onto the metal mesh surface. This relates to the lower substrate roughness (~ 4 ± 1 nm), higher sheet resistance (~ 107 Ω/sq), higher transparency (~ 85%) and lower haze (~ 4%) when compared to the ALD mesh. The haze of the sputtered mesh is 1% higher than the evaporated mesh due to the slightly higher surface roughness (4 nm versus 1.7 nm).

4.9.2.4 Transparency, haze and sheet resistance of metal meshes on rigid substrates

The transparency (with and without substrate absorption), haze (with substrate absorbance) and sheet resistance values of Pt mesh devices were found for all three metal deposition methods on glass (Figure 4.33). The transparency and R_S values increased with increasing open mesh area as expected. However, due to the problems with the dry etching process, the ALD and sputtered meshes displayed varying results. The % haze value in the plot was limited to 10%. Of the 54 devices measured, 12 showed haze values > 10%. Only one mesh sample from the evaporation set had a haze > 10% (5 µm circle) but this can be attributed to its high metal coverage (~ 47%). The other nine samples were from sputtered or ALD meshes.

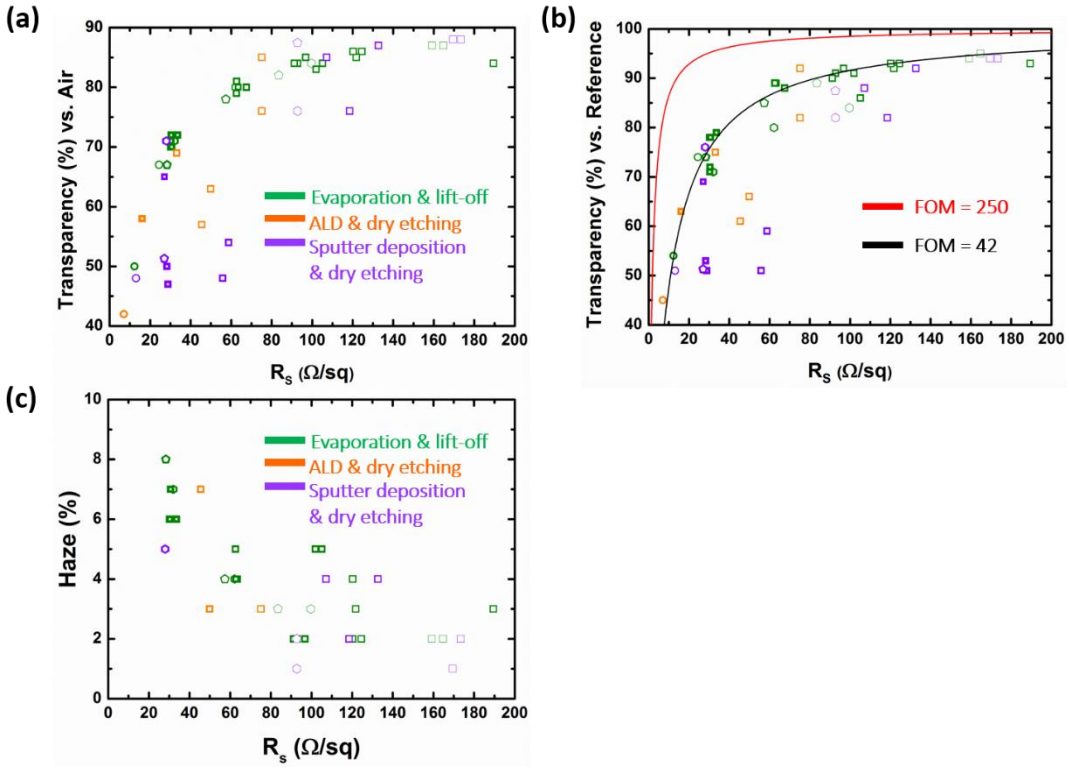

Figure 4.33: (a) Plot of % transparency (measured against air) values at a wavelength, λ, of 550 nm versus R_S of Pt metal meshes deposited on glass by evaporation, ALD and sputter deposition. (b) Plot of % transparency (measured against reference) values at a wavelength, λ, of 550 nm versus R_S of Pt metal meshes deposited on glass by evaporation, ALD and sputter deposition. Two curves based on a figure of merit (FOM) of ~ 250 for ITO on glass and a FOM of ~ 42 (mean FOM for evaporated Pt meshes) are present. (c) Plot of % haze (capped at 10%) versus sheet resistance.

The four Pt mesh samples with the highest figure of merit (based on geometry) via evaporation and lift-off were the following; hexagonal mesh (5 µm linewidth, 11% metal area coverage, evaporation and lift-off) with a figure of merit ~ 51, square mesh (5 µm linewidth, 10% metal area coverage, evaporation and lift-off) with a figure of merit ~ 50, circular mesh (5 µm linewidth, 27% metal area coverage, evaporation and lift-off) with a figure of merit ~ 48 and pentagonal mesh (5 µm linewidth, 27% metal area coverage, evaporation and lift-off) with a figure of merit ~ 40. For ALD meshes, the highest figure of merit ~ 49 was measured for a circular mesh (5 µm linewidth, 47% metal area coverage, ALD and dry etch). Although this is higher than the figure of merit achieved for circular mesh devices by evaporation, its transparency value (measured against reference) of T ~ 45% is too low for use as a transparent electrode. A figure of merit ~ 46 was achieved with a 5 µm linewidth hexagonal mesh with 22% metal area coverage deposited by sputtering and subsequent dry etch. A hexagonal mesh (1 µm, 7%) which suggested having a large figure of merit based on the work by Kim *et al.*, only had a value of figure of merit ~ 25, but differs due to the AZO capping layer (~ 75 nm thick) utilised in their publication [30]. The highest figure of merits mentioned previously agree favourably with some literature publications. For instance, a Ni mesh (~ 50 nm thickness) on glass had a figure of merit of ~ 22 (Rs ~ 28 Ω/sq, T ~ 76.5%) [1]. However, some publications have reported much higher figure of merits for metal meshes on glass. An Au mesh (~ 60 nm thickness) had a reported figure of merit of ~ 484 (Rs ~ 5.4 Ω/sq, T ~ 87%) using a novel templating method [88]. While another Au mesh (~ 300 nm thickness) had a figure of merit of ~ 1350 (Rs ~ 1 Ω/sq, T ~ 77%) [89]. This can be attributed to using lower resistivity metal e.g. Au and thicker metal in relation to Pt meshes herein.

The haze was consistent for Pt meshes by E-beam evaporation (Figure 4.33 (c)). The haze was at its largest for smallest open area and decreased when the open area increased. This is expected as the more open area available, the less the light will be scattered. Insufficient dry etching was again evident on ALD and sputtered meshes with the largest haze value measured of ~ 31% (sputtering) compared to the value of ~ 4% for the corresponding mesh by evaporation. The haze differed greatly between sputtered samples, with a 29% difference between the smallest and largest haze value. A difference of 14% was observed between the smallest and largest haze value for ALD meshes. Many literature publications fail to report on haze for metal meshes.

However, the largest haze values herein are comparable with silver nanowire networks (haze ~ 32%) with a diameter of ~ 150 nm [35] and suggest that nanowire networks are to be avoided if the application requires small haze values. While smaller nanowire diameters produced a haze of ~ 12% which is more than the range of haze values measured for evaporated meshes on glass i.e. 2% to 9%. Note that this excludes the high % metal coverage circle where the haze was ~ 14%. Rolith Inc. have demonstrated Al meshes on glass with a haze of ~ 4% to 5% [20]. These values are in agreement with some metal meshes in Figure 4.33 (c).

The sample sets with the largest standard deviation for the figure of merit were the ALD and sputtered meshes at ~ 32 ± 15 and ~ 26 ± 11 respectively (mean figure of merits for these data sets). Evaporated meshes had a low standard deviation for figure of merit of ~ 42 ± 6. This once again shows the problems associated with the dry etching process and the consistency provided by E-beam evaporation of Ti:Pt and lift-off. Although the figure of merit (FOM) values are quite low in relation to values of ITO on glass of ~ 250 (R_S ~ 9 Ω/sq, T ~ 85%) [90] and Rolith ~ 2612 [21]. In Figure 4.33 (b), the expected transparency and sheet resistance values (up to 200 Ω/sq) based on the figure of merit of ITO on glass (~ 250) is shown. The expected transparency and sheet resistance values based on a FOM of ~ 42 (based on the mean FOM for evaporated Pt meshes) is also shown and implies that most of the evaporated meshes follow this trend. To increase the FOM to that of ITO or beyond, the open area of the mesh can be used to increase the transparency, however the sheet resistance will also increase. The best solution to increase the FOM is by increasing the thickness of the metal to a few hundred nanometres before metal shadowing effects are observed and using lower resistivity metals (e.g., Cu).

4.10 Conclusion

In this study, ALD and E-beam evaporated Pt thin films were fabricated to gain an insight into thin film growth. Pt ALD films on borofloat-Al_2O_3 of thicknesses ranging from 1 nm to 50 nm were grown and their properties were measured. Films below 8 nm suggested discontinuous growth due to unmeasurable sheet resistance. The same was observed for evaporated Pt films. The resistivity of the Pt thin films was larger than that of bulk Pt which may be due to microscopic cracks. The resistivity decreases to that of bulk when the thickness increases.

Pt metal mesh structures were assessed on their fabrication method (evaporation and lift-off, ALD and dry etching and sputtering and dry etching) in relation to their transparency, haze and sheet resistance values. Various geometric structures were utilised on a photolithography mask such as squares, circles, hexagons and new recently discovered pentagon tiling [31]. To this author's knowledge, no literature reports exist for the comparison of metal deposition technique for micron-scale metal meshes. Although this is not an advance over the state of the art present in the literature, it does provide suitable evidence that evaporation is the most suitable metal deposition technique for metal meshes in relation to ALD and sputter deposition. The mesh samples prepared by evaporation provided the highest figure of merit and lowest standard of deviation i.e. ~ 42 ± 6. This metal deposition technique provided a more consistent film thickness and low substrate roughness as discussed in this chapter. ALD and sputtered meshes had inherent problems from the dry etching process and resulted in inconsistent film thickness and a large variation in transparency, optical haze and sheet resistance. Following from this work, metal meshes fabricated on flexible substrates is discussed in the next chapter to gauge the mechanical stability of these devices based on geometry.

4.11 Bibliography

1. Ghosh, D.S., T.L. Chen, and V. Pruneri, *High figure-of-merit ultrathin metal transparent electrodes incorporating a conductive grid.* Applied Physics Letters, 2010, **96**(4), 041109
2. Zhu, Y., et al., *Rational Design of Hybrid Graphene Films for High-Performance Transparent Electrodes.* Acs Nano, 2011, **5**(8), p. 6472-6479
3. Jang, H.Y., et al., *Fabrication of Metallic Nanomesh: Pt Nano-Mesh as a Proof of Concept for Stretchable and Transparent Electrodes.* Chemistry of Materials, 2013, **25**(17), p. 3535-3538
4. Lee, J.Y., et al., *Solution-processed metal nanowire mesh transparent electrodes.* Nano Letters, 2008, **8**(2), p. 689-692
5. Hu, L., et al., *Scalable Coating and Properties of Transparent, Flexible, Silver Nanowire Electrodes.* ACS Nano, 2010, **4**(5), p. 2955-2963
6. Rathmell, A.R., et al., *The Growth Mechanism of Copper Nanowires and Their Properties in Flexible, Transparent Conducting Films.* Advanced Materials, 2010, **22**(32), p. 3558-3563
7. Sam, F.L.M., et al., *Thin film hexagonal gold grids as transparent conducting electrodes in organic light emitting diodes.* Laser and Photonics Reviews, 2014, **8**(1), p. 172-179
8. Dong, P., et al., *Graphene on Metal Grids as the Transparent Conductive Material for Dye Sensitized Solar Cell.* Journal of Physical Chemistry C, 2014, **118**(45), p. 25863-25868
9. Galagan, Y., et al., *Scaling Up ITO-Free Solar Cells.* Advanced Energy Materials, 2014, **4**(2), 1300498
10. Kang, M.G., et al., *Transparent Cu nanowire mesh electrode on flexible substrates fabricated by transfer printing and its application in organic solar cells.* Solar Energy Materials and Solar Cells, 2010, **94**(6), p. 1179-1184
11. Kang, M.G., et al., *Toward Low-Cost, High-Efficiency, and Scalable Organic Solar Cells with Transparent Metal Electrode and Improved Domain Morphology.* IEEE Journal of Selected Topics in Quantum Electronics, 2010, **16**(6), p. 1807-1820
12. Kang, M.G. and L.J. Guo, *Nanoimprinted semitransparent metal electrodes and their application in organic light-emitting diodes.* Advanced Materials, 2007, **19**(10), p. 1391-1396
13. Guo, C.F., et al., *Highly stretchable and transparent nanomesh electrodes made by grain boundary lithography.* Nat Commun, 2014, **5**, 3121
14. Sepulveda-Mora, S.B. and S.G. Cloutier, *Figures of Merit for High-Performance Transparent Electrodes Using Dip-Coated Silver Nanowire Networks.* Journal of Nanomaterials, 2012, **2012**, p. 7, 286104
15. Ahn, B.Y., D.J. Lorang, and J.A. Lewis, *Transparent conductive grids via direct writing of silver nanoparticle inks.* Nanoscale, 2011, **3**(7), p. 2700-2702
16. Jeong, J.-A., J. Kim, and H.-K. Kim, *Ag grid/ITO hybrid transparent electrodes prepared by inkjet printing.* Solar Energy Materials and Solar Cells, 2011, **95**(7), p. 1974-1978
17. Galagan, Y., et al., *Evaluation of ink-jet printed current collecting grids and busbars for ITO-free organic solar cells.* Solar Energy Materials and Solar Cells, 2012, **104**, p. 32-38

18. Jang, Y., J. Kim, and D. Byun, *Invisible metal-grid transparent electrode prepared by electrohydrodynamic (EHD) jet printing.* Journal of Physics D: Applied Physics, 2013, **46**(15), 155103
19. Levinson, H.J., *Chapter 3 - Photoresists in Princicples of Lithography (Second Edition).* 2005, p. 53-98
20. Aryal, M., et al., *16.1: Sub-Micron Transparent Metal Mesh Conductor for Touch Screen Displays.* SID Symposium Digest of Technical Papers, 2014, **45**(1), p. 194-196
21. Seitz, O., et al., *Antireflective surface patterned by rolling mask lithography.* Proceedings of SPIE - The International Society for Optical Engineering, 2014, **8974**, 89740v
22. Chung, C.H., et al., *Solution-processed flexible transparent conductors composed of silver nanowire networks embedded in indium tin oxide nanoparticle matrices.* Nano Research, 2012, **5**(11), p. 805-814
23. Hu, L., H. Wu, and Y. Cui, *Metal nanogrids, nanowires, and nanofibers for transparent electrodes.* MRS Bulletin, 2011, **36**(10), p. 760-765
24. Song, D.H., et al., *Process optimization of organic thin-film transistor by ink-jet printing of DH4T on plastic.* Applied Physics Letters, 2007, **90**(5), 053504
25. Singh, M., et al., *Inkjet Printing—Process and Its Applications.* Advanced Materials, 2010, **22**(6), p. 673-685
26. Ko, S.H., et al., *All-inkjet-printed flexible electronics fabrication on a polymer substrate by low-temperature high-resolution selective laser sintering of metal nanoparticles.* Nanotechnology, 2007, **18**(34), 345202
27. Kang, J., et al., *An Ag-grid/graphene hybrid structure for large-scale, transparent, flexible heaters.* Nanoscale, 2015, **7**(15), p. 6567-6573
28. Park, J. and J. Hwang, *Fabrication of a flexible Ag-grid transparent electrode using ac based electrohydrodynamic Jet printing.* Journal of Physics D: Applied Physics, 2014, **47**(40), 405102
29. Seong, B., et al., *Metal-mesh based transparent electrode on a 3-D curved surface by electrohydrodynamic jet printing.* Journal of Micromechanics and Microengineering, 2014, **24**(9), 097002
30. Kim, W.K., et al., *Cu mesh for flexible transparent conductive electrodes.* Scientific Reports, 2015, **5**, 10715
31. Mann , C., McLoud-Mann, J., Von Derau, D., *Convex pentagons that admit i-block transitive tilings. 2015, arXiv:metric geometry/ 1510.01186v1*
32. Rossnagel, S., *8 - Sputtering and Sputter Deposition A2 - Seshan, Krisna,* in *Handbook of Thin Film Deposition Processes and Techniques (Second Edition).* 2001, William Andrew Publishing: Norwich, NY. p. 319-348.
33. Schiller, S. and G. Jäsch, *Deposition by electron beam evaporation with rates of up to 50 μm s−1.* Thin Solid Films, 1978, **54**(1), p. 9-21
34. Musgrave, C.B., *Theoretical Modeling of ALD Processes*, in *Atomic Layer Deposition of Nanostructured Materials*. 2011, Wiley-VCH Verlag GmbH & Co. KGaA. p. 1-21.
35. Preston, C., et al., *Optical haze of transparent and conductive silver nanowire films.* Nano Research, 2013, **6**(7), p. 461-468
36. De, S., et al., *Silver nanowire networks as flexible, transparent, conducting films: Extremely high DC to optical conductivity ratios.* ACS Nano, 2009, **3**(7), p. 1767-1774

37. Longrie, D., et al., *Plasma-Enhanced ALD of Platinum with O-2, N-2 and NH3 Plasmas.* Ecs Journal of Solid State Science and Technology, 2012, **1**(6), p. Q123-Q129
38. Puurunen, R.L., *Surface chemistry of atomic layer deposition: A case study for the trimethylaluminum/water process.* Journal of Applied Physics, 2005, **97**(12), 121301
39. Puurunen, R.L., *A Short History of Atomic Layer Deposition: Tuomo Suntola's Atomic Layer Epitaxy.* Chemical Vapor Deposition, 2014, **20**(10-12), p. 332-344
40. Kim, H., *Atomic layer deposition of metal and nitride thin films: Current research efforts and applications for semiconductor device processing.* Journal of Vacuum Science and Technology B: Microelectronics and Nanometer Structures, 2003, **21**(6), p. 2231-2261
41. Suntola, T., *Atomic layer epitaxy.* Thin Solid Films, 1992, **216**(1), p. 84-89
42. Suntola, T., *Atomic layer epitaxy.* Materials Science Reports, 1989, **4**(5), p. 261-312
43. Butler, J.E. and A.V. Sumant, *The CVD of nanodiamond materials.* Chemical Vapor Deposition, 2008, **14**(7-8 SPEC. ISS.), p. 145-160
44. Dücsö, C., et al., *Deposition of tin oxide into porous silicon by atomic layer epitaxy.* Journal of the Electrochemical Society, 1996, **143**(2), p. 683-687
45. Kim, D.J., et al., *Applicability of ALE TiN films as Cu/Si diffusion barriers.* Thin Solid Films, 2000, **372**(1), p. 276-283
46. Solanki, R. and B. Pathangey, *Atomic layer deposition of copper seed layers.* Electrochemical and Solid-State Letters, 2000, **3**(10), p. 479-480
47. Gordon, R.G., et al., *A Kinetic Model for Step Coverage by Atomic Layer Deposition in Narrow Holes or Trenches.* Chemical Vapor Deposition, 2003, **9**(2), p. 73-78
48. Meng, X., X.-Q. Yang, and X. Sun, *Emerging Applications of Atomic Layer Deposition for Lithium-Ion Battery Studies.* Advanced Materials, 2012, **24**(27), p. 3589-3615
49. Johnson, R.W., A. Hultqvist, and S.F. Bent, *A brief review of atomic layer deposition: from fundamentals to applications.* Materials Today, 2014, **17**(5), p. 236-246
50. Saleem, M., *Impact of atomic layer deposition to nanophotonic structures and devices.* Frontiers in Materials, 2014, **1**(18), p. 1-15
51. Cromwell, J.E., *Chemical methods of thin film deposition: Chemical vapor deposition, atomic layer deposition, and related technologies.* Journal of Vacuum Science & Technology A, 2003, **21**, p. S88-S95
52. Miikkulainen, V., et al., *Crystallinity of inorganic films grown by atomic layer deposition: Overview and general trends.* Journal of Applied Physics, 2013, **113**(2), 021301
53. Aaltonen, T., et al., *Reaction mechanism studies on atomic layer deposition of ruthenium and platinum.* Electrochemical and Solid State Letters, 2003, **6**(9), p. C130-C133
54. Mattox, D.M., *Chapter 1 - Introduction*, in *Handbook of Physical Vapor Deposition (PVD) Processing (Second Edition)*. 2010, William Andrew Publishing: Boston. p. 1-24.
55. Kim, J.S., et al., *Indium-tin oxide treatments for single- and double-layer polymeric light-emitting diodes: The relation between the anode physical,*

chemical, and morphological properties and the device performance. Journal of Applied Physics, 1998, **84**(12), p. 6859-6870
56. Holloway, P.H. and C.C. Nelson, *In situ formation of diffusion barriers in thin film metallization systems.* Thin Solid Films, 1976, **35**(1), p. L13-L16
57. Hong, D., *Fabrication and characterization of thin-film transistor materials and devices*. 2008, Oregon State.
58. Ohring, M., *Chapter 4 - Discharges, Plasmas, and Ion–Surface Interactions*, in *Materials Science of Thin Films (Second Edition)*. 2002, Academic Press: San Diego. p. 145-202.
59. Barna, P.B. and M. Adamik, *Fundamental structure forming phenomena of polycrystalline films and the structure zone models.* Thin Solid Films, 1998, **317**(1-2), p. 27-33
60. Hornyak, G.L., *Fundamentals of nanotechnology - Chapter 7: Nanostructure and Nanocomposite Thin Films*. 2009, Boca Raton: CRC Press.
61. Thornton, J.A. *Structure-Zone Models Of Thin Films*. 1988.
62. Bauer, E., *Phänomenologische Theorie Der Kristallabscheidung An Oberflächen. I.* Zeitschrift fur Kristallographie - New Crystal Structures, 1958, **110**(1-6), p. 372-394
63. Sree Harsha, K.S., *Chapter 9 - Nucleation and Growth of Films*, in *Principles of Vapor Deposition of Thin Films*. 2006, Elsevier: Oxford. p. 685-829.
64. Venables, J.A., *Introduction to Surface and Thin Film Processes - Chapter 5: Surface processes in epitaxial growth*. 2000: Cambridge University Press.
65. Dubrovskii, V., *Fundamentals of Nucleation Theory*, in *Nucleation Theory and Growth of Nanostructures*. 2014, Springer Berlin Heidelberg: Berlin, Heidelberg. p. 1-73.
66. Maluf, M., Williams, K., *Chapter 3 - Processes for Micromachining*, in *An Introduction to Microelectromechanical Systems Engineering (Second Edition)*. 2004, Artech House, Inc. p. 41-42.
67. Levinson, H.J., *Chapter 10 - Immersion lithography and the limits of optical lithography*, in *Principles of Lithography*. 2005, SPIE Press.
68. Koellensperger, P.A., et al., *Patterning of platinum (Pt) thin films by chemical wet etching in Aqua Regia.* Journal of Micromechanics and Microengineering, 2012, **22**(6), 067001
69. Williams, K.R. and R.S. Muller, *Etch rates for micromachining processing*. Journal of Microelectromechanical Systems, 1996, **5**(4), p. 256-269
70. Williams, K.R., K. Gupta, and M. Wasilik, *Etch rates for micromachining processing - Part II.* Journal of Microelectromechanical Systems, 2003, **12**(6), p. 761-778
71. Haacke, G., *New figure of merit for transparent conductors.* Journal of Applied Physics, 1976, **47**(9), p. 4086-4089
72. Morales, J. and A. Flores-Riveros, *The generalization of the binomial theorem.* Journal of Mathematical Physics, 1989, **30**(2), p. 393-397
73. Galagan, Y., et al., *ITO-free flexible organic solar cells with printed current collecting grids.* Solar Energy Materials and Solar Cells, 2011, **95**(5), p. 1339-1343
74. Stein, R., *A new pentagon tiler*. Mathematics magazine, 1985, **58**(5), 308
75. Heesch, H. and O. Kienzle, *Flächenschluß: System der Formen lückenlos aneinanderschließender Flachteile*. 1963: Springer-Verlag.
76. Niven, I., *Convex Polygons that Cannot Tile the Plane.* The American Mathematical Monthly, 1978, **85**(10), p. 785-792

77. Sugimito, T., *Tiling Problem: Convex Pentagons for Edge-to-Edge Monohedral Tiling and Convex Polygons for Aperiodic Tiling. 2016, arXiv:metric geometry/ 1508.01864v3.*
78. Zhu, D., et al., *Recent progress in tissue optical clearing.* Laser & Photonics Reviews, 2013, **7**(5), p. 732-757
79. Durkan, C. and M.E. Welland, *Size effects in the electrical resistivity of polycrystalline nanowires.* Physical Review B, 2000, **61**(20), p. 14215-14218
80. Zhang, Q.G., et al., *Influence of grain boundary scattering on the electrical properties of platinum nanofilms.* Applied Physics Letters, 2006, **89**(11), 114102
81. Van der Pauw, L.J., *A method of measuring specific resistivity and Hall effect of discs of arbitrary shape.* Philips Research Reports, 1958, **13**(1), p. 1-9
82. Shimamoto, A., et al., *A Nondestructive Evaluation Method: Measuring the Fixed Strength of Spot-Welded Joint Points by Surface Electrical Resistivity.* Journal of Pressure Vessel Technology, 2013, **135**(2), 021501
83. Ramadan, A.A., R.D. Gould, and A. Ashour, *On the Van der Pauw method of resistivity measurements.* Thin Solid Films, 1994, **239**(2), p. 272-275
84. Pardon, G., et al., *Pt-Al2O3 dual layer atomic layer deposition coating in high aspect ratio nanopores.* Nanotechnology, 2013, **24**(1), 015602
85. Dameron, A.A., et al., *Aligned carbon nanotube array functionalization for enhanced atomic layer deposition of platinum electrocatalysts.* Applied Surface Science, 2012, **258**(13), p. 5212-5221
86. Aaltonen, T., et al., *Atomic layer deposition of noble metals: Exploration of the low limit of the deposition temperature.* Journal of Materials Research, 2004, **19**(11), p. 3353-3358
87. Marzi, G.D., et al., *Probing intrinsic transport properties of single metal nanowires: Direct-write contact formation using a focused ion beam.* Journal of Applied Physics, 2004, **96**(6), p. 3458-3462
88. Rao, K.D.M. and G.U. Kulkarni, *A highly crystalline single Au wire network as a high temperature transparent heater.* Nanoscale, 2014, **6**(11), p. 5645-5651
89. Kiruthika, S., R. Gupta, and G.U. Kulkarni, *Large area defrosting windows based on electrothermal heating of highly conducting and transmitting Ag wire mesh.* RSC Advances, 2014, **4**(91), p. 49745-49751
90. Guillén, C. and J. Herrero, *Comparison study of ITO thin films deposited by sputtering at room temperature onto polymer and glass substrates.* Thin Solid Films, 2005, **480**–**481**, p. 129-132

5 Metal meshes for use as flexible transparent conductive electrodes

5.1 Introduction

In the previous chapter, metal meshes were fabricated on rigid glass substrates. Three metal deposition techniques were used to find the most reliable method. Out of the three deposition methods, evaporation (lift-off) was chosen based on stable metal thicknesses, low surface roughness and their optoelectronic properties (highest figure of merit values). Following this work, it is important to test the mechanical stability of metal mesh devices. ITO, the most popular transparent conductive electrode suffers from large electrical conductivity changes when the material is flexed [1, 2]. Usually an annealing process is undertaken on ITO to increase its electrical conductivity. This annealing temperature is incompatible with flexible substrates [3]. In relation to transparent metal meshes, many publications fail to report on their mechanical stability following a set number of bending cycles.

Thirteen metal mesh devices with a fixed linewidth of 5 μm and four different geometries were fabricated on PET. These devices were bent over a rod of known radius of curvature and their two terminal resistance was measured every 200 cycles (up to 1,000 bending cycles) to gauge their mechanical stability after cyclic bending. The change in transparency after 1,000 bending cycles was also measured.

5.2 Materials and methods

5.2.1 Fabrication of Pt metal meshes on flexible plastic substrates[a]

The metal mesh devices were patterned on 125 μm thick heat-stabilised polyethylene terephthalate (PET) substrate "Melinex" (DuPont Teijin UK, item # ST504). A 4" wafer sized piece was used for processing. The same method was used for lithography, Pt evaporation and lift-off as described in Chapter 4, Section 4.7.2. Individual mesh devices were of size 7 mm x 11 mm (total die size of 12 mm x 15 mm) with two macro electrodes (7 mm x 2mm) for two-terminal resistance measurements. Four smaller mesh devices of size 2 mm x 2 mm (same linewidth and open area) were utilised for four-terminal sheet resistance measurements.

[a] UV lithography, metal evaporation and lift-off was carried out by Mr. Dan O' Connell and Mr. Colin Lyons in Tyndall (Speciality Product and Services group).

5.3 Characterisation

5.3.1 Optical characterisation

Transparency and haze values were found by using a Perkin Elmer 950 Spectrophotometer as depicted in Chapter 4, Section 4.8.2. Optical microscopy images were taken using a Leica DMRB microscope in transmission mode at 5x, 10x and 50x magnifications.

5.3.2 Electrical characterisation

Initial sheet resistance (R_S) values of the mesh devices were evaluated from four-terminal current-voltage measurements performed at room temperature under ambient conditions using an Agilent E5270B parameter analyser interfaced to a LakeShore Desert TTPX probe station (10 mV – 200 mV bias voltage range) as described in Chapter 4, Section 4.8.3. The same setup was used for two-terminal resistance measurements. To test the mechanical stability of the mesh devices, they were manually flexed (tensile based strain) over a Teflon rod with a known radius of curvature (~ 3.8 mm), held in place with a clamp. The resistance ratio (R_n/R_0) was used to compare changes in resistance across different geometries, where R_n is the 2 terminal resistance measured after every n bending cycles (n = 200, 400, 600, 800, 1000) and R_0 is the initial 2 terminal resistance.

5.4 Results and discussion

5.4.1 Transparency and haze of flexible substrates

The transparency of the flexible PET substrate (Melinex) was measured as ~ 88% at a wavelength of 550 nm and its optical haze was measured as ~ 1%, in agreement with the manufacturer's specifications (~ 0.8%) [4]. After bending the PET substrate 1,000 times, its transparency was measured as ~ 84% and the haze increased to ~ 5%. The transparency spectra for both substrates is plotted in Figure 5.1. A series of peaks are present for both substrates. These are interference fringes caused by the internal refraction and reflection by the adhesive coating on the substrate surface as stated by the manufacturer. The thickness of this adhesive coating can be estimated using the interference fringes that exist in the transmission spectrum (Figure 5.1). The following equation was used to estimate the thickness, d, of the adhesive coating [5]

$$d = \frac{m}{2n(\nu_1 - \nu_2)} \quad \textbf{(5.1)}$$

where m is the number of peak maxima between measured interference fringe minima, n is the refractive index and ν_1 and ν_2 are the associated wavenumbers of the measured interference fringe minima. For the Melinex substrate, the first minima has a wavelength value of ~ 410 nm which corresponds to a wavenumber value of 2.44 x 10^4 cm^{-1}. The second minima has a wavelength value of ~ 674 nm which corresponds to a wavenumber value of ~ 1.48 x 10^4 cm^{-1}. Between these two minima, six peak maxima exist, i.e. m = 6. Using an estimated value of the refractive index of PET as, n ~ 1.6 [6], the thickness of the adhesive coating calculated from equation (5.1) was found to be ~ 2 µm.

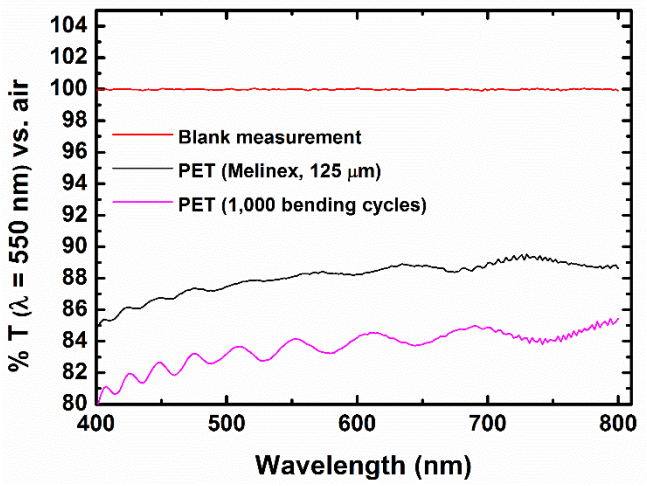

Figure 5.1: Transparency versus wavelength of a blank measurement (air) and flexible PET (as fabricated) and PET (post-1,000 bending cycles). For both PET spectra, interference fringes can be seen which are created from the adhesive coating on the substrate according to the manufacturer.

5.4.2 Two terminal resistance, sheet resistance, transparency and haze of transparent metal meshes fabricated on flexible PET

Following the fabrication of metal meshes on flexible PET as described in section 5.2.1, the two terminal resistance, sheet resistance, % transparency and % haze was found for all 13 metal mesh devices. A photo and optical microscopy image of a pentagonal mesh (5 µm linewidth, 14% metal area coverage) on flexible PET is shown in Figure 5.2 below.

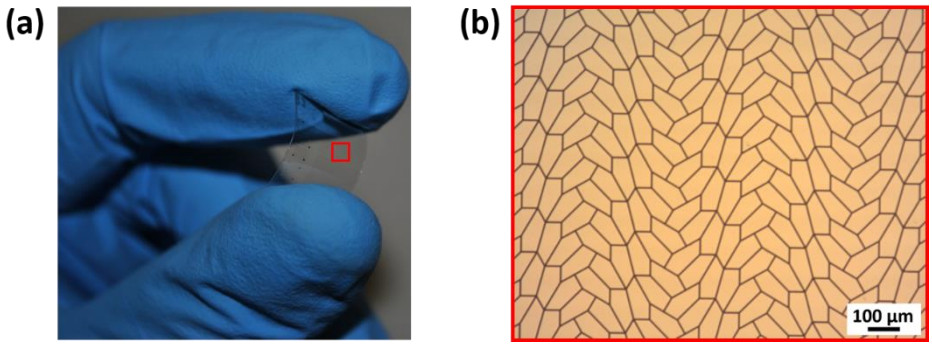

Figure 5.2: (a) A photo of a pentagonal mesh patterned on 125 µm thick PET film (Melinex). (b) Optical image in transmission mode of a pentagonal mesh with a linewidth of 5 µm (14% metal area coverage).

The devices with the lowest sheet resistance values for each geometry were achieved for the samples with the highest % metal area coverage, which were as follows; R_S ~ 33.53 Ω/sq (hexagon, 5 µm, 22%), ~ 13.72 Ω/sq (circle, 5 µm, 47%), ~ 30.99 Ω/sq (square, 5 µm, 19%) and ~ 27.83 Ω/sq (pentagon, 5 µm, 27%). Conversely the highest transparency values (referenced against air) were achieved for devices with the lowest % metal area coverage which were as follows; T ~ 82 % (hexagon, 5 µm, 7%), ~ 65% (circle, 5 µm, 27%), ~ 84 % (square, 5 µm, 4%) and ~ 78% (pentagon, 5 µm, 4%). There appeared to be no influence of solvent compatibility and UV exposure for the processing on the Melinex substrates. The change in optical properties after processing is minute. This is evident from the measured transparency values (versus air), which agree within 2% of the expected value for all devices. The lower measured transparency is likely due to lithographic residue rather than process incompatibilities. The manufacturer has stated that minimal shrinkage occurs for Melinex at a temperature of 150 ºC for 30 minutes [4]. A temperature of 150 ºC was used on the Melinex during processing when baking the LOR3A resist, but this was only for 3 minutes. A literature reported has stated that the transparency of the Melinex did not change after being exposed to UV light for 24 hours [7]. Also it has been suggested that a wide range of solvents that are used in lithography processes are compatible with the material [8]. The lowest haze value of ~ 2% was measured for a square mesh device (5 µm, 19%). It's expected that the haze value will be larger for devices with a larger % metal area coverage as the probability of light scatter is higher. For all 13 devices, the haze never exceeded 10%, except for the 5 µm linewidth circle with large

metal coverage (~ 47%). A 2D scatter plot of % transparency (referenced against PET) at a wavelength of 550 nm versus the sheet resistance is shown in Figure 5.3 (a). The number in brackets represents the % metal area coverage. The highest values of the figure of merit (FOM) for each geometry was as follows; $\frac{\sigma_{DC}}{\sigma_{OP}}$ ~ 52 (hexagon, 5 µm, 11% metal coverage), ~ 46 (circle, 5 µm, 27% metal coverage), ~ 46 (square, 5 µm, 10% metal coverage) and ~ 36 (pentagon, 5 µm, 9% metal coverage). The mean value of the FOM of ~ 42 ± 5 is in agreement with the value obtained for Pt evaporated meshes on glass (~ 42 ± 6) in the previous chapter indicating the reliability of evaporation and lift-off. Figure 5.3 (b) the expected transparency and sheet resistance values (up to 200 Ω/sq) based on the figure of merit of ITO on PET (~ 300) [9] is shown. The expected transparency and sheet resistance values based on a FOM of ~ 42 (based on the mean FOM for evaporated Pt meshes) is also shown and once again follows the trend as in the previous chapter. The suggestions of improving the FOM are still valid i.e. increasing the metal thickness and using a lower resistivity metal.

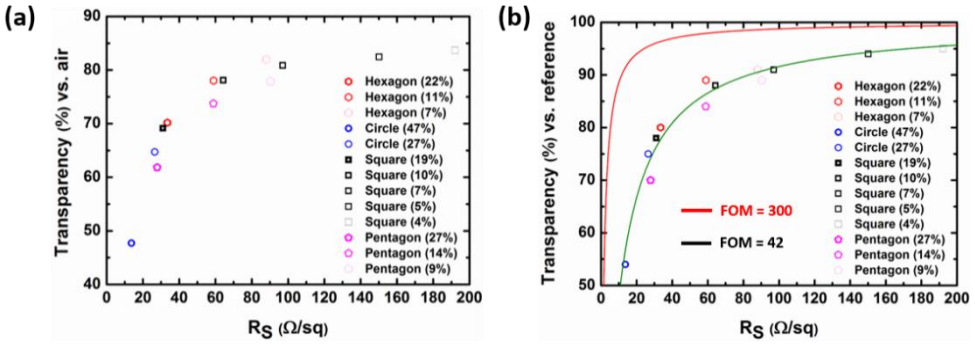

Figure 5.3: A plot of transparency (referenced against air) values at a wavelength, λ, of 550 nm against sheet resistance for all 13 metal mesh devices on flexible PET. The device with the largest % metal area coverage had the lowest sheet resistance and lowest transparency as expected. (b) A plot of transparency (referenced against PET) values at a wavelength, λ, of 550 nm against sheet resistance for all 13 metal mesh devices on flexible PET. Two curves based on a figure of merit (FOM) of ~ 300 for ITO on glass and a FOM of ~ 42 (mean FOM for evaporated Pt meshes) are present. In both plots, he number in brackets represents the % metal area coverage.

5.4.3 Effect of mechanical stability based on fractional resistance change, transparency change and figure of merit

Following the initial measurements of two terminal resistance in the previous section, the mechanical stability of metal mesh structures on PET was investigated. The samples underwent tensile bending (bent at support ends) a rod with known radius of curvature of ~ 3.8 mm. For tensile based strain, the metal features are forced to move towards the free surface i.e. air. Following the approach of Suo *et al.*, the strain was calculated using the following formula:

$$\varepsilon = \frac{\delta_f + \delta_s}{2r_c}\left[\frac{1 + 2\eta + \chi\eta^2}{1 + \eta + \chi n + \chi\eta^2}\right] \quad \textbf{(5.2)}$$

where δ_f and δ_s are the thicknesses of the metal (~ 60 nm in total) and substrate (~ 125 µm) respectively, r_c is the radius of curvature (~ 3.8 mm), $\eta = \delta_f/\delta_s$ and $\chi = Y_{Pt}/Y_{PET}$, where Y_{Pt} and Y_{PET} are the Young's moduli of the film and substrate respectively [10]. A strain of ~ 1.6% was calculated using equation (5.2) for this work using elastic constant values for bulk Pt.

The two terminal resistance was measured periodically after each 200 cycle interval (Figure 5.4). As expected, increasing the open area of the sample, generally results in a larger increase in two terminal resistance. The point of most strain is expected to be the edges of the mesh where the linewidths meet and the center of the sample. Many of the samples, in particular hexagon (5 µm, 11%), square (5 µm, 4%) and pentagon (5 µm, 9%) experienced a large change between 600 and 1,000 cycles, $\frac{R_{1,000}}{R_{600}}$ ~ 6.2, ~ 12.2 and ~ 2.2 respectively. Note that the percentage values in the previous sentence are the % metal area coverage in relation to the total unit cell area. A plot of the fractional resistance change for all 13 devices is shown in Figure 5.4. The lowest resistance increase for each geometry was as follows; $\frac{R_{1,000}}{R_0}$ ~ 2.3 (hexagon, 5 µm, 22%), ~ 2.2 (circle, 5 µm, 27%) ~ 3.7 (square, 5 µm, 19%) and ~ 1.6 (pentagon, 5 µm, 14%). Some literature publications apply strain on flexible devices by bending over a rod of known radius of curvature [11, 12]. The resistance changes are quite large herein and may be due to the aggressive nature of bending over the rod. However, the 14% metal coverage based pentagon devices suggest good mechanical performance. This may be due to the asymmetric design on the newly discovered

pentagonal tiling. The author hypothesises that the asymmetry may have the ability to distribute forces when strain, leading to improved mechanical stability when compared to symmetric designs. The rate of strain is another important parameter in relation to the mechanical stability of flexible devices. Many publications fail to report on the strain rate when bending devices over a fixed radius of curvature, which leads to varying results in the literature. In this chapter, the strain rate of all devices was ~ 30 cycles per minute. A literature table based on cyclic bending is given in the next chapter. For example, a fractional resistance change of ~ 2.5 was measured after 1,000 bending (tension) cycles for an embedded Au square mesh (thickness ~ 1.8 µm, linewidth ~ 0.9 µm) on a cyclic olefin copolymer substrate with a similar bending radius i.e. 4 mm [13]. This compares well to Pt metal meshes with values of $\frac{R_{1,000}}{R_0}$ ~ 2.3 (hexagon, 5 µm, 22% metal area coverage), ~ 2.2 (circle, 5 µm, 27% metal area coverage) and ~ 1.6 (pentagon, 5 µm, 14% metal area coverage). However, due to the use of lower resistivity metal i.e. Au and larger metal thickness, the resistance only increase from 0.1 Ω/sq to ~ 0.25 Ω/sq. An Au hexagonal mesh (~ 500 nm thickness, linewidth ~ 10 µm) with a comparable bending radius (5 mm) had a fractional resistance change of ~ 1.42 [14]. Although this was only measured after 200 bending cycles. Therefore one can assume that the value would be higher after 1,000 bending cycles. This increase compares favourably with the fractional resistance increase of ~ 1.6 after 1,000 bending cycles for the Pt pentagonal metal mesh (5 µm, 14% metal area coverage).

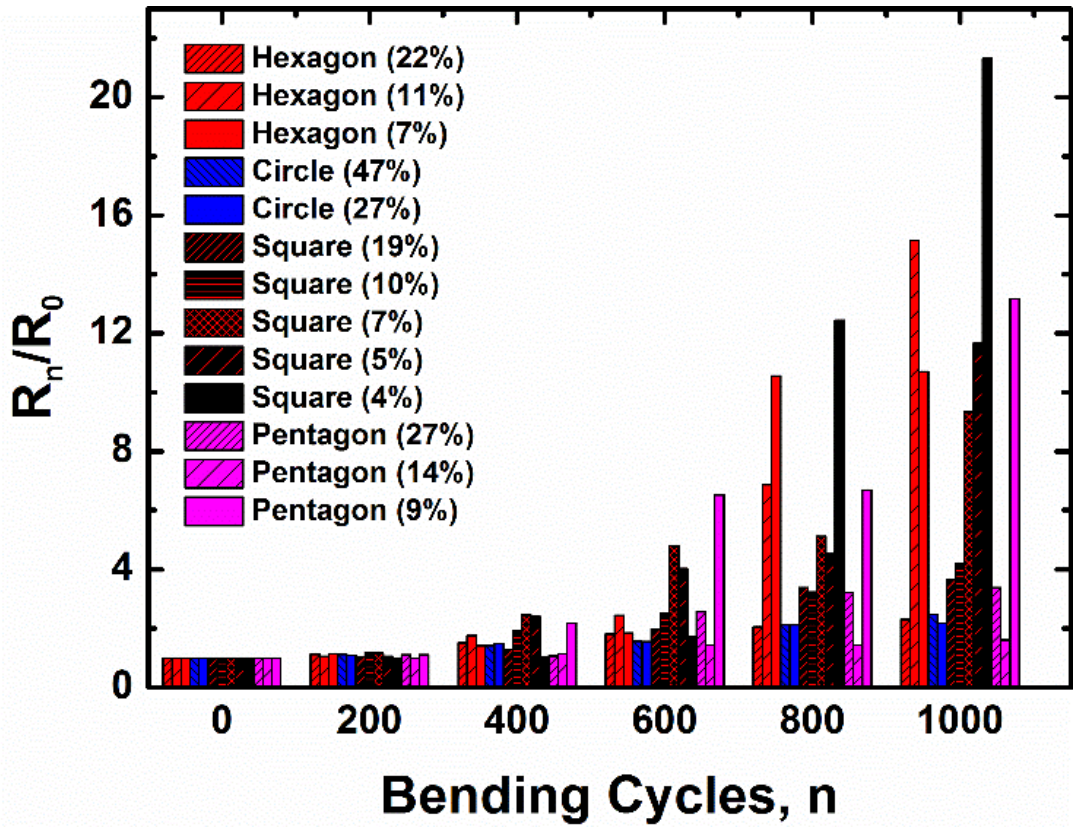

Figure 5.4: Fractional two-terminal resistance change (R_n/R_0) versus number of bending cycles (n) for all 5 µm linewidth metal meshes for all four geometries (hexagons, squares, circles and pentagons). The two-terminal resistance was measured after each 200 bending cycle interval up to 1,000 bending cycles. Generally, the larger the open area, the larger the two terminal increase. A pentagonal mesh of linewidth 5 µm and 14% metal area coverage showed the lowest fractional resistance increase of ~ 1.6 after 1,000 bending cycles. The thicker edged symbols represent geometries with a larger % metal area coverage. The numbers in brackets represents the % metal area coverage.

A plot of the devices with the lowest fractional resistance increase for each geometry is shown in Figure 5.5. The y-axis in the inset graph is normalised by dividing the fractional resistance increase by 1 - % metal area coverage i.e. the transparency. The lowest fractional resistance change based on normalisation was also for the pentagonal mesh device (5 µm, 14%) ~ 1.9.

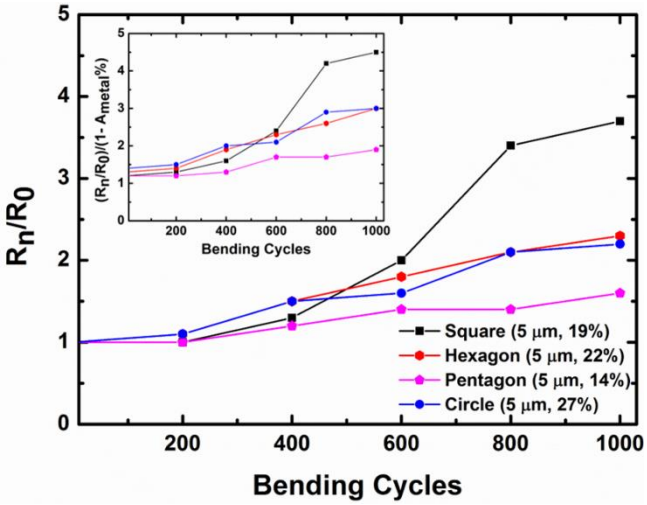

Figure 5.5: Fractional two terminal increase versus number of bending cycles for four devices based on the lowest fractional resistance increase from the previous figure. Inset: Resistance normalised by expectant transparency of the mesh i.e. 1 - % metal area coverage.

The transparency values were also measured for each sample after 1,000 bending cycles to see the effect of bending the devices had on the transparency. The largest transparency change, ΔT, ~ 6% was measured for a hexagonal mesh (5 µm, 11% metal area coverage) and a square mesh (5 µm, 7% metal area coverage). The lowest transparency change of ~ 1% was measured for both circular meshes (5 µm, 47%, 27% metal area coverage), a square mesh (5 µm, 5% metal area coverage) and a pentagonal mesh (5 µm, 27% metal area coverage). A plot ΔT against $\frac{R_{1,000}}{R_0}$ for all 13 devices is shown below in Figure 5.6. The change in the transparency (versus air) of the Melinex substrate itself after 1,000 bending cycles was measured as ΔT ~ 4% for two samples (Figure 5.1). Some of the mesh devices showed a value of ΔT < 4% after 1,000 bending cycles, which does not agree with the transparency change of the bare substrate. However, in the case of the circular meshes (47% and 27% metal area coverage) and pentagonal mesh (27% metal area coverage), the minute change in the transparency may be attributed to the large metal area coverage which may mask micro cracks that would be present on the bare substrate. Also, the use of metal on the PET substrate may change the behaviour of crack formation on the bare substrate when the devices are subject to mechanical strain.

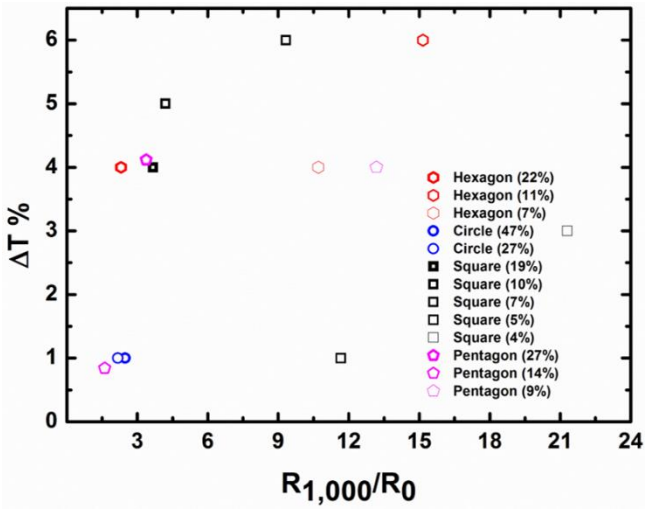

Figure 5.6: The change in transparency (referenced against air) values at a wavelength, λ, of 550 nm against the fractional two terminal resistance increase after 1,000 cycles. The highest resistance ratio increase of ~ 21.3 was observed for a square mesh of linewidth 5 μm and 4% metal area coverage. This device had a value of ΔT ~ 3%. The largest value of ~ 6% was measured for a hexagonal mesh (5 μm, 11% metal area coverage) and a square mesh (5 μm, 7% metal area coverage). The lowest value of ΔT ~ 1% was measured for both circular meshes (5 μm, 47%, 27% metal area coverage), a square mesh (5 μm, 5% metal area coverage) and a pentagonal mesh (5 μm, 27% metal area coverage). The thicker edged symbols represent geometries with a larger % metal area coverage. The number in brackets represents the % metal area coverage.

The figure of merit in relation to the number of bending cycles was found for the devices with the lowest fractional resistance change based on geometry (Figure 5.5). The two point resistance was measured every 200 bending cycles up to 1,000 cycles, therefore the sheet resistance was approximated by using $R_S = R\left(\frac{W}{L}\right)$, where R is the 2 point resistance of the device, w is the width of the total mesh (7 mm) and L is its length (11 mm). Referring to Figure 5.7, the pentagonal mesh (5 μm, 14%) had the highest value for the figure of merit after 1,000 bending cycles of ~ 12 (initial figure of merit value ~ 19). It appears that the decrease of the figure of merit is more affected by the large change of resistance rather than the small change of the transparency for these devices.

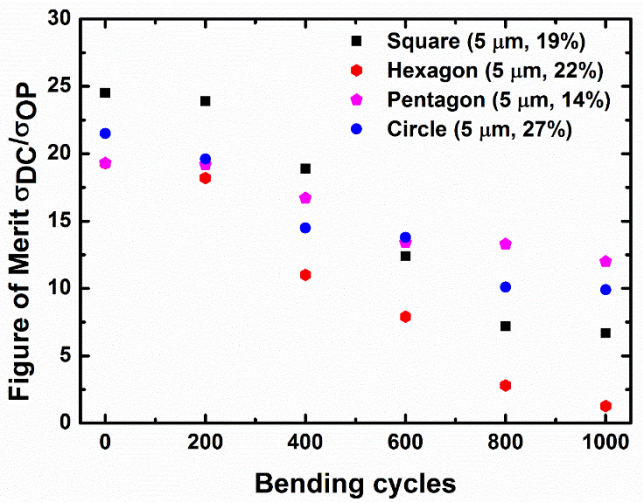

Figure 5.7: Figure of merit against the number of bending cycles for the devices with the lowest fractional resistance change. The sheet resistance values for the figure of merit were approximated by using $R_S=R\left(\frac{W}{L}\right)$, where R is the two point resistance of the device, w is the width of the total mesh (7 mm) and L is its length (11 mm). The highest figure of merit value after 1,000 cycles was ~ 23 (pentagon, 5 μm, 14% metal area coverage). The number in brackets represents the metal area coverage.

5.4.4 SEM comparison of as fabricated and flexed metal meshes on flexible substrates

To see the effect of mechanical bending on the surface morphology of the metal meshes, SEM images were taken on a hexagonal (5 μm, 22% metal area coverage), circular (5 μm, 27% metal area coverage), square (5 μm, 5% metal area coverage) and pentagonal (5 μm, 9% metal area coverage) mesh for as fabricated devices and post-1,000 bending cycles. It was difficult to achieve proper focus on the as fabricated samples as evident from the SEM images in Figure 5.8 (a), (c), (e) and (g). This was due to the charging of the substrate surface. However, the SEM images after 1,000 cycles provided much better contrast. The samples were not charging as much which suggests the insulating PET substrate was damaged. This agrees with the change in the transparency of the bare substrate after 1,000 bending cycles (ΔT ~ 4%). Micro cracks can be seen on the SEM images below in Figure 5.8 (b), (d), (f) and (h) after

1,000 bending cycles which accounts for the increase in the two-terminal resistance after bending.

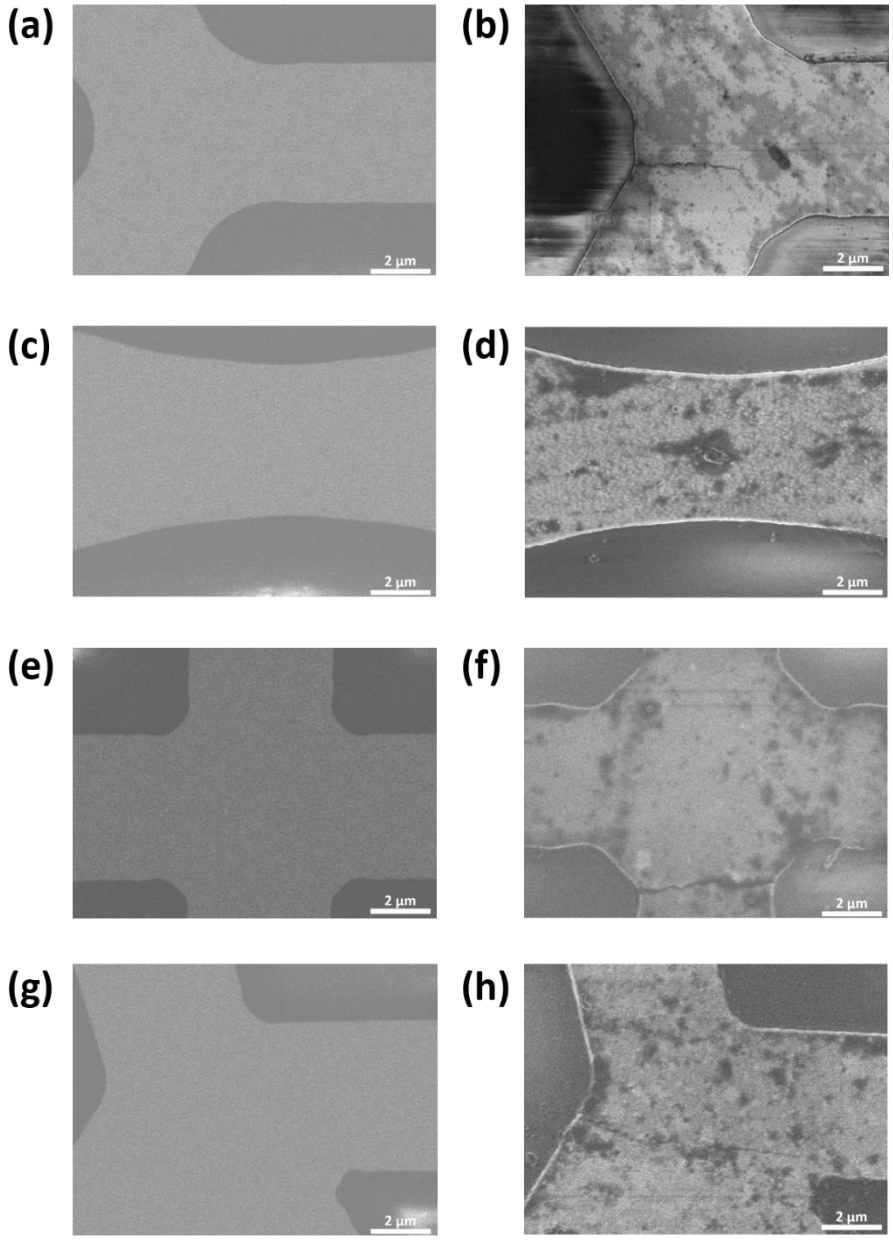

Figure 5.8: SEM images of four mesh samples on 125 µm thick PET (Melinex) of as fabricated samples ((a), (c), (e) and (g)) (hexagon, circle, square and pentagon) and the same sample after 1,000 bending cycles ((b), (d), (f) and (h)). Note the presences of micro cracks on the metal mesh patterns after 1,000 bending cycles for all geometries.

5.5 Conclusion

Pt mesh structures were applied on flexible PET (Melinex) by UV lithography, evaporation and lift-off. For consistency, the linewidth of all devices was kept constant at 5 µm. To test the mechanical stability of the Pt metal meshes, the devices were flexed over a rod with a known radius of curvature (~ 3.8 mm) up to 1,000 tensile bending cycles. The two terminal resistance was measured every 200 bending cycles.

The contribution to knowledge in this chapter is the use of the newly discovered asymmetric pentagonal tiling on flexible substrates. Reports in literature often focus on symmetrical geometries. It appears from experimental data, that the asymmetric pentagon has improved mechanical stability in relation to symmetrical geometries. The asymmetric design may have the potential ability to distribute forces when strained leading to better mechanical stability. A fractional resistance change of ~ 1.6 was measured for a pentagonal mesh (5 µm, 14% metal area coverage) after 1,000 bending cycles, which demonstrates its adequate mechanical stability.

UV lithography was used as the patterning technique in this chapter. However it is an expensive and slow throughput process. It is currently limited to a maximum substrate size of 4" in Tyndall's current clean room fabrication facilities. However, industrial companies such as Rolith Inc. have demonstrated patterning of metal mesh structures over large areas (~ 1.1 m x 0.3 m) using their patented rolling mask lithography. Therefore it may be possible to pattern the newly discovered asymmetric pentagonal tiling over large areas. Thus metal meshes have the potential of overcoming the monopoly that ITO has on the transparent conductive electrode industry due to potential large area patterning and the ability to undergo mechanical strain without a large resistance increase.

Further work will involve investigating failure modes thoroughly after device bending and using other patterning techniques such as nanoimprint lithography to achieve sub-micron linewidths to reduce the effect of Moire fringes. Metal electroplating may prove to be a cost effective method for metal deposition that will also be considered for future work. The potential ability of the asymmetric pentagonal tiling to distribute forces when strained could be investigated in future work by using finite element analysis. In the next chapter, Pt pentagonal metal meshes are used as transparent heaters, followed by their subsequent characterisation.

5.6 Bibliography

1. De, S., et al., *Transparent, flexible, and highly conductive thin films based on Polymer-nanotube composites.* ACS Nano, 2009, **3**(3), p. 714-720
2. Chen, Z., et al., *A mechanical assessment of flexible optoelectronic devices.* Thin Solid Films, 2001, **394**(1-2), p. 202-206
3. Masatoshi, H., et al., *Postdeposition Annealing Influence on Sputtered Indium Tin Oxide Film Characteristics.* Japanese Journal of Applied Physics, 1994, **33**(1R), p. 302
4. *DuPont Teijin Films - Melinex ST504 Data Sheet.*
5. Plummer, B.F., *Measuring polymer film thickness by interference patterns.* Journal of Chemical Education, 1984, **61**(5), p. 439
6. Elman, J.F., et al., *Characterization of biaxially-stretched plastic films by generalized ellipsometry.* Thin Solid Films, 1998, **313–314**, p. 814-818
7. Tricot, F., et al., *Photochromic Ag:TiO2 thin films on PET substrate.* RSC Advances, 2014, **4**(106), p. 61305-61312
8. MacDonald, W.A., et al., *Latest advances in substrates for flexible electronics.* Journal of the Society for Information Display, 2007, **15**(12), p. 1075-1083
9. Guillén, C. and J. Herrero, *Comparison study of ITO thin films deposited by sputtering at room temperature onto polymer and glass substrates.* Thin Solid Films, 2005, **480–481**, p. 129-132
10. Suo, Z., et al., *Mechanics of rollable and foldable film-on-foil electronics.* Applied Physics Letters, 1999, **74**(8), p. 1177-1179
11. Zhu, Y., et al., *Rational Design of Hybrid Graphene Films for High-Performance Transparent Electrodes.* Acs Nano, 2011, **5**(8), p. 6472-6479
12. Kim, W.K., et al., *Cu mesh for flexible transparent conductive electrodes.* Scientific Reports, 2015, **5**, 10715
13. Khan, A., et al., *High-Performance Flexible Transparent Electrode with an Embedded Metal Mesh Fabricated by Cost-Effective Solution Process.* Small, 2016, **12**(22), p. 3021-3030
14. Gao, T., et al., *Hierarchical Graphene/Metal Grid Structures for Stable, Flexible Transparent Conductors.* ACS Nano, 2015, **9**(5), p. 5440-5446

6 Asymmetric pentagonal metal meshes for flexible transparent electrodes and heaters[a]

[a] The work presented in this chapter has been published in a peer reviewed journal.
Lordan, D. *et al.*, Asymmetric pentagonal metal meshes for flexible transparent electrodes and heaters. ACS Applied Materials & Interfaces, 2017, 9 (5), p 4932–4940.

6.1 Introduction

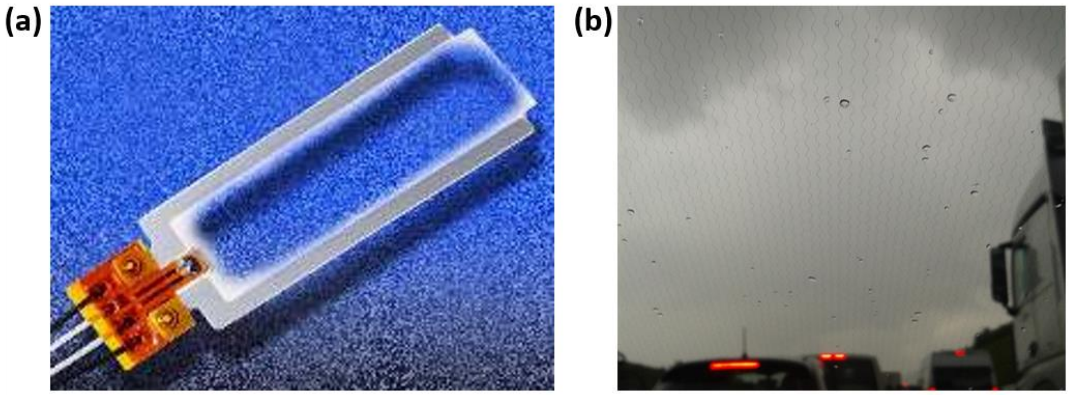

Figure 6.1: (a) Commercial transparent heater based on tin-doped indium oxide (ITO) [1]. (b) Current offering by Ford Motor Company for de-icing an automobile windscreen based on an array of metal line heaters. Note that the metal lines are still visible under normal driving conditions.

Recently, a promising application of metal meshes as a replacement candidate material for ITO in visible transparent heater technology has been proposed [2, 3]. Visible transparent heaters are used for the de-icing and defrosting of automotive windows, advertisement boards and aviation displays, which require visual transparency in cold environments [4]. The generated heat occurs due to the Joule effect. Joule heating is the heat generated from resistive losses in a conductive material under current flow. As electrons move through the conductive material, electrical energy is converted to thermal energy. Some of the energy of the moving electrons is lost to the vibrational modes of the lattice (phonons) [5]. As more of the electron energy is lost, the vibrational energy of the lattice increases and subsequently causes the temperature of the conducting material to increase. Besides visual transparency, which can be achieved using suitable metal mesh parameters and invisible metal lines, low sheet resistance is another important criteria for visible transparent heaters. Higher values of sheet resistance require higher operating voltages i.e. higher power consumption to achieve a high steady state temperature (referred to in this chapter as the saturation temperature). Thus a pragmatic approach is required for the use of this technology in automobiles. Automotive and aviation windscreen based transparent heaters are embedded in the acrylic or glass which are predominantly curved surfaces [6]. Therefore, adequate mechanical stability is required for such de-icing applications.

Here we report on the electrical characteristics of asymmetric metal meshes, tiled using a new class of pentagons described in previous chapters. The pentagons were chosen for this study as the last chapter suggested improved mechanical stability over symmetrical geometries. This may be due to the asymmetry of the pentagon which may have the potential ability to distribute forces when strained, leading to improved mechanical stability. Three different pentagon designs were assessed, each with the same pentagonal tessellation pattern and linewidth (5 μm), but with different sizes of the fundamental pentagonal unit, corresponding to different areal coverage of metal. Mechanical stability was assessed for both tensile strain and compressive strain. We also report on the performance of the pentagonal metal mesh devices as visible transparent heaters.

6.2 Materials and methods[b]

6.2.1 Fabrication of metal mesh devices on flexible plastic substrates

The metal mesh devices were patterned on 125 μm thick heat-stabilised polyethylene terephthalate (PET) substrate "Melinex" (DuPont Teijin UK, item # ST504). A 70 mm x 70 mm sized piece was used for processing. The method used for lithography, metal evaporation and lift-off was described in Section 4.7.2. Individual mesh devices were of size 7 mm x 11 mm (total die size of 12 mm x 15 mm) with two macro electrodes (7 mm x 2mm) for two-terminal resistance measurements. Four smaller mesh devices of size 2 mm x 2 mm (same linewidth and open area) were utilised for four-terminal sheet resistance measurements. Most of the mesh devices were made using Ti (10 nm)/Pt (50 nm) for the metal features and a smaller number of devices were fabricated using Ti (10 nm)/Al (50 nm) or Ti (10 nm)/Au (50 nm).

6.3 Characterisation

6.3.1 Optical and electrical characterisation

Optical and electrical characterisation measurements were performed as described in chapters 4 & 5. To test the mechanical stability of the mesh devices, they were

[b] UV lithography, metal evaporation and lift-off was carried out by Mr. Dan O' Connell and Mr. Colin Lyons in Tyndall (Speciality Product and Services group).

manually flexed over a known radius of curvature (~ 3.8 mm) in air. The two-terminal resistance was measured periodically every 200 cycles (up to 1,000 bending cycles).

6.3.2 Transparent heater characterisation

Thermal images, temperature and time plots were taken using a FLIR ONE Thermal Imager interfaced to an Android smartphone with a resolution of 120 x 160 pixels. The data was analysed using the FLIR Tools software using an "Iron" colour palette. For the mesh-graphene hybrid heater, a "Rainbow" colour palette was used. The camera was at a fixed working distance of ~ 4.5 cm when taking the thermal images and temperature readings. The accuracy of the FLIR One temperature readings in comparison to a temperature probe (IKA Werke ETS-D4) is given in Table C.1 in Appendix C. The power consumption of each heater was found by finding the mean and maximum temperature of each heater at 90 s after applying a constant bias voltage. When the thermal image was taken, the current value was found by using a digital multimeter (Mercurcy MTTR01) which was connected to the power supply (Aim – TTi EX752M).

To test the viability of the pentagonal mesh device for use as a transparent heater, a thin mist of water was sprayed on a 1 cm x 1cm glass coupon (1.2 mm thick) which was subsequently held above liquid nitrogen vapour. This process was repeated several times until an ice layer of thickness ~0.5 mm was observed. The glass substrate was then placed on the mesh device which was connected to a power supply (Aim – TTi EX752M) and a constant bias voltage was then applied.

6.4 Results and discussion

6.4.1 Transparency and haze of pentagonal metal meshes on flexible PET

Devices with a fixed linewidth of 5 μm and metal thickness (Ti ~ 10 nm, Pt ~ 50 nm) were fabricated on PET as described earlier for substrate sizes up to 4" (Figure C.1 in Appendix C). This approach could potentially be scaled up for manufacturing using roll-to-roll photolithography or nanoimprint lithography. The pentagonal metal mesh devices were based on targeting a lower transmission threshold of ~ 70% for the mesh itself as discussed in Chapter 4, section 4.6. The intrinsic transparency of a metal mesh structure, T_{mesh}, can be approximated from the geometric design as

$$T_{mesh} \approx 1 - A_{metal}/A_{total} \quad \textbf{(6.1)}$$

where A_{metal} is the area within the unit cell covered by metal and A_{total} is the total unit cell area. A 10x optical microscopy image of the newly discovered asymmetric pentagon design is shown in Figure 6.2 (a). For this particular pentagon, the (non-unique) unit cell consists of an array of twelve pentagons (one example shaded in grey). Following equation (6.1), the expected intrinsic transparency of the pentagonal mesh, T_{mesh} was estimated (see Appendix B) as

$$T_{mesh} \approx (1 - 1.36\, w/d) \quad \textbf{(6.2)}$$

where w is the linewidth of the mesh and d is the length of the smallest side ($w << d$).

The intrinsic transparency values of the three individual mesh designs (T_{mesh}) were estimated using equation (6.2 as T_{mesh} ~ 73% (Design#1, d = 25 μm), T_{mesh} ~ 86% (Design#2, d = 50 μm) and T_{mesh} ~ 91% (Design#3, d = 75 μm). Figure 6.2 (b) shows a photograph taken in natural light of a resultant metal mesh device (Design#3, 9% metal area coverage) patterned on PET. Each die fabricated contains a two-terminal rectangular device (mesh area 7 mm x 11 mm) for resistance and transparency measurements and four small square meshes (2 mm side) with the same mesh parameters as the rectangular device. The sheet resistance (four-terminal) was measured using the smaller mesh devices.

In order to assess the optical properties of the metal mesh devices, the transparency and haze of the metal meshes on PET substrates were measured in the wavelength range of 400 nm to 800 nm as described in the section 6.3.1. All absorption spectra were measured vs air. Thus the measured transparency (T) includes the absorption by the 125 μm thick PET substrate, $T = T_{PET}$ x T_{mesh}. The transparency of bare PET substrates was measured as ~ 88% at a wavelength, λ, of 550 nm. The transparency values at λ = 550 nm of the three pentagonal designs are given below in Table 6.1 and their spectra are in Figure 6.3.

Table 6.1: Estimated and Measured transparency values (with and without the effect of the underlying PET substrate) of all pentagonal metal mesh designs along with subsequent haze values (substrate effect not taken into account).

Pentagon type:	T_{mesh} (%) Estimated	T_{mesh} (%) Measured	T_{total} (%) Estimated	T_{total} (%) Measured	Haze (%) Measured
Design#1	73	70	64	62	9
Design#2	86	84	76	74	4
Design#3	91	89	80	78	5

The finite width of the mesh lines ($w/d = 0.2$) and residue from the lithographic process may have contributed to the slightly lower measured values of transparency compared to the estimated values ($\Delta T \sim 2\%$ for all three designs).

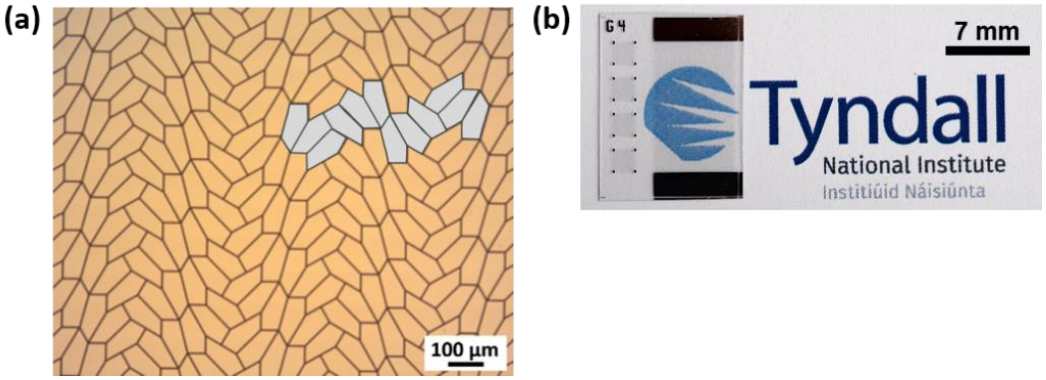

Figure 6.2: (a) High-resolution transmission-mode optical microscopy image at 10x magnification showing the asymmetric Pt pentagonal tiling with a linewidth of 5 µm (Design#2, 14% metal area coverage). The gray shaded twelve pentagon array is the unit cell (non-unique unit cell). (b) Photo depicting Pt metal mesh Design#3 (9% metal area coverage) on a PET substrate with two macro electrodes (7 mm x 2 mm) for two-terminal resistance measurements. Four smaller devices are used for four-terminal resistance measurements.

Haze, the ratio of diffusive transmittance (the difference between total and specular transmittance) to total transmittance is another critical parameter for transparent conductive electrodes [7]. Total transparency includes the contribution of scattered light and is measured using an integrating sphere setup. For example, a general requirement for touch screen displays are values of haze of < 3% [8]. Large haze values result in blurriness and reduces clear visibility of the device, which is

important for applications such as visible transparent heaters. The haze of the "Melinex" PET substrate was measured as ~ 1% at λ = 550 nm (Figure 6.3 inset) in good agreement with the manufacturers' specification of ~ 0.8% in the material data sheet (Figure 6.3 inset) [9] . The oscillatory type behavior of the transparency and haze spectra (Figure 6.3) is likely due to optical interference caused by the adhesive coating on one side of the Melinex substrate as received. The haze of the pentagon devices, taken at a wavelength of 550 nm were ~ 9% (Design#1, 27% metal area coverage), ~ 4% (Design#2, 14% metal area coverage), ~ 5% (Design#3, 9% metal area coverage). The large haze value of design 1 is expected due to the large metal coverage which can increase the likelihood of light scatter.

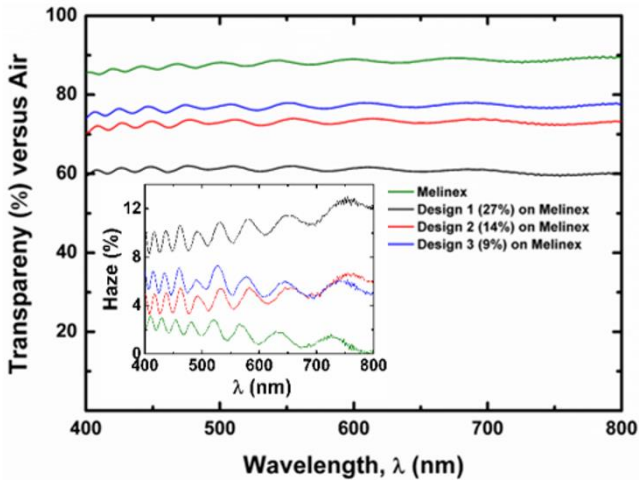

Figure 6.3: Plot of transparency (referenced against air) versus wavelength for all 3 Pt pentagonal metal mesh devices of linewidth 5 μm along with the Melinex substrate. (Inset) plot of haze versus wavelength for all mesh devices and the Melinex substrate. The number in brackets represents the % metal area coverage based on the unit cell. The oscillatory nature of transparency and haze spectra is due to the adhesive coating on one side of the PET substrate.

6.4.2 Two point resistance and sheet resistance of asymmetric pentagonal metal meshes

The electrical properties of mesh patterned metal films are dictated by the metal area coverage, the metal linewidth and the thickness and resistivity of the chosen metal. A reduced sheet resistance is easily obtained from varying these parameters when compared to increasing the transparency which is controlled by a solitary parameter,

the mesh open area. However, the thickness of the metal is limited after a certain point due to fabrication costs and metal shadowing, which affects the transparency. The two-terminal resistance and sheet resistance (four terminal) were measured as described in section 6.3.1. The smaller mesh devices (Figure 6.2 (b)) were used for sheet resistance measurements. The smaller mesh devices were of equal length and width (2 mm x 2 mm) along with metal electrodes at the periphery. The two–terminal resistance (averaged over seven Pt devices for a particular pentagon design) yielded values of ~ 55.7 ± 3.2 Ω (Design#1, d = 25 μm), ~ 109.6 ± 7.7 Ω (Design#2, d = 50 μm) and ~ 147.5 ± 6.5 Ω (Design#3, d = 75 μm). The initial sheet resistance values (averaged over seven Pt devices for a particular pentagon design) were subsequently measured as ~ 30.3 ± 2.2 Ω/sq (Design#1, d = 25 μm), ~ 69.1 ± 4.8 Ω/sq (Design#2, d = 50 μm) and ~ 91.7 ± 3.9 Ω/sq. (Design#3, d = 75 μm).

Using a lower resistivity metal can lower the sheet resistance of these asymmetric metal meshes without altering the transparency. For example, Pt has a bulk resistivity value of ~ 10.8 μΩcm, while the resistivity values of gold and aluminium are lower at ~ 2.4 μΩcm and 2.8 μΩcm respectively [10]. Proof of concept devices were obtained for each design based on Ti (10 nm)/Au (50 nm) and Ti (10 nm)/Al (50 nm). The averaged two–terminal resistance values and sheet resistance values of each pentagon design for the three different types of metal are given in Table 6.2.

Table 6.2: Average values of the two-terminal resistance, sheet resistance and figure of merit (σ_{DC}/σ_{op}) for Pt, Au and Al pentagonal metal meshes on flexible PET.[a, b ,c]

Pentagon design:	Metal:	R_0 (Ω/sq):	Rsh_0 (Ω/sq):	σ_{DC}/σ_{op}:
Design 1	Ti (10 nm):Pt (50 nm)[a]	55.7 ± 3.2	30.3 ± 2.2	32 ± 2
Design 1	Ti (10 nm):Au (50 nm)[b]	20.1 ± 1.5	10.6 ± 0.2	91 ± 1
Design 1	Ti (10 nm):Al (50 nm)[c]	33.4 ± 3.1	15.9 ± 0.9	68.2 ± 0.5
Design 2	Ti (10 nm):Pt (50 nm)[a]	109.6 ± 7.7	69.1 ± 4.8	30.1 ± 2.1
Design 2	Ti (10 nm):Au (50 nm)[b]	39.3 ± 3.9	22.9 ± 0.3	91.2 ± 1.8
Design 2	Ti (10 nm):Al (50 nm)[c]	56 ± 2	30.3 ± 0.2	61 ± 3
Design 3	Ti (10 nm):Pt (50 nm)[a]	147.5 ± 6.5	91.7 ± 3.9	34.3 ± 1.5
Design 3	Ti (10 nm):Au (50 nm)[b]	49.8 ± 0.6	28.3 ± 1.1	111 ± 4
Design 3	Ti (10 nm):Al (50 nm)[c]	82.2 ± 2.3	46.5 ± 0.9	68 ± 1

[a] Values averaged over 7 devices. [b] Values averaged over 3 devices. [c] Values averaged over 3 devices

A figure of merit has been proposed to quantitatively assess the performance of a transparent conductive electrode by relating the parameters of sheet resistance and transparency [11, 12] as described in the Chapter 1, section 1.4. It's commonly denoted as the ratio of electrical conductivity to optical conductivity:

$$\sigma_{DC}/\sigma_{op} = Z_0/\left(2R_S\left(T^{-1/2}-1\right)\right) \quad \textbf{(6.3)}$$

where Z_0 is the impedance of free space (~ 377 Ω) and R_S and T are the sheet resistance and intrinsic transparency (transparency of the mesh itself) of the device. Using equation (6.3), values of σ_{DC}/σ_{op}~ 32 ± 2 (Pt, Design#1, d = 25 μm), ~ σ_{DC}/σ_{op}~ 30.1 ± 2.1 (Pt, Design#2, d = 50 μm) and σ_{DC}/σ_{op}~ 34.3 ± 1.5 (Pt, Design#3, d = 75 μm) were achieved for these devices (averaged over 7 devices for each pentagon design). Although this is lower than the value for ITO on PET (with values of R_S ~ 7 Ω/sq and T ~ 84%) of σ_{DC}/σ_{op} ~ 296 [13]. See The sheet resistance of a metal grid has been defined previously [14]:

$$R_S = \xi \frac{\rho_G}{t_G F_f} \quad \textbf{(6.4)}$$

where ξ is a correction factor, ρ_G is the resistivity of the grid, t_G is the thickness of the grid and F_f is a geometric filling factor based on the geometry of the metal mesh. The figure of merit could also be improved to match or even exceed the ITO values by employing a metal with lower resistivity. Future work will focus on demonstration of transparent meshes using lithographic patterning of copper (e.g., through sputtering or electrodeposition). For example, using Design#2 with a copper mesh of thickness 100 nm would yield a figure of merit σ_{DC}/σ_{op} ~ 370 (since ρ_{Pt}/ρ_{Cu} ~ 6.2).

6.4.3 Mechanical stability of pentagonal metal meshes after cyclic bending

Mechanical stability is another important criteria for transparent conductive electrodes due to recent consumer demands for flexible electronics. ITO's ceramic nature severely limits its flexibility. Chen *et al.* reported catastrophic device failure for a ~ 110 nm film at tensile strain values < 1.7% on 188 μm thick PET [15]. ITO coated on PET (thickness of ~ 130 μm) undergoes failure strain at ~ 1.2% [16]. Cyclic bending tests are undertaken to gauge the effect of bending on device performance which reflects repeated consumer device use. ITO also fails in this regard [17]. Mechanical

bending tests Figure 6.4 were undertaken on all 3 pentagonal mesh designs. 3 devices of each pentagon design (9 devices in total) were used for tensile bending strain, while 3 devices of each pentagon design (9 devices in total) were used for compressive bending strain. All devices were bent (supported ends) at a radius of curvature, r_C ~ 3.8 mm. The strain was the same at ~ 1.6% and found using the method in the previous chapter (section 5.4.3). The resistance was measured after every 200 bending cycles up to 1,000 bending cycles.

Figure 6.4 (a) presents the variation of the two terminal resistance after *n* cycles, R_n, in relation to the original two terminal resistance, R_0, as a function of bending cycles for all three designs (based on Pt metal deposition) under tensile strain. Good mechanical stability was observed, however all devices showed measurable increases in resistance. After 1,000 bending cycles, devices subjected to tensile strain showed fractional resistance increases in the range 8% to 17% (i.e. $1.08 < R_{1000}/R_0 < 1.17$) with the lowest changes observed for Design#2. Our results compare favorably with literature reports (see Table 6.3). For example, a value of R_{1000}/R_0 ~ 2.5 was achieved for a copper mesh (thickness ~ 1.8 μm, linewidth ~ 900 nm) with a comparable bending radius of 4 mm [18]. This fractional resistance change exceeds values obtained for metal mesh devices that underwent tensile strain herein. An Au mesh (thickness ~ 500 nm, linewidth 10 μm) was reported to have a fractional resistance change of ~ 1.42 under tensile strain with a comparable bending radius of 5 mm [19]. Note that this was only after 200 cycles and the metal meshes herein display a much lower change even after 800 more bending cycles.

Kim *et al.*, reported fractional sheet resistance changes < 8% for hexagonal Cu mesh structures (metal thickness ~ 60 nm, linewidth ~ 1 μm) protected with an aluminum doped zinc oxide capping layer (~ 75 nm thick, R_S ~ 8 kΩ/sq.) after 1,000 bending cycles at a radius of curvature ~ 2 mm [20]. Devices subjected to compressive strain (Figure 6.4 (b)) showed lower fractional resistance increases after 1000 cycles than tensile-strained devices (for Pt mesh devices), again in agreement with literature reports (see Table 6.3) Fractional resistance changes in the range 0% to 7% were observed (i.e. $1 < R_{1000}/R_0 < 1.07$) with best results observed for Design#1. Very recently, Li and co-workers reported an elegant method for fabrication of thick Cu meshes (~ 1.8 μm) with sub-micron linewidths (~ 900 nm) embedded in cyclic olefin

co-polymers. Those structures showed lower resistance variation for compressive strain than tensile strain under a bending radius of 4 mm [18]. A value of R_{1000}/R_0 ~ 1.07 was achieved for the aforementioned Cu mesh under compressive strain [18] after 1,000 bending cycles with a comparable radius of curvature of ~ 4 mm. This value is comparable to some fractional resistance changes obtained after 1,000 bending cycles for metal meshes in this chapter (see Table 6.3). A fractional resistance change of ~ 1.9 was achieved for an Au mesh (thickness ~ 50 nm) under compressive strain after 500 bending cycles. Even though the value reported is higher than the values obtained for metal mesh devices in this chapter, the value was achieved with a much smaller bending radius of << 1 mm [21].

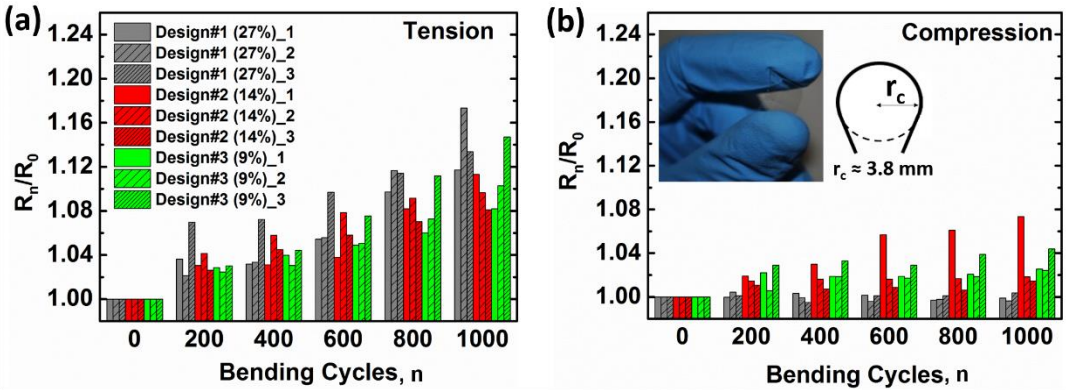

Figure 6.4: (a) Two-terminal resistance ratio (R_n/R_0) versus number of bending cycles (n) for all 3 Pt pentagonal mesh designs (3 devices of each pentagon design, 9 devices in total) under tensile strain in air for a radius of curvature, r_c, = 3.8 mm. Percentage values in parentheses in the legend represents metal areal coverage (b) Corresponding data (different devices) for compressive strain. (Inset) photo showing bending of the metal mesh on a PET substrate and a schematic depicting the radius of curvature that was used.

Cyclic bending was also undertaken on pentagonal metal meshes based on Ti (10 nm)/Au (50 nm) and Ti (10 nm)/Al (50 nm) (Figure 6.5). Gold has the highest ductility among metals and this is reflected in the cyclic bending data in Fractional resistance increases in the range 0% to 5% were observed (i.e. $1 < R_{1000}/R_0 < 1.05$) for Au pentagonal meshes under tensile strain. Under compressive strain, fractional resistances increase in the range of 0% to 3% were observed (i.e. $1 < R_{1000}/R_0 < 1.03$)

for Au metal meshes. Au is also the most malleable metal, allowing it to undergo compressive strain without catastrophic failure. However, the same cannot be said for Al meshes where larger fractional resistance changes were observed for compressive-based strain ($1.18 < R_{1000}/R_0 < 1.23$). Moderate values were observed for tensile-based strain ($1.04 < R_{1000}/R_0 < 1.10$). Based on the malleable properties of metals, Al is expected to outperform Pt. However, this is not the case and may be due to using a metal thin film rather than bulk metal and the existence of the 10 nm Ti adhesion layer which can also influence the mechanical stability of these devices.

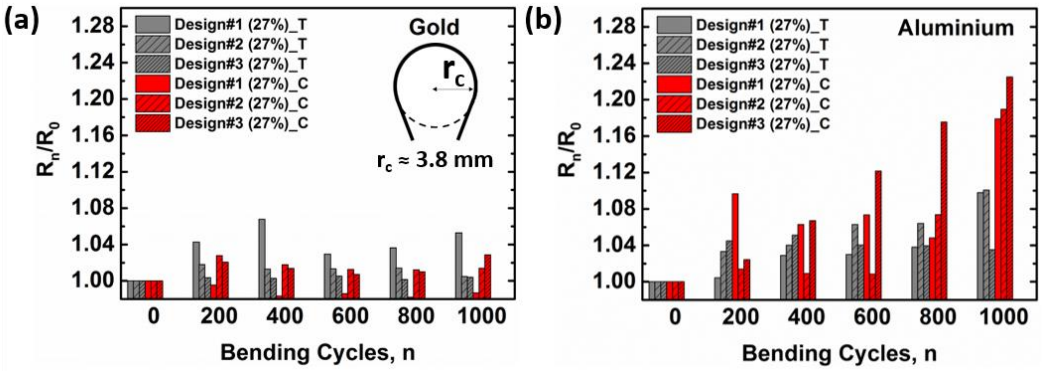

Figure 6.5: (a) Two-terminal resistance ratio (R_n/R_0) versus number of bending cycles (n) for all Au pentagonal mesh designs (3 devices of each pentagon design, 9 devices in total) under both tensile (denoted as "T") and compressive (denoted as "C") strain in air for a radius of curvature, r_c, = 3.8 mm. Percentage values in parentheses in the legend represents metal areal coverage. (Inset) schematic depicting the radius of curvature that was used. (b) Corresponding tensile and compressive strain data for Al pentagonal metal meshes.

From Table 6.3, the fractional resistance change after 1,000 bending cycles of the metal mesh devices herein are lower than those reported by some literature publications. Thus, the author hypothesises that the asymmetric design of this newly discovered pentagon may potentially offer advantages for mechanical stability of metal mesh based technologies. The non-unique unit cell may prevent re-occurring mechanical failure at specific locations when the device is subjected to uni-axial and/or multi-axial strain. However, further experimental work and simulation will be required to assess and optimize device design (e.g., modification of asymmetric patterns by locally increasing feature minimum radius of curvature at "pinch points" to reduce stress concentrations).

We note that the resistance changes are considerably lower than for devices flexed over a rigid rod (Chapter 5). This is likely due to the fact that bending over a substrate can result in local adhesion and stress concentration "pinch points". The rate of strain can also influence the mechanical stability of flexible devices. When devices were flexed over a rod, the strain rate was ~ 30 cycles per minute. For devices flexed in air, the strain rate was ~ 15 cycles per minute. This lower rate of strain may account for the improved mechanical properties of pentagonal metal meshes when compared to the previous chapter. Also, to ensure that the radius of curvature was kept constant while bending in air, bending was undertaken in 50 cycle intervals followed by resting for 1 minute in-between. To ensure accurate measurements of the two-terminal resistance, all devices were placed immediately in the probe station after each 200 bending cycle intervals.

Increases in device resistance due to cyclic bending can be linked to the formation of defects and/or dislocations in the metal mesh. Fatigue theory predicts longer device life under compression-compression fatigue when compared to both tension-tension fatigue and tension-compression fatigue [22]. Back and forth movement of dislocations results in formation of persistent surface deformations (extrusions/intrusions) that ultimately lead to micro-cracks and eventual device failure. If the fatigue cycle is tension-tension or tension-compression, dislocations are forced to move towards the free surface leading to persistent surface deformations after a certain number of cycles. On the other hand if the cycle is compression-compression, dislocation movement is largely away from the free surface decreasing the possibility of persistent surface deformation.

Optical inspection was undertaken on each device after 1,000 cycles of bending (tension and compression) to investigate the adhesion of the metal mesh on the PET substrate. No delamination of the metal mesh was observed over all devices, suggesting that the resistance increase is due to micro-crack formation rather than delamination. Representative transmission-mode optical microscopy images of Design#3 as fabricated and post-1,000 bending cycles (tensile strain) is included in Figure C.2 in Appendix C. Optical microscopy images acquired after adhesion "tape tests" on devices following cyclic bending tests (see Figure C.3 in Appendix C) also showed no evidence of delamination.

Table 6.3: Literature comparison of cyclic bending for metal meshes. For Pt metal meshes, the largest resistance change is given for tensile and compressive bending based on each design. For Au and Al meshes, all cyclic bending devices are given.

Substrate:	Material:	Metal thickness (nm):	Metal linewidth (μm):	Bending type:	Bending Radius (mm):	Bending Cycles:	R_n/R_0:	Ref:
Polyimide	Cu	60	1	-[a]	2	1000	1.08	[20]
Cyclic olefin copolymer	Cu	1800	0.9	Tension	4	1000	2.5	[18]
Cyclic olefin copolymer	Cu	1800	0.9	Compression	4	1000	1	[18]
PET	Cu	40	-	-	-	1200	1	[23]
PDMS	Au	350	0.35	-	3	100	1	[24]
PEN	Au	90	90	-	-	1000	1	[25]
PET	Au	100	10	Tension	5	200	1.15	[19]
PET	Au	500	10	Tension	5	200	1.42	[19]
PET	Cu	20	0.1	Tension	12.7	150	1.21	[26]
PET	Cu	20	0.1	Compression	12.7	150	1.06	[26]
PDMS	Au	50	-	Compression	<< 1	500	1.9	[21]
PET	Cr/Au	5/20	5	-	2.5	500	8	[27]
PET	Graphene + Al	100	5	Tension	5	500	1.2	[28]
PET	Graphene + Al/Cu	5/100	10	Tension	5	500	1.5	[28]
(D#1_T_2)	Ti/Pt	10/50	5	Tension	3.8	1,000	1.17	Our work
(D#1_C_1)	Ti/Pt	10/50	5	Compression	3.8	1,000	1	Our work
(D#2_T_1)	Ti/Pt	10/50	5	Tension	3.8	1,000	1.11	Our work
(D#2_C_1)	Ti/Pt	10/50	5	Compression	3.8	1,000	1.07	Our work
(D#3_T_1)	Ti/Pt	10/50	5	Tension	3.8	1,000	1.15	Our work
(D#3_C_3)	Ti/Pt	10/50	5	Compression	3.8	1,000	1.04	Our work
(D#1_T_1)	Ti/Au	10/50	5	Tension	3.8	1,000	1.05	Our work
(D#1_C_1)	Ti/Au	10/50	5	Compression	3.8	1,000	1	Our work
(D#2_T_1)	Ti/Au	10/50	5	Tension	3.8	1,000	1	Our work
(D#2_C_1)	Ti/Au	10/50	5	Compression	3.8	1,000	1.01	Our work
(D#3_T_1)	Ti/Au	10/50	5	Tension	3.8	1,000	1	Our work
(D#3_C_1)	Ti/Au	10/50	5	Compression	3.8	1,000	1.03	Our work
(D#1_T_1)	Ti/Al	10/50	5	Tension	3.8	1,000	1.10	Our work
(D#1_C_1)	Ti/Al	10/50	5	Compression	3.8	1,000	1.18	Our work
(D#2_T_1)	Ti/Al	10/50	5	Tension	3.8	1,000	1.10	Our work
(D#2_C_1)	Ti/Al	10/50	5	Compression	3.8	1,000	1.19	Our work
(D#3_T_1)	Ti/Al	10/50	5	Tension	3.8	1,000	1.04	Our work
(D#3_C_1)	Ti/Al	10/50	5	Compression	3.8	1,000	1.23	Our work

[a]-, lack of reported data in the article.

6.4.4 Platinum pentagonal metal meshes for use as transparent heaters

All 3 designs were studied to demonstrate their use as visible transparent heaters. Although the transparency of Design#1 (T ~ 62%) is less than the industrial standard required for automobile windscreens of 70% [29], its efficacy as a transparent heater was evaluated. A DC bias was applied to the pentagonal mesh devices which caused Joule heating. Voltages in the range of 2 V to 5 V in steps of 0.5 V were applied to the pentagonal mesh devices for 90 s until a saturation temperature range was observed. The exception is Design#1 (27% metal area coverage) as voltages above 4 V resulted in temperatures above 120 ^{o}C. The FLIR One thermal camera is specified to accurately read temperatures to 120 ^{o}C [30]. The temperature was recorded every second using an infrared thermal camera at a fixed working distance of ~ 4.5 cm. A thermal image of the pentagonal mesh (Design#2, 14% metal area coverage) depicted in Figure 6.6 (a) resulted in a max temperature of ~ 86 ^{o}C achieved after 90 s seconds by applying 5 V to the device. A thermal image of the mesh device, 40 s after removing the power source and thermal images of Design#1 and Design#3, 90 s after applying 5 V are given in Figure C.4 in Appendix C.

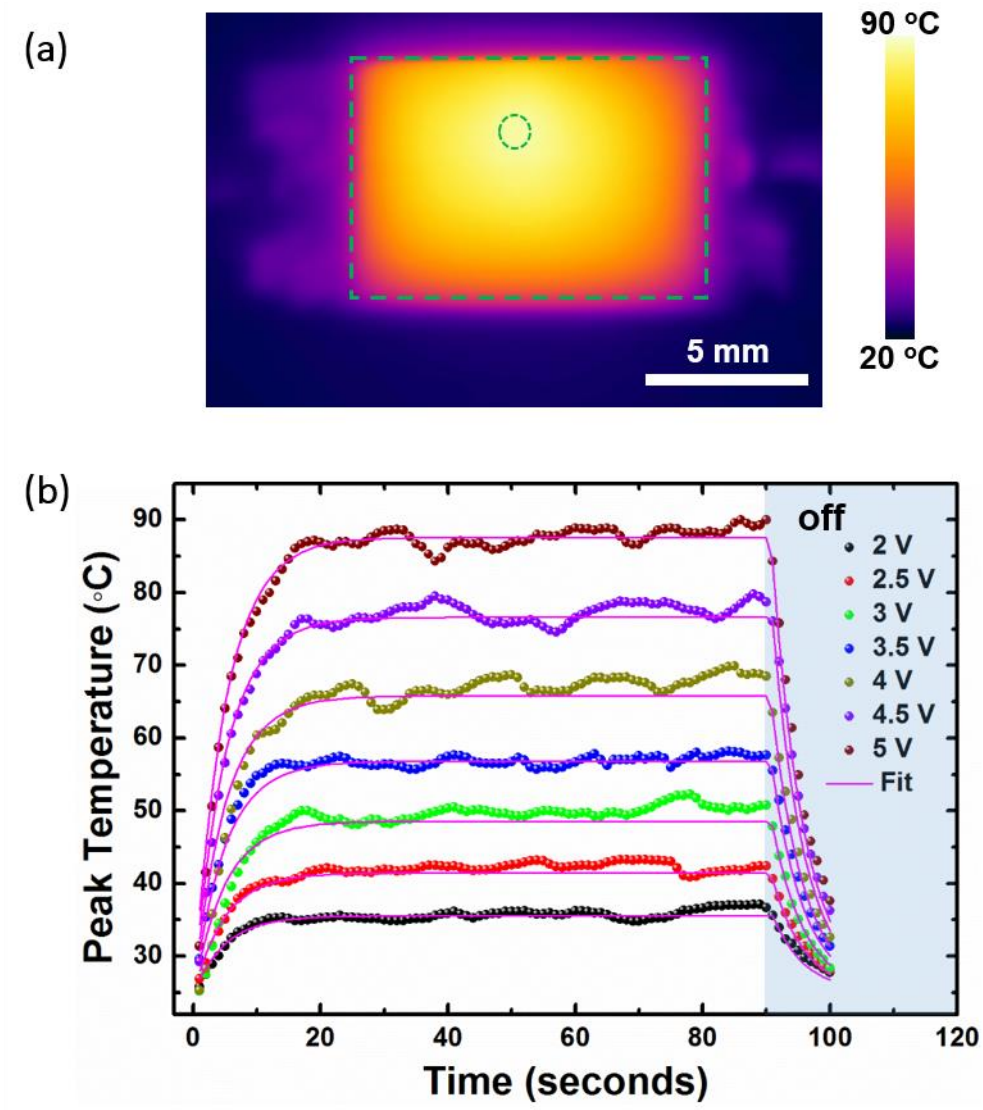

Figure 6.6: (a) Thermal image of pentagonal metal mesh based transparent heater (Design#2, 14% metal area coverage) taken at 90 s after applying 5 V bias. The temperature distribution in the rectangular region is shown in Figure S6. Dashed circle indicates peak device temperature (b) Measured peak temperature versus time of this device at various bias voltages (2 V to 5 V). All data were fitted (solid curves) using equation (6.5) with the same heat transfer coefficient (h_{Fit} = 42 Wm^2K^{-1}) and time constant (τ = 5 s).

Various groups have investigated alternative heaters based on metal meshes and metal nanowire networks which allow the use of lower applied voltages to achieve suitable saturation temperatures when compared to carbon-based transparent heaters. Kiruthika *et al.* demonstrated an Ag mesh (~ 300 nm thick) formed from a crackle templating method [31]. Voltages of 3 V, 6 V and 9 V were applied with maximum temperatures of ~ 50 ^{o}C, ~ 105 ^{o}C and ~ 175 ^{o}C achieved respectively. The higher saturation temperature achieved by this Ag mesh compared to this work is due to the mesh's low sheet resistance (~ 1 Ω/sq) and the use of higher voltages. The active area of the pentagonal mesh devices herein are 0.7 cm x 1.1 cm and lower temperatures were observed at the edges of the devices which is evident from the thermal image in Figure 6.6 (a) and temperature distribution plot in (Figure C.5, Appendix C) with a mean temperature distribution over the marked area of ~ 69 ± 12 ^{o}C. Lower temperatures at the edge of a transparent heater has been suggested to occur due to radiative heat loss [31, 32]. Inhomogeneous temperatures at the device periphery has also been reported by Kiruthika *et al.* where a temperature distribution of ~ 128 ± 43.5 ^{o}C was measured over a device with an applied voltage of 9 V. The device area of 10 x 8 cm^2 explains the larger temperature distribution compared to the pentagonal metal mesh devices in this work. Metal nanowire network based transparent heaters require uniformly interconnected nanowires to obtain homogenous temperatures. To achieve uniform interconnects, Kim *et al.* prepared an Ag nanowire device (R_S ~ 10 Ω/sq and T ~ 90%) of size 50 mm x 75 mm [33]. By applying 7 V, the Ag nanowire film achieved a maximum temperature of ~ 105 ^{o}C. A maximum temperature of ~ 70 ^{o}C was reported by applying 5 V for this Ag nanowire network. A larger peak temperature of ~ 86 ^{o}C was observed for the pentagonal metal mesh (Design#2, 14% metal area coverage) at 5 V, likely due to the smaller device area.

Figure 6.6 (b) shows the measured peak temperature (single point) versus time (t) for the Design#2 device shown in Figure 6.6 (a) for a range of (constant) bias voltages (2 V to 5 V). Each peak temperature value was measured after 90 seconds of constant applied voltage and the corresponding current was also recorded to estimate the (instantaneous) power at t = 90 s. Increased fluctuations in peak temperature were observed for larger bias voltages, likely reflecting the influence of spatially inhomogeneous heat transfer and also circulating air in the laboratory.

The thermal resistance for each heater design were obtained from linear

regression of the peak temperature versus power density (W/cm^2) data (Figure C.6, Appendix C). The extracted thermal resistance values were in the range 213-258 ^{o}C cm^2/W (see Table 6.4) and compare favorably with literature reports for transparent heaters (see Table 6.5). A large thermal resistance is desirable for transparent heater applications. The state of the art values for thermal resistances in the current literature are ~ 515 ^{o}C cm^2/W and ~ 255.2 ^{o}C cm^2/W [2, 31]. The thermal resistance of the Design#2 device (~ 235 ^{o}C cm^2/W) is higher than values obtained for other heaters reported in the literature based on single walled carbon nanotubes (~ 140 ^{o}C cm^2/W) [34], graphene (~ 163 ^{o}C cm^2/W) [35] and Ag nanowires (~ 85 ^{o}C cm^2/W) [4], and compares well to the thermal resistance achieved for an Au wire network transparent heater (~ 189 ^{o}C cm^2/W) [3].

The temperature response of the heater after applied bias voltage can be described by using a simple model for heat transfer across a single interface[68]:

$$\mathrm{T_{heater}} = \mathrm{T_0} + \left(\frac{P}{hA}\right)\left(1 - \mathrm{e}^{-\mathrm{t}/\tau}\right) \qquad \textbf{(6.5)}$$

where T_{heater} is the heater temperature, T_0 is the ambient temperature, P is the power, h is the heat transfer coefficient (Wm^{-2}K^{-1}), A is the surface area of the heater, t is the time elapsed after applying the bias voltage and τ is a time constant. Experimental values for the heat transfer coefficient (h_{Exp}) for each design were estimated from the inverse of the thermal resistance (see Table 1). The solid curves in Figure 4b show fits to the temperature vs. time data using Equation 7 with the same value of the heat transfer coefficient (h_{Fit} = 42 Wm^{-2}K^{-1}) and time constant (τ = 5 s) for all data. The same parameters were used to fit the temperature decay when the bias voltage was switched off. The fits using this simple model show excellent agreement with the data and the fit value for the heat transfer coefficient agrees well with the value extracted from the thermal resistance data (h_{Exp}; see Table 6.4). Fits to heater devices fabricated using Design#1 and Design#3 also show good agreement with experimental data (Figure C.7, Appendix C). The agreement between the experimental and fit values for the heat transfer coefficient is excellent for Design#3, however the fit to the Design#1 device yielded a slightly lower value for h_{Fit}.

Table 6.4: Thermal resistance, heat transfer coefficient, time constant and saturation temperature for each design.

Pentagon design	Thermal resistance ($°Ccm^2W^{-1}$)	h_{Exp} (Wm^{-2} K^{-1})	h_{Fit} (Wm^{-2} K^{-1})	τ (s)
Design#1	213 ± 7	47.0 ± 1.5	44	5
Design#2	235 ± 7	42.6 ± 1.3	42	5
Design#3	258 ± 5	38.8 ± 0.8	39	5

The fits also allow a reasonable estimate of the response time, since for an exponential fit, the temperature will be within 5% of the saturation temperature at $t_{response} = 3\tau$. A low response time is desired at low input power. An automobile battery voltage is commonly 12 V, with voltages less than this value required for this heater application, to minimize power consumption. The low response time in this work agrees favourably with graphene-based [36] (response time ~ 100 s) and nanowire network-based [33] (response time ~ 60 s) transparent heaters which required higher voltages of 12 V and 7 V respectively. The graphene-based heaters with a response time of ~ 100 s is likely due to the use of an additional PET layer on both graphene devices, which was used to protect the device against atmospheric environmental stresses. Kang *et al.* reported two graphene based heater on PET which achieved saturation temperatures of ~ 65 ^oC (4 layer graphene doped with HNO_3) and ~ 100 ^oC (4 layer graphene doped with $AuCl_3$-CH_3NO_2) [36]. Although the temperature of ~ 100 ^oC for the second graphene device is higher than the saturation temperature achieved in this work of ~ 88 ± 1 ^oC (device 2, 14% metal area coverage), it required an applied voltage of 12 V. A comparison of the pentagonal mesh devices compared to transparent heaters reported in literature is shown in Table 6.5.

Table 6.5: Visible Transparent Heater Comparison and De-Icing Parameters[a, b, c, d, e]

Material:	Substrate:	Tmaterial[a] (%):	Ttotal[b] (%):	R_{sheet} (Ω/sq):	Area (cm^2):	Ice Formation:	Voltage (V):	Power Density (W/cm^2):	Peak Temp. (^oC):	Thermal Resistance ($^oC\ cm^2/W$):	Response time (s):
Ag mesh[31]	Glass	77	71	1	10 x 8	Liquid N_2	8.5	0.57	170	255	-[c]
Ag mesh[2]	PET	86	76	6	4 x 3	NA[d]	-	0.13	100	515	20
Ag mesh[2]	Convex lens	86	79	6	-	Liquid N_2	6	-	60	-	-
Ag mesh -graphene[37]	PET	89	78	4	5 x 5	NA	4	0.2	140	-	< 30
Ag NW[33]	PET	90	79	10	5 x 7.5	NA	7	-	105	-	~ 60
Ag NW[33]	PET	90	79	10	5 x 7.5	NA	5	-	70	-	~ 60
Ag NW[33]	Glass	-		50	5 x 7.5	Freezer	12	-	-	-	-
Au mesh[3]	Glass	87	80	5.4	2.5 x 2.5	NA	15	2.8	600	189	~ 38
Design#1_Heater (27% metal area coverage)	PET (125 µm)	70	62	29	0.7 x 1.1	NA	4	0.39	111[e]	213	~ 15 (3τ)[f]
Design#2_Heater (14% metal area coverage)	PET (125 µm)	84	74	77	0.7 x 1.1	Liquid N_2	5	0.26	86[e]	235	~ 15 (3τ)[f]
Design#3_Heater (9% metal area coverage)	PET (125 µm)	89	78	94	0.7 x 1.1	NA	5	0.18	69[e]	258	~ 15 (3τ)[f]

[a]Transparency of the transparent electrode material only i.e. transparency of mesh, mesh + graphene or nanowires. [b]Total transparency (including the absorbance of the underlying substrate) calculated by using the value of ~ 88% for the PET substrate measured in this work. [c]-, Lack of reported data. [d]NA, not applicable. [e] Mean temperature achieved by the heaters in this work at 90 s after applying the constant bias voltage. [f] Maximum temperature achieved by the heaters in this work at 90 s after applying the constant bias voltage.

Thermal expansion is another important property for transparent heaters which is often overlooked in the literature. Thermal strain can be produced due to the differential thermal expansion of the metal (Ti and Pt) and the underlying PET substrate. This thermal strain can cause unwanted effects such as cracks when under thermal cycling (heating and cooling) [38, 39]. For instance, the thermal expansion coefficients of bulk Ti and bulk Pt are ~ 8.6 x 10^{-6} $^{o}C^{-1}$ and ~ 9.1 x 10^{-6} $^{o}C^{-1}$ respectively for a temperature range of 20 ^{o}C to 100 ^{o}C [40]. While for PET (Melinex) it's estimated at ~ 1.8 x 10^{-5} $^{o}C^{-1}$ from the material data sheet [9]. Note that the manufacturer only specified this thermal expansion coefficient value between 20 ^{o}C to 50 ^{o}C. The thermal stress can de deduced from the following formula [39]

$$\varepsilon = \Delta\alpha . \Delta T \tag{6.6}$$

where $\Delta\alpha$ is the difference between the thermal expansion coefficient of the materials and ΔT is the change in temperature. Since the difference in the thermal expansion coefficient between Ti and Pt is small, the thermal stress between the metal and substrate was found by using the thermal expansion coefficient of Pt and the substrate. For example, a thermal stress of ε ~ 5.7 x 10^{-4} was deduced for the Design#2 heater using equation (6.6) where the initial temperature was ~ 22 ^{o}C and the final temperature was ~ 86 ^{o}C after applying a bias voltage of 5 V for 90 s (see Table 6.5). This value assumes that bulk metal is used, that $\Delta\alpha$ is independent of temperature and that the temperature of the PET substrate was equal to that of the Pt metal mesh. The last assumption was made as the temperature of the heater under various voltages was measured on the front side of the device, so the heat lost to the PET substrate was not taken into account. Although the estimated value of the thermal stress is small, continual thermal cycling could cause unwanted mechanical damage of the metal features. Optical microscopy images (Figure C.8, Appendix C) show that no mechanical damage has occurred for Design#2 which underwent a total of 10 thermal cycles (heating and cooling) for all voltages i.e. 2 V to 5 V in steps of 0.5 V.

6.4.5 Platinum pentagonal metal mesh and graphene hybrid electrode[c]

Kang *et al.* have reported that the use of a graphene layer in conjunction with a square Ag mesh (linewidths of 10 µm) has shown to improve the temperature homogeneity of a transparent heater. Its suggested that this occurs due to graphene's high thermal conductivity [37]. Subsequently, CVD graphene was transferred on to Design#2 using the procedure in Chapter 3, section 3.3.1 and a thermal images were taken after 90 s of applying 5 V (Figure 6.7 (a) and (c)). The temperature distribution over the heater area for the hybrid heater was ~ 66 ± 18 ºC, while it was ~ 69 ± 12 ºC for the stand alone heater. A lower minimum temperature was also observed for the hybrid heater of ~ 26 ºC in comparison to the mesh heater of ~ 33 ºC. A larger maximum temperature was present for the hybrid heater (92 ºC versus 86 ºC). Therefore a "comparison area" was taken when comparing both devices. A temperature distribution over the marked "comparison area" was taken for Design#2 and Design#2 with graphene (Figure 6.7 (b) and (d)) as it appeared to be more uniform for the hybrid heater by eye. However, the mean temperature across the marked "comparison area" increased from ~ 81 ± 3 ºC to ~ 86 ± 4 ºC when the graphene layer was transferred on top of the metal mesh. Since the metal mesh and graphene layer act as a resistors in parallel, one would expect the resistance of the metal mesh to decrease slightly with the introduction of the graphene layer, even though its resistance is typically on the order of ~ kΩ. This explains the slight increase in mean temperature. Lower temperatures observed at the edges of the hybrid heater may be due to edge defects on the graphene film. In the aforementioned paper, the mean temperature decreased with the hybrid heater. This difference may have occurred because the mesh was applied over the graphene layer, rather than the graphene layer being placed on the mesh as is the case in this work.

[c] Graphene transfer was undertaken by Ms. Roxane Puicervert in Tyndall (Nanotechnology group).

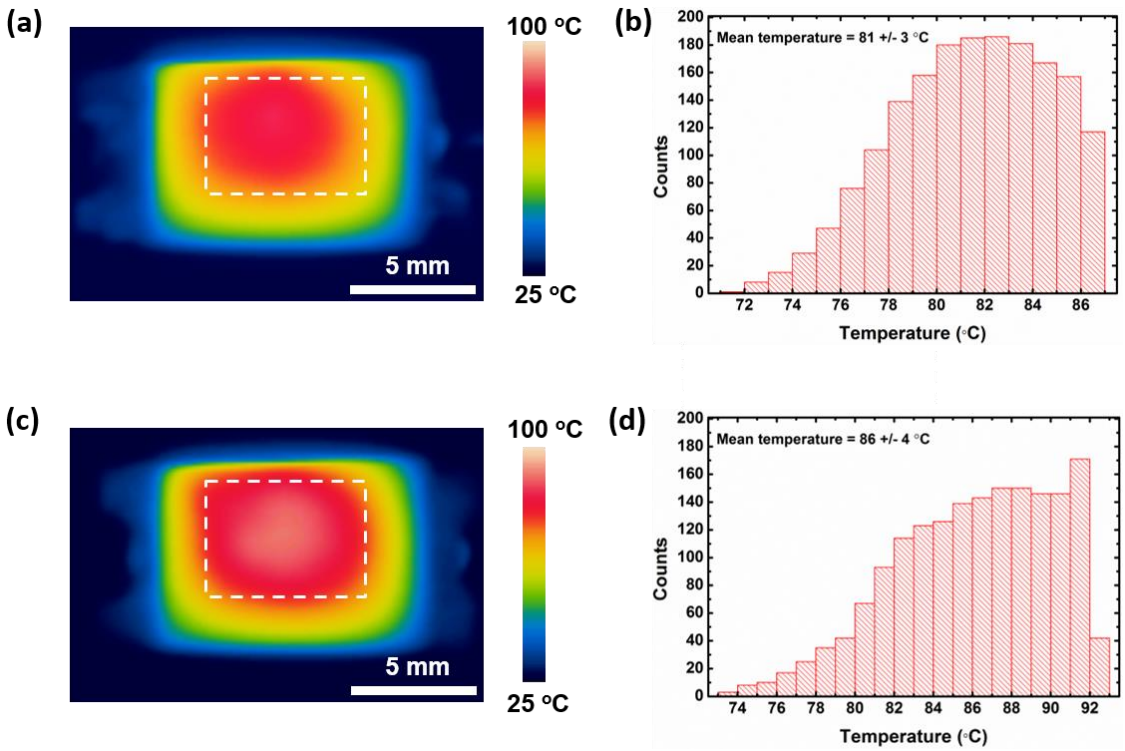

Figure 6.7: (a) Thermal image of pentagonal metal mesh based transparent heater (Design#2, 14% metal area coverage) taken at 90 s after applying 5 V. (b) Temperature distribution of the marked "comparison area" in (a). (c) Thermal image of pentagonal metal mesh (Design#2, 14% metal area coverage)-graphene hybrid transparent heater taken at 90 s after applying 5 V. (d) Temperature distribution of the marked "comparison area" in (c).

Kang *et al.* demonstrated that the temperature homogeneity of the hybrid heater was also sensitive to the Ag grid pitch [37]. For example, the Au grid with a pitch of 150 µm resulted in a similar standard deviation for the mean temperature of the grid and the hybrid heater. Once the grid pitch was increased to 250 µm, the standard deviation for the mean temperature of the hybrid heater was less than that of the grid itself (19.8 ^{o}C versus 13.3 ^{o}C) and decreased even more when the pitch was increased further. Using equation (5) in Appendix A for the % metal area coverage of a square mesh, the device with a 150 µm pitch (10 µm linewidth) corresponds to ~ 9.1% metal coverage. While the next device with a pitch of 250 µm, results in ~ 7.9% metal coverage. This may explain why the temperature distribution for Design#2 (14% metal area coverage)-graphene hybrid heater is not more homogenous than the stand alone metal mesh heater. To test this, graphene was also transferred to Design#1 (27%

metal area coverage) and Design#3 (9% metal area coverage). The mean temperature over the heater area for the hybrid and standalone mesh heater based on Design#3 were the same. Although, the standard deviation was larger for the hybrid film (13 ^{o}C versus 9 ^{o}C). This suggests that very low metal coverage (< 8%) is required to obtain more homogenous temperatures when using a metal mesh graphene hybrid heater. See Table 6.6 for a comparison between the pentagonal mesh and pentagonal mesh-graphene hybrid heaters.

Table 6.6: A comparison table between Pt pentagonal mesh heaters and hybrid heaters (with graphene).[a]

Device:	R_0 (Ω):	Min Temperature (Heater Area) (^{o}C):	Min Temperature (Heater Area) (^{o}C):	Max Temperature (Heater Area) (^{o}C):	Mean Temperature (Comparison Area) (^{o}C):
Design#1	53.31	87 ± 16	37	111	103 ± 5
D#1-graphene[a]	47.62	89 ± 20	32	117	110 ± 4
Design#2	119.72	69 ± 12	33	86	81 ± 3
D#2-graphene	102.68	66 ± 18	26	92	86 ± 4
Design#3	159.98	56 ± 9	29	69	65 ± 2
D#3-graphene	140.81	56 ± 13	25	75	70 ± 3

[a]-, Design#1 is designated as D#1. Design#2 is designated as D#2. Design#3 is designated as D#3.

6.4.6 Platinum pentagonal metal mesh heater as a de-icer

The Joule effect was used to demonstrate the use of the asymmetric pentagonal metal mesh as a visible transparent heater for de-icing purposes. For its use of de-icing windscreens, the mesh device would be embedded in the glass rather than being fabricated on the glass surface itself where delamination can occur. Therefore using a

frozen glass piece which is placed on the mesh device followed by application of a voltage is a better reflection of the transparent heater's de-icing performance. Many publications have carried out de-icing on films where ice formation is achieved by placing the film in a freezer [33, 41]. In this work, a similar reported approach was used [2, 31], which consisted of applying a thin layer of water over liquid nitrogen vapours with sequential addition of a thin water layer using a spray bottle. Before the voltage was applied to the mesh device, the temperature (~ 19.6 ^{o}C) and humidity (~ 56 %) in the lab were recorded. Once the glass piece with frozen water was placed on the mesh device (Design#2, 14% metal area coverage), a DC bias of 5 V was applied. The de-icing process took ~ 45 s and the visualisation of the "Tyndall" logo after de-icing is evident (Figure 6.8 (b)). The time taken to de-ice compares favourably with similar methods using liquid nitrogen vapors [2, 31], where de-icing occurred in ~ 120 s under 6 V and ~ 120 s under 8.5 V respectively. Larger voltages and longer de-icing times were required in those literature reports since the voltage was applied in the presence of liquid nitrogen vapor in each case. Also the large device area of ~ 10 x 8 cm^2 used by Kiruthika *et al.* also explains why a longer de-icing time was required [31], when compared to the device area of ~ 0.7 x 1.1 cm^2 in this work.

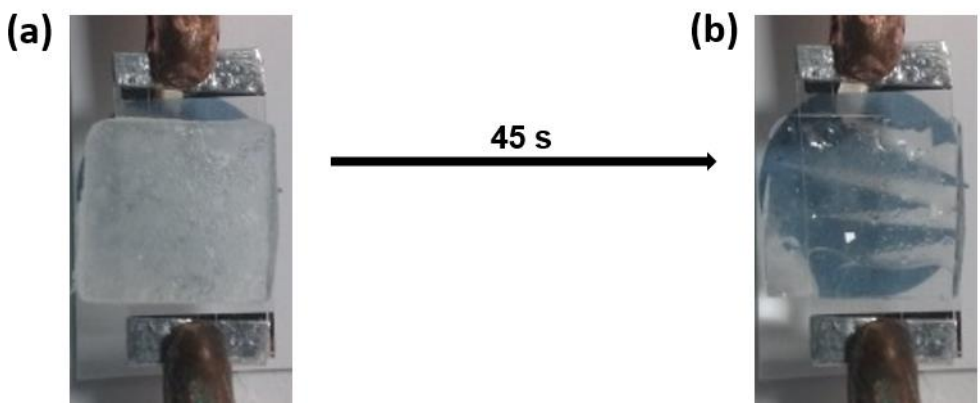

Figure 6.8: (a) Ice formation on a glass coupon of size ~ 1 cm x 1 cm (thickness of ~ 1.2 mm) by liquid nitrogen vapours which was subsequently placed on top of device 2 (14% metal area coverage) on PET. (b) Demonstration of ice removal by applying 5 V for ~ 45 seconds, allowing the visibility of the "Tyndall" logo underneath.

6.5 Conclusion

Transparent platinum mesh electrodes and heaters based on a newly discovered asymmetric pentagonal tiling have been demonstrated. Initial results of Au and Al based mesh electrodes are also included. Measured devices showed good mechanical performance with modest increases in device resistance after cyclic bending under tensile strain (8-17%) and smaller increases (0-7%) for compressive strain. Device performance compares well with literature reports for flexible transparent electrodes and proof-of-concept demonstrations of heaters/de-icers, with rapid response times was observed. The response time for each heater was estimated using a multiple of the time constant, τ and gives a more accurate estimation of its value. The expected temperature of each heater was estimated using a simple model for heat transfer across a single interface. The heaters displayed good thermal resistance values which exceeded those reported for graphene, single walled carbon nanotubes and silver nanowire networks. The values also compare favourably with an Au wire network transparent heater reported in the literature. Thus the asymmetric pentagonal platinum meshes could be used as flexible transparent heaters due to their good mechanical and thermal characteristics.

Future work will focus on development of methods for patterning of meshes using low-cost ductile metals, e.g., Cu, using either sputtering or electrodeposition. Additional investigations will focus on investigating the influence of asymmetry on failure under multi-axial strain. Design optimisation based on simulations will target highly reliable or even self-healing flexible, transparent electrodes, e.g. by pattern modification to reduce minimum radius of curvature in features at “pinch-point” junctions and features.

6.6 Bibliography

1. *Transparent Heater utilizes ITO technology*. 2003; Available from: http://news.thomasnet.com/fullstory/transparent-heater-utilizes-ito-technology-27584.
2. Gupta, R., et al., *Spray Coating of Crack Templates for the Fabrication of Transparent Conductors and Heaters on Flat and Curved Surfaces.* ACS Applied Materials & Interfaces, 2014, **6**(16), p. 13688-13696
3. Rao, K.D.M. and G.U. Kulkarni, *A highly crystalline single Au wire network as a high temperature transparent heater.* Nanoscale, 2014, **6**(11), p. 5645-5651
4. Celle, C., et al., *Highly flexible transparent film heaters based on random networks of silver nanowires.* Nano Research, 2012, **5**(6), p. 427-433
5. Ragab, T. and C. Basaran, *Joule heating in single-walled carbon nanotubes.* Journal of Applied Physics, 2009, **106**(6), 063705
6. Peterson, J.D., *Control system for eliminating ice from a transparent windshield panel*. Google Patents.
7. Preston, C., et al., *Optical haze of transparent and conductive silver nanowire films.* Nano Research, 2013, **6**(7), p. 461-468
8. Gupta, R., et al., *Visibly Transparent Heaters.* ACS Applied Materials and Interfaces, 2016, **8**(20), p. 12559-12575
9. *Melinex ; Product No. ST504 [Online]; Flexible Electronics Dupont Teijin Films; USA: Chester, VA. http://www.dupontteijinfilms.com/FilmEnterprise/Datasheet.asp?Result=Print&ID=269&Version=US (accessed May 10, 2016).*
10. Cutnell, J. and K. Johnson, *Physics - 8th Edition*. 2009, Wiley: New York. p. 603.
11. Sepulveda-Mora, S.B. and S.G. Cloutier, *Figures of Merit for High-Performance Transparent Electrodes Using Dip-Coated Silver Nanowire Networks.* Journal of Nanomaterials, 2012, **2012**, p. 7, 286104
12. De, S. and J.N. Coleman, *Are there fundamental limitations on the sheet resistance and transmittance of thin graphene films?* ACS Nano, 2010, **4**(5), p. 2713-2720
13. Guillén, C. and J. Herrero, *Comparison study of ITO thin films deposited by sputtering at room temperature onto polymer and glass substrates.* Thin Solid Films, 2005, **480-481**, p. 129-132
14. Ghosh, D.S., T.L. Chen, and V. Pruneri, *High figure-of-merit ultrathin metal transparent electrodes incorporating a conductive grid.* Applied Physics Letters, 2010, **96**(4), 041109
15. Chen, Z., et al., *A mechanical assessment of flexible optoelectronic devices.* Thin Solid Films, 2001, **394**(1-2), p. 202-206
16. Bouten, P.C.P. *Failure test for brittle conductive layers on flexible display substrates*. in *SID Conference Record of the International Display Research Conference*. 2002.
17. Cairns, D.R. and G.P. Crawford, *Electromechanical properties of transparent conducting substrates for flexible electronic displays.* Proceedings of the IEEE, 2005, **93**(8), p. 1451-1458

18. Khan, A., et al., *High-Performance Flexible Transparent Electrode with an Embedded Metal Mesh Fabricated by Cost-Effective Solution Process.* Small, 2016, **12**(22), p. 3021-3030
19. Gao, T., et al., *Hierarchical Graphene/Metal Grid Structures for Stable, Flexible Transparent Conductors.* ACS Nano, 2015, **9**(5), p. 5440-5446
20. Kim, W.K., et al., *Cu mesh for flexible transparent conductive electrodes.* Scientific Reports, 2015, **5**, p. 3519−3521
21. Guo, C.F., et al., *Highly stretchable and transparent nanomesh electrodes made by grain boundary lithography.* Nat Commun, 2014, **5**, 3121
22. Fleck, N.A., C.S. Shin, and R.A. Smith, *Fatigue crack growth under compressive loading.* Engineering Fracture Mechanics, 1985, **21**(1), p. 173-185
23. Zhou, W., et al., *Copper Mesh Templated by Breath-Figure Polymer Films as Flexible Transparent Electrodes for Organic Photovoltaic Devices.* ACS Applied Materials & Interfaces, 2016, **8**(17), p. 11122-11127
24. Jang, S., et al., *A three-dimensional metal grid mesh as a practical alternative to ITO.* Nanoscale, 2016, **8**(29), p. 14257-14263
25. Park, J.H., et al., *Flexible and Transparent Metallic Grid Electrodes Prepared by Evaporative Assembly.* ACS Applied Materials & Interfaces, 2014, **6**(15), p. 12380-12387
26. Gao, T., et al., *Uniform and Ordered Copper Nanomeshes by Microsphere Lithography for Transparent Electrodes.* Nano Letters, 2014, **14**(4), p. 2105-2110
27. Qiu, T., et al., *Hydrogen reduced graphene oxide/metal grid hybrid film: towards high performance transparent conductive electrode for flexible electrochromic devices.* Carbon, 2015, **81**, p. 232-238
28. Zhu, Y., et al., *Rational Design of Hybrid Graphene Films for High-Performance Transparent Electrodes.* Acs Nano, 2011, **5**(8), p. 6472-6479
29. Smith, R.T., M.J. Chern, and R.G. Hegg, *Automotive head-up display with high brightness in daytime and high contrast in nighttime*. Google Patents: USA.
30. Bel Hadj Tahar, R., et al., *Tin doped indium oxide thin films: Electrical properties.* Journal of Applied Physics, 1998, **83**(5), p. 2631-2645
31. Kiruthika, S., R. Gupta, and G.U. Kulkarni, *Large area defrosting windows based on electrothermal heating of highly conducting and transmitting Ag wire mesh.* RSC Advances, 2014, **4**(91), p. 49745-49751
32. Bae, J.J., et al., *Heat Dissipation of Transparent Graphene Defoggers.* Advanced Functional Materials, 2012, **22**(22), p. 4819-4826
33. Kim, T., et al., *Uniformly Interconnected Silver-Nanowire Networks for Transparent Film Heaters.* Advanced Functional Materials, 2013, **23**(10), p. 1250-1255
34. Kang, T.J., et al., *Thickness-dependent thermal resistance of a transparent glass heater with a single-walled carbon nanotube coating.* Carbon, 2011, **49**(4), p. 1087-1093
35. Sui, D., et al., *Flexible and Transparent Electrothermal Film Heaters Based on Graphene Materials.* Small, 2011, **7**(22), p. 3186-3192
36. Kang, J., et al., *High-Performance Graphene-Based Transparent Flexible Heaters.* Nano Letters, 2011, **11**(12), p. 5154-5158
37. Kang, J., et al., *An Ag-grid/graphene hybrid structure for large-scale, transparent, flexible heaters.* Nanoscale, 2015, **7**(15), p. 6567-6573

38. MacDonald, W.A., et al., *Latest advances in substrates for flexible electronics.* Journal of the Society for Information Display, 2007, **15**(12), p. 1075-1083
39. Mönig, R., R.R. Keller, and C.A. Volkert, *Thermal fatigue testing of thin metal films.* Review of Scientific Instruments, 2004, **75**(11), p. 4997-5004
40. Cverna, F., *Thermal Properties of Metals - Chapter 2: Thermal Expansion*. 2002, ASM International. p. 11.
41. Yoon, Y.H., et al., *Transparent Film Heater Using Single-Walled Carbon Nanotubes.* Advanced Materials, 2007, **19**(23), p. 4284-4287

7 Conclusion

Tin-doped indium oxide, which is a wide bandgap semiconductor dominants the transparent conductive electrode market due to its high optical transparency and low sheet resistance. However, it has several disadvantages, such as the rising cost of indium and its brittle nature. These drawbacks will impede its use for future flexible optoelectronic devices. This thesis investigates alternative materials to compete with ITO in the flexible transparent conductive electrode market.

The first material that was investigated was monolayer graphene. Chapter 2 demonstrated the growth of graphene by thermal chemical vapour deposition. The electrical performance of CVD graphene films is influenced by domain boundaries which act as charge carrier scattering sites. Domain sizes were increased i.e. number of domain boundaries were reduced by investigating certain factors such as the use of acid pre-treatment before growth, the substrate geometry and growth pressure. Although, the results were not an advance over the state of the art, this chapter raised an important issue of CVD graphene growth. This issue is the reliability of the CVD system for graphene growth, which is overlooked in the literature. Although, four large area continuous growth runs were achieved, the reliability of the CVD system diminished over time, with a lower presence of graphene on the Cu foil on subsequent runs. The author proposes the use of a small quartz tube CVD system, which would easily allow regular maintenance (cleaning and repairing) and the use of a gas purifier in the methane gas line.

Chapter 3 showcased the transfer of CVD graphene to Si/SiO_2 and glass substrates using a wet chemical transfer process. The removal of the PMMA support layer for graphene during the transfer process is critical, as residual layers can influence the sheet resistance of the film. Therefore a novel approach was demonstrated in this chapter which involved the usual room temperature removal of PMMA by acetone followed by two heated acetone cleans at 60 ^{o}C for 10 minutes. Statistical analysis was undertaken on eight samples transferred to Si/SiO_2 (90 nm thermal oxide) via optical microscopy, atomic force microscopy (AFM) and Raman spectroscopy. Statistical analysis suggests that it would be beneficial to only carry out one heated acetone clean. The continuous growth runs from the previous chapter were

transferred to Si/SiO_2 and glass substrates. A high transparency of ~ 97% was measured along with a sheet resistance of ~ 2.4 kΩ/sq. The sheet resistance decreased to ~ 400 Ω/sq after non-covalent molecular functionalisation with TFSA.

The next alternative material which was discussed in chapter 4 was lithographically patterned micron-scale metal meshes. Platinum meshes were fabricated on rigid glass substrates by three different deposition techniques; evaporation and lift-off, ALD and dry etching and sputter deposition and dry etching. The comparison of differing metal deposition techniques for metal meshes has not been discussed in the literature to this author's knowledge. Metal mesh geometries included symmetric geometries (square, hexagonal and circular) and newly discovered asymmetric pentagonal tiling. AFM analysis suggested that evaporation and lift-off provided the most consistent mesh height and the lowest substrate roughness. ALD and sputter deposition suggested incomplete dry etching, with vary mesh height and higher substrate roughness. The sheet resistance, transparency and haze of all platinum meshes based on the three deposition techniques were measured. Evaporated meshes produced the highest figure of merit along with the lowest standard of deviation, FOM ~ 42 ± 6 and thus was the technique used for metal deposition in the rest of the thesis.

In chapter 5, platinum metal meshes, with a constant metal linewidth of 5 µm, were fabricated on flexible PET substrates by evaporation and lift-off. Thirteen mesh devices were bent over a rod with a known radius of curvature of ~ 3.8 mm. The two-terminal resistance was measured every 200 cycles up to 1,000 bending cycles. The lowest fractional resistance increase after 1,000 cycles, R_{1000}/R_0 ~ 1.6 was measured for an asymmetric pentagonal metal mesh (5 µm linewidth, 14% metal coverage). The author hypothesises that the asymmetry of the pentagonal mesh may have the potential ability to distribute forces when strained, which leads to better mechanical stability over symmetrical geometries.

In chapter 6, platinum meshes based on the newly discovered asymmetric pentagonal tiling were fabricated. Devices were subjected to both tensile and compressive based strain around a radius of curvature of ~ 3.8 mm in air up to 1,000 bending cycles. Results for both tensile and compressive based strain suggest good mechanical performance in relation to literature. The asymmetric pentagonal metal meshes were then used as flexible transparent heaters via Joule heating. All devices

showcased good thermal characteristics such as low response times (~ 15 s) under low bias voltages (≤ 5 V) and high thermal resistances (213−258 °C cm^2/W). Finally, the efficacy of the pentagonal metal mesh transparent heater as a de-icer was demonstrated by applying water over liquid nitrogen vapours on a thick piece of glass. Subsequently, the frozen glass coupon was placed over Device#2 and de-icing occurred in ~ 45 s under an applied voltage of 5 V.

8 Suggestion for future work

Following the fabrication of transparent metal meshes based on differing geometries, future work could involve failure mode analysis to gauge points of failure after a set number of bending cycles. The thermal camera could be used in conjunction with this work. Initial thermal images of bent metal meshes suggest that devices must undergo catastrophic failure mechanisms to observe any hot spots on thermal images.

Besides the metal deposition techniques used in this thesis, electrochemical plating may provide a fast and cost effective method of patterning metal meshes. Preliminary results were based on fabricating Pt on top of Ti:Pt metal meshes on rigid glass substrates using a Teflon electrochemical cell and a solution of 2% H_2PtCl_6 (Figure 8.1). However the Pt thickness increase was not uniform with Pt thicknesses measured from 300 nm to 1 µm (metal thickness as fabricated ~ 70 nm) using a Tencor profilometer. Optimisation of the plating time and the uniformity of the plated metal film is essential. Future work could involve Cu electrochemical plating as copper is less expensive that platinum, gold and silver. The mesh structures will first be patterned by optical lithography on glass followed by the creation of a polydimethylsiloxan**e** (PDMS) mould. Resist will then be applied to the PDMS mold and will be bought into contact with a rigid glass substrate. The glass substrate containing the mesh structures will then undergo pyrolisation. Following this the mesh patterns will be applied to flexible substrates and metal plating will commence.

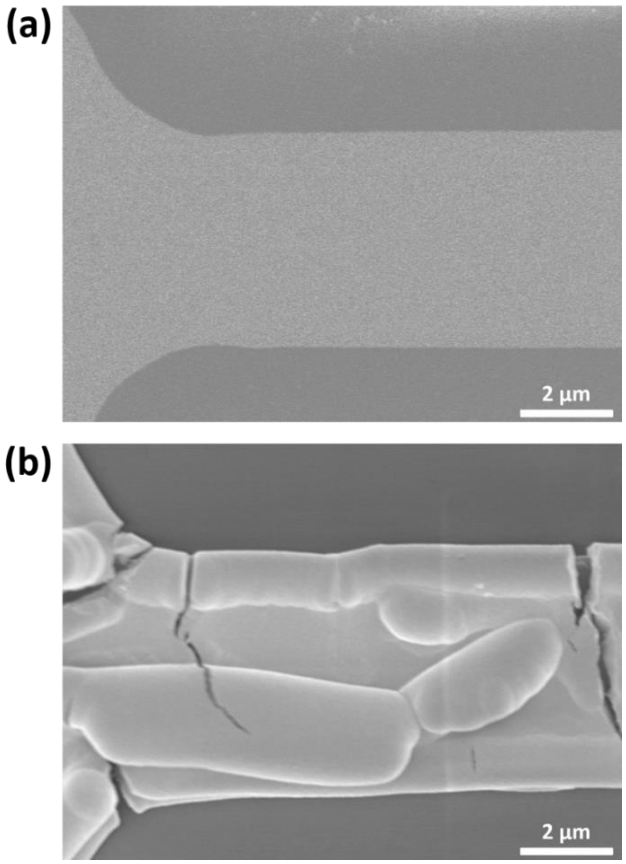

Figure 8.1: SEM images of (a) hexagon (5 µm, 22%) as fabricated and (b) SEM image of the same device following Pt electroplating at -0.5 V for 30s using a solution of 2% H_2PtCl_6. Tencor profilometer measurements confirmed Pt electroplating in the thickness range of 300 nm to 1 µm.

Only one type of convex pentagon was used in thesis, which was discovered at the end of 2015. Nanoimprint lithography could be investigated as an alternative to optical lithography. Although this is an expensive method due to the creation of the patterns by electron beam lithography, the mould can withstand alot of use. Rolith have shown that the use of sub-micron linewidths is an effective method to reduce the haze of metal mesh devices. Therefore, nanoimprint lithography will be investigated with differing classes of convex pentagons.

1 Appendix A:

Degradation of thermal CVD system in Tyndall

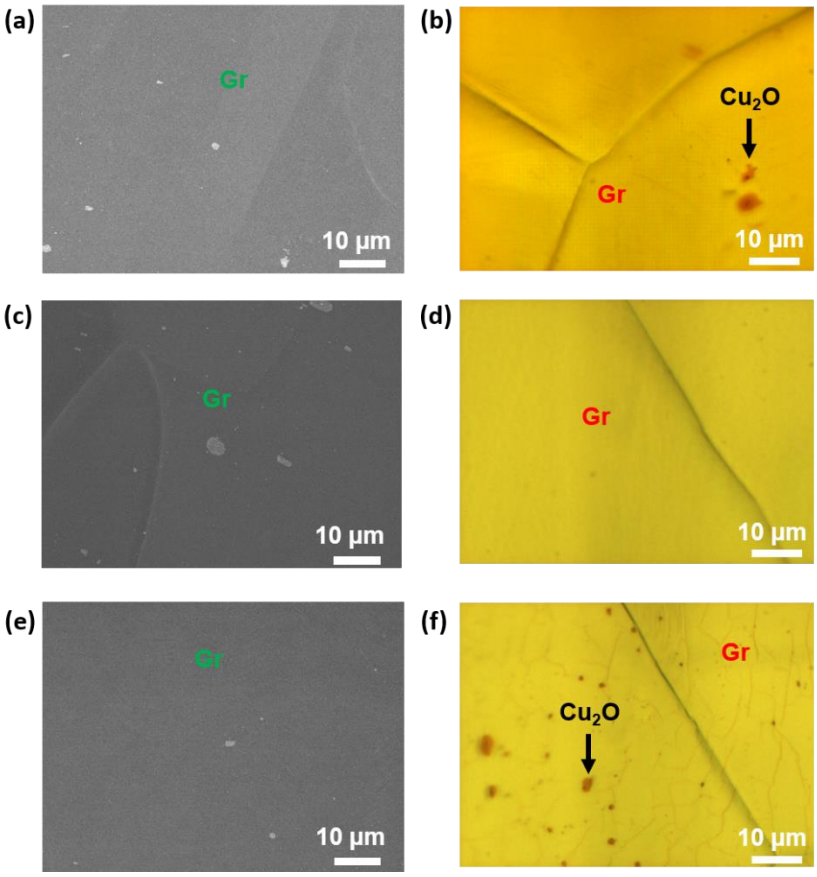

Figure A.1: Representative SEM images (left panel) and 100x optical microscopy images (right panel) of three continuous growth runs (runs 49, 50 and 51) based on the same growth parameters of the first successful continuous run in Tyndall (run 48). (a) and (b), (c) and (d) and (e) and (f) each represent one run. These growth runs consisted of applying an acid pre-treatment to Cu tube foil geometry followed by annealing in H_2 at 1,035 ^oC for 15 minutes, growth using CH_4 for 15 minutes and subsequent cooling to room temperature in H_2 as discussed in the main text. In all three cases, high graphene coverage was obtained. The presence of graphene and Cu_2O was confirmed by Raman spectroscopy.

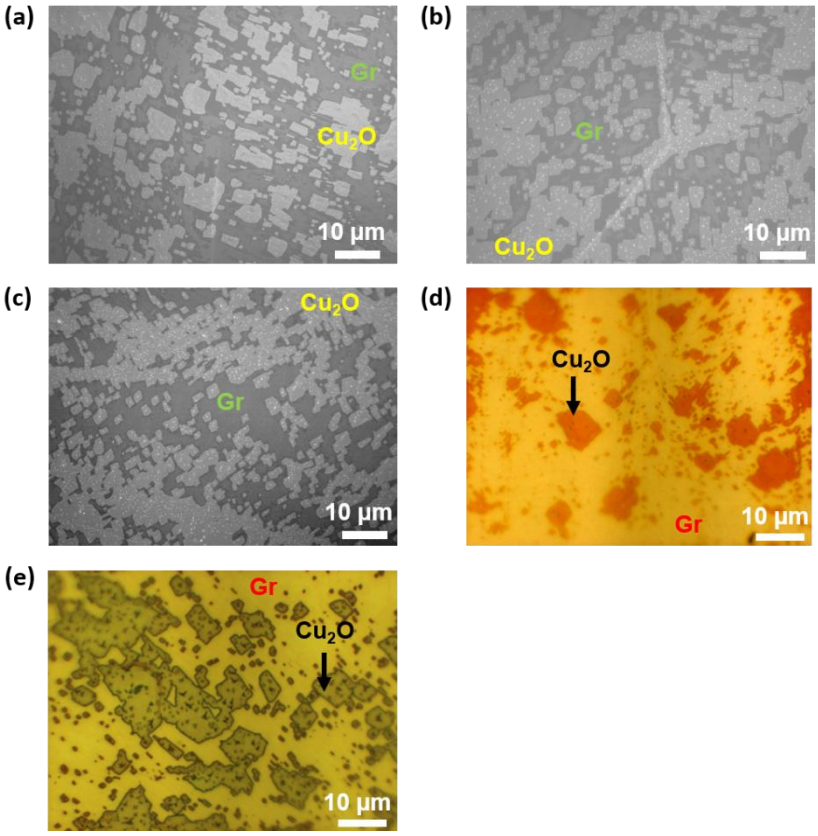

Figure A.2: Representative SEM and 100x optical microscopy images of five continuous growth runs corresponding to (a) run 63, (b) run 64, (c) run 65, (d) run 69 and (e) run 72. These runs were carried out using the same parameters as the previous continuous growth runs (runs 48 to 51) in Figure A.1. Note the larger presence of Cu_2O to graphene, which was confirmed by Raman spectroscopy.

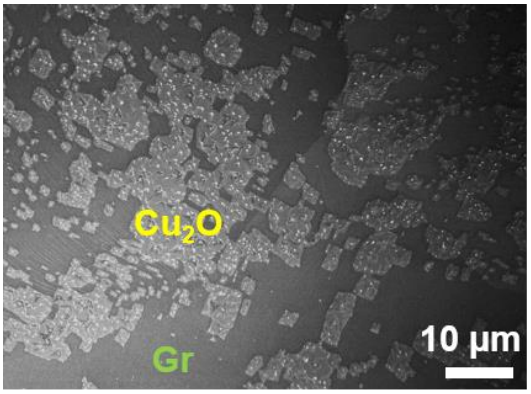

Figure A.3: Representative SEM image of a CVD run 76 which consisted of an acid pre-treatment on the foil, followed by annealing at 1,035 ^{o}C in H_2 for 15 minutes in the CVD system. The foil was then taken out of the CVD system and another acid pre-treatment was used. The foil was then placed in the CVD system for graphene growth (CH_4, 15 minutes at 1,035 ^{o}C). However, inconsistent growth was still observed with a large presence of Cu_2O which was confirmed by Raman spectroscopy.

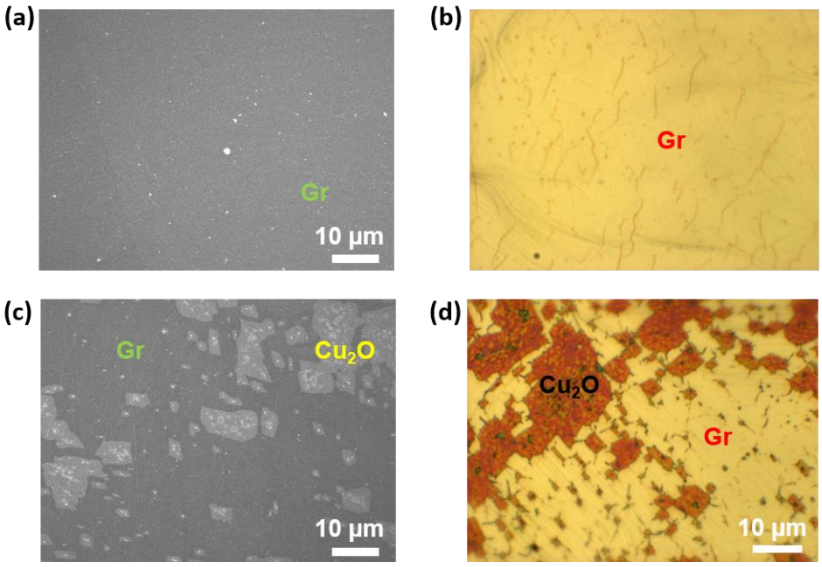

Figure A.4: Representative SEM and 100x optical microscopy images of two CVD runs (runs 108 and 109) carried out after changing the quartz tube, quartz gas injector and quartz thermocouple sheath. (a) and (b) represent run 108, while (c) and (d) represent run 109. Note that high graphene coverage was obtained for the first run after changing the system components. However the second run once again displayed insufficient graphene growth. The presence of Cu_2O was confirmed by Raman spectroscopy.

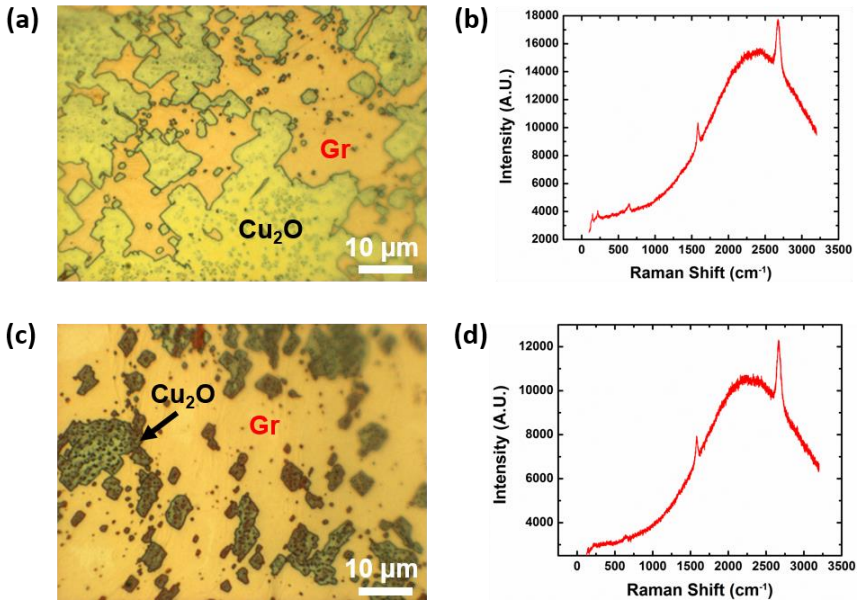

Figure A.5: Representative 100x optical microscopy images of two CVD runs (runs 112 and 113) carried out with (a) a 2" diameter quartz vapour trapping tube (run 112) and (c) a 1" diameter quartz vapour trapping tube (run 113). (b) & (d) Representative Raman spectra showing showing the *G* (~ 1589 cm^{-1} & ~ 1585 cm^{-1}) and *2D* (~ 2666 cm^{-1} & ~ 2674 cm^{-1}) peaks of graphene in both cases. Minute Cu_2O peaks can be seen at ~ 642 cm^{-1}, ~ 218 cm^{-1} and ~ 152 cm^{-1} in both spectra.

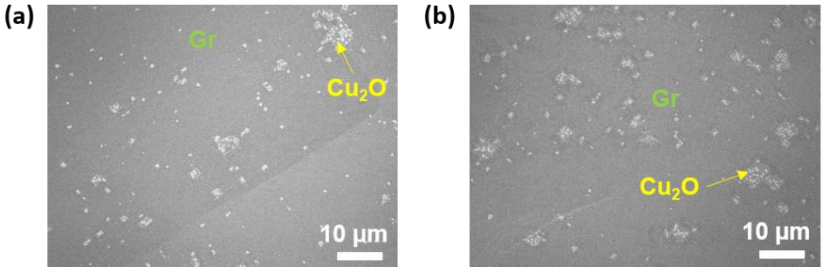

Figure A.6: Representative SEM images of two CVD runs (run 124 and 125) after the installation of a gas purifier in the methane gas line. (a) Represents run 124, while (b) represents run 125. The growth quality improved from the previous attempts, but the graphene coverage was not as continuous as observed in the first four continuous CVD runs (runs 48 to 51).

2 Appendix B:

Derivations of transmission for mesh geometries

2.1 Square mesh geometry

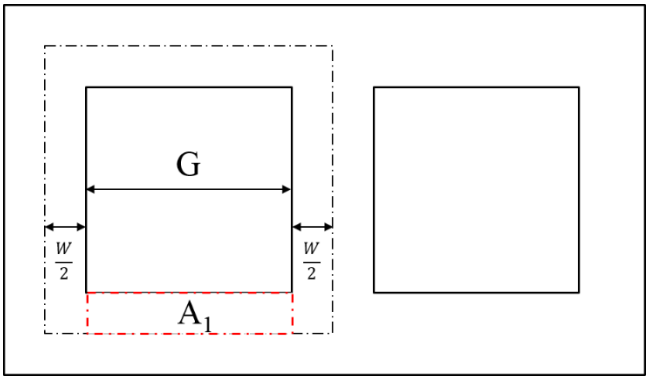

Figure B.1: Schematic of square mesh with unit cell (dashed area).

G = Grid Spacing, W = linewidth

Unit cell area:

$$A_{cell} = \left(G + \frac{W}{2} + \frac{W}{2}\right)^2 = (G + W)^2 \quad \textbf{(1)}$$

Mesh area:

$$A_{mesh} = 4A_1 + 4\left(\frac{W}{2}\right)^2 \quad \textbf{(2)}$$

Where;

$$A_1 = G\left(\frac{W}{2}\right) = \frac{GW}{2} \quad \textbf{(3)}$$

Therefore:

$$A_{mesh} = 4\left(\frac{GW}{2}\right) + 4\left(\frac{W}{2}\right)^2 = 2GW + W^2 \quad \textbf{(4)}$$

% Area covered by metal ≡ Q:

$$Q = \frac{A_{mesh}}{A_{cell}} = \frac{2GW + W^2}{(G+W)^2} \quad \textbf{(5)}$$

Transparency = 1 – Q:

$$T = 1 - Q \approx 1 - \frac{2GW + W^2}{(G+W)^2} \quad \textbf{(6)}$$

2.2 Circular mesh geometry

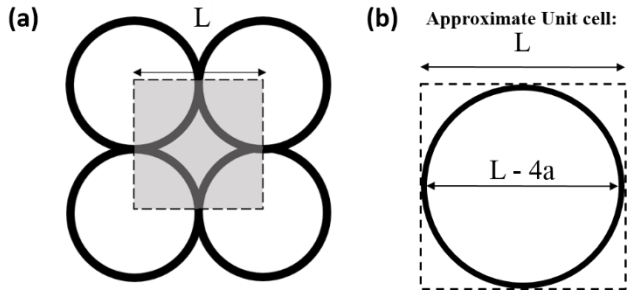

Figure B.2: (a) Schematic of circle mesh with unit cell (dashed area). (b) Approximate unit cell is one circle and is the unit cell used for this derivation.

Let: a = linewidth/2, L = outer diameter of circle.

Unit cell area:

$$A_{cell} = L^2 \tag{7}$$

Mesh area:

$$A_{outer\ circle} = \pi\left(\frac{L}{2}\right)^2 = \frac{\pi}{4} L^2 \tag{8}$$

$$A_{inner\ circle} = \pi\left(\frac{L-2W}{2}\right)^2 = \frac{\pi}{4} (L^2 - 4WL + 4W^2) \tag{9}$$

$$A_{mesh} = A_{outer\ circle} - A_{inner\ circle} \tag{10}$$

$$A_{mesh} = \frac{\pi}{4} (L^2 - L^2 + 8aL - 16a^2) = \frac{\pi}{4} (4WL - 4W^2) \tag{11}$$

% Area covered by metal ≡ Q:

$$\mathrm{Q} = \frac{\mathrm{A_{mesh}}}{\mathrm{A_{cell}}} = \frac{\frac{\pi}{4}\left(4\mathrm{WL} - 4\mathrm{W}^2\right)}{\mathrm{L}^2} = \frac{\pi}{4}\left(\frac{4\mathrm{WL} - 4\mathrm{W}^2}{\mathrm{L}^2}\right) \quad \textbf{(12)}$$

Transparency = 1 – Q:

$$T = 1 - Q \approx 1 - \frac{\pi}{4}\left(\frac{4WL - 4W^2}{L^2}\right) \quad \textbf{(13)}$$

2.3 Hexagonal mesh geometry

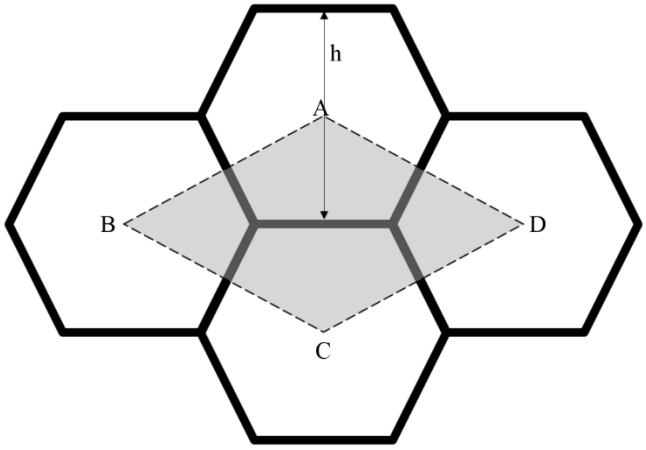

Figure B.3: Schematic of hexagonal mesh with unit cell (dashed area).

Let: L = length of one side of hexagon, W = linewidth, a = W/2

Unit cell area:

$$Area\ \Delta_{ACD} = Area\ \Delta_{ACB} = \frac{1}{2}\ b \times h = \frac{1}{2}\ AB\ Sin\ C \quad \textbf{(14)}$$

$$= \frac{1}{2}\left(\sqrt{3}\ L\right)\left(\sqrt{3}\ L\right) Sin\ 60°$$

$$Area\ \Delta_{ACD} = \frac{3}{2}\ L^2\ \left(\frac{\sqrt{3}}{2}\right) = \frac{3\sqrt{3}}{4}\ L^2 \quad \textbf{(15)}$$

$$A_{cell} = Area\ \Delta_{ACD} + Area\ \Delta_{ACB} = 2\ Area\ \Delta_{ACD} = 2\left(\frac{3\sqrt{3}}{4}\ L^2\right) \quad \textbf{(16)}$$

$$= \frac{3\sqrt{3}}{2}\ L^2$$

Mesh area:

$$A_{mesh} = 3WL \tag{17}$$

% Area covered by metal ≡ Q:

$$Q = \frac{A_{mesh}}{A_{cell}} = \frac{3WL}{\frac{3\sqrt{3}}{2} L^2} = \frac{2W}{\sqrt{3}\, L} \tag{18}$$

Transparency = 1 – Q:

$$T = 1 - Q = 1 - \frac{2W}{\sqrt{3}\, L} \tag{19}$$

To get T in terms of hexagon height h, from Δ_{ACD} (equilateral triangle):

$$h = \sqrt{3}\, L \tag{20}$$

Therefore:

$$T = 1 - Q \approx 1 - \frac{2W}{h} \tag{21}$$

2.4 Pentagonal mesh geometry

The unit cell of the new pentagon mesh consists of an array of 12 pentagons (Figure B**.4**). Note that the unit cell is not unique. Any other array of 12 pentagons can also be the repeatable pattern.

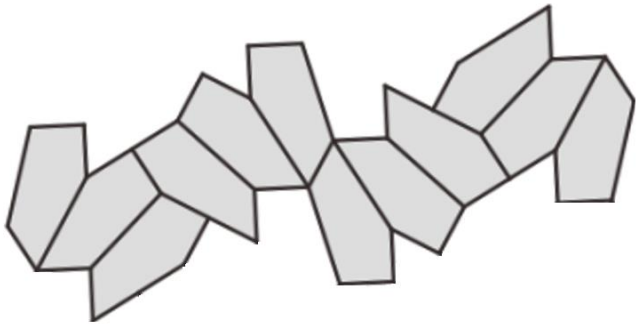

Figure B.4: Unit cell of new pentagon shape which consists of an array of 12 pentagons.

The area covered by the new pentagon shape is calculated by dividing the shape into two triangles and a square. The area of each shape is gotten individually. The length of one of the smallest sides is denoted by *d*.

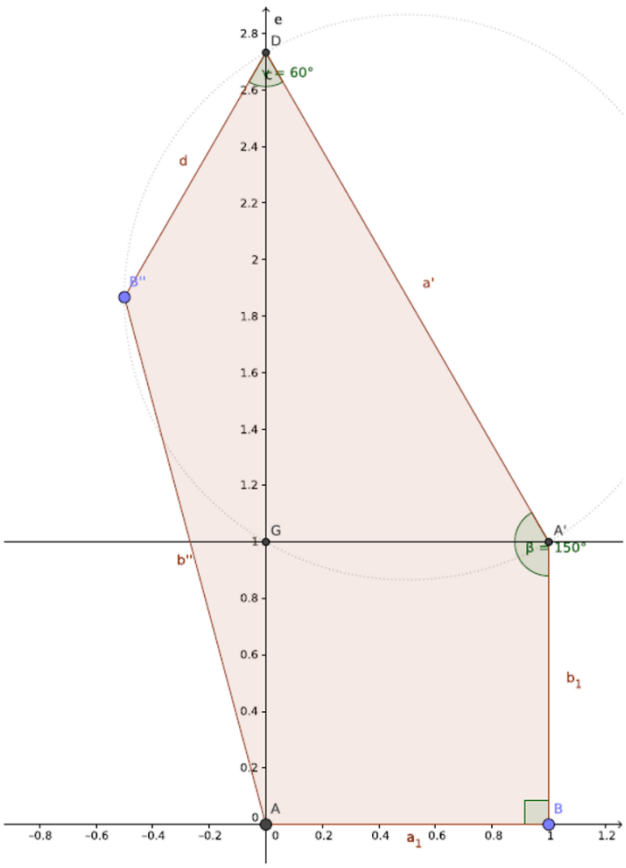

Figure B.5: Geometry of new pentagon shape used in derivation of shape's transparency.

The length from point G to D is

$$\overline{\mathrm{GD}} = \sqrt{2^2 - 1^2}\mathrm{d} = \sqrt{3}\mathrm{d} \tag{22}$$

The three areas (one square and two triangles) are calculated as the following

$$\mathrm{A}_{\mathrm{ABA'G}} = \mathrm{d}^2 \tag{23}$$

$$\mathrm{A}_{\mathrm{GA'd}} = \frac{1}{2} \times \mathrm{d} \times \sqrt{3}\mathrm{d} = \frac{\sqrt{3}}{2}\mathrm{d}^2 \tag{24}$$

$$\mathrm{A_{ADB''}} = \frac{1}{2} \times \left(1 + \sqrt{3}\right)\mathrm{d} \times \frac{1}{2}\mathrm{d} = \frac{1 + \sqrt{3}}{4}\mathrm{d}^2 \quad \textbf{(25)}$$

Using all three areas above, the total area of the fundamental pentagon is

$$\mathrm{A_T} = \mathrm{d}^2 + \frac{\sqrt{3}}{2}\mathrm{d}^2 + \frac{1 + \sqrt{3}}{4}\mathrm{d}^2 \approx 2.55\mathrm{d}^2 \quad \textbf{(26)}$$

For the total length of the tile perimeter

$$\overline{AB} = \overline{BA'} = \overline{DB^{"}} = d \quad \textbf{(27)}$$

$$\overline{A'D} = 2d \quad \textbf{(28)}$$

$$\overline{B^{"}A} = \sqrt{\left(\frac{1}{2}\right)^2 + \left(1 + \frac{\sqrt{3}}{2}\right)^2}\, d \approx 1.93d \quad \textbf{(29)}$$

The total perimeter is

$$\mathrm{L} = \left[5 + \sqrt{2 + \sqrt{3}}\right]\mathrm{d} \approx 6.93\ \mathrm{d} \quad \textbf{(30)}$$

To find the transparency, we calculate the area covered by the lines of one pentagon as the width of the lines w times the perimeter L (strictly valid for d >> w)

$$A_L = wL = \left[5 + \sqrt{2 + \sqrt{3}}\right] Wd \approx 6.93\, Wd \tag{31}$$

This total area is divided by two to prevent double-counting for adjacent pentagonal tiles. Therefore the fraction Q of the total area covered by metal is

$$Q = \frac{A_L}{2A_T} \approx \frac{6.93\, Wd}{5.1\, d^2} \approx 1.36 \frac{W}{d} \tag{32}$$

Thus the transparency is

$$T = 1 - Q \approx 1 - 1.36 \frac{W}{d} \tag{33}$$

3 Appendix C

Supplementary material for chapter 6

Temperature accuracy of FLIR One thermal camera

The accuracy of the temperature readings from the FLIR One thermal camera for Android was found by comparing the temperature readings measured from a temperature probe. 3 M Scotch Super 33+ black vinyl electrical tape, with a known emissivity of ~ 0.95 [1], was wrapped around a beaker (Duran, 25 mL) containing ~ 20 mL of deionised water. The beaker was then placed on a hotplate (Fluke) and the temperature was measured by using a temperature probe (IKA Werke, ETS-D4). The thermal images were taken at a fixed working distance of ~ 12 cm. Note that the maximum temperature on the hotplate was set to ~ 105 ºC as 3 M Scotch Super 33+ black vinyl electrical tape is designed to work continually up to this temperature [2].

Table C.1. Comparison between the temperature readings of heated deionized water in a beaker measured by a temperature probe with that of the FLIR One thermal camera.

Temperature probe reading (ºC):	FLIR One mean temperature reading (ºC):
50.1	49.7
60.5	58.9
70.6	70.1
80.1	79.7
90	89.3
100	99.1

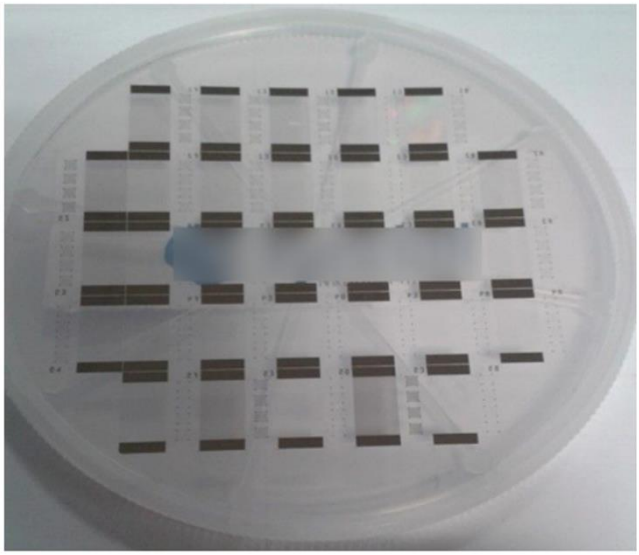

Figure C.1: Patterning of metal mesh devices on a 100 mm diameter piece of PET sheet (125 μm thick) by lithography, metal evaporation (Ti 10 nm, Pt 50 nm) and lift-off.

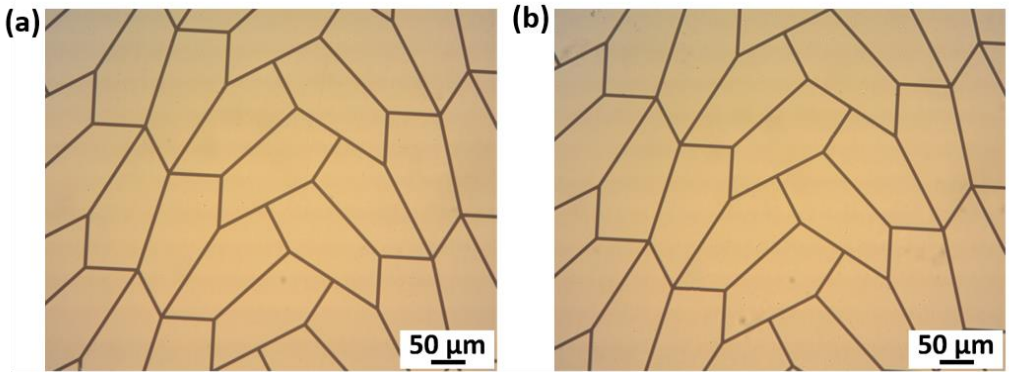

Figure C.2: (a) Representative high-resolution transmission-mode optical microscopy image of a region from the central part of a Design#3 device (5 μm linewidth, 9% metal area coverage) after fabrication. (b) Optical image of a region from the central part of the same device after 1,000 tensile bending cycles.

Adhesion Testing. The adhesion of the metal mesh to the PET substrate was undertaken using 3M scotch tape, as described by IPC-TM-650 (tape adhesion test) [3]. No delamination was observed after this adhesive test.

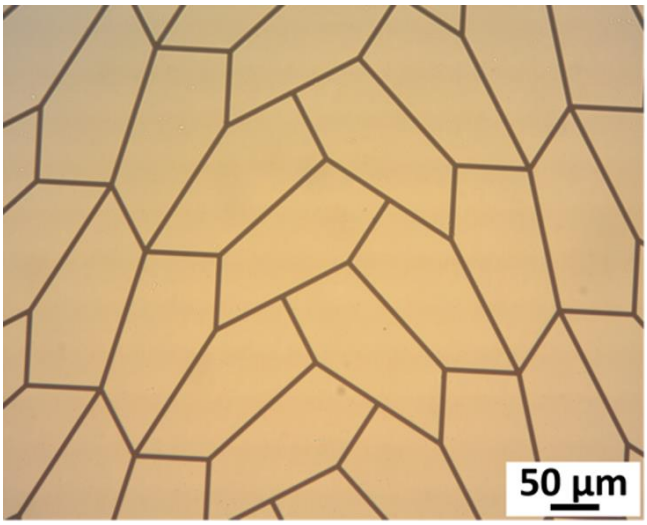

Figure C.3: (a) Representative high-resolution transmission-mode optical microscopy image of Design#3 (5 µm linewidth, 9% metal area coverage) after an adhesion tape test (IPC-TM-650).

Thermal Characterization.

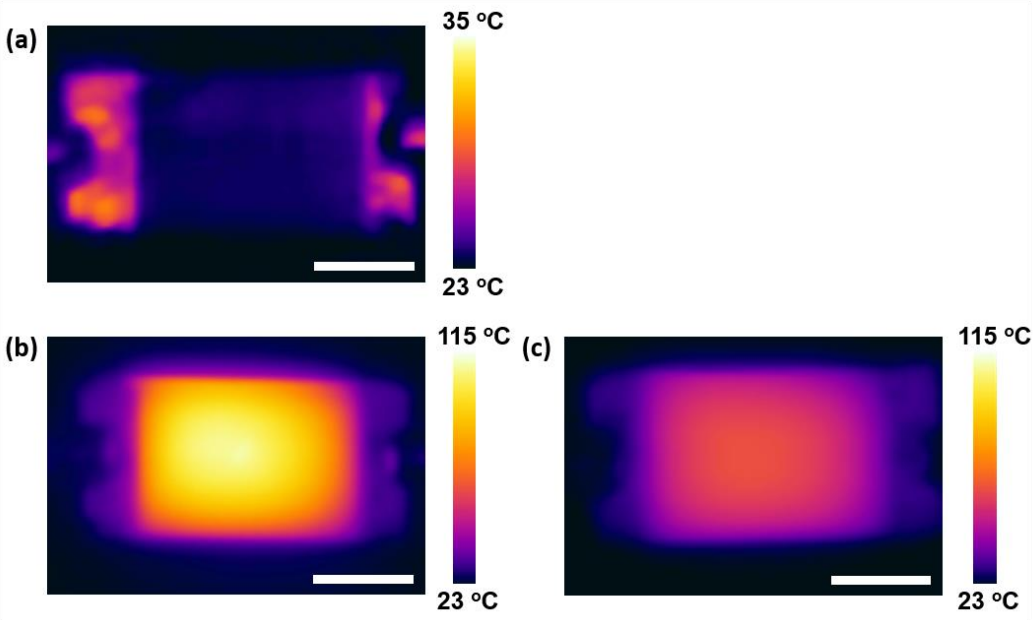

Figure C.4: (a) Thermal image of Design#2 (14% metal area coverage) 40 s after the bias voltage of 5 V was turned off. (b) Thermal image of Design#1 (27% metal area coverage) at 90 s of applying 4 V. (c) Thermal image of Design#3 (9% metal area coverage) at 90 s of applying 5 V. All scale bars in the above images are 5 mm.

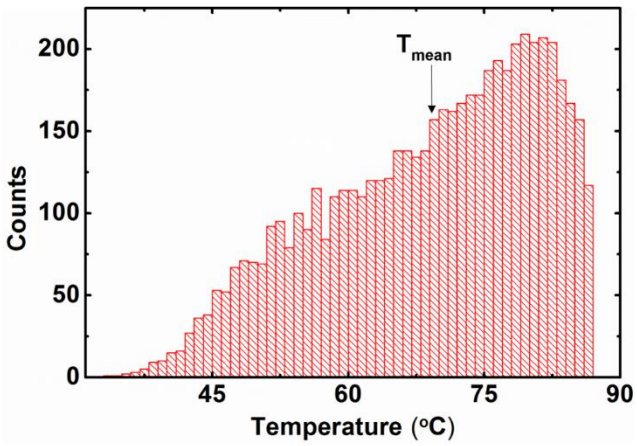

Figure C.5: Temperature distribution over the marked rectangular area in Figure 4a in the main text of Design#2 taken 90 s after applying a constant bias voltage of 5 V. The mean temperature value is 69 ± 12 °C.

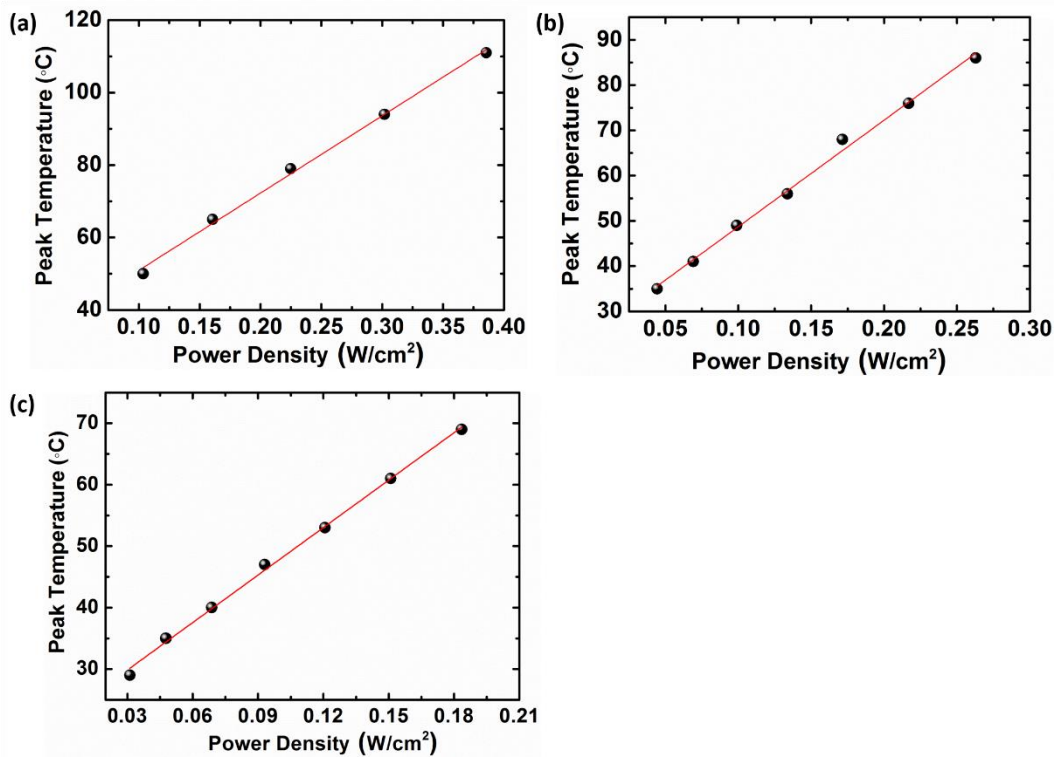

Figure C.6: (a) Peak temperature versus power density for Design#1 (27% metal area coverage) from 2 V to 4 V in steps of 0.5 V with a corresponding thermal resistance value of ~ 213 ± 7 ^{o}C cm^2/W. (b) Peak temperature versus power density for Design#2 (14% metal area coverage) from 2 V to 5 V in steps of 0.5 V with a corresponding thermal resistance value of ~ 235 ± 7 ^{o}C cm^2/W. (b) Peak temperature versus power density for Design#3 (9% metal area coverage) from 2 V to 5 V in steps of 0.5 V with a corresponding thermal resistance value of ~ 258 ± 5 ^{o}C cm^2/W.

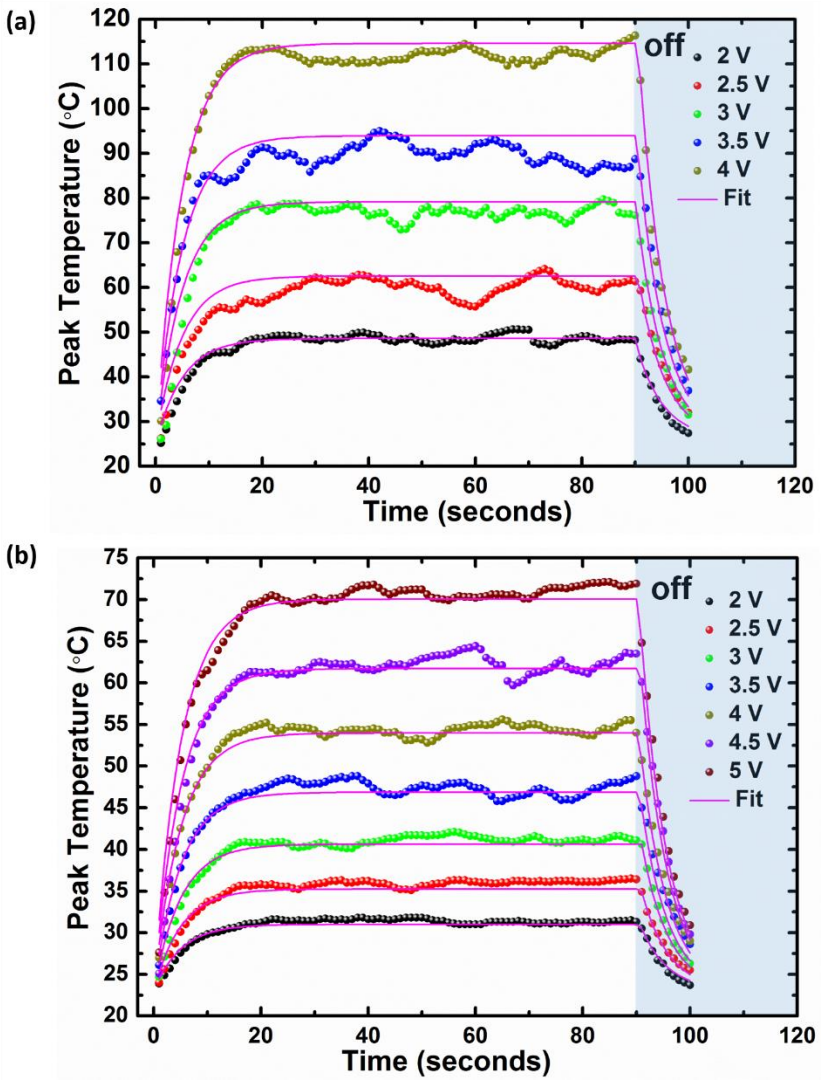

Figure C.7: (a) Temperature versus time for Design#1 for voltages in the range of 2 V to 4 V in steps of 0.5 V. The data was fitted using a heater transfer coefficient value of $h \sim 44$ $Wm^{-2}K^{-1}$ and a time constant, $\tau = 5$ s. (b) Temperature versus time for Design#3 for voltages in the range of 2 V to 5 V in steps of 0.5 V. The data was fitted using a heater transfer coefficient value of $h \sim 39$ $Wm^{-2}K^{-1}$ and a time constant, $\tau = 5$ s.

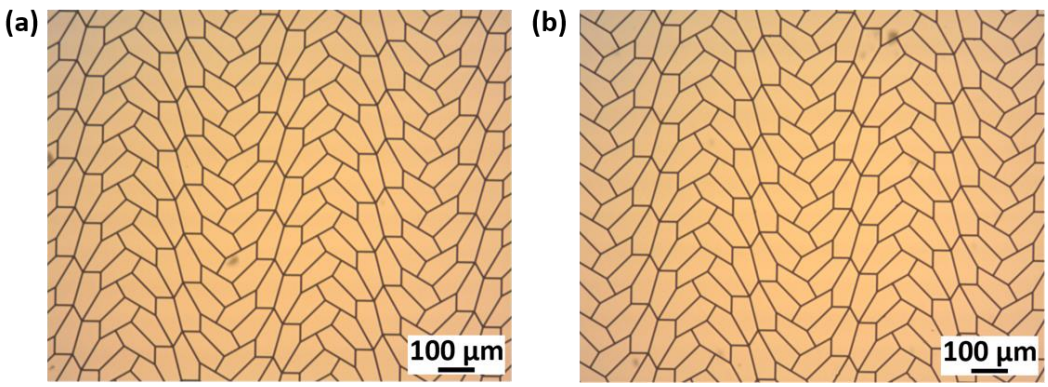

Figure C.8: (a) & (b) Representative high-resolution transmission-mode optical microscopy image of Design#2 (5 µm linewidth, 14% metal area coverage) after 10 thermal cycles (heating and cooling). No mechanical damage of the metal mesh occurred due to thermal cycling. Each thermal cycle consisted of applying a bias voltage range of 2 V to 5 V in steps of 0.5 V. Each bias voltage was applied for 90 seconds and was then switched off for 40 seconds before applying the next bias voltage.

4 Appendix D - Miscellaneous

4.1 Publications

- Lordan, D. *et al*. - Asymmetric pentagonal metal meshes for flexible transparent electrodes and heaters, ACS Applied Materials & Interfaces, 2017, 9 (5), pp 4932–4940

4.2 Outputs

- Outreach: Discovery Exhibition, City Hall, Cork November 2012 & 2013

- Conference talk:

"Molecular Functionalization of Exfoliated Graphene and Transferred CVD Graphene"

Materials Research Society, Symposium LL on Transparent Electrodes, April 2014, San Francisco

- Tyndall poster competition 2012, 2014, 2015 and 2016 (top 8 finalist)

4.3 Modules (5 credits each, 40 credits in total)

- LW6104: Intellectual Property law for entrepreneurs
- SE6001: Compound semiconductor device fabrication
- UE6005: Nanoelectronics
- PG6001: STEPS (Scientific Training for enhanced Postgraduate Study)
- SE6003: Polymer Materials
- PG6009: Graduate information literary skills
- UE6022: Packaging and reliability
- IS6306: Technology business planning

4.4 Other

- Top 10 finalist of UCC entrepreneur of the year award 2015
  "Smart Needle" (Lisa Helen, Niamh Creedon and Daniel Lordan)

Bibliography:

1. Hsiao, Y. S., *Characterization of Lesion Formation and Bubble Activities During High-Intensity Focused Ultrasound Ablation Using Temperature-Derived Parameters.* Infrared Physics and Technology, 2013**, 60**, p. 108-117.
2. Scotch® Super 33+™ Vinyl Electrical Tape Product Page. http://solutions.3m.com/wps/portal/3M/en_US/EMDCI/Home/Products/ProductCatalog/~/Scotch-Super-33-Vinyl-Electrical-Tape?N=5432987+3294355633&rt=rud (accessed 1 Oct, 2016).
3. IPC-TM-650 Adhesion Test. https://www.ipc.org/TM/2.4.1E.pdf (accessed 21 Nov,2016).